Università degli Studi di Ferrara

ISTITUTO ITALIANO DI TECNOLOGIA

DOCTORAL COURSE IN
TRANSLATIONAL NEUROSCIENCE AND
NEUROTECHNOLOGIES

CYCLE XXXVIII

COORDINATOR Prof. Luciano Fadiga

Enhancing the Response of Electrolyte-Gated Organic Transistors by Surface Chemistry, Low Dimensional Materials, and Multivariate Data Analysis

Scientific/Disciplinary Sector (SDS) BIO/09

Candidate
Dott. Genitoni Matteo

_____
(signature)

Supervisor
Prof. Biscarini Fabio

_____
(signature)

Year 2022/2025

This page is left blank intentionally

Abstract

Organic bioelectronics is aimed to seamlessly interface devices based on organic semiconductors with biological systems. These devices, operated in an electrolyte, transduce biological signals into an electronic response. The unique properties of organic electronic materials-including mixed ionic-electronic conductive channels, low-voltage operations, stability in aqueous environment, biocompatibility, flexibility, and ease of fabrication-make them an ideal bridge between biology and technology. Among them, Electrolyte-Gated Organic Transistors (EGOTs) amplify minute polarization changes at the functional material-electrolyte interface into a multiparametric change of the current characteristics. Their high sensitivity makes them especially suitable for modulating and processing signals generated by ionic and molecular interactions with biological systems.

This PhD thesis demonstrates the synergy between materials design and advanced data analysis of the EGOT's multiparametric response with the aim to significantly advance biosensing and neuromorphic applications. In the first part of the work, a label-free EGOT immunosensor is developed for the discrimination of Tryptophan (Trp) enantiomers. By optimizing the antibody anchoring protocol, unprecedented levels of detection are achieved. Furthermore, a novel approach leveraging the sensor's multiparametric response with a multivariate analysis (Principal Component Analysis, PCA) enables the discrimination between L- and D-Trp at the sub-picoMolar level.

The versatility of EGOT biosensors for detecting small-molecule biomarkers is further explored by integrating MXenes as a functionalization layer in a Poly(3,4-ethylenedioxythiophene) polystyrene sulfonate (PEDOT:PSS) device for Dopamine (DA) detection. MXenes are an emerging class of two-dimensional materials which are promising for bioelectronic sensing for their high stability of the response and their versatile surface chemistry. MXenes with different chemical properties are demonstrated to successfully detect DA in the femtoMolar range. Furthermore, the analysis of the EGOT's response provides insights into the interaction mechanism between DA and the MXene surface.

Finally, the thesis delves into the fundamental understanding of the EGOT device physics to support their translational potential. This is achieved by studying cation interactions at the interface with two key materials: reduced Graphene Oxide (rGO)

and PEDOT:PSS. A novel method for fabricating rGO-based electrolyte-gated transistors (EGTs) via *in-situ* electrodeposition is presented. After optimizing a specific conditioning protocol, these devices exhibit reliable multilevel memory behaviour, driven by cation intercalation. The investigation of ion dynamics is then extended to PEDOT:PSS-based EGOTs operating in electrolytes of different composition. Here, the device's multiparametric response is leveraged to correlate its steady-state electrical behaviour with the physicochemical properties of the electrolyte, providing a deeper understanding of the sensing and transduction mechanisms.

Sommario

La bioelettronica organica si propone di integrare dispositivi basati su semiconduttori organici con sistemi biologici. Questi dispositivi, operanti in presenza di elettrolita, trasducono i segnali biologici in una risposta elettrica. Le proprietà peculiari dei materiali elettronici organici, tra cui la conduzione ionica-elettronica, l'operatività a bassi voltaggi, la stabilità in ambiente acquoso, la biocompatibilità, la flessibilità e la facilità di fabbricazione, rappresentano la connessione ideale tra il mondo biologico e quello tecnologico. Tra questi dispositivi, gli Electrolyte-Gated Organic Transistors (EGOTs) amplificano le più piccole variazioni di polarizzazione che possono avvenire all'interfaccia tra il materiale attivo e l'elettrolita, convertendole in una variazione multiparametrica delle caratteristiche del transistor. L'elevata sensibilità mostrata da questi dispositivi li rendono particolarmente adatti per modulare e processare il segnale generato da interazioni ioniche e molecolare con sistemi biologici.

Questa tesi dimostra come combinando strategie di funzionalizzazione ottimizzate con metodologie di analisi dati avanzate della risposta multiparametrica tipica dei dispositivi EGOTs, è possibile migliorarne sensibilmente le applicazioni in ambito (bio)sensoristico e neuromorfico. Nella prima parte di questo lavoro è stato sviluppato un immuno-sensore a base EGOT per la discriminazione degli enantiomeri del Triptofano. Ottimizzando il processo di ancoraggio dell'anticorpo è possibile raggiungere livelli di detection senza precedenti. Inoltre, un approccio innovativo basato sull'integrazione della risposta multiparametrica del sensore con metodologie di analisi multivariata (Principal Component Analysis, PCA) ha permesso di discriminare le forme enantiomeriche L- e D-Trp a concentrazione nel range del sub-picoMolare.

Inoltre, è stata esplorata la versatilità dei biosensori EGOT a rilevare molecole che rappresentano importanti biomarcatori integrando i MXeni come layer di funzionalizzazione di un dispositivo a base di Poli(3,4etilendiossitiofene) polistirene solfonato (PEDOT:PSS) per la rilevazione di Dopamina. I MXeni sono una classe di materiali bidimensionali emergenti che sono promettenti per applicazioni sensoristiche nella bioelettronica in quanto presentano elevata stabilità della risposta e una chimica superficiale versatile. In questo lavoro di tesi si è dimostrato come MXeni con diverse proprietà chimiche sono in grado di rilevare Dopamina in

un range di concentrazione pari al femtoMolare. Inoltre, l'analisi della risposta degli EGOTs ha fornito importanti informazioni sul meccanismo di interazione tra la Dopamina e la superficie di MXene.

Infine, questa tesi approfondisce gli aspetti fondamentali della fisica dei dispositivi EGOT per supportare la loro applicazione in un'ottica traslazionale. Per fare questo, si è studiata l'interazione dei cationi all'interfaccia con due materiali chiave nelle applicazioni della bioelettronica: l'ossido di grafene ridotto (rGO) e il PEDOT:PSS. In particolare, questo lavoro presenta un nuovo metodo di fabbricazione di rGO-EGT mediante l'elettrodeposizione *in-situ*. Dopo aver ottimizzato un protocollo di condizionamento specifico, questi dispositivi mostrano un affidabile comportamento di memoria multilivello, guidato dall'intercalazione di cationi. Lo studio della dinamica degli ioni è quindi esteso ad EGOTs a base PEDOT:PSS che operano in elettroliti di diversa composizione. Si è sfruttata la risposta multiparametrica dei dispositivi per correlare il loro comportamento allo stato stazionario con le proprietà fisico-chimiche dell'elettrolita, fornendo una comprensione più approfondita dei meccanismi di sensing e di trasduzione.

Contents

List of Figures

***Figure 4.3**: Comparison of EGOT performance post. SBR functionalization. Representative transfer characteristics of TIPS-pentacene EGOTs featuring SBR-functionalized gate electrodes with areas of 4 mm^2 (black line) and 15.85 mm^2 (red line).*

***Figure 4.4**: Schematic of the antibody immobilization strategies on the gold (Au) gate electrode. (a) The Schiff Base Reaction (SBR) protocol: a cysteamine (CYS) SAM is activated by glutaraldehyde (GA), which crosslinks the SAM's primary amines to the antibody's amine groups via imine bond formation. (b) The EDC-NHS protocol: A mixed SAM of 11-mercaptoundeanoic acid (11-MUA) and 6-mercaptohexanol (6-MH) is formed. The carboxyl groups of 11-MUA are activated by EDC and NHS to form a stable N-succinimidyl ester, which subsequently reacts with the antibody's amine groups to form a covalent amide bond.*

***Figure 4.5**: Summary of possible forms of GA in aqueous solution. Adapted from:*[45].

***Figure 4.6**: Proposed reaction mechanism of (polymeric) GA with primary amines (cysteamine linked to gold surface) exposing terminated amino group*.

***Figure 4.7**: Electrochemical characterization. The cyclic voltammetry is plot before (dashed lines) and after (continuous line) incubation with Tryptophan antibody. The four panels highlight the effect of pH, in the glutaraldehyde step, on recorded CV current, pH 4 (orange, panel a), pH 6 (green, panel b), pH 8 (cyan, panel c), pH 10 (blue, panel d). e) Oxidation peak current for electrodes covered with CYS and GA (SAM) and after incubation with antibody (SAM+ANTI) vs pH of the GA solution. f) Reduction peak current for the same electrodes as in panel e.*

***Figure 4.8**: Electrochemical Impedance Spectroscopy (EIS) on electrodes functionalized with SBR strategy. a) complete Nyquist plot of faradic EIS, reported with the same colour code as in Figure 4.7; b) magnification of the Nyquist plot that shows the limited increase of charge-transfer resistance obtained upon antibody incubation when GA is processed at 4 < pH < 8.*

***Figure 4.9**: Integration of functionalized electrodes in EGOT architecture. a) the variability of I_{DS} @V_{GS} = -0.7V (reported as the SD of I_{DS} @V_{GS} = -0.7V) in PBS before the addition of the target analyte. Error bars are the standard deviation of three different devices. b-f) Representative transfer characteristics collected with gate electrodes functionalized at different GA pHs, in PBS (light grey) and at increasing concentration of L-Trp (11 pM, 60 pM, 425 pM).*

***Figure 4.10**: Representative transfer characteristics of the EGOT device (V_{DS} = -0.2 V) obtained after the consecutive steps of functionalization with SBR protocol at pH=10. It appears evident the increase of resistance after the formation of GA polymeric layer and a further decrease of maximum current is evident when the antibody is anchored and the final passivation is performed with ethanolamine.*

***Figure 4.11**: Electrochemical comparison between SBR (blue) and EDC-NHS (red) functionalization strategies. CV voltammograms before (dashed line) and after (continuous line) incubation with anti-L-Trp antibody for SBR (a) and EDC-NHS (b). EIS Nyquist's plots for SBR (c) and EDC-NHS (d) that evidences the increase of the impedance upon antibody binding.*

***Figure 4.12**: Topography of (functionalized) gate electrodes. Atomic Force Microscopy (AFM) images of a) bare gold electrode after cleaning procedure; b) morphology of EDC-NHS-functionalized electrode; c) morphology of electrode activated with SBR functionalization showing wavy feature.*

***Figure 4.13**: Electrical characterization in presence of increasing concentration of L-Trp. Representative transfer curves of EGOT device (V_{DS} = -0.2 V) with gate electrode functionalized with SBR (blue, a) and with the EDC-NHS protocol (red, b) upon interaction with L-Trp. Transconductance (viz., first derivative $\frac{dI_{DS}}{dV_{GS}}$) vs V_{GS} for SBR (blue, c) and EDC-NHS (red, d) upon increasing concentration of target analyte.*

***Figure 4.14**: L-Tryptophan sensing with SBR (blue) and EDC-NHS (red). a) Semilog plot of the current signal SI_{DS} vs [L-Trp]. In the inset of panel a, a representative transfer curve is fitted according to Equation 4.1. b) Semilog plot of the signal $Sg_{m,I}$ vs [L-Trp]. In the inset of Figure 4.14b the dashed line is power law used as guide to the eye to describe $\Delta g_{m,max}$ vs [L-Trp]. c) Semilog plot of the turn-on voltage shift ΔV_T vs [L-Trp]. d) Semilog plot of the shift of the parameter α vs [L-Trp]. Dashed lines are guide-to-the-eye obtained by best fit with ULM Equation 4.2.*

***Figure 4.15**: Control experiments. a) Signal calculated on current in control experiments performed with gate electrodes functionalized with or and without the monoclonal anti-L-Trp antibody. b) Device response when the functionalized gate electrodes functionalized with the complete SBR protocol is exposed to L-Arginine (magenta dots). In the semilog plot of the signal vs [analyte], the experimental data are fitted with ULM Equation 4.3 as guide for the eyes.*

***Figure 4.16**: Analysis of the response of SBR functionalized EGOT upon exposure to L-Trp (blue markers) and D-Trp (orange markers) solutions. a) Representative transfer curves of EGOT device (V_{DS} = -0.2 V) with the gate electrode functionalized with optimum SBR protocol. The inset shows the chemical structure of L and D Tryptophan enantiomers. b) Semilog plot of the signal $Sg_{m,I}$ vs [Trp]. The inset shows the semilog of the current signal at V_{GS} -0.4 V vs [Trp]. c) Semilog plot of the renormalized turn-on voltage shift ΔV_T vs [Trp]. d) Semilog plot of the shift of the parameter Δα vs [Trp]. Dashed lines are guide-to-the-eye obtained by best fit with ULM Equation 4.3.*

***Figure 4.17**: ELISA assays. a) Normalized results obtained from the ELISA test for L-Trp (black marker) and D-Trp (red marker), performed using the mouse monoclonal anti-L-Trp antibody (the same used in the EGOT immunosensor). The sensitivity range is between 1 pM and 1 μM. Dashed lines represent the best-fit curves obtained using the following expression: $\frac{B}{B_0} = START + (END - START)\left(1 - \frac{{K_A}^n[Trp]^n}{1+{K_A}^n[Trp]^n}\right)$. b) Normalized results obtained from the ELISA test using the rabbit polyclonal anti-L-Trp antibody for L-Trp (grey marker) and D-Trp (light red marker), within the sensitivity range declared by the manufacturer (from 10 μM to 1 mM).*

***Figure 4.18**: PCA analysis EGOT immunosensor. (a) Scores (black axes) and loadings (green axes) biplot obtained from the PCA analysis from SBR functionalized EGOTs for L-Trp (orange markers) and D-Trp (blue markers). (b) Same data of Figure 4.18a with their respective parabolic fit (continuous lines) and their prediction ranges at 90% level (shadowed areas). Two unknown concentration samples (star and pentagon) assigned to L or D clusters in the PC biplot and later correlated to the points on the dose curve Δα vs [Trp] (inset) yielding their concentration. (c) PCA score plot computed by combining all points of the best fit curves of the four variables shown in Figure 4.16 (empty markers, ULM for the dose curves) superimposed to the experimental ones (filled markers, exp). Parabolic fit is plotted as guide for the eyes. (d) The score plot of PC3 versus PC4 obtained from PCA analysis carried out on the entire dataset for L-Trp (blue markers) and D-Trp (orange markers). The clusterization of the two enantiomeric forms is highlighted by the parabolic fit (reported with 95% confidence bands, shadowed areas) included as a guide for the eyes. The EGOT-PCA model si validated with four independent experimental points.*

***Figure 4.19**: Validation of EGOT-chemometric model through Partial Least Square-Discriminant Analysis (PLS-DA). a) Illustration of PLS-DA classification model based on predicted response calculated for L-Trp (blue markers) and D-Trp (orange markers) at all concentrations. The black dashed line represents the calculated classification threshold (y=0.47): samples falling above the line are assigned to D-Trp, while samples falling below are assigned to L-Trp. b-c) Receiver Operating Characteristic (ROC) curves for PLS-DA model for L-Trp (b) and D-Trp (c) samples. d) Plot of predicted response against the concentration to highlight the correct association of four independent validation points to the enantiomeric group (blue stars for L-Trp and orange pentagons for D-Trp).*

***Figure 5.1**: Comprehensive characterization of the MAX phase. a) X-ray diffraction patterns of MAX phase (black) and HF-MX (grey). b) Raman spectra of MAX phase (black) and HF-MX (grey). c) The high-resolution C1s, O1s, N1s, F1s, Al2p, Ti2p XPS spectra of MAX phase and HF-MX. d) The SEM images at low (left) and high (right) magnification for MAX phase (top) and HF-MX samples (bottom).*

***Figure 5.2**: Comprehensive characterization of the chemically-engineered MXenes. a) Raman spectra of HF-MX (grey), Ar-MX (blue), H_2-MX (red), N-MX (green). b) FITR spectra of HF-MX (grey), Ar-MX (blue), H_2-MX (red), N-MX (green). c) The high-resolution C1s, O1s, N1s, F1s, Al2p, Ti2p XPS spectra of Ar-MX (left), H_2-MX (center), N-MX (right). d) The SEM images at low (left) and high (right) magnification for Ar-MX (left), H_2-MX (center), N-MX (right).*

***Figure 5.3**: Functionalization of gold electrodes with chemically-modified MXenes. a) Low and b) high magnification SEM images of gold electrodes covered with surface-engineered MXenes. c) CVs of the Au and Au/MXenes electrodes, recorded in the $K_3[Fe(CN)_6]$ redox probe, scan rate 100 mV/s. d) EIS Nyquist plots of the Au and Au/MXenes electrodes, recorded in the $K_3[Fe(CN)_6]$ redox probe, E = 260 mV vs Ag/AgCl*

***Figure 5.4**: Architecture and electrical characterisation of the MXene-functionalized EGOT device. a) Scheme of the EGOT device; b) Layout of the DA sensor; c) Representative transfer curves recorded with gold (yellow), H_2-MX (red), N-MX (green), Ar-MX (blue) electrode; d) corresponding transconductance (viz., first derivative of I_{DS}) V_{DS} = -0.2 V, 50 mM PBS as electrolyte.*

***Figure 6.3**: Evaluation of the GO dispersion concentration over the electrical behaviour of rGO-EGTs. a) Dependency of the thickness of the electrodeposited rGO channels on the concentration of GO dispersions ($n_{samples}$=3, SD as error bars). Dashed lines are linear fitting used as guide for the eyes. b) Representative transfer characteristics (I_{DS} vs V_{GS} plot) after cycling conditioning (viz., the 30th transfer curves, see discussion below for further details) for rGO-EGTs fabricated from GO dispersion at different concentrations. c-f) Details of transfer characteristics with 0.1 wt% (c), 0.2 wt% (d), 0.3 wt% (e), 0.4 wt% (f).*

***Figure 6.4**: Dependency of thickness of electrodeposited rGO channels on V_{end} ($n_{samples}$=3, SD as error bars). Dashed lines are linear fitting used as guide for the eyes.*

***Figure 6.5**: Electrical characterization of rGO-EGTs. a) rGO-EGT schematics for steady state characterization. b) Transfer characteristic after rGO growth on IDE channels. c) Evaluation of the transfer curves upon iterative VGS cycling (starting from black line to blue line). d) Dependency of VCNP vs the number of the gate sweep cycles ($n_{samples}$ = 9, SEM as error bars).*

***Figure 6.6**: Effect of the conditioning process on the electrical performance of rGO-EGTs. a) Transfer characteristics of rGO-EGTs before (solid blue line) and after DC gate voltage reconditioning step (green solid line) (n_{sample} = 8 SEM as error bars). b) Improved transconductance (g_m) in rGO-EGTs after reconditioning step (green, solid line) compared to the g_m profile of rGO-EGTs after the 30th V_{GS} sweep (blue solid line) (n_{sample} = 8 SEM as error bars). Negative shift of V_{CNP} after reconditioning is shown as the point at null g_m (red dot-dashed lines). c) 3D representative of I-V characteristics of a representative rGO-EGT.*

***Figure 6.7**: Single pulse response of rGO-EGTs. a) rGO-EGT schematics for neuromorphic device characterization. b) Representative chronovoltammogram (top) and chronoamperogram (bottom) for positive (red solid line) and negative (black solid line) single voltage pulse administration with a pulse with of 1s. c) Dependency of the pulse current amplitude $I_{DS,t2} – I_{DS,0}$ on $V_{GS,p}$ (n_{sample} = 4, standard error of the mean as error bars). d) DCP_i vs $V_{GS,p}$ trend for Δt = 1 s, highlighting operational windows to achieve tailorable plasticity. It is possible to distinguish four regions: i) $V_{GS,p}$ > 0.15 V elicits potentiation; ii) small values of $V_{GS,p}$ (either positive or negative) do not elicit plasticity, with DCPi values oscillating ≈ 0 μA (zoom in the inset); iii) - 0.65V < $V_{GS,p}$ < −0.15 V elicits potentiation; iv) $V_{GS,p}$ < −0.65V elicits depression (n_{sample} = 4, standard error of the mean as error bars). e) DCP_i vs $V_{GS,p}$ trend for different pulse duration: Δt = 1 s (green), Δt = 2 s (yellow), Δt = 5 s (orange), Δt = 10 s (brown).*

***Figure 6.8**: Response of rGO-EGTs upon pulse train administration. a) Typical input positive square voltage train (top panel, red, $V_{GS,p}$ = +0.5 V, V_{DS} = +0.3 V) and recorded neuromorphic I_{DS} response (bottom panel, red). b) Typical input negative square voltage train (top panel, black, $V_{GS,p}$ = -0.5 V, V_{DS} = +0.3 V) and recorded neuromorphic I_{DS} response (bottom panel, black). Dependency of the baseline current modulation $\Delta I_{DS,n}$ upon the number of administered pulses (n) and upon pulse amplitude ($V_{GS,p}$) (n_{sample} = 3). d) Number of accessible memory states as a function of $V_{GS,p}$ (n_{sample} = 3, SEM as error bars. e) Typical input positive pulse train administration (top panel, red, $V_{GS,p}$ = +0.5 V) and the recorded neuromorphic I_{DS} response (bottom panel, red). f) Typical input negative pulse train administration (top panel, black, $V_{GS,p}$ = -0.5 V) and the recorded neuromorphic I_{DS} response (bottom panel, black).*

***Figure 6.9**: Architecture and experimental design for assessment of the influence of the electrolyte solution pH on PEDOT:PSS-based EGOT. a) Schematic representation of the EGOT architecture. b-c) Electrical characterization of the steady state conditions, including (b) the typical transfer characteristics (I_{DS} vs V_{GS}) and the current (c) collected at a constant V_{DS} and V_{GS} values (both V_{GS} and V_{DS} equal to -0.8 V) with a measurement time of one hour to reach stability*.

***Figure 6.10**: Influence of pH on PEDOT:PSS-based EGOTs. SI_{DS} trend vs pH for devices after a pre-hydration process in water overnight (blue markers, a) and without the pre-hydration step (brown markers, b). Error bars are the standard error of the mean for 8 devices for each pH value. Cubic fits are used as guide for the eye.*

***Figure 6.11**: Average channel conductance (G_{DS}) at different V_{GS} for 1 mM electrolyte solution of HCl (blue), NaCl (red) and LiCl (green).*

***Figure 6.12**: Setup used to characterize the influence of different cations on PEDOT:PSS channel in the EGOT architecture. a) Design of the experimental setup consisting in an Ag/AgCl top-gate architecture. b) Average transfer characteristics (number of independent channels = 11) of the PEDOT:PSS-EGOT device with VDS = -0.3 V c) Stability of the device during 50 consecutive transfer curve cylces at VDS = -0.3 V. d) Influence of the gate electrode material (Ag/AgCl vs gold) on the PEDOT:PSS-based EGOT.*

***Figure 6.13**: Influence of increasing concentration of alkali metal chloride solutions on PEDOT:PSS-based EGOT performance. a) Representative transfer characteristics collected at increasing concentration of KCl at V_{DS} = -0.3 V. The same trend is observed for also for LiCl and NaCl. b) Semilogplot of the relative variation of the channel conductance in the on state (viz., V_{GS} = -0.2 V) vs XCl concentration. Equation 6.4 is used as guide for the eyes. c) Semilogplot of the relative variation of the channel conductance in the off state (viz., V_{GS} = 0.6 V) vs XCl concentration. d) Semilog plot of ΔVx vs [XCl], fitted according to Equation 6.4. LiCl are green markers, NaCl red markers, KCl purple markers. Error bars represent the standard error of the mean (SEM) for nine independent devices collected at V_{DS} = -0.3 V, -0.5 V,-0.7 V.*

Chapter 1: Introduction

This introductory chapter defines the background and the vision of this work. Starting with the presentation of the scientific and technological framework of organic electronics, the focus is placed on the Electrolyte-Gated Organic Transistor (EGOT) architecture. This section highlights the fundamental theoretical and practical aspects of EGOT devices, as well as their applications as (bio)sensing platforms and for neuromorphic computing.

This chapter also provides a comprehensive review of the state-of-the-art functionalization strategies employed to tailor the surface chemistry of EGOTs. This review covers functionalization strategies for grafting biorecognition element on the gate electrode surface and the integration of two-dimensional (2D) materials, which can be employed either as a sensing probe on the gate or as the semiconductor in the channel. Finally, multivariate data analysis techniques are presented, and their integration within the organic electronic landscape is discussed.

1.1 Organic Electronics

Organic electronics is an interdisciplinary field at the intersection of organic chemistry, materials science, solid-state physics, and electrical engineering, focused on developing electronic devices based on carbon-containing materials. A major milestone in the field occurred in 1977, when Hideki Shirakawa and colleagues successfully controlled the intrinsic conductivity of polyacetylene[1], originally synthesized by Natta and co-workers in 1958.[2] The discovery and subsequent development of conductive polymers led to Alan Heeger, Alan MacDiarmid, and Hideki Shirakawa being awarded the Nobel Prize in Chemistry in 2000. Unlike conventional silicon-based electronics, organic electronics utilizes Organic Semiconductors (OSCs) as active materials. OSCs are π-conjugated molecules or polymers, characterized by alternating single and double bonds, which enable charge delocalization and transport.[3] Organic electronic materials offer several advantages over traditional electronic technologies, including large-area processability, mechanical flexibility, conformability, biocompatibility, and low production cost. These properties enable the design and fabrication of high-performance, flexible electronic devices, such as solar cells[4], Organic Light-Emitting Diodes (OLEDs)[5], neural interfaces[6], and biosensors.[7] Beyond these technological and manufacturing benefits, organic electronic materials can facilitate the conduction and processing of both electronic and ionic signals, including those originating from biological systems.[8] Moreover, the chemical synthesis of organic molecules and polymers can be tailored to optimize the electronic, physical, and chemical properties of the device, making organic electronics a versatile platform capable of bridging the interface between biological systems and electronic processing.[9] These capabilities have contributed to the emergence and rapid growth of the field of organic bioelectronics.[10–12]

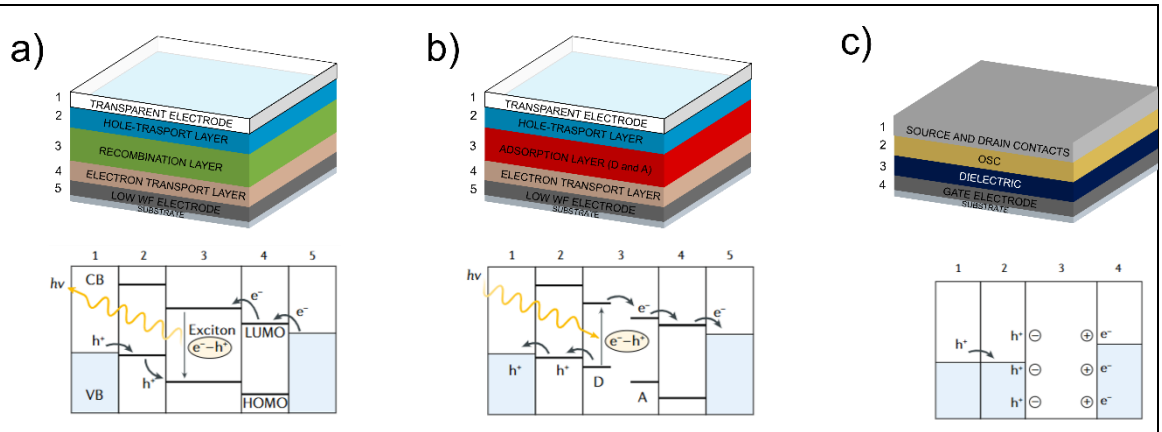

***Figure 1.1**: Examples of organic electronic devices (up) with the role of the interfaces for each device (bottom). a) an organic light-emitting diode. b) an organic photovoltaic solar cell. c) an organic field-effect transistors (OFET). Adapted from:*[13].

Organic electronic devices can be broadly classified into three main categories based on their primary operating function, as illustrated in **Figure 1.1**.

- Organic Light-Emitting Diodes (OLEDs) directly convert electrical current into light and represent one of the most commercially established organic electronic devices, driving the development of modern high-contrast, flexible, and curved displays.[14,15]
- Organic Photovoltaic Cells (OPVs) transduce light into electrical current, offering a cost-effective and mechanically flexible alternative to conventional silicon-based solar cells. Their operation relies on the photovoltaic effect, which involves light absorption, the generation of excitons (bound electron-hole pairs), and subsequent charge separation at a donor-acceptor interface.[16,17]
- Organic Thin-Film Transistors (OTFTs) are three-electrode devices designed for signal modulation and amplification. In an OTFT, a small variation in the gate voltage induces a significant change in the conductivity of the organic active layer, enabling efficient switching and signal amplification.[18]

At this point, it is important to note that the field of organic electronics is not limited to these devices. A significant area of research involves hybrid devices that merge the functionalities of the classes mentioned above, such as Organic Light-Emitting Transistors (OLETs)[19] Light-Modulated Electrolyte-Gated Organic Transistors

(LEGOTs)[20], Electrolyte-Gated Light-Emitting Transistors (EGLETs)[21], Organic Photodetectors (OPs)[22], and dual-mode OPV-OLED devices.

Although OLED and OPV devices have achieved impressive technological and commercial development, their direct interfacing with biological systems remains complex. In contrast, OTFTs are uniquely suited for the development of sensing interfaces bridging the gap between electronics and biology, for their solution processability and the biocompatibility of many organic active materials which allow the development of flexible, disposable and biodegradable devices for *in-vivo* applications.[23]

According to their device structure, the OTFTs devices could be classified in Organic Field Effect Transistors (OFETs) and Electrolyte-Gated Organic Transistors (EGOTs).

OFETs are three-electrode devices wherein a thin film of an OSC connects the source (S) and drain (D) electrodes, forming the device channel. The third electrode, the gate (G), is separated from the channel by a thin dielectric layer. Depending on the physical arrangement of these components with respect to the thin film channel, OFETs can be fabricated in several architectures: top-gate/top-contact, top-gate/bottom-contact, bottom-gate/top-contact, and bottom-gate/bottom-contact (**Figure 1.2**).[18,24]

The working principle of an OFETs is based on the field-effect charge carrier generation. The device structure (Gate/Dielectric/Semiconductor) acts as a capacitor. When a potential difference (V_{GS}) is applied between the gate and source electrodes a transversal electric field is generated across the dielectric. This field induces and accumulates mobile charge carriers (either electrons or holes, depending on the OSC) at the interface between the semiconductor and the dielectric. This accumulation of charges forms the conductive channel at the OSC/dielectric interface.[25] Thus, V_{GS} controls the charge carrier density within the channel. When a potential difference is applied between the source and drain (V_{DS}), a drain-source current (I_{DS}) flows through the gate-induced channel. The magnitude of I_{DS} is therefore modulated by the gate voltage V_{GS}, allowing the device to function as a switch or an amplifier.[26]

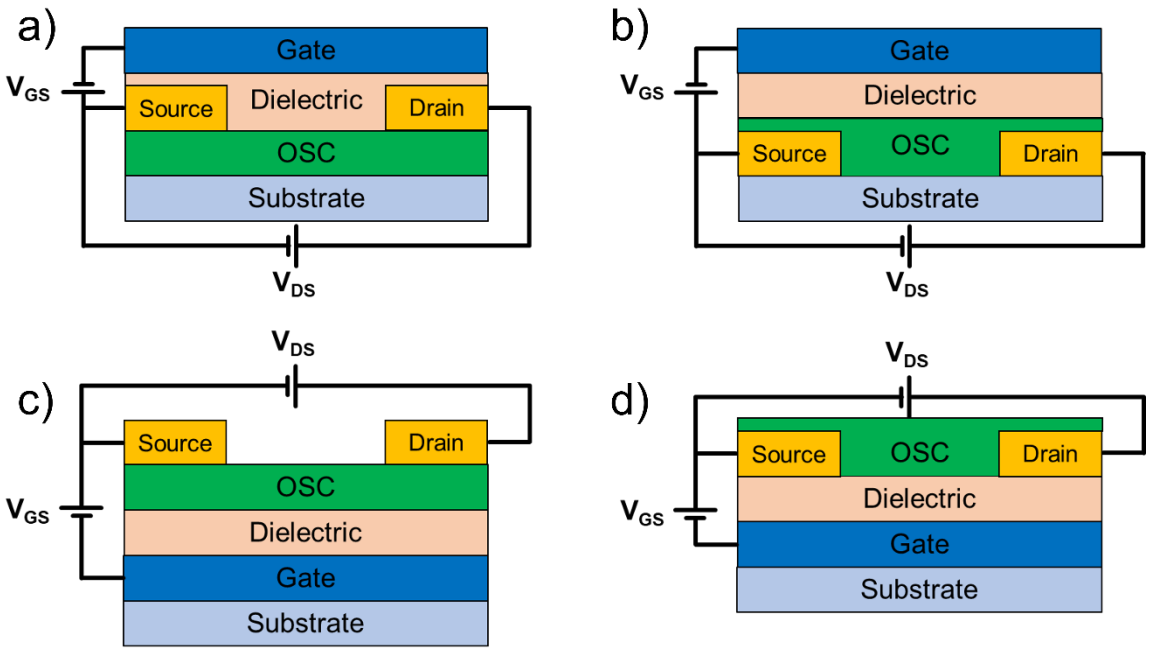

***Figure 1.2**: Different OFET architectures. a) Top Gate Top Contact. b) Top Gate Bottom Contact. c) Bottom Gate Top Contact. d) Bottom Gate Bottom Contact. Adapted from:*[18].

The current I_{DS} begins to flow once V_{GS} exceeds a threshold voltage (V_{th}). This voltage represents the minimum gate bias required to induce a significant population of mobile charge carriers (electrons or holes) at the semiconductor/dielectric interface.[27]. In thin-film OTFTs, V_{th} is heavily influenced by the presence of trap states within the semiconductor bandgap. These traps must be filled or emptied (depending on their nature and that of charge carriers) before mobile charge carriers can accumulate, thus V_{th} is strongly dependent on the density of deep trap states (Q_{trap}) and the dielectric capacitance per unit area (C_i).[26]

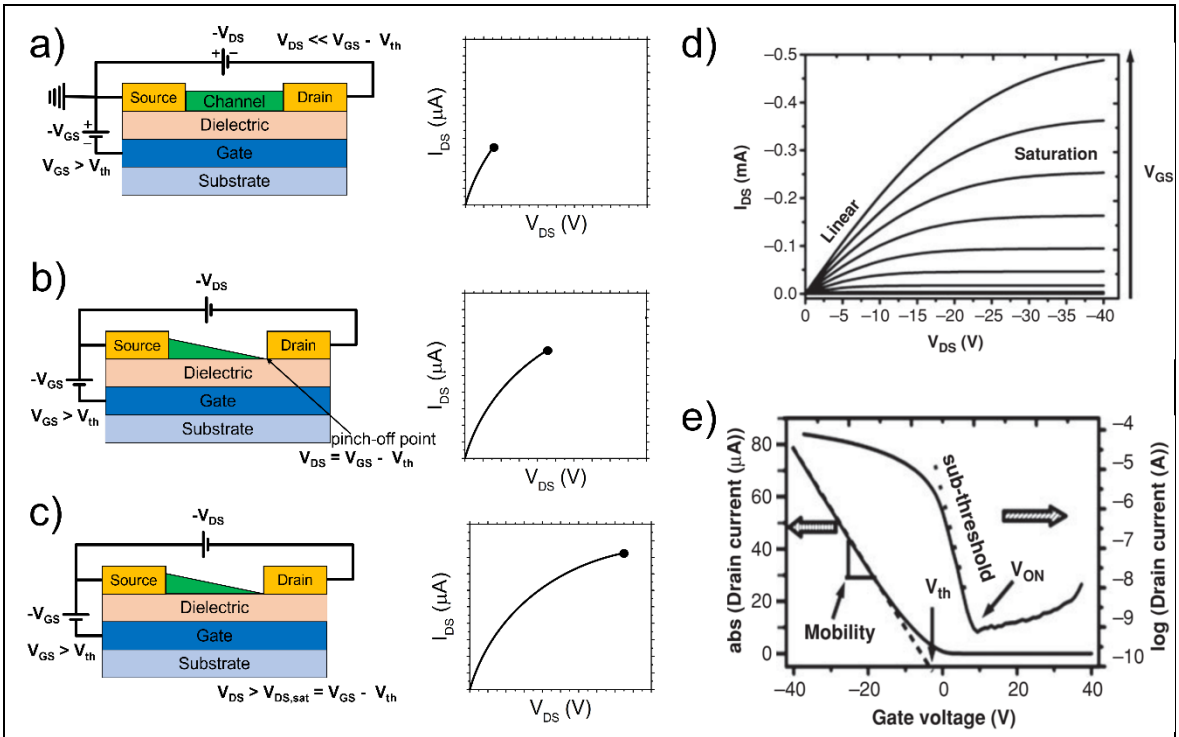

***Figure 1.3**: OFET working mechanism. Illustration of operating regime and corresponding I-V characteristics for (a) linear regime, (b) start of saturation regime at pinch-off point, (c) saturation regime. d) output and e) transfer characteristics of a pentacene OFET. Adapted from:*[27].

By measuring I_{DS} as a function of V_{DS} at fixed V_{GS} bias, the OFET output characteristics exhibits three operational regimes (**Figure 1.3**). When the drain-source voltage (V_{DS}) is much smaller than the gate overdrive voltage (V_{GS}-V_{th}), the induced channel exhibits a relatively uniform charge carrier density along its entire length. The I_{DS} current is linearly proportional to V_{DS} and follows a relationship analogous to Ohm's law (**Figure 1.3a**). This linear regime is described by Equation 1.1:

$$I_{DS} = \frac{W}{L} C_i \mu (V_{GS} - V_T) V_{DS} \text{ with } V_{DS} << (V_{GS} - V_{th}) \qquad \text{(Eq. 1.1)}$$

where W is the channel width, L is the channel length, μ is the charge carrier mobility, and C_i is the capacitance per unit area of the insulating layer.

As V_{DS} is increased, the local potential within the channel, $V_{ch}(x)$ is no longer negligible. It changes from 0 V at the source to V_{DS} at the drain. Consequently, the local effective gate voltage responsible for charge accumulation, V_{GS}-V_{th}-$V_{ch}(x)$, decreases along the channel and results lower than V_{th}.

When V_{DS} becomes equal to the gate overdrive voltage (*viz.,* $V_{DS} = V_{GS} - V_{th}$), the carrier concentration at the drain end of the channel ideally drops to zero. (**Figure 1.3c**).

By further increasing V_{DS} beyond this "pinch-off" voltage ($V_{DS,sat} = V_{GS} - V_{th}$), the depletion region forms next to the drain contact because the difference between the local potential and V_{GS} is below V_{th} (*viz.,* $V_{ch}(x) - V_{GS} < V_{th}$).[23] With further increasing V_{DS}, the pinch-off point moves from the drain contact towards the source. A depletion region forms between this new pinch-off point and the drain, which sustains the excess voltage ($V_{DS} - V_{DS,sat}$). Because the voltage drop across the conductive part of the channel remains "pinned" at $V_{DS,sat}$, the current (ideally) no longer increases with V_{DS} and saturates (**Figure 1.3d**). The saturation current $I_{DS,sat}$ is given by Equation 1.2:

$$I_{DS} = \frac{W}{2L} C_i \mu (V_{GS} - V_T)^2 \text{ with } V_{DS} > (V_{GS} - V_{th}) \quad \text{(Eq. 1.2)}$$

The dependency of I_{DS} on V_{DS} potential at a fixed gate voltage results in the output characteristics. (**Figure 1.3d**) In contrast, when V_{DS} is held constant (in the linear or in the saturation regime) and V_{GS} is swept, the transfer characteristic is collected (**Figure 1.3e**).

Although OFET platforms leveraged the characteristic flexibility and solution processability of organic semiconductors for developing displays, chemical and biological sensors[24,26,28], wearable devices[29], and circuits[30], they are severely limited for interfacing with aqueous and biological environments. This limitation stems from their high operating voltages, which are typically on the order of tens of volts. To overcome this limitation, another class of OTFT, known as electrolyte-gated organic transistors (EGOTs) is developed. In this architecture, the conventional solid-state dielectric is replaced by a liquid (or solid-state) electrolyte containing mobile ions.[31] Below, the fundamental aspects of EGOT are discussed.

1.2 Electrolyte Gated Organic Transistors (EGOTs)

In EGOT architectures, the OSC channel is coupled to the gate electrode via an electrolyte solution: the mobile ions in the electrolyte drift upon the action of the gate field to/from the gate from/to the OSC channel, and the ion/OSC interactions modulate the channel conductivity. The operation of EGOT devices involves the application of potential between S and D (V_{DS}) that generates a current inside the channel (I_{DS}). The gate bias (V_{GS}) sets the doping level of the channel, modulating

the I_{DS} current. The modulation of I_{DS} current when a V_{GS} is applied represents a prominent figure of merit of a EGOT and describes the signal amplification of the device.[32] This parameter is known as transconductance and could be quantitatively described by the first derivative of I_{DS} vs V_{GS} (*viz.,* g_m, = $\partial I_{DS}/\partial V_{GS}$). When a potential difference is applied across the electrolyte (between the gate and the channel), cations or anions from the electrolyte drift to the respective interfaces, depending on the polarity and magnitude of the applied voltage.[31] For example, when a positive bias is applied to the gate, anions (negative ions) will accumulate at the gate/electrolyte interface, while cations (positive ions) will accumulate at the OSC/electrolyte interface (**Figure 1.4**).

These accumulated ions form Electrical Double Layers (EDLs) at both interfaces. The ionic charges within the EDL at the channel/electrolyte interface then electrostatically induce the accumulation or depletion of electronic charges (holes or electrons) within the semiconductor.[33]

The interfacial capacitances (C_{DLG} and $C_{DL,ch}$) of the electric double layers are inversely proportional to their effective thickness (d). Because this thickness is on the sub-nanometre scale - defined by the Debye screening length - the specific capacitance (C_i) generated by the EDL at the channel interface is exceptionally high, typically on the order of several μFcm^{-2}. This value is orders of magnitude higher than the capacitance measured for polymer dielectrics (often in the $nFcm^{-2}$ range).[33] This phenomenon is known as capacitive coupling and perfectly describes the working mechanism of EGOTs based on ion-impermeable semiconductors (*viz.,* Electrolyte Gated Organic Field Effect Transistors, EGOFETs).[31,34] However, to describe the entire energy/electrostatic potential landscape of OSC including the ion-permeable semiconductor, it is necessary to introduce the chemical capacitance ($C_{q,ch}$) of the active material. At the state of the art, ion-permeable channels are based on Organic Mixed Ionic-Electronic Conductors (OMIECs), such as Poly(3,4-ethylenedioxythiophene)polystyrene sulfonate (PEDOT:PSS), which readily solvate and transport ionic species.[35–37] In OMIECs-based EGOT, known also as Organic Electrochemical Transistors (OECTs), the ionic-electronic interaction between electrolyte and OSC includes the bulk of the semiconductor, and the effective capacitance of the device is dominated by the chemical capacitance.[34] The chemical capacitance, which depends on the electronic structure (*viz.,* the Density of States, DOS) of the active material[34], is a “non-electrostatic” term describing the ability of the semiconductor to accept and

release ions. Therefore, the chemical capacitance is related to the ability of the organic semiconductor to store energy when subjected to a transversal electric field.[38] Moreover, the chemical capacitance describes also the percolation and the interaction of ions in molecular organic semiconductors[39] and the behaviour of 2D-material, such as reduced Graphene Oxide (rGO), where the chemical capacitance is termed quantum capacitance.[40–42]

This extremely high effective capacitance, resulting from the contribution of interfacial capacitances (C_G, $C_{DL,ch}$) and the areal capacitance of the OSC ($C_{q,ch}$) is the key advantage of EGOTs, as it enables efficient channel modulation (and thus, transistor operation) at very low operating voltages, often below 1 Volt. The liquid gating mechanism, operating at biologically compatible potentials, provides an intimate coupling between the physiological environment and the electrical response of the transistor channel, making EGOTs ideal candidates for the development of organic bioelectronic devices.[9]

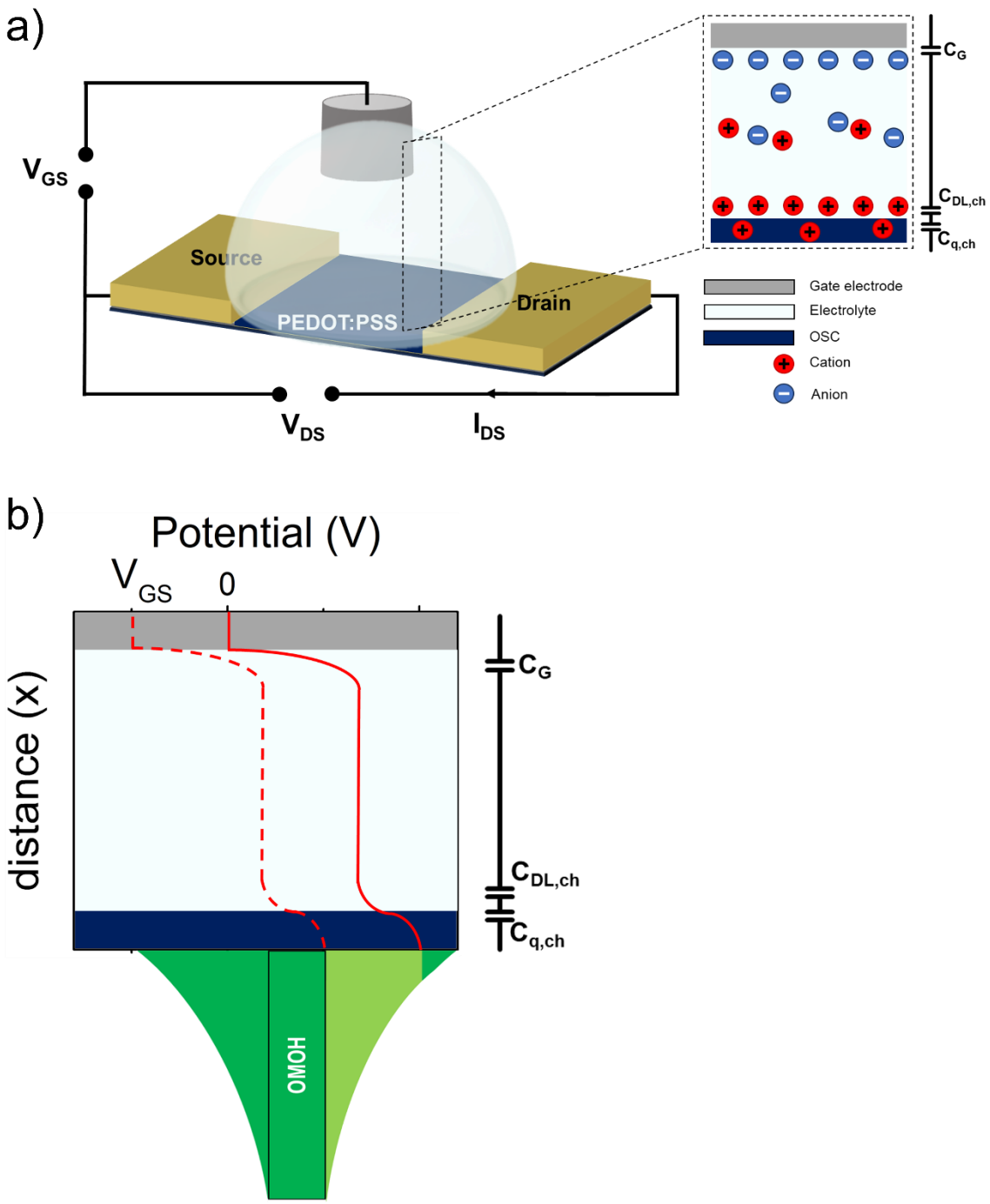

***Figure 1.4**: Working mechanism of EGOT-device. a) Schematic representation of an EGOT device. The inset shows the electric double layer in conjunction with their equivalent capacitances. b) Potential profile of the EGOT with a metal gate electrode, in the hypothesis of constant potential along the channel. Adapted from:*[34].

Figure 1.4a shows the typical top-gate EGOT architecture, where the gate is positioned directly over the channel. This constitutes the most prevalent configuration for developing both neuromorphic devices[43,44] and EGOT-based

biosensing platforms, where either the gate electrode[45–47] or the channel material[48] can be functionalized.

Alternative device architectures are summarized in **Figure 1.5**.[31] In the less common bottom-gate geometry (**Figure 1.5b**), a solid electrolyte (depicted in blue) separates the metallic gate from the semiconductor channel[49]; this layout represents a promising candidate for physiological recordings.[50] In the side-gate (or coplanar) architecture (**Figure 1.5c**), the gate electrode lies on the same plane as the semiconductor.[51–54] A fourth EGOT geometry is the floating- (or extended-) gate architecture (**Figure 1.5d**). Here, the gate and the channel are located in two separate electrolyte compartments connected by a gold electrode with two pads, known as the floating gate.[31] The floating gate is capacitively coupled to both the OSC channel and the control gate through the electrolyte solution.[55] This design is particularly advantageous for EGOT-biosensor platforms: sensing probes can be immobilized on one arm of the floating gate, while the target analyte is introduced into the corresponding compartment. This setup prevents non-specific adsorption of the target molecule onto the OSC, as direct contact between the channel and the analyte is avoided.

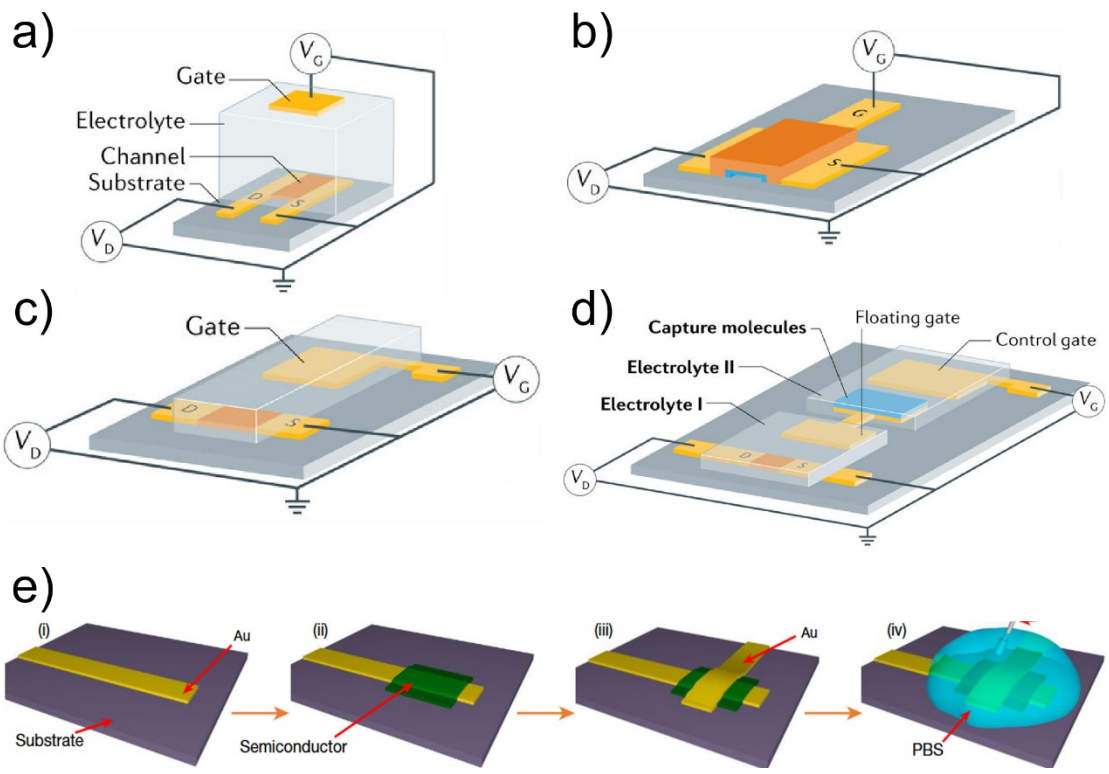

***Figure 1.5**: Different EGOT architectures. a) Top-gate. b) Bottom-gate. c) Sided-gate. d) Floating gate. e) Schematic representation of the fabrication process of vertical EGOTs. a-d) Adapted from:*[31]*. e) Adapted from:*[56]*.*

The architectures presented in **Figure 1.5a–d** involve the fabrication of in-plane devices, with channel lengths (L) ranging from a few micrometres to a few millimetres. To increase transconductance in these planar devices, thicker semiconducting films are typically required, which inevitably compromises performance in terms of on/off ratio and ion interaction speed.[57] To overcome these limitations, vertical EGOTs (vEGOT, **Figure 1.5e**) are developed. In this configuration, the transistor channel is sandwiched between vertically displaced source and drain electrodes. These transistors feature extremely short channel lengths (*viz.,* a few nanometres), enabling them to support large currents and deliver high transconductance.[56,58] Moreover, vEGOTs benefit from a reduced device footprint, allowing for a large number of transistors to be monolithically integrated onto the same substrate.[59] However, although this architecture is highly promising for the development of high-transconductance EGOT active-matrix arrays, exploiting the third dimension remains challenging regarding device fabrication.

Having illustrated the working mechanism and the various architectures of EGOTs, Chapter 1 proceeds to provide an overview of the different channel semiconductors (Section 1.3) and the functionalization strategies explored to enhance biosensing performance (Section 1.4). Finally, the chapter concludes with a brief overview of multivariate analysis techniques applicable to EGOT devices (Section 1.5).

1.3 Organic semiconductors

In this thesis, different Organic Semiconductor (OSC) materials are investigated to improve the performance of EGOT-based devices. As discussed in Section 1.1, OSCs present a compelling alternative to inorganic semiconductors due to their lower fabrication costs, high scalability, mechanical flexibility, conformability, and compatibility with solution-processing techniques, including water-based methods.[60–62] At the molecular level, OSCs consist of conjugated molecules or polymers characterized by alternating single and double bonds. The σ electrons establish a planar molecular backbone, while delocalized π electrons form an electron density cloud above and below the molecular plane, enabling electronic delocalization.[63] This π-conjugation produces a relatively small energy gap between the Highest Occupied Molecular Orbital (HOMO) and the Lowest Unoccupied Molecular Orbital (LUMO), which facilitates charge transfer.[64] Consequently, the electronic properties of OSCs are largely governed by these frontier orbitals, whose strong π-character underpins conduction. In the solid state, π-π interactions between adjacent molecules generate narrow electronic bands, allowing electrons and holes to move across the material.[65]

The injection of excess charge carriers induces a **local geometric relaxation** of the lattice. This structural distortion couples with the charge, resulting in the formation of quasiparticles known as polarons.[66] In certain conductive polymers, such as polythiophene, polypyrrole, and polyaniline, a higher-order energetic state called a bipolaron can form, corresponding to a di-cationic configuration.[67] Despite these intrinsic transport pathways, solution-processed organic films frequently exhibit amorphous structures. The absence of long-range order localizes charge carriers, so that transport occurs predominantly via a hopping mechanism, where charges move between discrete molecular sites.

The π-orbital delocalization in OSCs also confers distinctive electrochemical properties, including low Ionization Potential (IP) and high Electron Affinity (EA).

Molecules with low IP function as electron donors and are readily oxidized, typically behaving as p-type semiconductors, with hole transport mediated by the HOMO. Conversely, molecules with high EA act as electron acceptors, prone to reduction, and exhibit n-type behaviour, where charge transport occurs through the LUMO of the conjugated system.[13]

In an EGOT configuration, when a bias voltage is applied, ions from the electrolyte migrate towards the OSC interface. These ions interact with the charge carriers in the OSC, leading to a readjustment of bond lengths. In a simplified yet effective description, ions approaching the channel interface can stabilize OSC charge carriers of the opposite sign or immobilize those of the same sign. Specifically, anions can dope (accumulate charges in) p-type materials, while cations can dope n-type materials. Conversely, cations can de-dope (trap holes in) p-type materials, whereas anions de-dope n-type materials.[36][68] Recently, our group published a novel description of the gating mechanism that unifies the understanding of EGOT operation, independent of the specific nature of the OSC (*viz.,* its permeability to ions).[34] This model elucidates how the charge carrier density in an EGOT channel is modulated by the gate-source voltage V_{GS} and how the chemical capacitance of the organic semiconductor - rooted in the DOS of the HOMO and LUMO levels - is influenced by the applied voltage. As demonstrated in Chapters 4 and 5, this unified model allows for a comprehensive analysis of EGOT transfer characteristics, leveraging the device's intrinsic multi-parametric response. In this thesis work, two p-type semiconductors (*viz.,* 6,13-Bis(triisopropylsilylethynyl)pentacene, TIPS-pentacene, Poly(3,4-ethylenedioxythiophene) poly(styrene sulfonate), PEDOT:PSS) and a 2D, ambipolar semiconductor (*viz.,* reduced Graphene Oxide, rGO) are used as the active channel materials for the EGOTs and they will be discussed in the next paragraphs. The chemical structures of these organic (semi)conductors are reported in (**Figure 1.6**).

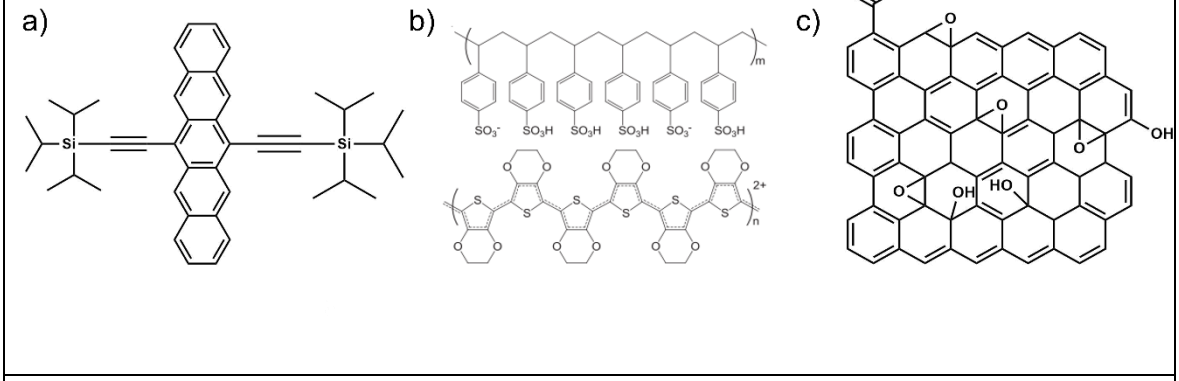

***Figure 1.6**: Chemical structures of the OSC used in this thesis. (a) TIPS-pentacene, (b) PEDOT:PSS, and (c) rGO*.

1.3.1. TIPS-pentacene

6,13-Bis(triisopropylsilylethynyl)pentacene (TIPS-pentacene) (**Figure 1.6a**) is the p-type organic semiconductor (OSC) selected for the development of the enantioselective L-Tryptophan EGOT-based immunosensor presented in Chapters 4. Structurally, TIPS-pentacene is derived from the functionalization of the pentacene core with two bulky triisopropylsilylethynyl groups at the 6 and 13 positions. Pentacene, consisting of five fused benzene rings, is one of the first and most extensively studied organic semiconductors due to the extended conjugation of its π-orbitals.[39,45,69,70] However, its application is limited by its solid-state arrangement: pentacene crystallizes in a herringbone motif (edge-to-face packing), where each acene backbone is positioned nearly perpendicular to its neighbour. This configuration results in poor overlap between the HOMOs of adjacent molecules, thereby severely restricting charge carrier mobility.[61] Furthermore, unsubstituted pentacene is insoluble in common organic solvents, necessitating the use of costly, ultra-high vacuum, physical vapour deposition techniques.[39,45] Additionally, it is prone to photo-oxidation, where reaction with atmospheric oxygen disrupts the conjugated system.[71]

The introduction of bulky silyl-ethynyl side groups in TIPS-pentacene overcomes these limitations. These groups disrupt the herringbone packing, inducing the molecules to adopt a two-dimensional "brick-wall" π-stacking arrangement (face-to-face packing).[72,73] This structural reorganization significantly enhances the overlap of π-orbitals, leading to higher charge carrier mobility compared to pristine pentacene. Moreover, the side groups confer excellent solubility in common organic solvents, enabling low-cost, large-area solution processing.[61]

1.3.2 PEDOT:PSS

Poly(3,4-ethylenedioxythiophene) ($PEDOT^+$) doped with poly(styrene sulfonate) (PSS^-) (**Figure 1.6b**) stands as the most prevalent conductive polymer in bioelectronics. Its widespread adoption spans EGOT-based biosensors[52,53,74], low-impedance Multi-Electrode Arrays (MEAs) for in vivo recordings[75], neural interfaces[76,77], EGOT-based transducers for electrophysiological signal amplification[78,79], organic electrochemical ion pumps[80], and organic artificial synapses.[81,82]

The primary advantage of integrating PEDOT:PSS into bioelectronic interfaces contacting aqueous electrolytes lies in its high chemical (*viz.,* effective) capacitance. This property arises from the film's bulk permeability to ions, which provides a vast electroactive surface area, supported by the material's hydrophilicity and efficient ion-transport capabilities.[76] Structurally, the PEDOT:PSS bulk comprises two distinct phases that facilitate mixed ionic-electronic conductivity. The PEDOT-rich phase acts as the hole transport pathway, while the PSS-rich phase functions as the ion transport medium. These interconnected grains are distinguishable at the nanometre scale, typically described as a continuous, insulating PSS matrix hosting conductive PEDOT crystallites.[83]

Chemically, PEDOT:PSS is obtained via the oxidative polymerization of the 3,4-ethylenedioxythiophene (EDOT) monomer in the presence of PSS^-, which acts as a counterion to stabilize the positive charges on the PEDOT backbone. While PEDOT:PSS films can be fabricated directly on electrodes via electrochemical polymerization (galvanostatic or potentiostatic deposition of EDOT)[84,85], this thesis work utilizes solution processing of a commercially available aqueous dispersion (Clevios™, Heraeus). The active material is deposited onto the EGOT channel via drop-casting using formulations with varying concentrations. Typically, pristine PEDOT:PSS exhibits conductivities in the range of 0.1–10 S cm^{-1}.[86] This can be significantly augmented by incorporating polar, low-molecular-weight organic molecules, such as Ethylene Glycol (EG)[87] or Dimethyl Sulfoxide (DMSO)[88] into the dispersion, or by post-treating the film with acidic solutions.[89,90] Specifically, the addition of organic solvents like DMSO induces phase separation and intermolecular interactions with the PSS sulfonic acid groups. This process effectively reduces the excess of the insulating PSS shell and promotes the

reorientation and enlargement of conductive $PEDOT^+$ grains, thereby boosting conductivity.[88]

To ensure structural integrity in aqueous environments, (3-Glycidyloxypropyl)trimethoxysilane (GOPS) is commonly added as a cross-linking agent and surface adhesion promoter preventing film delamination.[91] Finally, PEDOT:PSS is highly valued for its biocompatibility[84] and the versatility of thiophene chemistry, which allows for the modification of monomer side chains to finely tailor the material's mixed ionic-electronic transport properties.

1.3.3 Reduced Graphene Oxide

Graphene is a carbon nanomaterial consisting of a single two-dimensional layer of sp^2-bonded carbon atoms arranged in a hexagonal honeycomb lattice.[92] It was first mechanically isolated from bulk graphite and transferred onto a silicon wafer using the well-known “Scotch Tape” exfoliation technique, a breakthrough that demonstrated the stability of a truly one-atom-thick crystal.[93] This discovery ultimately led to the award of the 2010 Nobel Prize in Physics to Konstantin Novoselov and Andre Geim for their "groundbreaking experiments regarding the two-dimensional material graphene".[94] Structurally, graphene resembles a vast network of fused benzene rings where hydrogen atoms are replaced by carbon atoms (**Figure 1.6c**). It is inherently hydrophobic due to the absence of oxygen-containing functional groups.[95] Being a carbon allotrope, its planar structure features a bond length of 1.42 A. These graphene layers stack to form graphite with an inter-planar spacing of 3.35 A.[96] Specifically, the carbon atoms in graphene exhibit hybridized sp^2 bonding, forming three in-plane σ bonds and a single π orbital perpendicular to the plane. The strong σ bonds constitute the rigid hexagonal backbone, while the out-of-plane π bonds govern the interactions between adjacent graphene layers.[92] This unique atomic architecture underpins graphene’s remarkable physical properties. Its tensile strength reaches approximately 125 GPa, while its elastic modulus approaches 1.1 TPa, making graphene more than one hundred times stronger than steel.[97] The material also exhibits an exceptionally high thermal conductivity of about $5 \cdot 10^3$ W/Mk - nearly an order of magnitude higher than copper (401 W/mK). In addition, graphene shows outstanding electronic performance, with an electrical conductivity on the order of 10^6 S/m and a sheet

resistance of around 31 Ω/sq, resulting in an ultra-high carrier mobility of up to $2 \cdot 10^5$ $cm^2/V \cdot s$.[98]

Despite these extraordinary properties, the application of graphene is still hindered by the limited scalability of synthesis methods such as chemical vapour deposition (CVD)[99], chemical exfoliation[100] and chemical synthesis.[101] This poor manufacturing scalability and high production costs have driven the exploration of alternative graphene-like materials, most notably reduced Graphene Oxide (rGO). rGO is typically fabricated through the oxidation and exfoliation of graphite to produce graphene oxide (GO), which is subsequently reduced via chemical, thermal, or electrochemical routes.[102] GO consists of a monolayer of chemically modified graphene, characterized by an abundance of oxygen-containing functional groups (*viz.,* hydroxyl, epoxy, carboxyl, and carbonyl) on the basal plane and edges, with a carbon-to-oxygen ratio typically close to 2:1.[103] While these functional groups enhance aqueous solubility - facilitating large-scale, environmentally sustainable processing[104] - they also disrupt the sp^2 crystalline network. This disruption degrades electrical and thermal transport properties[105], thereby limiting GO's direct application in organic bioelectronics. However, reducing GO to rGO decreases the oxygen content and partially restores the conductivity of the conjugated sp^2 network.[106] The fabrication of rGO-based devices generally involves the initial deposition of a GO film via spray coating[107], screen printing[108], dip coating[109], or spin coating[110], followed by reduction. Strategies for reduction include chemical, thermal, biological, electrochemical, and ionization methods.[111] Chemical reduction is currently the most prevalent approach, utilizing reducing agents such as hydrazine, sodium borohydride ($NaBH_4$), hydrogen iodide, or L-ascorbic acid.[112] However, the cost of reagents and the generation of toxic chemical waste render this methodology less desirable for industrial scaling.[113] Thermal reduction offers an attractive alternative due to its lower environmental impact, involving the annealing of GO under a controlled atmosphere to release desorption products like H_2O, CO_2, and CO.[114] By tuning parameters such as temperature, atmosphere, and duration, one can tailor the electronic, mechanical, and morphological properties of the rGO film.[114,115] Nevertheless, the high temperatures required are energetically demanding and often incompatible with plastic, flexible substrates essential for wearable electronics. Consequently, the electrochemical reduction of GO films emerges as a promising solution. It combines low environmental impact (aqueous-based, low-temperature processing) with high tunability of the oxygen functionalities

that govern charge transport.[116] These characteristics render the electrochemical fabrication of rGO-based devices highly suitable for flexible applications, including supercapacitors[117], sodium-ion batteries[118], biosensors[41,48,119,120], and biomedical devices.[121] Furthermore, the versatility of rGO is enhanced by residual oxygen functionalities post-reduction, which can be exploited to tether recognition elements directly onto the surface for specific analyte detection in biosensing.[48,122] In this thesis, a novel and straightforward method for fabricating rGO-based electrolyte-gated transistors (EGTs) is proposed. This approach relies on the direct, electrochemically driven growth of rGO flakes onto the channel electrode of the device from a GO dispersion, effectively bypassing the need for a preliminary casting of the GO layer.

1.4 EGOT applications

With the working principles and materials established, Section 1.4 focuses on the validation of EGOT devices through two specific applications: biosensors and neuromorphic systems.

1.4.1 EGOT-based (bio)sensors

The International Union of Pure and Applied Chemistry (IUPAC) defines a biosensor as “a device which uses specific biochemical reactions mediated by isolated enzymes, immunosystems, tissues, organelles or whole cells to detect chemical compounds, usually by electrical, thermal or optical signals”.[123] Essentially, a biosensor integrates a biological recognition element with an electronic component that detects, records, and transduces information regarding a physiological change into a measurable signal.[124] As depicted in **Figure 1.7**, a typical biosensor comprises a bioreceptor (*viz.,* the biological sensing probe), a transducer which converts the biorecognition event into a measurable electrical signal, and an electronic system where the signal is amplified, digitized, and displayed.

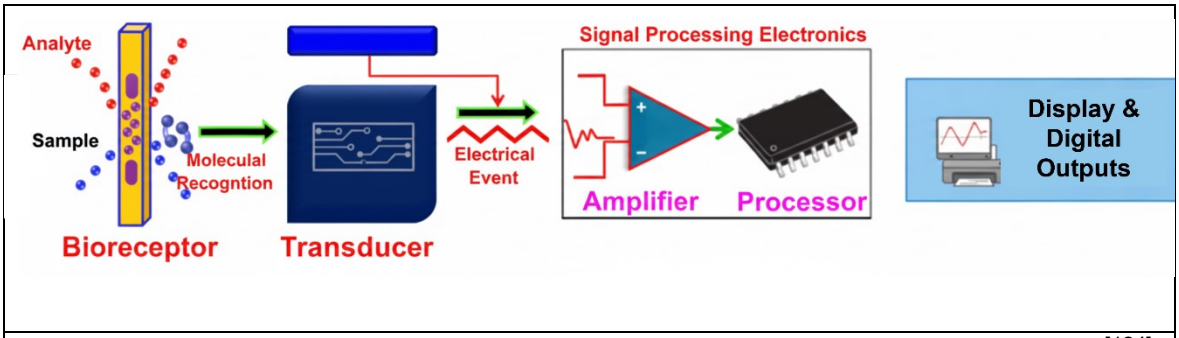

***Figure 1.7**: Schematic layout of the typical biosensor structure. Adapted from:*[124].

Although Clark had demonstrated the feasibility of continuous blood oxygen detection as early as 1956[125], it is only in 1962, with the development of enzyme-based electrodes, that the concept of biosensors is properly defined. In this pioneering work, a glucose biosensor is developed by electrochemically detecting the oxygen consumption or hydrogen peroxide (H_2O_2) production resulting from the enzymatic reaction of glucose.[126] Biosensors are commonly categorized into three generations, based on how the biorecognition element is integrated with the transducer. In the first generation, following Clark's classical concept, the sensor detects the products of the biochemical reaction. These products diffuse from the biorecognition layer to the transducer surface, where they generate an electrical signal proportional to the analyte concentration. The second generation incorporates additional components, such as artificial redox mediators, within the biological layer to improve electron transfer and increase analytical performance. In the third generation, the biorecognition element becomes an intrinsic component of the transducer itself. Here, biomolecules are directly immobilized on the sensing electrode, enabling direct electron transfer between the analyte and the sensing interface without the need for diffusion steps or mediating agents.[124]

To develop an effective and reliable biosensing platform with commercial potential, specific performance criteria must be met.[127] Key figures of merit include selectivity, which is the capability of the biosensor to detect the specific target analyte in a sample containing a complex mixture of interfering species, and sensitivity, defined as the change in output signal per unit change in analyte concentration. Furthermore, the device must exhibit a low limit of detection (LOD), representing the minimum amount of analyte reliably detectable, as well as high stability, which assesses the device's vulnerability to environmental noise over time. Finally, reproducibility is essential to ensure the biosensor yields identical results when the sample is measured multiple times under the same conditions.

Among the various transduction mechanisms for biochemical events[128], transistor-mediated mechanisms - specifically field-effect transistors -are pursued for decades due to their high sensitivity, selectivity, and speed.[129] Notably, these devices allow for the detection of ionic and enzymatic changes, as well as immunometric or genomic interactions.[130]

As detailed in Section 1.2, conventional OFETs are outperformed by EGOTs in biosensing applications. EGOTs can operate at low voltages (< 1 V) in aqueous electrolytes, the natural physiological environment for biological targets and receptors.[33] Furthermore, EGOT-based biosensors offer intrinsic advantages stemming from their organic (bio)electronic nature: they are environmentally friendly, cost-effective to fabricate, compatible with flexible substrates, and utilize OSCs that are biocompatible and stable in harsh biological environments.[32]

In terms of performance, EGOT biosensors exhibit excellent behaviour, having been proven capable of detecting biomarkers at the physical limit of a single molecule, reaching LODs in the zeptoMolar range.[131] This tremendous sensitivity is attributed to the working mechanism described in Section 1.2: the capacitive coupling between the gate and the channel enables the amplification of subtle electrostatic potential variations - triggered, for instance, by a biorecognition event - into a potential drop at the OSC/electrolyte interface that can be up to three orders of magnitude larger.[32] This potential variation at the interface governs the charge carrier density in the channel, effectively transducing the potential change at the gate into a significant modulation of the transistor parameters.[33,130]

Like widely employed bioassays such as Enzyme-Linked Immunosorbent Assay (ELISA) and Surface Plasmon Resonance (SPR), a crucial step in developing EGOT-based biosensors is the surface immobilization of the biorecognition element. Conceptually, the most straightforward strategy is to immobilize the biorecognition element directly at the OSC/electrolyte interface. In this configuration, the interaction between the target analyte and the biorecognition probe grafted onto the OSC directly impacts charge transport within the channel, altering the transistor's figures of merit. Various EGOT biosensors featuring biorecognition elements confined to this interface are demonstrated.[132,133] In particular, the oxygenated groups provided by rGO thin films are widely used as anchoring sites to graft biorecognition probes.[48,120] However, functionalizing the OSC with biomolecules is non-trivial, as the OSC-forming molecules are typically highly hydrophobic, in contrast to the hydrophilic nature of most biorecognition elements. Moreover, functionalizing the

OSC surface with anchoring chemical groups often leads to a reduction in charge carrier mobility.[134]

Conversely, EGOT platforms provide a second addressable interface: the gate/electrolyte interface. Here, potentiometric perturbations caused by interfacial changes (*e.g.,* binding events or conformational transitions) are transduced into electrical changes in the transistor via capacitive coupling.[32] Generally, grafting biorecognition probes onto the gate electrode is more reproducible and less detrimental to the device's electronic properties. Gate electrodes are typically composed of materials (predominantly gold) for which surface derivatization procedures are well-optimized. This has led to numerous successful examples of EGOT biosensors employing a functionalized gate as the core sensing unit. The versatility of gate-functionalized EGOT platforms has enabled the successful detection of a wide variety of clinically relevant molecular targets[135], including neurotransmitters[136], metabolites[53], nucleic acids[46][129], inflammatory cytokines[137], protein biomarkers[138][139], anti-drug antibodies[41], viruses[140], and bacteria.[141]

This thesis highlights the critical importance of optimizing the gate electrode derivatization process. Specifically, two functionalization strategies are explored. First, the grafting of an anti-L-Tryptophan (L-Trp) antibody is optimized to harness the full sensitivity of the EGOT-based immunosensor, which is crucial to achieve discrimination of Trp enantiomers (Chapter 4). Second, a novel class of 2D transition metal carbides, nitrides, and carbonitrides - namely MXenes - is introduced into an EGOT-based platform to detect Dopamine in the femtoMolar range (Chapter 5). To provide the necessary background, various antibody immobilization strategies are presented in Section 1.4.1.1, while the characteristics of MXenes are discussed in Section 1.4.1.2.

1.4.1.1 Antibody-immobilization strategies in EGOT-based biosensors

Electrolyte-Gated Organic Transistor (EGOT) architectures for (bio)sensing applications rely on the immobilization of a biorecognition layer at either the gate/electrolyte or the channel/electrolyte interface. Early efforts in the field focused on the direct functionalization of the Organic Semiconductor (OSC) channel.[142][143] However, most OSCs are intrinsically hydrophobic and chemically fragile, which

makes them unsuitable for the stable immobilization of biorecognition elements and leads to deterioration of their electronic properties upon functionalization. As a result, effective and reproducible channel surface modification has so far been largely limited to PEDOT:PSS and reduced Graphene Oxide (rGO)[48], whose more hydrophilic and chemically active surfaces can accommodate grafting of biorecognition element, while preserving device performance.

The most adopted EGOT-based biosensor architecture features a large-area gate electrode functionalized with a biorecognition moiety.[136] The immobilization of the biorecognition probe is crucial to achieve an effective biorecognition process and to guarantee the long-term stability of the biosensor. The strategies for grafting biorecognition layers depend on the nature of the interactions between the surface and the biosensing probe (**Figure 1.8**).[144] Potentiometric perturbations occurring at the gate/electrolyte interface -caused by the binding of the target analyte to biorecognition probes fixed on the gate surface - are directly transduced into an amplified electrical change in the EGOT device via capacitive coupling.[32,130]

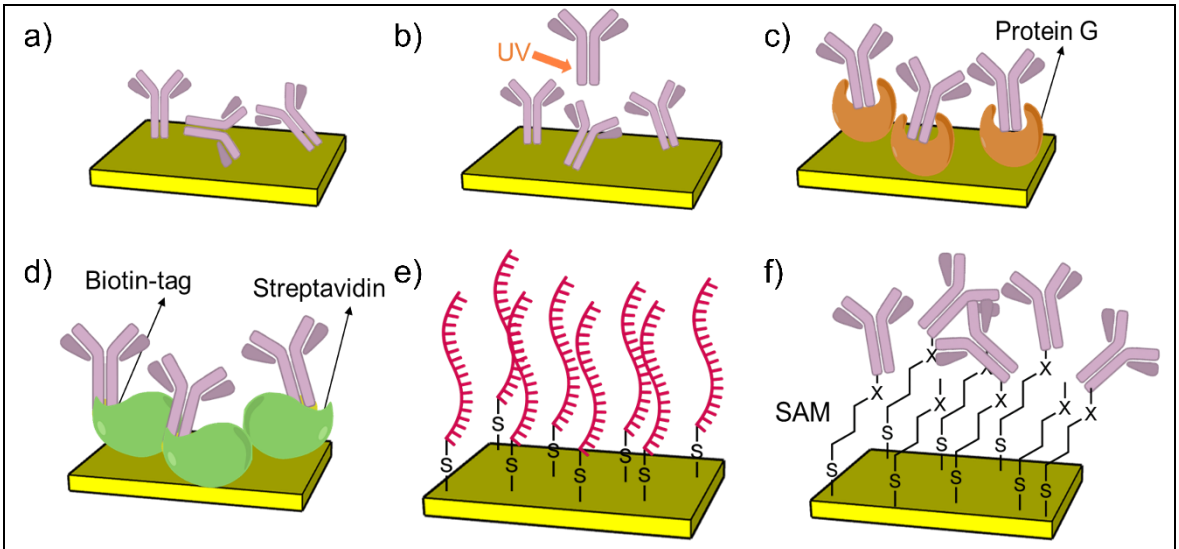

***Figure 1.8**: Sketched representation of the most common biofunctionalization routes. a-b) Physical immobilization including physisorption (a) and activated physisorption (b). c-d) Bioaffinity coupling including engineered protein G (or protein A) (c) and biotin-streptavidin interaction (d). e-f) Covalent interactions established between the biorecognition element (usually thiolated oligonucleotides) directly on the surface (e) and mediated by the formation of a Self-Assembled Monolayer (SAM) (f).*

Physical immobilization strategies involve the direct approach of the biorecognition element onto the solid surface.

Physisorption (**Figure 1.8a**) occurs when the biorecognition probe approaches the solid substrate without any surface pretreatment, relying only on non-covalent, weak interactions. Although this strategy is cost-effective, fast, and compatible with printing techniques as well as green chemistry[145], this immobilization method often compromises high performance due to its lack of uniformity and poor long-term stability.[145–147] The stability and orientation of the physically immobilized biorecognition element can be enhanced by optimizing experimental conditions, including activation with light[148], pH[149], and ionic strength[150] (**Figure 1.8b**).

The second strategy for immobilizing a biorecognition probe relies on bioaffinity interactions between a biomolecule acting as a linker and the biorecognition elements. Grafting the sensing probe onto the linker biomolecule occurs via the formation of several weak interactions and enables the oriented immobilization of the biorecognition moiety on the surface.[151] Among the techniques exploiting bioaffinity interactions, the most used in EGOT-based biosensors involves grafting an engineered protein (usually Protein G or Protein A) bearing a polyhistidine Tag to the metal surface (**Figure 1.8c**).[45,152–154] In the case of immunosensors, the specific orientation of the antibody guaranteed by these immobilization methods is due to the affinity interactions established between the protein's functional active site and the highly conserved fragment (crystallisable fragment, Fc) of the antibody. As demonstrated by Casalini and co-workers, a Protein G-mediated immobilization strategy for antibodies yields a coverage of available antibodies for recognition three-times larger than a non-optimized approach involving covalent bindings (see below for further details).[152] Furthermore, bioaffinity coupling results in good specificity, even in complex fluids.[45] Another common approach for bioaffinity coupling exploits biotin-streptavidin interactions, with biotin molecules immobilized on a streptavidin layer at the interface (**Figure 1.8d**).[122,155] However, the most widely used strategy to immobilize biorecognition elements on a gate electrode surface for the development of an EGOT-based biosensor involves the formation of a covalent bond between the surface and the biorecognition probe. The functional groups (*viz.,* carboxylic, hydroxyl, amine, and thiol groups) provided by the biosensing element are usually involved in covalently binding the biomolecule onto solid supports. By exploiting the metal-sulphur covalent bond, thiolated oligonucleotides and aptamers can be directly bound to the surface of the gate

electrode (**Figure 1.8e**). For example, White and co-workers developed a label-free DNS sensing platform by directly immobilizing single-stranded DNA on the gate electrode surface.[156] Moreover, Selvaraj and colleagues extended this concept for the detection of miRNA-21.[46] However, this strategy is limited to biorecognition probes that exhibit terminal thiol groups. To introduce chemical functions or groups onto the gate electrode surface, the widely employed method relies on the formation of a Self-Assembled Monolayer (SAM).[157] According to Whitesides and Grzybowski, "self-assembly is the autonomous organization of components into patterns and structures, without human intervention".[158] SAMs are formed by the self-alignment of molecules in two dimensions on surfaces, forming a quasi-crystalline structure.[144] Although different SAM systems exist depending on the molecular components, the most widely adopted strategy involves the use of alkanethiols on a gold surface. The sulphur atoms of alkanethiols adhere to the gold surface, and the tightly packed alkyl chains are tilted by an angle of 30° to the gold surface.[159] Alkanethiol monolayers on gold are easy to prepare, cost-effective, and yield highly ordered and large 2D crystalline domains.[157] Such molecules present two different head and tail functional groups, where one end binds to the sensor surface and the other end anchors the biorecognition probe (**Figure 1.8f**). The resulting interaction between the biomolecule and the surface is governed by a stable covalent bond, ensuring high stability of the biorecognition layer.[154] Moreover, substrates modified with SAMs having different reactive terminal groups can be used for multicomponent immobilization, and therefore for multianalyte detection.[144] The high packing density, the enhanced stability in ambient conditions, and the ability to control the interfacial properties of the systems guaranteed by SAM chemistry overcome the issue of non-oriented antibody grafting, making SAMs the most utilized strategy to anchor biorecognition probes in EGOT-based biosensors.[41,47,160–162]

The existing classification of biorecognition probe immobilization strategies fails to consider the complex interactions between the functionalization layer and the electrode surface. In fact, examples can be found of EGOT biosensors where the biorecognition element interacts directly with the electrode surface via non-covalent interactions without any biological and/or molecular layer[140,153,163], or where a SAM chemically linked to the electrode acts as the sensing probe.[47,136]

Tailoring the surface chemistry of the gate electrode is therefore a critical strategy for developing high-performance EGOT-based biosensors. For example, Casalini

and collaborators showed that an approach yielding more oriented antibody grafting outperforms methods that guarantee covalent albeit random immobilization.[152] More recently, Macchia and co-workers demonstrated a phenomenological sensing amplification mechanism, arising from pH-conditioning that drives protein-based recognition elements into a metastable state, enabling single-molecule detection.[164]

In this thesis work, the immobilization strategy for the anti-L-Tryptophan antibody on the gate electrode of an EGOT-based biosensor platform is optimized by comparing two SAM-mediated approaches. The first protocol is based on an optimized Schiff Base Reaction (SBR) and involves the formation of a cysteamine (CYS) SAM, which is then functionalized with glutaraldehyde (GA), a homo-bifunctional crosslinker. The remaining free aldehyde moieties subsequently react with the exposed amino groups of the monoclonal L-Trp antibodies, forming a stable imine (C=N) bond. To harness the response of the EGOT-based biosensor towards L-Tryptophan, the pH of the aqueous GA solution in the SBR functionalization strategy is systematically investigated, reaching an optimum value at alkaline pH (pH = 10). The second strategy involves the formation of a binary SAM (11-mercaptoundecanoic acid (11-MUA) and 6-mercaptohexanol (6-MH)). The exposed -COOH groups of the SAM monolayer are further activated via N-(3-dimethylaminopropyl)-N-ethylcarbodiimide (EDC) and N-Hydroxysuccinimide (NHS) coupling chemistry to covalently bind the antibody through an amide bond. The experimental details and the results are reported in Section 3.3 and in Chapter 4, respectively.

1.4.1.2 MXenes

MXenes ($M_{n+1}X_nT_x$) are a large class of 2D materials, typically composed of transition metal carbides, nitrides, or carbonitrides, where T_x denotes surface terminations such as -F, -OH, or =O. These materials first emerged in 2011.[165] through the selective etching of the 'A' element from their MAX phase precursors ($M_{n+1}AX_n$). In the MAX phase, 'M' is an early transition metal (*e.g.,* Ti, Sc, Nb, Mo, Ta, V), 'A' is an element from group IIIA or IVA (*e.g.,* Al or Si), and 'X' is C and/or N. While nearly 80 single-M MAX phases are reported.[166]

The focus in this thesis is centred on the most common $Ti_3C_2T_x$. The selective extraction of the A-element layers is enabled by the difference in bond strength: the M-A bonds are metallic and more chemically active than the stronger, predominantly

covalent-ionic M-X bonds. Aqueous, fluoride-containing acidic solutions, such as HF, selectively etches the A element layers from the MAX phase.[167] This extraction generates unstable, unsaturated metallic sites on the newly formed surfaces. These sites are instantaneously passivated by inorganic species present in the reaction environment (typically F^-, HO-, O^{2-}, O_2^{2-}), thus creating the stabilizing surface termination layer, T_x.[168] The wide array of possible elements and stoichiometric combinations provides MXenes with a unique blend of properties. These features can be broadly categorized into electronic, thermal, mechanical, optical, and magnetic properties, all of which can be tailored by tuning the surface chemistry of the T_x terminations.[169,170] In particular, MXenes exhibit exceptional electrical conductivity (consistent with their metallic nature). Reported values range widely, from as low as 1 $S \cdot cm^{-1}$ to over 1500 $S \cdot cm^{-1}$, depending on the precursor, synthesis route, and post-synthesis conditions.[171] Furthermore, the strong covalent-ionic M-X bond within the structure contributes to their unique mechanical strength. This is augmented by the strong hydrogen bonding between adjacent MXene nanosheets, which is shown to be significantly stronger than the interlayer forces in materials like graphite or MoS_2.[172] Many MXenes also exhibit high transparency; for example, thin films can achieve a transmittance (%T) of about 91%[173], making them promise for transparent electrodes and optoelectronics. Magnetic properties are dictated by the octahedral coordination of the transition metal atoms and the occupation of their d-orbitals. Finally, their demonstrated biocompatibility and biodegradability[174,175] are critical factors favouring their integration into organic bioelectronic devices.

Building on their diverse and tailorable properties, MXenes have emerged as highly versatile materials for a wide range of applications, including supercapacitors[167,176] and lithium-ion batteries.[177] Moreover, the combination of their exceptional electrical conductivity, large electroactive surface area – arising from their layered morphology - and the tunability of their surface terminations (T_x), which provides abundant active sites, makes MXenes particularly attractive for biosensing applications.[178,179] Their chemical and structural versatility enables MXenes to assume multiple functional roles in biosensor design, serving both as efficient signal-transduction layers[180] and as robust platforms for biomolecule immobilization.[181–183]

MXene-based electrochemical (bio)sensors are successfully demonstrated for the detection of a multitude of target analytes, including biomarkers, pathogens, metabolites, chemical molecules, and pesticides.[183–185] The substantial volume of

published research attests to the versatility of MXenes integrated into various sensor typologies. However, the integration of pure MXenes into EGOT architectures is still remarkably limited.

To the best of our knowledge, only a few studies report the use of pure MXene as an active material within an EGOT-based platform.[186–188] In the seminal work by Xu *et al.,* they developed an ultrathin MXene-micropattern field-effect transistor for Dopamine (DA) sensing.[186] Subsequently, Cai and co-workers developed a MXene-based EGOT biosensor with both the channel and the gate electrode functionalized with MXenes to detect ions, urea, and glucose.[187] The fabrication methods are further refined by Zeglio *et al.*, who demonstrated the influence of layer-by-layer deposition on EGOT characteristics.[188] It is important to highlight that while other studies integrating the Field-Effect Transistor architectures with MXenes exist, these works either employ MXenes as blended materials (e.g., with graphene[189], PEDOT:PSS[190], or metals[191]) or operate within the standard organic FET architecture, typically requiring high gate voltages (>1 V).[192,193]

In this thesis (Chapter 5), a series of chemically-engineered MXenes are employed as functionalization layers for the gate electrode and integrated into an EGOT platform for the ultrasensitive detection of DA. MXenes exhibit strong interactions with primary amines, including DA, which are often attributed to the potential formation of highly stable Ti-N bonds, as reported in previous studies.[194–196]

The sensor response across the tested concentration range (100 fM to 10 μM) is interpreted by considering two distinct MXene-DA interaction mechanisms. At low DA concentrations (below 1 μM), the signal is primarily governed by a high-affinity and specific interaction between DA and the MXene surface, dominated by electrostatic attraction and possible coordination effects. At higher concentrations (above 1 μM), the response is instead dominated by a non-specific process associated with DA electro-oxidation and subsequent adsorption of oxidation products.

Finally, by exploiting the multiparametric response of EGOT-based devices, Principal Component Analysis (PCA) is used to investigate and compare the interaction mechanisms occurring between the different functionalized MXenes with DA. This multivariate approach enables the formulation of hypotheses linking the surface termination groups (*viz.,* the structure) of the MXenes with the parameters extracted from MXene-EGOT transfer curves collected in presence of DA.

1.4.2 Organic Neuromorphic Electronics

The concept of neuromorphic systems is pioneered by Carver Mead in 1990, envisioning a novel technological paradigm aimed at replicating the core functionalities of the biological brain using digital technologies.[197] The impetus for this field is rooted in the remarkable efficiency of biological systems, which manage highly complex data processing with extraordinary energy economy, typically consuming only 10 - 20 W. Furthermore, the brain exhibits an unparalleled degree of interconnectivity between computational units - neurons and synapses -and an intrinsic capability for adaptation and learning.[198] This outstanding biological architecture is the foundation for neuromorphic science, generally divided into neuromorphic computing (the development of energy-efficient hardware to mimic biological information processing) and neuromorphic electronics (the design of electronic devices that simulate specific cognitive functions of the brain).[199,200] The successful development of neuromorphic electronic systems capable of emulating brain functions fundamentally requires a deep understanding of the physiological mechanisms of the Central Nervous System (CNS). Comprising the brain and spinal cord, the central nervous system (CNS) is responsible for receiving sensory input, processing this information, and generating appropriate responses.[201] The primary functional unit of the CNS is the neuron (**Figure 1.8a**), a specialized cell of the nervous system. Structurally, the neuron consists of the soma, or cell body, which houses metabolic organelles; dendrites, branched extensions that receive signals from adjacent neurons; and the axon, a long projection responsible for transmitting information, known as the action potential, to target cells. Communication between neurons occurs at specialized junctions known as synapses. The neuron's primary electrical signal, the action potential (**Figure 1.8b**), is initiated at the axon hillock in response to a stimulus that perturbs the resting membrane potential (approximately -70 mV). This perturbation arises from the regulated transmembrane flux of ions, predominantly Na^+, K^+, and Cl^-. When the resulting depolarization reaches the threshold voltage (typically around -50 mV), an action potential is triggered in an all-or-none fashion, rapidly reaching a positive peak of approximately +40 mV within milliseconds. The membrane then undergoes a rapid repolarization, which is often followed by a brief hyperpolarization before returning to the resting potential.[202] This transient electrical signal is subsequently propagated along the axon until it reaches the synaptic terminals.

Synapses are broadly categorized as either chemical or electrical (**Figure 1.8c, d**). Chemical synapses lack physical contact, featuring a narrow synaptic cleft. Here, the electrical signal of the action potential is converted into a chemical signal via the release of neurotransmitters into the cleft. These molecules bind to receptors on the postsynaptic neuron, causing a change in the postsynaptic membrane polarization and initiating an electrical response.[203] Conversely, electrical synapses ensure direct transmission of the electrical signal between the pre- and postsynaptic neurons through specialized channels called gap junctions.[204]

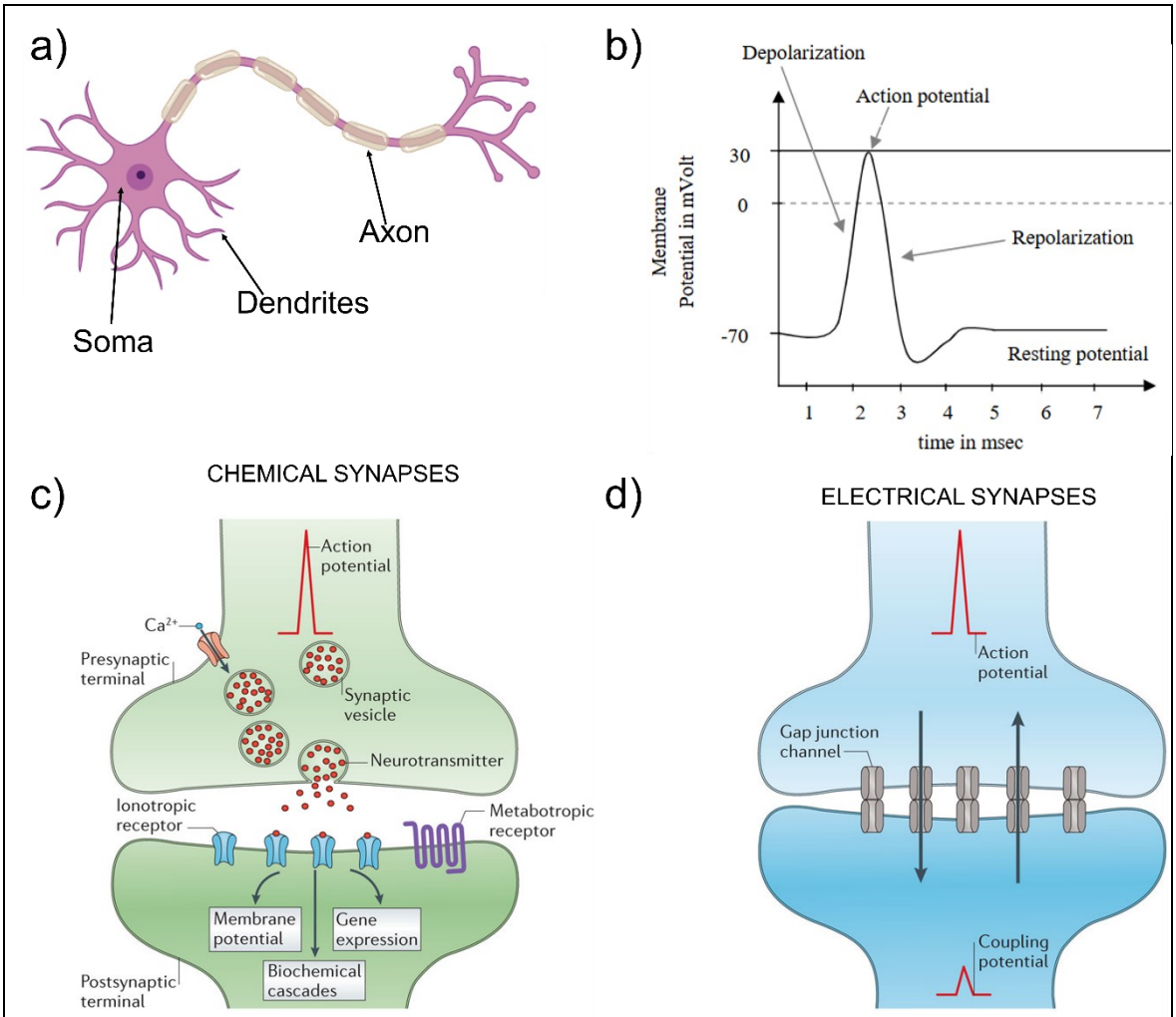

***Figure 1.9**: Schematic representation of the neuron structure and of the synaptic transmission of physiological electrical signals. a) Sketched of neuron structure, created with https://BioRender.com. b) Typical waveform of an axon potential. Representation of chemical (c) and electrical (d) synapses, respectively. Adapted from:*[204].

Synaptic transmission is inherently a dynamic, rather than static, process. The strength of the connection between neurons is not fixed, as the underlying molecular and ionic mechanisms require characteristic recovery times. Consequently, due to repetitive pre-synaptic stimulation, synapses can exhibit activity-dependent modifications, a phenomenon known as synaptic plasticity. This process allows synapses to either potentiate (increase in synaptic strength, making transmission more effective) or, conversely, depress (decrease in synaptic strength, weakening the connection).[205] Synaptic plasticity is critically related to the brain's high-level computational capabilities, serving as the fundamental mechanism for signal filtering, learning, adaptation, and memory formation.[206–208] The expression of plasticity is dependent on the temporal scale of input processing and is generally differentiated into two main categories: Short-Term Plasticity (STP), which operates on time scales ranging from tens of milliseconds up to a few minutes, and Long-Term Plasticity (LTP), which underlies changes lasting from minutes to hours or even years.[209]

Neuromorphic electronic systems derive their core inspiration from the human brain, which uniquely integrates computation and memory within the same physical space and utilizing the same underlying building blocks. The fundamental goal of the neuromorphic paradigm is the development of robust hardware and software components based on the plasticity phenomena. These systems must be capable of adapting and improving performance over time, thereby directly mimicking the brain's intrinsic learning and cognitive processes.

Within this technological context, organic bioelectronic devices have emerged as prime candidates for neuromorphic applications. Their suitability stems from inherent material properties, including flexibility and biocompatibility[210], which facilitate effective and seamless integration with biological systems. Crucially, the ionic-electronic coupling characteristic of organic materials plays a pivotal role. This coupling allows the electrical behaviour of OSCs, particularly OMIECs which exhibit high ion permeability, to be dynamically tuned. This unique mechanism makes various organic bioelectronics device architectures - including EGOTs[79,211], two-terminal artificial synapses[81,82], and electrolyte-gated switching[212] - eligible as key building blocks for neuromorphic circuits.

The underlying physics of the neuromorphic features in these devices relies on the kinetic imbalance generated by the significantly slower transport of mobile ions compared to the drift of electronic charge carriers. This inherent delay causes the

devices to operate as history-dependent, out-of-equilibrium systems, where the current response is intrinsically modulated by the prior interaction between mobile ions and the active material. By harnessing this dynamic interplay (*viz.,* through changing the input signal protocol or the nature of the electrolyte ion), organic bioelectronic platforms, and particularly EGOTs, have successfully demonstrated the emulation of essential brain functions. These include different forms of synaptic plasticity such as Short-Term Plasticity (STP)[79], Long-Term Plasticity (LTP)[44], Spike-Timing Dependent Plasticity (STDP)[213], and even global connectivity features.[214]

EGOT-based devices are successfully optimized for applications ranging from brain-machine interfaces capable of processing and transducing signals with minimum power consumption[215,216], to EGOT-arrays demonstrated to distinguish dynamic input patterns for complex biological signal recognition.[217]

Despite these advancements, the most of EGOT devices for neuromorphic application utilize unipolar semiconductors (p-type or n-type), limiting their operation to the conduction of only a single type of charge carrier (holes or electrons, respectively). To overcome this limitation, ambipolar materials, which can conduct both electrons and holes depending on the gating conditions, offer a significant advantage. Ambipolarity enables circuit design simplification, leading to increased space- and power-efficiency in circuitry by reducing the number of necessary components. Among the different ambipolar materials, rGO exhibits highly efficient ion-to-electron transduction. Moreover, rGO provides several fabrication advantages (detailed in Section 1.3), including excellent aqueous processability, tunability of its conductivity and surface functionalities (according to the degree of reduction of GO), and a large surface-to-volume ratio.[218] Ambipolarity, coupled with the charge carriers' (de-)trapping kinetics, can be exploited to mimic sophisticated functions like bidirectional signal transmission and neurotransmitter intake/release typical of biological synapses.[219,220] In this thesis, a straightforward and tunable approach for controlled-fabrication of rGO-based Electrolyte-Gated Transistors (EGTs) is introduced, developing an *in-situ* electrochemical reduction from GO dispersions. This procedure results in the spontaneous formation of a high-performance rGO thin film that exhibits current plasticity with pulse widths significantly lower than those recorded for thermally reduced rGO thin films.[218] This notable reduction in the required input pulse width directly translates into an increased operational speed and reduced energy consumption per synaptic event,

addressing a critical limit of neuromorphic computing. This confirms that the novel fabrication technique introduced here is crucial for significantly enhancing the performance of rGO-EGT based neuromorphic devices.

1.5 Multivariate Data Analysis

Multivariate analysis encompasses a suite of techniques designed to analyse datasets characterized by multidimensional variables. These techniques are particularly advantageous when dealing with correlated variables, offering robust methods for information extraction, regression, and classification. The application of these analytical tools to chemical data laid the foundation for the discipline of chemometrics[221], an interdisciplinary science combining statistics, mathematics, and chemistry to address complex analytical problems beyond the traditional boundaries of chemistry.[222,223] The primary aims of chemometrics focus on experimental design, the extraction of relevant information from studied systems, and the clear visualization of data structures.[224] To this purpose, chemometric methods found extensive utility in processing high-dimensional spectroscopic data, such as Nuclear Magnetic Resonance (NMR), Raman, Infrared (IR), and UV-visible spectra.[225] Among these techniques, Principal Component Analysis (PCA) is the most widely employed exploratory tool. It reduces the dimensionality of large datasets - typical of spectroscopic outputs - thereby enhancing result interpretability while minimizing information loss.[226] For quantitative analysis, chemometrics utilizes multivariate regression methods, primarily Principal Component Regression (PCR) and Partial Least Squares (PLS) regression.[227] Furthermore, classification methods, including k-nearest neighbour (k-NN) and PLS-Discriminant Analysis (PLS-DA), represent another crucial sector, aiming to build predictive models that assign qualitative attributes to samples based on experimental data.[228]

The integration of chemometrics into biosensing platforms has followed its established success in spectroscopy. Traditionally, the high intrinsic selectivity of biorecognition elements has meant that biosensor calibration rarely required sophisticated mathematical tools, with simple univariate regression often sufficient to relate the sensor response to the analyte concentration.[229] However, achieving ultra-low detection limits within complex real-world matrices frequently introduces significant interference effects. While these challenges can sometimes be addressed by engineering highly specific sensing interfaces, such strategies

inevitably increase development time and cost. A more robust and versatile alternative relies on the application of advanced data-processing approaches - namely, chemometrics - which enable the construction of reliable calibration models even in the presence of interfering signals or non-ideal sensor responses.[229,230] Consequently, chemometric techniques have garnered considerable interest for enhancing the performance of diverse biosensing platforms, including both electrochemical[231,232] and spectroscopic devices.[233] Despite this potential, the application of chemometric tools to EGOT-based biosensors remains, to the best of our knowledge, limited to a few select instances. In 2024, Sensi *et al.,* introduced the application of principal component analysis (PCA) to tackle the complexity inherent in EGOT responses, demonstrating that the integration of multiple parameters provides a more comprehensive monitoring of the biorecognition process.[234] Furthermore, recent studies on Single-Molecule with a large Transistor (SiMo-T) arrays have highlighted the critical role of multivariate analysis in clinical diagnostics. Scandurra *et al.,* first demonstrated that integrating multivariate analysis with SiMo-T electronic readouts is essential to effectively discriminates patients based on pancreatic cystic lesion severity, a distinction not achievable with standard chemiluminescent immunoassays.[235] Building on this, Genco and co-workers confirmed that applying an exploratory PCA coupled with a k-NN classifier to multiplexed SiMo-T arrays enables the accurate discrimination of these patient groups.[236] Finally, the influence of signal preprocessing on the data analysis presented in these recent works is comprehensively discussed by Caputo *et al.,*.[237] Furthermore, this chapter provides a concise overview of the multivariate data analysis methods employed throughout this thesis work.

1.5.1 Principal Component Analysis (PCA)

Principal Component Analysis (PCA) is a multivariate explorative tool that allows to reduce the dimensionality of the original dataset by capturing and evaluating similarities, differences, outliers and cluster tendency of the data matrices.[238] PCA is a bilinear decomposition/projection technique capable to transform the correlated variables of the original data into a fewer number of independent and uncorrelated variables, called Principal Components (PCs), orthogonal each other.[239,240] The first PC is constructed through detecting among the infinite directions of the n-dimensional space (where n is the number of variables), the one that involves the

largest variability in the data. The second PC is constructed orthogonally to the first, incorporating the largest source of variability not expressed from the first one, and so on. Using this approach, it is possible to create a new projection space, smaller in size, whose coordinates are represented by the PCs.[226]

As reported in **Figure 1.10a**, PCA decomposes the data matrix as reported in Equation 1.3:

$$\mathbf{X}_{(I,J)} = \mathbf{T}_A \bullet \mathbf{V}_A^T + \mathbf{E}_{(I,J)} \quad \text{(Eq. 1.3)}$$

where, **X** is a data matrix composed by I rows (observations) and J columns (variables) (**Figure 1.10b**), **A** is the number of the extracted components, $\mathbf{T}_A = [\mathbf{t}_1, \mathbf{t}_2 \ldots \mathbf{t}_A]$ represents the score matrix, giving the coordinates of the i-sample in the PCs space (**Figure 1.10c**), whereas $\mathbf{V}_A = [\mathbf{v}_1, \mathbf{v}_2 \ldots \mathbf{v}_A]$ is the loading matrix and expresses the weight (*viz.,* the influence) with which each original variable contributes to the principal components. **E** is the residual matrix, that contains the unmodelled variation and has the same dimensions of X.

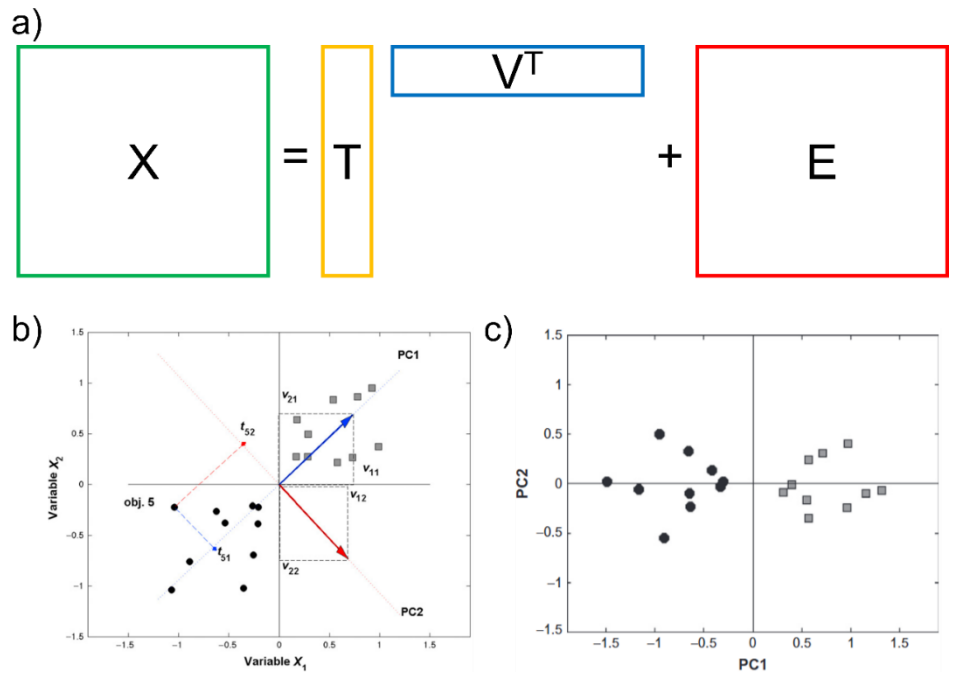

***Figure 1.10**: Geometry of PCA. a) PCA decomposition of X. b) A simulated example with 20 samples plotted in the space of the original variables x1 and x2. The blue and the red lines represent the direction of PC1 and PC2 axes, respectively. c) The representation of the simulated 20 samples represented in the PCs space: PC1 vs PC2. Adapted from:*[239].

From an algebraic point of view, PCs are a linear combination of the original variables (Equation 1.4):

$$\mathbf{t_a = X \cdot v_a} \quad \text{(Eq. 1.4)}$$

where $\mathbf{v}_a$, that represents the loading vectors, is normalized (*viz.,* $\mathbf{v_a^T v_a} = 1$) and orthogonalized (*viz.,* $\mathbf{v_a^T v_b} = 0$). Moreover, the PCA relies on maximizing the variance for each component; therefore, var($\mathbf{t}_a$) must be maximized. For **a** ranging from 1 to **A**, the variance var($\mathbf{t_a}$) can be expressed as in Equation 1.5:

$$\text{var}(\mathbf{t_a}) = (\mathbf{X v_a})^T(\mathbf{X v_a}) = \mathbf{v_a^T X^T X v_a} = \mathbf{v_a^T}\text{cov}(\mathbf{X})\mathbf{v_a} \quad \text{(Eq. 1.5)}$$

where “cov” stends for the covariance.

Assuming that X is mean-centred, the solution can be formulated as an eigenvector/eigenvalues problem. For each value of **a**:

$$\text{cov}(\mathbf{X})\mathbf{v_a} = \boldsymbol{\lambda_a v_a} \quad \text{(Eq. 1.6)}$$

Equation 1.6 means that the unknown values for the loadings correspond to the eigenvectors of the **X** covariance matrix and **λ** are the corresponding eigenvalues. In other words, the computation of the PCs entails the diagonalization of the covariance matrix of X, when **X** is column mean-centred. Consequently, the PCs are sort in decreasing variance order.[239]

Considering the algebraic property of the conservation of the trance, the sum of the eigenvalues equals the total variance of the **X** matrix (Equation 1.5):

$$\sum_a \lambda_a = \text{var}(\mathbf{X}) \quad \text{(Eq. 1.7)}$$

Equation 1.6 can be solved using standard eigenvalues/eigenvectors decomposition algorithms, yielding the loading vectors. The corresponding score vectors are obtained from Equation 1.8:

$$\mathbf{T = X \cdot V^T} \quad \text{(Eq. 1.8)}$$

1.5.2 Partial Least Square Discriminant Analysis (PLS-DA)

Partial Least Square Discriminant Analysis (PLS-DA) is originally proposed to extend the advantages of Partial Least Square (PLS) Regression[241], a calibration method based on the partial least squares algorithms. PLS Regression is a multivariate linear regression technique, whose aim is therefore, to find the best (linear) relationship between a set of predictors (the matrix **X**) and one or more responses (the matrix **Y**).

PLS Regression operates by projecting both the **X** and the **Y** matrix onto a reduced (low-dimensional) common set of latent variables (**T** and **U**)

$$\mathbf{T = XP} \quad \text{(Eq. 1.9)}$$

$$\mathbf{U = YQ} \quad \text{(Eq. 1.10)}$$

where **T** and **U** are the score matrices for **X** and **Y** respectively, **P** are the **X** loadings and **Q** the **Y** loadings.

Differently from PCA, the decomposition operated by PLS explains as much as possible of the variability of X and maximizes the covariance between the two matrices.[228]

The maximum covariance criterion is imposed through a regression model for each component between the scores of **X** ($\mathbf{t_i}$, the i_{th} columns of the **T** score matrix) and **Y** ($\mathbf{u_i}$). The linear dependence between the **X** and the **Y** blocks is achieved by imposing **U** to be linearly proportional to **T** component-wise

$$\mathbf{u_i = t_i c_i \rightarrow U = TC} \quad \text{(Eq. 1.11)}$$

where $\mathbf{c_i}$ is the inner regression coefficients collected in diagonal matrix **C**.

By combining Equation 1.10 and Equation 1.11 it is possible to explicitly express the predicted response in terms of the scores:

$$\mathbf{\hat{Y} = TCQ^T} \quad \text{(Eq. 1.12)}$$

so that by further incorporating Equation 1.12 in Equation 1.9 one obtains:

$$\mathbf{\hat{Y} = XPCQ^T = XB_{PLS}} \quad \text{(Eq. 1.13)}$$

where the PLS regression coefficients BPLS are defined as

$$\mathbf{B_{PLS} = PCQ^T} \quad \text{(Eq. 1.14)}$$

In other words, scores and loadings in PLS possess the same mathematical properties as in PCA; however, in PLS the latent variables (LVs) are constructed to capture the directions in **X** that are most strongly related to the variation in **Y**. The use of a small number of orthogonal score vectors (**T**) as regressors for the response matrix allows more stable and reliable estimates of the model parameters. Moreover, Equation 1.13 shows that the PLS model can be expressed directly in terms of the original measured variables through the regression coefficient matrix $\mathbf{B_{PLS}}$, which greatly facilitates the prediction of new samples.[228]

To employ PLS regression for classification purposes, the qualitative class information must first be encoded into a numerical response matrix **Y**. This is achieved by constructing a **Y** matrix with as many the number of the classes and applying a binary (dummy) coding scheme: for each sample, the corresponding row contains zeros in all columns except for that representing its class, which is assigned a value of one.

This transformation enables the use of the PLS regression algorithm to derive discriminant classification models, giving rise to the method known as Partial Least Squares Discriminant Analysis (PLS-DA).[228,242,243] In PLS-DA, a PLS regression model is built between the experimental data matrix **X** and the binary-coded **Y**, yielding a continuous predicted response ŷ for each sample. In this thesis, PLS-DA is employed as a classification strategy to validate the EGOT-chemometric model developed to achieve enantiodiscrimination between the L-Trp and D-Trp enantiomers.

For two-class problems, the dummy matrix **Y** can be reduced to a single-column vector, where values of 1 and 0 denote the samples belonging to the first and second class, respectively. As depicted schematically in **Figure 1.11** for a typical binary PLS-DA problem, classification is finally obtained by applying an appropriate threshold to the predicted response *ŷ*.

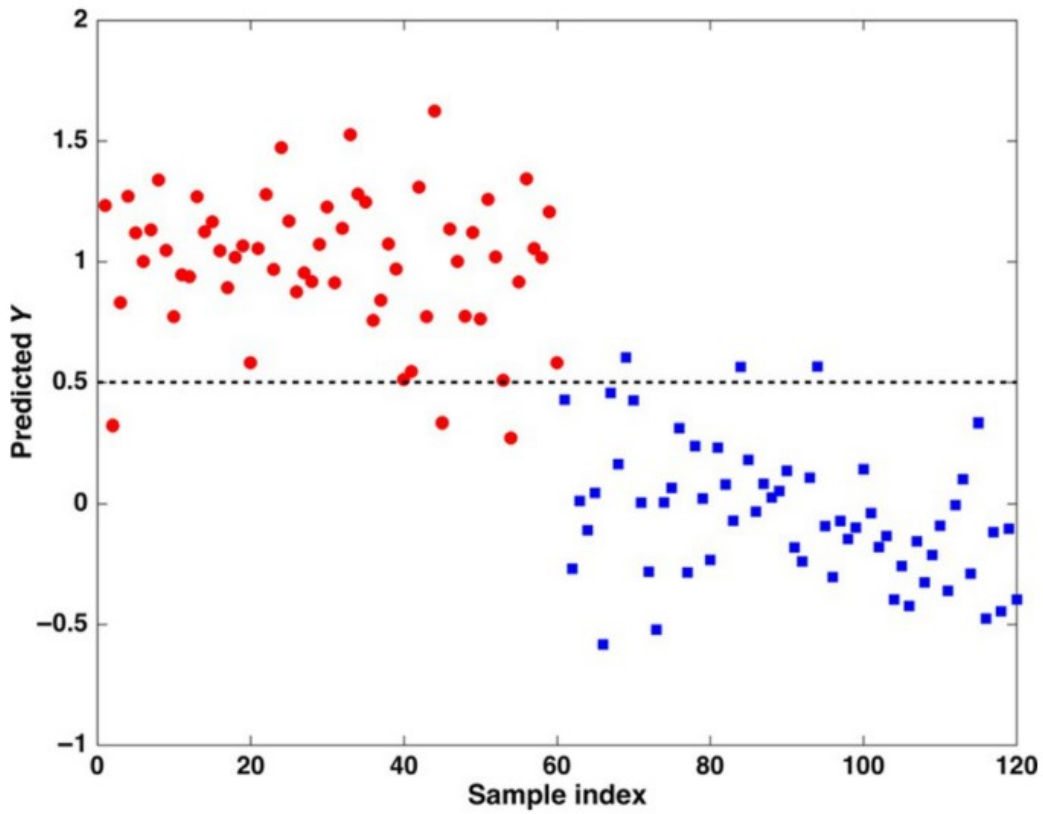

***Figure 1.11**: Schematic illustration of PLS-DA classification based on predicted Y for a problem involving two categories (red circles and blue squares). The black dashed line represents the classification threshold (ŷ = 0.5): samples falling above the line are assigned to the red class, while samples falling below are assigned to the blue one. Adapted from:*[228].

The PLS-DA model must be validated to assess both its predictive performance and its interpretative reliability. To ensure a rigorous evaluation of the proposed classification approach, validation is carried out using a completely independent subset of samples (the test set), which is not involved in model calibration and therefore provides an unbiased estimate of its classification ability.

1.6 Bibliography

1. Shirakawa H *et al.* “Synthesis of electrically conducting organic polymers: Halogen derivatives of polyacetylene, (CH)x.” *J Chem Soc Chem Commun* 1977; (16): 578–580. doi:10.1039/C39770000578.
2. Natta G. “Progress in Five Years of Research in Stereospecific Polymerization.” *SPE J* 1959.
3. Coropceanu V *et al.* “Charge Transport in Organic Semiconductors.” *Chem Rev* 2007: 926–952.
4. Fukuda K *et al.* “The Future of Flexible Organic Solar Cells.” *Adv Energy Mater* 2020; 10(25): 1–10. doi:10.1002/aenm.202000765.
5. Nam M *et al.* “Highly reliable and stretchable OLEDs based on facile patterning method: toward stretchable organic optoelectronic devices.” *npj Flex Electron* 2024; 8(1). doi:10.1038/s41528-024-00303-5.
6. Lago N, Cester A. “Flexible and organic neural interfaces: A review.” *Appl Sci* 2017; 7(12). doi:10.3390/app7121292.
7. Song J *et al.* “Flexible Organic Transistors for Biosensing: Devices and Applications.” *Adv Mater* 2024; 36(20): 1–49. doi:10.1002/adma.202300034.
8. Kim H *et al.* “Organic Mixed Ionic–Electronic Conductors for Bioelectronic Sensors: Materials and Operation Mechanisms.” *Adv Sci* 2024; 11(27): 1–28. doi:10.1002/advs.202306191.
9. Simon DT *et al.* “Organic Bioelectronics: Bridging the Signaling Gap between Biology and Technology.” *Chem Rev* 2016; 116(21): 13009–13041. doi:10.1021/acs.chemrev.6b00146.
10. Berggren M, Richter-Dahlfors A. “Organic bioelectronics.” *Adv Mater* 2007; 19(20): 3201–3213. doi:10.1002/adma.200700419.
11. Malliaras GG. “Organic bioelectronics: A new era for organic electronics.” *Biochim Biophys Acta - Gen Subj* 2013; 1830(9): 4286–4287. doi:10.1016/j.bbagen.2012.10.007.

12. Biscarini F *et al.* “Elettronica organica.” *Encicl Ital di Sci Lett ed arti - IX Append* 2015.
13. Fahlman M *et al.* “Interfaces in organic electronics.” *Nat Rev Mater* 2019; 4(10): 627–650. doi:10.1038/s41578-019-0127-y.
14. Tang CW, Vanslyke SA. “Organic electroluminescent diodes.” *Appl Phys Lett* 1987; 51(12): 913–915. doi:10.1063/1.98799.
15. Burroughes JH *et al.* “Light-emitting diodes based on conjugated polymers.” *Nature* 1990; 347(6293): 539–541. doi:10.1038/347539a0.
16. Li G *et al.* “High-efficiency solution processable polymer photovoltaic cells by self-organization of polymer blends.” *Nat Mater* 2005; 4(11): 864–868. doi:10.1038/nmat1500.
17. C. W. Tang. “Two Layer Organic Photovoltaic Cell.” *Appl Phys Lett* 1986; 48(183): 183–185. Available at: http://link.aip.org/link/APPLAB/v48/i2/p183/s1.
18. Jakher S, Yadav R. “Organic thin film transistor review based on their structures, materials, performance parameters, operating principle, and applications.” *Microelectron Eng* 2024; 290(December 2023): 112193. doi:10.1016/j.mee.2024.112193.
19. Miao Z *et al.* “Organic light-emitting transistors with high efficiency and narrow emission originating from intrinsic multiple-order microcavities.” *Nat Mater* 2025; 24(6): 917–924. doi:10.1038/s41563-025-02191-0.
20. Di Lauro M *et al.* “A Bacterial Photosynthetic Enzymatic Unit Modulating Organic Transistors with Light.” *Adv Electron Mater* 2020; 6(1): 1–5. doi:10.1002/aelm.201900888.
21. Liu J *et al.* “Electrolyte-gated light-emitting transistors: Working principle and applications.” *Mater Chem Front* 2018; 2(2): 253–263. doi:10.1039/c7qm00258k.
22. Zou J *et al.* “Recent Advances in Organic Photodetectors.” *Photonics* 2024; 11(11). doi:10.3390/photonics11111014.
23. Melzer K, Scarpa G. “Organic thin-film transistors for biological applications.” 2018.
24. Kergoat L *et al.* “Advances in organic transistor-based biosensors: From organic electrochemical transistors to electrolyte-gated organic field-effect transistors.” *Anal Bioanal Chem* 2012; 402(5): 1813–1826. doi:10.1007/s00216-011-5363-y.

25. Dinelli F *et al.* “Spatially Correlated Charge Transport in Organic Thin Film Transistors.” *Phys Rev Lett* 2004; 92(11): 90–93. doi:10.1103/PhysRevLett.92.116802.
26. Torsi L *et al.* “Organic field-effect transistor sensors: A tutorial review.” *Chem Soc Rev* 2013; 42(22): 8612–8628. doi:10.1039/c3cs60127g.
27. Casalini S *et al.* “LOW-DIMENSIONALITY EFFECTS IN ORGANIC FIELD EFFECT TRANSISTORS.” In: *Organic Nanomaterials*., 2013: 397–419.
28. Wang Y *et al.* “Structured and functionalized organic semiconductors for chemical and biological sensors based on organic field effect transistors.” *Mater Chem Front* 2020; 4(3505).
29. Someya T, Amagai M. “Toward a new generation of smart skins.” *Nat Biotechnol* 2019; 37(4): 382–388. doi:10.1038/s41587-019-0079-1.
30. Mandal S, Noh YY. “Printed organic thin-film transistor-based integrated circuits.” *Semicond Sci Technol* 2015; 30(6). doi:10.1088/0268-1242/30/6/064003.
31. Torricelli F *et al.* “Electrolyte-gated transistors for enhanced performance bioelectronics.” *Nat Rev Methods Prim* 2021; 1(1). doi:10.1038/s43586-021-00065-8.
32. Bortolotti CA *et al.* “Biosensing with Electrolyte Gated Organic Field Effect Transistors.” In: *Organic Bioelectronics for Life Science and Healthcare*, Vol 56., 2019: 71–96.
33. Piro B. “Electrolyte-gated FET Biosensors.” In: *Field-effect Transistor Biosensors for Rapid Pathogen Detection*., 2024.
34. Zanotti R *et al.* “Charge Carrier Density in Organic Semiconductors Modulates the Effective Capacitance: A Unified View of Electrolyte Gated Organic Transistors.” *Adv Mater* 2024; 36(49). doi:10.1002/adma.202410940.
35. Paulsen BD *et al.* “Organic mixed ionic–electronic conductors.” *Nat Mater* 2020; 19(1): 13–26. doi:10.1038/s41563-019-0435-z.
36. Bernards DA, Malliaras G. “Steady-State and Transient Behavior of Organic Electrochemical Transistors.” *Adv Funct Mater* 2007; 17: 3538–3544.
37. Friedlein JT *et al.* “Device physics of organic electrochemical transistors.” *Org Electron* 2018; 63: 398–414.
38. Jamnik J, Maier J. “Generalised equivalent circuits for mass and charge transport: Chemical capacitance and its implications.” *Phys Chem Chem Phys* 2001; 3(9): 1668–1678. doi:10.1039/b100180i.

39. Drakopoulou S *et al.* “Nanoscale Quantized Oscillations in Thin-Film Growth Greatly Enhance Transconductance in Organic Transistors.” *Adv Electron Mater* 2023; 9(10): 1–11. doi:10.1002/aelm.202300320.
40. Xia J *et al.* “Measurement of the quantum capacitance of graphene.” *Nat Nanotechnol* 2009; 4(8): 505–509. doi:10.1038/nnano.2009.177.
41. Sensi M *et al.* “Reduced Graphene Oxide Electrolyte-Gated Transistor Immunosensor with Highly Selective Multiparametric Detection ofAnti-Drug Antibodies.” *Adv Mater* 2023; 35(2211352).
42. Sensi M *et al.* “How Biorecognition Affects the Electronic Properties of Reduced Graphene Oxide in Electrolyte-Gated Transistor Immunosensors.” *Adv Funct Mater* 2024; 34(19): 1–14. doi:10.1002/adfm.202313871.
43. Gkoupidenis P *et al.* “Neuromorphic device architectures with global connectivity through electrolyte gating.” *Nat Commun* 2017; 8(May): 1–8. doi:10.1038/ncomms15448.
44. Gerasimov JY *et al.* “An Evolvable Organic Electrochemical Transistor for Neuromorphic Applications.” *Adv Sci* 2019; 6(7): 1–8. doi:10.1002/advs.201801339.
45. Berto M *et al.* “Biorecognition in organic field effect transistors biosensors: The role of the density of states of the organic semiconductor.” *Anal Chem* 2016; 88(24): 12330–12338. doi:10.1021/acs.analchem.6b03522.
46. Selvaraj M *et al.* “Label free detection of miRNA-21 with electrolyte gated organic field effect transistors (EGOFETs).” *Biosens Bioelectron* 2021; 182(December 2020): 113144. doi:10.1016/j.bios.2021.113144.
47. Zanotti R *et al.* “Fluorophobic Effect Enables Selective Detection of PFAS in Water with Electrolyte-Gated Organic Transistors.” *Adv Funct Mater* 2025; 08425: 1–12. doi:10.1002/adfm.202508425.
48. Guermonprez P *et al.* “An electrolyte-gated transistor for the monitoring of a CRISPR/Cas activity.” *Biosens Bioelectron X* 2025; 23(September 2024): 0–6. doi:10.1016/j.biosx.2025.100590.
49. Spyropoulos GD *et al.* “Internal ion-gated organic electrochemical transistor: A building block for integrated bioelectronics.” *Sci Adv* 2020; 5(2). doi:10.1126/SCIADV.AAU7378.
50. Cea C *et al.* “Enhancement-mode ion-based transistor as a comprehensive interface and real-time processing unit for in vivo electrophysiology.” *Nat Mater* 2020; 19(6): 679–686. doi:10.1038/s41563-020-0638-3.

51. Sensi M *et al.* “Modulating the Faradic Operation of All-Printed Organic Electrochemical Transistors by Facile in Situ Modification of the Gate Electrode.” *ACS Omega* 2019; 4(3): 5374–5381. doi:10.1021/acsomega.8b03319.
52. Gualandi I *et al.* “Textile Organic Electrochemical Transistors as a Platform for Wearable Biosensors.” *Sci Rep* 2016; 6(September): 1–10. doi:10.1038/srep33637.
53. Diacci C *et al.* “Diurnal in vivo xylem sap glucose and sucrose monitoring using implantable organic electrochemical transistor sensors.” *iScience* 2021; 24(1). doi:10.1016/j.isci.2020.101966.
54. Diacci C *et al.* “Organic Electrochemical Transistor Aptasensor for Interleukin-6 Detection.” *ACS Appl Mater Interfaces* 2024; 16(45): 61467–61474. doi:10.1021/acsami.3c12397.
55. White SP *et al.* “Operating and Sensing Mechanism of Electrolyte-Gated Transistors with Floating Gates: Building a Platform for Amplified Biodetection.” *J Phys Chem C* 2016; 120(1): 108–117. doi:10.1021/acs.jpcc.5b10694.
56. Huang W *et al.* “Vertical organic electrochemical transistors for complementary circuits.” *Nature* 2023; 613(7944): 496–502. doi:10.1038/s41586-022-05592-2.
57. Paudel PR *et al.* “Tuning the Transconductance of Organic Electrochemical Transistors.” *Adv Funct Mater* 2021; 31(3): 1–12. doi:10.1002/adfm.202004939.
58. Koutsouras DA *et al.* “Submicron Vertical Channel Organic Electrochemical Transistors with Ultrahigh Transconductance.” *Adv Electron Mater* 2023; 9(2). doi:10.1002/aelm.202200868.
59. Kim J *et al.* “Monolithically integrated high-density vertical organic electrochemical transistor arrays and complementary circuits.” *Nat Electron* 2024; 7(3): 234–243. doi:10.1038/s41928-024-01127-x.
60. Forrest SR. *Organic Electronics: Foundation to Applications*., 2020.
61. Stewart Z. “Organic Thin-Film Transistors and TIPS-Pentacene Organic Thin-Film Transistors and TIPS-Pentacene.” 2013.
62. Katz HE, Bao Z. “The Physical Chemistry of Organic Field-Effect Transistors.” *J Phys Chem B* 2000; 104(4): 671–678. doi:10.1021/jp992853n.
63. Bässler H, Köhler A. “Charge transport in organic semiconductors.” *Top Curr*

Chem 2012; 312: 1–65. doi:10.1007/128_2011_218.

64. Cornil J *et al.* “Interchain Interactions in Organic π-Conjugated Materials: Impact on Electronic Structure, Optical Response, and Charge Transport.” *Adv Mater* 2001; 13(14).
65. Köhler A, Bässler H. “The Electronic Structure of Organic Semiconductors.” *Electron Process Org Semicond* 2015; (i): 1–86. doi:10.1002/9783527685172.ch1.
66. Fishchuk II *et al.* “Unified description for hopping transport in organic semiconductors including both energetic disorder and polaronic contributions.” *Phys Rev B - Condens Matter Mater Phys* 2013; 88(12): 1–11. doi:10.1103/PhysRevB.88.125202.
67. Plieth W. “Intrinsically Conducting Polymers.” *Electrochem Mater Sci* 2008: 323–363. doi:10.1016/b978-044452792-9.50013-0.
68. Ohayon D *et al.* “Influence of Side Chains on the n-Type Organic Electrochemical Transistor Performance.” *ACS Appl Mater Interfaces* 2021; 13(3): 4253–4266. doi:10.1021/acsami.0c18599.
69. Asadi K *et al.* “Single-Layer Pentacene Field-Effect Transistors Using Electrodes Modified With Self-assembled Monolayers.” *Adv Mater* 2009; 21.
70. Roberts ME *et al.* “Cross-linked polymer gate dielectric films for low-voltage organic transistors.” *Chem Mater* 2009; 21(11): 2292–2299. doi:10.1021/cm900637p.
71. Fudickar W, Linker T. “Why triple bonds protect acenes from oxidation and decomposition.” *J Am Chem Soc* 2012; 134(36): 15071–15082. doi:10.1021/ja306056x.
72. Anthony JE. “The larger acenes: Versatile organic semiconductors.” *Angew Chemie - Int Ed* 2008; 47(3): 452–483. doi:10.1002/anie.200604045.
73. Park SK *et al.* “Environmental and operational stability of solution-processed 6,13-bis(triisopropyl-silylethynyl) pentacene thin film transistors.” *Org Electron* 2009; 10(3): 486–490. doi:10.1016/j.orgel.2009.02.007.
74. Sensi M *et al.* “Monitoring DNA Hybridization with Organic Electrochemical Transistors Functionalized with Polydopamine.” *Macromol Mater Eng* 2022; 307(2100880).
75. Khodagholy D *et al.* “Highly conformable conducting polymer electrodes for in vivo recordings.” *Adv Mater* 2011; 23(36): 268–272. doi:10.1002/adma.201102378.

76. Bianchi M *et al.* “Poly(3,4-ethylenedioxythiophene)-Based Neural Interfaces for Recording and Stimulation: Fundamental Aspects and In Vivo Applications.” *Adv Sci* 2022; 9(2104701).
77. Khodagholy D *et al.* “Organic electronics for high-resolution electrocorticography of the human brain.” *Sci Adv* 2016; 2(11): 1–8. doi:10.1126/sciadv.1601027.
78. Di Lauro M *et al.* “A Novel Biasing Scheme of Electrolyte-Gated Organic Transistors for Safe In Vivo Amplification of Electrophysiological Signals.” *Adv Mater Interfaces* 2022; 9(2101798).
79. Di Lauro M *et al.* “Tunable Short-Term Plasticity Response in Three-Terminal Organic Neuromorphic Devices.” *ACS Appl Electron Mater* 2020; 2: 1849–1854.
80. Jakešová M *et al.* “Wireless organic electronic ion pumps driven by photovoltaics.” *npj Flex Electron* 2019; 3(1). doi:10.1038/s41528-019-0060-6.
81. Giordani M *et al.* “Specific Dopamine Sensing Based on Short-Term Plasticity Behaviour of a Whole Organic Artificial Synapse.” *ACS Sensors* 2017; 2: 1756–1760.
82. Giordani M *et al.* “Neuromorphic Organic Devices that Specifically Discriminate Dopamine from Its Metabolites by Nonspecific Interactions.” *Adv Funct Mater* 2020; 30(28): 1–13. doi:10.1002/adfm.202002141.
83. Volkov A V. *et al.* “Understanding the Capacitance of PEDOT:PSS.” *Adv Funct Mater* 2017; 27(28): 1–10. doi:10.1002/adfm.201700329.
84. Lunghi A *et al.* “Flexible Neural Interfaces Based on 3D PEDOT:PSS Micropillar Arrays.” *Adv Mater Interfaces* 2022; 9(25). doi:10.1002/admi.202200709.
85. Lunghi A *et al.* “Ultra-Flexible μ-ECoG Arrays Based on PEDOT:PSS Micropillars.” *Adv Mater Interfaces* 2025; 12(12): 1–11. doi:10.1002/admi.202500051.
86. Kim YH *et al.* “Highly Conductive PEDOT:PSS Electrode with Optimized Solvent and Thermal Post-Treatment for ITO-Free Organic Solar Cells.” *Adv Funct Mater* 2011; 21: 1076–1081.
87. Zhang S *et al.* “Solvent-induced changes in PEDOT:PSS films for organic electrochemical transistors.” *APL Mater* 2015; 3(1). doi:10.1063/1.4905154.
88. Lee SH *et al.* “Modified physico-chemical properties and supercapacitive performance via DMSO inducement to PEDOT:PSS active layer.” *Org*

Electron 2014; 15(12): 3423–3430. doi:10.1016/j.orgel.2014.09.020.

89. Alam J *et al.* “Enhancing thermoelectric performance of PEDOT: PSS: A review of treatment and nanocomposite strategies.” *Adv Nanocomposites* 2024; 1(1): 16–38. doi:10.1016/j.adna.2023.08.001.
90. Modarresi M *et al.* “Microscopic Understanding of the Granular Structure and the Swelling of PEDOT:PSS.” *Macromolecules* 2020; 53(15): 6267–6278. doi:10.1021/acs.macromol.0c00877.
91. Håkansson A *et al.* “Effect of (3-glycidyloxypropyl)trimethoxysilane (GOPS) on the electrical properties of PEDOT:PSS films.” *J Polym Sci Part B Polym Phys* 2017; 55(10): 814–820. doi:10.1002/polb.24331.
92. Mbayachi VB *et al.* “Graphene synthesis, characterization and its applications: A review.” *Results Chem* 2021; 3: 100163. doi:10.1016/j.rechem.2021.100163.
93. Shams SS *et al.* “Graphene synthesis: A Review.” *Mater Sci Pol* 2015; 33(3): 566–578. doi:10.1515/msp-2015-0079.
94. Novoselov KS *et al.* “Electric field in atomically thin carbon films.” *Science (80-)* 2004; 306(5696): 666–669. doi:10.1126/science.1102896.
95. Dasari Shareena TP *et al.* “A Review on Graphene-Based Nanomaterials in Biomedical Applications and Risks in Environment and Health.” *Nano-Micro Lett* 2018; 10(3): 1–34. doi:10.1007/s40820-018-0206-4.
96. Bera B. “A Review on Polymer, Graphene and Carbon Nanotube: Properties, Synthesis and Applications.” *Imp J Interdiscip Res (IJIR* 2017; 3(10): 61–70.
97. Kim KS *et al.* “Large-scale pattern growth of graphene films for stretchable transparent electrodes.” *Nature* 2009; 457(7230): 706–710. doi:10.1038/nature07719.
98. Gosling JH *et al.* “Universal mobility characteristics of graphene originating from charge scattering by ionised impurities.” *Commun Phys* 2021; 4(1). doi:10.1038/s42005-021-00518-2.
99. Jian YH *et al.* “In situ observation of graphene sublimation and multi-layer edge reconstructions.” *Proc Natl Acad Sci U S A* 2009; 106(25): 10103–10108. doi:10.1073/pnas.0905193106.
100. Viculis LH *et al.* “A chemical route to carbon nanoscrolls.” *Science (80-)* 2003; 299(5611): 1361. doi:10.1126/science.1078842.
101. Park S, Ruoff RS. “Chemical methods for the production of graphenes.” *Nat Nanotechnol* 2009; 4(4): 217–224. doi:10.1038/nnano.2009.58.

102. Rowley-Neale SJ *et al.* “An overview of recent applications of reduced graphene oxide as a basis of electroanalytical sensing platforms.” *Appl Mater Today* 2018; 10: 218–226. doi:10.1016/j.apmt.2017.11.010.
103. Dreyer DR *et al.* “The chemistry of graphene oxide.” *Chem Soc Rev* 2010; 39(1): 228–240. doi:10.1039/b917103g.
104. Laraba SR *et al.* “Graphene-based composites for biomedical applications.” *Green Chem Lett Rev* 2022; 15(3): 724–748. doi:10.1080/17518253.2022.2128698.
105. Dave SH *et al.* “Chemistry and Structure of Graphene Oxide via Direct Imaging.” *ACS Nano* 2016; 10(8): 7515–7522. doi:10.1021/acsnano.6b02391.
106. Nagaoka DA *et al.* “Can reduced graphene oxide look like few-layer pristine graphene?” *Diam Relat Mater* 2021; 120(May): 108616. doi:10.1016/j.diamond.2021.108616.
107. Mahalingam DK *et al.* “Spray-coated graphene oxide hollow fibers for nanofiltration.” *J Memb Sci* 2020; 606(November 2019): 118006. doi:10.1016/j.memsci.2020.118006.
108. Roy A *et al.* “Emplacement of screen-printed graphene oxide coating for building thermal comfort discernment.” *Sci Rep* 2020; 10(1): 1–13. doi:10.1038/s41598-020-72670-8.
109. Liu J *et al.* “Graphene dip coatings: An effective anticorrosion barrier on aluminum.” *Appl Surf Sci* 2015; 327(37): 241–245. doi:10.1016/j.apsusc.2014.11.187.
110. Mohammed S. “Graphene oxide: A mini-review on the versatility and challenges as a membrane material for solvent-based separation.” *Chem Eng J Adv* 2022; 12(September): 100392. doi:10.1016/j.ceja.2022.100392.
111. Agarwal V, Zetterlund PB. “Strategies for reduction of graphene oxide – A comprehensive review.” *Chem Eng J* 2021; 405(September 2020): 127018. doi:10.1016/j.cej.2020.127018.
112. Kurian M. “Recent progress in the chemical reduction of graphene oxide by green reductants–A Mini review.” *Carbon Trends* 2021; 5: 100120. doi:10.1016/j.cartre.2021.100120.
113. Li CJ, Trost BM. “Green chemistry for chemical synthesis.” *Proc Natl Acad Sci U S A* 2008; 105(36): 13197–13202. doi:10.1073/pnas.0804348105.
114. Valentini C *et al.* “Tuning the electrical properties of graphene oxide through

low-temperature thermal annealing." *Nanoscale* 2023; 15(12): 5743–5755. doi:10.1039/d2nr06091d.

115. Sengupta I *et al.* "Thermal reduction of graphene oxide: How temperature influences purity." *J Mater Res* 2018; 33(23): 4113–4122. doi:10.1557/jmr.2018.338.
116. Vasilijević S *et al.* "Electrochemical tuning of reduced graphene oxide in printed electrolyte-gated transistors. Impact on charge transport properties." *Electrochim Acta* 2021; 371: 137819. doi:10.1016/j.electacta.2021.137819.
117. Askari MB, Salarizadeh P. "State-of-the-art review on reduced graphene oxide for supercapacitor electrode applications." *Results Eng* 2025; 28(August): 107429. doi:10.1016/j.rineng.2025.107429.
118. He L *et al.* "The reduced graphene oxide conductive additives with a certain defect concentration enabling rate-capability of lithium-ion batteries." *Electrochim Acta* 2025; 511(September 2024). doi:10.1016/j.electacta.2024.145353.
119. Furlan de Oliveira R *et al.* "Liquid-Gated Transistors Based on Reduced Graphene Oxide for Flexible and Wearable Electronics." *Adv Funct Mater* 2019; 29(46). doi:10.1002/adfm.201905375.
120. Vasilijević S *et al.* "Graphene-based materials and their applications in electrolyte-gated transistors for sensing." *Synth Met* 2023; 295(December 2022). doi:10.1016/j.synthmet.2023.117355.
121. Karaca E, Acaralı N. "Application of graphene and its derivatives in medicine: A review." *Mater Today Commun* 2023; 37(August): 107054. doi:10.1016/j.mtcomm.2023.107054.
122. Fenoy GE *et al.* "'Clickable' Organic Electrochemical Transistors." *JACS Au* 2022; 2(12): 2778–2790. doi:10.1021/jacsau.2c00515.
123. Thévenot DR *et al.* "Electrochemical biosensors: Recommended definitions and classification." *Biosens Bioelectron* 2001; 16(1–2): 121–131. doi:10.1016/S0956-5663(01)00115-4.
124. Naresh V, Lee N. "A review on biosensors and recent development of nanostructured materials-enabled biosensors." *Sensors (Switzerland)* 2021; 21(4): 1–35. doi:10.3390/s21041109.
125. CLARK LC *et al.* "Continuous recording of blood oxygen tensions by polarography." *J Appl Physiol* 1953; 6(3): 189–193. doi:10.1152/jappl.1953.6.3.189.

126. Clark LC, Lyons C. “Electrode Systems for Continuous Monitoring in Cardiovascular Surgery.” *Ann N Y Acad Sci* 1962; 102(1): 29–45. doi:10.1111/j.1749-6632.1962.tb13623.x.
127. Turner APF. “Biosensors: Sense and sensibility.” *Chem Soc Rev* 2013; 42(8): 3184–3196. doi:10.1039/c3cs35528d.
128. Polat EO *et al.* “Transducer Technologies for Biosensors and Their Wearable Applications.” *Biosensors* 2022; 12(6). doi:10.3390/bios12060385.
129. Macchia E *et al.* “Organic Field-Effect Transistor Platform for Label-Free, Single-Molecule Detection of Genomic Biomarkers.” *ACS Sensors* 2020; 5(6): 1822–1830. doi:10.1021/acssensors.0c00694.
130. Picca RA *et al.* “Ultimately Sensitive Organic Bioelectronic Transistor Sensors by Materials and Device Structure Desig.” *Adv Funct Mater* 2020; 30(1904513).
131. Macchia E *et al.* “Single-molecule detection with a millimetre-sized transistor.” *Nat Commun* 2018; 9(1). doi:10.1038/s41467-018-05235-z.
132. Wang D *et al.* “Electrolytic gated organic field-effect transistors for application in biosensors—A review.” *Electron* 2016; 5(1). doi:10.3390/electronics5010009.
133. Seshadri P *et al.* “Low-picomolar, label-free procalcitonin analytical detection with an electrolyte-gated organic field-effect transistor based electronic immunosensor.” *Biosens Bioelectron* 2018; 104(December 2017): 113–119. doi:10.1016/j.bios.2017.12.041.
134. Macchia E *et al.* “Organic bioelectronics probing conformational changes in surface confined proteins.” *Sci Rep* 2016; 6: 1–12. doi:10.1038/srep28085.
135. Liu H *et al.* “Organic Electrochemical Transistors for Biomarker Detections.” *Adv Sci* 2024; 11(27): 1–30. doi:10.1002/advs.202305347.
136. Casalini S *et al.* “Organic field-effect transistor for label-free dopamine sensing.” *Org Electron* 2013; 14(1): 156–163. doi:10.1016/j.orgel.2012.10.027.
137. Berto M *et al.* “EGOFET Peptide Aptasensor for Label-Free Detection of Inflammatory Cytokines in Complex Fluids.” *Adv Biosyst* 2018; 2(1700072).
138. Solodka K *et al.* “Detection of Neurofilament Light Chain with Label-Free Electrolyte-Gated Organic Field-Effect Transistors.” *Adv Mater Interfaces* 2022; 9(2102341).
139. Koklu A *et al.* “Convection Driven Ultrarapid Protein Detection via Nanobody-

Functionalized Organic Electrochemical Transistors." *Adv Mater* 2022; 34(2202972).

140. Berto M *et al.* "Label free detection of plant viruses with organic transistor biosensors." *Sensors Actuators, B Chem* 2019; 281(October 2018): 150–156. doi:10.1016/j.snb.2018.10.080.
141. He RX *et al.* "Detection of bacteria with organic electrochemical transistors." *J Mater Chem* 2012; 22(41): 22072–22076. doi:10.1039/c2jm33667g.
142. Kergoat L *et al.* "Tuning the threshold voltage in electrolyte-gated organic field-effect transistors." *Proc Natl Acad Sci U S A* 2012; 109(22): 8394–8399. doi:10.1073/pnas.1120311109.
143. Mulla MY *et al.* "Capacitance-modulated transistor detects odorant binding protein chiral interactions." *Nat Commun* 2015; 6. doi:10.1038/ncomms7010.
144. Mulla MY *et al. Electronic biosensors based on EGOFETs*., 1st ed. Elsevier Inc., 2020. doi:10.1016/bs.mie.2020.07.003.
145. Sarcina L *et al.* "A stable physisorbed layer of packed capture antibodies for high-performance sensing applications." *J Mater Chem C* 2023; 11(27): 9093–9106. doi:10.1039/d3tc01123b.
146. Taheri RA *et al.* " Comparison of antibody immobilization strategies in detection of Vibrio cholerae by surface plasmon resonance ." *Biointerphases* 2016; 11(4). doi:10.1116/1.4971270.
147. Ruiz G *et al.* "Antibodies Irreversibly Adsorb to Gold Nanoparticles and Resist Displacement by Common Blood Proteins." *Langmuir* 2019; 35(32): 10601–10609. doi:10.1021/acs.langmuir.9b01900.
148. Della Ventura B *et al.* "Light assisted antibody immobilization for bio-sensing." *Biomed Opt Express* 2011; 2(11): 3223. doi:10.1364/boe.2.003223.
149. Ruiz G *et al.* "PH Impacts the Orientation of Antibody Adsorbed onto Gold Nanoparticles." *Bioconjug Chem* 2019; 30(4): 1182–1191. doi:10.1021/acs.bioconjchem.9b00123.
150. Mateos H, Oliver M. "Emerging Strategies for the formulation of Antibody–Nanoparticle Conjugation in Lateral Flow Immunoassays." *Curr Opin Colloid Interface Sci* 2025; 80: 101968. doi:10.1016/j.cocis.2025.101968.
151. Gan SY *et al.* "Linker-mediated oriented antibody immobilisation strategies for a more efficient immunosensor and diagnostic applications: A review." *Biosens Bioelectron X* 2023; 14(March): 100379. doi:10.1016/j.biosx.2023.100379.

152. Casalini S *et al.* “Multiscale sensing of antibody-antigen interactions by organic transistors and single-molecule force spectroscopy.” *ACS Nano* 2015; 9(5): 5051–5062. doi:10.1021/acsnano.5b00136.
153. Diacci C *et al.* “Label-free detection of interleukin-6 using electrolyte gated organic field effect transistors.” *Biointerphases* 2017; 12(5). doi:10.1116/1.4997760.
154. Ricci S *et al.* “Label-free immunodetection of α-synuclein by using a microfluidics coplanar electrolyte-gated organic field-effect transistor.” *Biosens Bioelectron* 2020; 167(March): 112433. doi:10.1016/j.bios.2020.112433.
155. Decataldo F *et al.* “BMP-2 functionalized PEDOT:PSS-based OECTs for stem cell osteogenic differentiation monitoring.” *Flex Print Electron* 2019; 4(044006). doi:DOI 10.1088/2058-8585/ab5bfc.
156. White SP *et al.* “Label-free DNA sensing platform with low-voltage electrolyte-gated transistors.” *Anal Chem* 2015; 87(3): 1861–1866. doi:10.1021/ac503914x.
157. Casalini S *et al.* “Self-assembled monolayers in organic electronics.” *Chem Soc Rev* 2017; 46(1): 40–71. doi:10.1039/c6cs00509h.
158. Whitesides GM, Grzybowski B. “Self-assembly at all scales.” *Science (80-)* 2002; 295(5564): 2418–2421. doi:10.1126/science.1070821.
159. Xia Y, Whitesides GM. “provides this patterned microstructure . Soft Lithography.” *Angew Chemie* 1998; 37: 550–575.
160. Paradisi A *et al.* “Robust Biosensor Based on Carbon Nanotubes/Protein Hybrid Electrolyte Gated Transistors.” *Chem - A Eur J* 2023; 29(55). doi:10.1002/chem.202301704.
161. MacChia E *et al.* “Label-Free and Selective Single-Molecule Bioelectronic Sensing with a Millimeter-Wide Self-Assembled Monolayer of Anti-Immunoglobulins.” *Chem Mater* 2019; 31(17): 6476–6483. doi:10.1021/acs.chemmater.8b04414.
162. Holzer B *et al.* “Characterization of Covalently Bound Anti-Human Immunoglobulins on Self-Assembled Monolayer Modified Gold Electrodes Brigitte.” *Adv Biosyst* 2017; 1(1700055).
163. Nguyen TTK *et al.* “Peptide-modified electrolyte-gated organic field effect transistor. Application to Cu 2+ detection.” *Biosens Bioelectron* 2019; 127(December 2018): 118–125. doi:10.1016/j.bios.2018.12.005.

164. Macchia E *et al.* “Plasmonic Single-Molecule Affinity Detection at 10−20 Molar.” *Adv Mater* 2025; 37(2418610).
165. Naguib M *et al.* “Novel Two-Dimensional Nanocrystals Produced by Exfoliation of Ti3AlC2.pdf.” *Adv Mater* 2011; 23: 4248–4253.
166. Sokol M *et al.* “On the Chemical Diversity of the MAX Phases.” *Trends Chem* 2019; 1(2): 210–223. doi:10.1016/j.trechm.2019.02.016.
167. Anasori B *et al.* “2D metal carbides and nitrides (MXenes) for energy storage.” *Nat Rev Mater* 2017; 2(2). doi:10.1038/natrevmats.2016.98.
168. Shekhirev M *et al.* “Characterization of MXenes at every step, from their precursors to single flakes and assembled films.” *Prog Mater Sci* 2021; 120(September 2020): 100757. doi:10.1016/j.pmatsci.2020.100757.
169. Rems E *et al.* “Pivotal Role of Surface Terminations in MXene Thermodynamic Stability.” *Chem Mater* 2024; 36(20): 10295–10306. doi:10.1021/acs.chemmater.4c02274.
170. Miao B *et al.* “Impact of various 2D MXene surface terminating groups in energy conversion.” *Renew Sustain Energy Rev* 2024; 199(December 2023): 114506. doi:10.1016/j.rser.2024.114506.
171. Shahzad F *et al.* “2D Transition Metal Carbides (MXenes): Applications as an Electrically Conducting Material.” *Adv Mater* 2020; 32(51): 1–23. doi:10.1002/adma.202002159.
172. Oyehan TA *et al.* “MXenes: Synthesis, properties, and applications for sustainable energy and environment.” *Appl Mater Today* 2023; 35(November): 101993. doi:10.1016/j.apmt.2023.101993.
173. Murali G *et al.* “A Review on MXene Synthesis, Stability, and Photocatalytic Applications.” *ACS Nano* 2022; 16(9): 13370–13429. doi:10.1021/acsnano.2c04750.
174. Chen L *et al.* “Biomedical Applications of MXenes: From Nanomedicine to Biomaterials.” *Accounts Mater Res* 2022; 3(8): 785–798. doi:10.1021/accountsmr.2c00025.
175. Lim GP *et al.* “Cytotoxicity of MXene-based nanomaterials for biomedical applications: A mini review.” *Environ Res* 2021; 201(May): 111592. doi:10.1016/j.envres.2021.111592.
176. Lukatskaya MR *et al.* “Cation intercalation and high volumetric capacitance of two-dimensional titanium carbide.” *MXenes From Discov to Appl Two-Dimensional Met Carbides Nitrides* 2013; 2(September): 665–675.

doi:10.1149/ma2015-01/42/2235.

177. Naguib M *et al.* “MXene: A promising transition metal carbide anode for lithium-ion batteries.” *Electrochem commun* 2012; 16(1): 61–64. doi:10.1016/j.elecom.2012.01.002.
178. Yao Y *et al.* “Progress towards ef fi cient MXene sensors Check for updates.” 2025.
179. Amani AM *et al.* “MXenes in biosensing: Enhancing sensitivity and flexibility – A review of properties, applications, and future directions.” *Sens Bio-Sensing Res* 2025; 47(January): 100732. doi:10.1016/j.sbsr.2024.100732.
180. Xie K *et al.* “Application of Two-Dimensional MXene materials in sensors.” *Mater Des* 2023; 228: 111867. doi:10.1016/j.matdes.2023.111867.
181. Barman SC *et al.* “Antibody-functionalized MXene-based electrochemical biosensor for point-of-care detection of vitamin D deficiency.” *Commun Mater* 2025; 6(1): 1–11. doi:10.1038/s43246-025-00756-9.
182. Wu L *et al.* “2D transition metal carbide MXene as a robust biosensing platform for enzyme immobilization and ultrasensitive detection of phenol.” *Biosens Bioelectron* 2018; 107(December 2017): 69–75. doi:10.1016/j.bios.2018.02.021.
183. Sengupta J, Hussain CM. “MXene-Based Electrochemical Biosensors: Advancing Detection Strategies for Biosensing (2020–2024).” *Biosensors* 2025; 15(3). doi:10.3390/bios15030127.
184. Wang Q *et al.* “MXene-based electrochemical (bio) sensors for sustainable applications: Roadmap for future advanced materials.” *Nano Mater Sci* 2023; 5(1): 39–52. doi:10.1016/j.nanoms.2022.07.003.
185. Nagaraja T *et al.* “MXene electrochemical phosphate sensors.” *Commun Eng* 2025; 4(1): 1–13. doi:10.1038/s44172-025-00519-x.
186. Xu B *et al.* “Ultrathin MXene-Micropattern-Based Field-Effect Transistor for Probing Neural Activity.” *Adv Mater* 2016; 28: 3333–3339.
187. Cai Z *et al.* “Ultrathin Ti3C2Tx MXene-based electrochemical transistor for highly sensitive determination of nitrite.” *J Electroanal Chem* 2023; 928(September 2022). doi:10.1016/j.jelechem.2022.117012.
188. Shakya J *et al.* “2D MXene electrochemical transistors.” *Nanoscale* 2024; 16(6): 2883–2893. doi:10.1039/d3nr06540e.
189. Li Y *et al.* “MXene-Graphene Field-Effect Transistor Sensing of Influenza Virus and SARS-CoV-2.” *ACS Omega* 2021; 6(10): 6643–6653.

doi:10.1021/acsomega.0c05421.

190. Farahmandpour M, Kordrostami Z. “Wearable MXene-enhanced organic Bio-FET paper patch for glucose detection in sweat with pH and temperature calibration.” *Sci Rep* 2025; 15(1): 1–18. doi:10.1038/s41598-025-00533-1.
191. Wang H *et al.* “Highly sensitive paraquat sensor based on Ag@TiO2/MXene functionalized solution-gate graphene field-effect transistor.” *Microchem J* 2025; 212(January). doi:10.1016/j.microc.2025.113362.
192. Siva S *et al.* “Electrohydrodynamic-printed ultrathin Ti3C2Tx-MXene field-effect transistor for probing aflatoxin B1.” *Chem Eng J* 2024; 479(November 2023): 147492. doi:10.1016/j.cej.2023.147492.
193. Wang H *et al.* “2D MXene–Molecular Hybrid Additive for High- Performance Ambipolar Polymer Field-Effect Transistors and Logic Gates.” *Adv Mater* 2021; 33(2008215).
194. Chen C *et al.* “Effect of glycine functionalization of 2D titanium carbide (MXene) on charge storage.” *J Mater Chem A* 2018; 6(11): 4617–4622. doi:10.1039/c7ta11347a.
195. Boota M *et al.* “Probing Molecular Interactions at MXene-Organic Heterointerfaces.” *Chem Mater* 2020; 32(18): 7884–7894. doi:10.1021/acs.chemmater.0c02662.
196. Shin H *et al.* “Grafting Behavior of Amine Ligands for Surface Modification of MXene.” *Langmuir* 2023; 39(6): 2358–2367. doi:10.1021/acs.langmuir.2c03094.
197. Mead C. “Neuromorphic Electronic Systems.” *Proc IEEE* 1990; 78(10): 1629–1636. doi:10.1109/5.58356.
198. Chen H *et al.* “Biological function simulation in neuromorphic devices: from synapse and neuron to behavior.” *Sci Technol Adv Mater* 2023; 24(1): 1–27. doi:10.1080/14686996.2023.2183712.
199. Marković D *et al.* “Physics for neuromorphic computing.” *Nat Rev Phys* 2020; 2(9): 499–510. doi:10.1038/s42254-020-0208-2.
200. Chicca E *et al.* “Neuromorphic electronic circuits for building autonomous cognitive systems.” *Proc IEEE* 2014; 102(9): 1367–1388. doi:10.1109/JPROC.2014.2313954.
201. Sousa AMM *et al.* “Evolution of the Human Nervous System Function, Structure, and Development.” *Cell* 2017; 170(2): 226–247. doi:10.1016/j.cell.2017.06.036.

202. Bean BP. “The action potential in mammalian central neurons.” *Nat Rev Neurosci* 2007; 8(6): 451–465. doi:10.1038/nrn2148.
203. Carnevale NT, Johnston D. “Electrophysiological characterization of remote chemical synapses.” *J Neurophysiol* 1982; 47(4): 606–621. doi:10.1152/jn.1982.47.4.606.
204. Pereda AE. “Electrical synapses and their functional interactions with chemical synapses.” *Nat Rev Neurosci* 2014; 15(4): 250–263. doi:10.1038/nrn3708.
205. Zucker RS, Regehr WG. “Short-term synaptic plasticity.” *Annu Rev Physiol* 2002; 64: 355–405. doi:10.1146/annurev.physiol.64.092501.114547.
206. Fortune ES, Rose GJ. “Short-term synaptic plasticity as a temporal filter.” *Trends Neurosci* 2001; 24(7): 381–385. doi:10.1016/S0166-2236(00)01835-X.
207. Motanis H *et al.* “Short-Term Synaptic Plasticity as a Mechanism for Sensory Timing.” *Trends Neurosci* 2018; 41(10): 701–711. doi:10.1016/j.tins.2018.08.001.
208. Magee JC, Grienberger C. “Synaptic Plasticity Forms and Functions.” *Annu Rev Neurosci* 2020; 43: 95–117. doi:10.1146/annurev-neuro-090919-022842.
209. Kelley P, Whatson T. “Making long-term memories in minutes: A spaced learning pattern from memory research in education.” *Front Hum Neurosci* 2013; 7(SEP): 1–9. doi:10.3389/fnhum.2013.00589.
210. Owens RM, Malliaras GG. “Organic electronics at the interface with biology.” *MRS Bull* 2010; 35(6): 449–456. doi:10.1557/mrs2010.583.
211. Rondelli F *et al.* “Pre-synaptic DC bias controls the plasticity and dynamics of three-terminal neuromorphic electrolyte-gated organic transistors.” *Neuromorphic Comput Eng* 2023; 3(1): 0–8. doi:10.1088/2634-4386/acb37f.
212. Van De Burgt Y *et al.* “Organic electronics for neuromorphic computing.” *Nat Electron* 2018; 1(7): 386–397. doi:10.1038/s41928-018-0103-3.
213. Gkoupidenis P *et al.* “Synaptic plasticity functions in an organic electrochemical transistor.” *Appl Phys Lett* 2015; 107(26). doi:10.1063/1.4938553.
214. Gkoupidenis P *et al.* “Neuromorphic device architectures with global connectivity through electrolyte gating.” *Nat Commun* 2017; 8(May): 1–8. doi:10.1038/ncomms15448.
215. De Salvo A *et al.* “Organic Electronics Circuitry for In Situ Real-Time

Processing of Electrophysiological Signals." *Adv Mater Interfaces* 2023; 10(34). doi:10.1002/admi.202300583.

216. Cucchi M *et al.* "In Liquido Computation with Electrochemical Transistors and Mixed Conductors for Intelligent Bioelectronics." *Adv Mater* 2023; 35(15). doi:10.1002/adma.202209516.
217. Pecqueur S *et al.* "Cation discrimination in organic electrochemical transistors by dual frequency sensing." *Org Electron* 2018; 57(March): 232–238. doi:10.1016/j.orgel.2018.03.020.
218. Selmi GS *et al.* "Pulse Dynamics in Reduced Graphene Oxide Electrolyte-Gated Transistors: Charge Memory Effects and Mechanisms Governing the Ion-To-Electron Transduction." *Adv Electron Mater* 2025; 11(8). doi:10.1002/aelm.202400791.
219. Sharbati MT *et al.* "Low-Power, Electrochemically Tunable Graphene Synapses for Neuromorphic Computing." *Adv Mater* 2018; 30(1802353).
220. Schranghamer TF *et al.* "Graphene memristive synapses for high precision neuromorphic computing." *Nat Commun* 2020; 11(1): 1–11. doi:10.1038/s41467-020-19203-z.
221. Oliveri P *et al. Analysis of Chemical Data*., Second Edi. Elsevier Inc., 2020. doi:10.1016/B978-0-12-813266-1/00002-4.
222. Altay K *et al.* "A geographically-registered Arapgir purple basil pesto sauce prepared with four different cheese varieties: Comparison of physical, bioactive and rheological properties." *Food Chem Adv* 2024; 4(December 2023): 100587. doi:10.1016/j.focha.2023.100587.
223. Jackson JE, Hearne FT. "Hotelling's tm2 for principal components—what about absolute values?" *Technometrics* 1979; 21(2): 253–255. doi:10.1080/00401706.1979.10489757.
224. Stanimirova I *et al.* "The role of chemometrics in improving clinical data analysis and diagnostics." *TrAC - Trends Anal Chem* 2024; 173(January): 117642. doi:10.1016/j.trac.2024.117642.
225. Kharbach M *et al.* "Current Application of Advancing Spectroscopy Techniques in Food Analysis: Data Handling with Chemometric Approaches." *Foods* 2023; 12(14): 1–46. doi:10.3390/foods12142753.
226. Jollife IT, Cadima J. "Principal component analysis: A review and recent developments." *Philos Trans R Soc A Math Phys Eng Sci* 2016; 374(2065). doi:10.1098/rsta.2015.0202.

227. Ergon R. “Principal component regression (PCR) and partial least squares regression (PLSR).” *Math Stat Methods Food Sci Technol* 2013: 121–142. doi:10.1002/9781118434635.ch08.
228. Cocchi M *et al. Chemometric Methods for Classification and Feature Selection*., 1st ed. Elsevier B.V., 2018. doi:10.1016/bs.coac.2018.08.006.
229. Martynko E, Kirsanov D. “Application of Chemometrics in Biosensing: A Brief Review.” *Biosensors* 2020; 10(8). doi:10.3390/bios10080100.
230. Hassan MM *et al.* “Recent progress in chemometrics driven biosensors for food application.” *TrAC - Trends Anal Chem* 2022; 156. doi:10.1016/j.trac.2022.116707.
231. Malavolta L *et al.* “Multivariate sensing of ions using machine learning and composite 2D-3D graphene oxide-hexacyanoferrate electrodes.” *Sensors Actuators B Chem* 2025; 427(September 2024). doi:10.1016/j.snb.2024.137194.
232. Monari A *et al.* “Electrochemical sensors for fast classification of different Cannabis sativa L. samples according to total Δ9-tetrahydrocannabinol content.” *Talanta* 2025; 126958.
233. Montes-García V *et al.* “Ultrasensitivie Isomer Discrimination: A Joint Surface-Enhanced Raman Scattering (SERS) Spectroscopy and Machine Learning Strategy.” *Adv Sens Res* 2025; 2400160.
234. Sensi M *et al.* “Investigation of transcription factor-DNA binding with electrolyte-gated organic transistors.” *J Mater Chem C* 2024; 12(21): 7596–7604. doi:10.1039/d4tc00260a.
235. Scandurra C *et al.* “Analysis of Clinical Samples of Pancreatic Cyst’s Lesions with A Multi-Analyte Bioelectronic Simot Array Benchmarked Against Ultrasensitive Chemiluminescent Immunoassay.” *Adv Sci* 2024; 11: 230814.
236. Genco E *et al.* “A Single-Molecule Bioelectronic Portable Array for Early Diagnosis of Pancreatic Cancer Precursors.” *Adv Mater* 2023; 35(2304102).
237. Caputo M *et al.* “Piercing the Shadows: Exploring the Influence of Signal Preprocessing on Interpreting Ultrasensitive Bioelectronic Sensor Data.” *Chempluschem* 2025; 90(2). doi:10.1002/cplu.202400520.
238. Wold S *et al.* “The multivariate calibration problem in chemistry solved by PLS method.” 1982; 46(2): 55. Available at: http://eprints.uanl.mx/5481/1/1020149995.PDF.
239. Li Vigni M *et al. Exploratory Data Analysis*., 1st ed. Copyright © 2013 Elsevier

B.V. All rights reserved., 2013. doi:10.1016/B978-0-444-59528-7.00003-X.

240. Bro R, Smilde AK. “Principal component analysis.” *Anal Methods* 2014; 6(9): 2812–2831. doi:10.1039/c3ay41907j.
241. Ståhle L, Wold S. “Partial least squares analysis with cross-validation for the two-class problem: A Monte Carlo study.” *J Chemom* 1987; 1(3): 185–196. doi:10.1002/cem.1180010306.
242. Brereton RG, Lloyd GR. “Partial least squares discriminant analysis: Taking the magic away.” *J Chemom* 2014; 28(4): 213–225. doi:10.1002/cem.2609.
243. Ruiz-Perez D *et al.* “So you think you can PLS-DA?” *BMC Bioinformatics* 2020; 21(Suppl 1): 1–10. doi:10.1186/s12859-019-3310-7.

Chapter 2: Aim and Structure of the Thesis

This chapter presents the aim and overall structure of the PhD dissertation. Reflecting the EGOT architecture described in Chapter 1, it introduces the research objectives and the strategies developed to enhance the performance of EGOT-based devices. The experimental approaches presented are subsequently validated in the context of both EGOT-based biosensors and neuromorphic platforms.

This dissertation focuses on optimizing the performance of Electrolyte-Gated Organic Transistor (EGOT) platforms. The primary goal is to present a comprehensive library of strategies that can be seamlessly integrated with EGOT-based devices to achieve superior performance in biosensing and neuromorphic applications.

The EGOT architecture exhibits two distinct, addressable interfaces - namely, the gate/electrolyte and the channel/electrolyte interfaces - that can be tailored to fine-tune the device's electrical characteristics. Furthermore, EGOT devices exhibit a complex multiparametric response that can be leveraged as an input matrix for chemometric tools, aiming to maximize the transistor's response when integrated into biosensing platforms.

The structure of this thesis mirrors the structural architecture of the EGOT itself. It systematically describes the tools and modifications applicable at the gate/electrolyte and at the channel/electrolyte interfaces, and demonstrates how the post-processing techniques (*viz.,* chemometrics) lead to optimize the device response. The impact of such hardware/software integrated approach is validated in two biosensing devices and one neuromorphic system as case studies.

Regarding biosensing platforms, a crucial aspect is the integration of a biorecognition probe capable of interacting selectively and robustly with the target analyte. Accordingly, **Chapter 4** explores the optimization of the surface chemistry for the formation of a controlled bilayer architecture based on the Schiff Base Reaction (SBR) between a cysteamine self-assembly monolayer on a planar gold electrode and glutaraldehyde, the latter able to graft the anti L-Tryptophan antibody. The optimized SBR functionalization strategy yields a higher sensitivity and a robust multiparametric response when compared to the gold-standard EDC-NHS activation strategy. Unexpectedly, we have faced the problem that the standard univariate analysis of a single parameter, as the relative current variation at a fixed gate and drain voltage, extracted from the transfer curves does not unambiguously differentiate L from D enantiomers, in the concentration range from 1 fM to 10 nM, despite the fact that the antibody is L-selective (literature studies showed unambiguous chiral discrimination but starting all at minimum 100 nM antibody concentration). To overcome this unprecedented finding, a novel approach to analyse EGOT biosensor data is presented to extract unambiguous multiparametric data set representing the transfer curves. Then, by leveraging the high sensitivity

and the whole multiparametric response with chemometric tools based on Principal Component Analysis (PCA), enantiomers are discriminated at 10 pM level, at least two orders of magnitude lower than the enantiodiscrimination levels previously reported with EGOT biosensor. The same approach is extended on the best fit dose curves allows to discriminate the two enantiomeric forms down to unprecedented level of detection of 100 fM. Finally, the combination between the multiparametric EGOT and the chemometric tools is validated with a classification method, the Partial Least Squares Discriminant Analysis (PLS-DA), that confirms the enantiomeric separation of four independent experimental points within a concentration range from 1 pM to 1 nM.

The versatility of the EGOT-based sensing platform for the detection of small-molecule biomarkers is further exemplified by incorporating MXenes as active sensing elements within an EGOT architecture for Dopamine (DA) detection. MXenes ($M_{n+1}X_nT_x$) constitute a broad family of two-dimensional (2D) materials - typically transition-metal carbides, nitrides, or carbonitrides - whose diverse stoichiometries confer a unique combination of electrical and chemical properties. **Chapter 5** details the synthesis strategies and material characterizations of three chemically-engineered MXenes. These functionalized MXenes are subsequently incorporated into a Poly(3,4-ethylenedioxythiophene)polystyrene sulfonate (PEDOT:PSS)-based EGOT device, enabling successful DA detection down to the pM range. Finally, by exploiting the multiparametric response extracted from MXene–EGOT transfer curves and combining it with PCA, hypothetical interaction mechanisms between the surface chemistry of the three engineered MXenes and DA are proposed.

Chapter 6 examines the channel/electrolyte interface which is not addressed in Chapters 4 and 5. This chapter elucidates the role of cation interactions at this interface, with the aim of providing deeper insight into the ion-π interactions and the kinetics of diffusion, binding and unbinding which are of fundamental relevance for the response of EGOT-based neuromorphic devices. The investigation focuses on two materials known for their high ionic permeability - so called Organic Mixed Ionic-Electronic Conductors OMIECs- *viz.,* reduced Graphene Oxide (rGO) and PEDOT:PSS. For rGO-based EGTs, a straightforward and tunable fabrication route based on the direct electrodeposition of a Graphene Oxide (GO) solution is presented. Following the optimization of a conditioning protocol centred on cation

de-intercalation, the resulting devices exhibit robust multilevel memory behaviour driven by cation intercalation.

The study of ion dynamics is subsequently extended to PEDOT:PSS-based EGOTs operated under steady-state conditions with electrolytes of varied composition, including solutions at different pH values and the homologous series of alkali-metal chlorides (*viz.,* LiCl, NaCl, KCl). The influence of pH is compared in pre-hydrated and non-pre-hydrated PEDOT:PSS EGOTs. Interestingly, while pre-hydrated devices display the expected increase in current when operated in acidic electrolytes, non-pre-hydrated devices show a decrease in current across all pH values, with the attenuation being less pronounced in alkaline solutions. This unexpected behaviour is rationalized by considering the swelling processes occurring in non-pre-hydrated films. Finally, the multiparametric response characteristic of EGOT architectures provides preliminary insight into how the physicochemical properties of homologous alkali cations modulate the behaviour of PEDOT:PSS films.

In summary, this thesis explores complementary strategies to enhance the performance and the applications of EGOT architecture. By tailoring the surface chemistry of the gate electrodes, the sensitivity and selectivity of EGOT-based biosensors for small-molecule detection are significantly improved. Furthermore, the role of ionic species at the channel/electrolyte interface is investigated to support the development of neuromorphic devices that leverage the ion-interactions occurring in the active organic materials. Finally, the use of chemometric tools is shown to be a powerful approach to extracting the full potential of EGOT devices, demonstrating how advanced data analysis can substantially strengthen the organic electronic applications and the reliability of the results.

Chapter 3: Materials and methods

This section provides a comprehensive overview of the chemicals, materials, and experimental procedures employed in this work, encompassing both fabrication methods and the morphological and electrical characterization protocols used for the devices discussed in Chapters 4, 5, and 6.

3.1 Materials and chemicals

All chemicals are of reagent grade or higher and used as received unless otherwise specified.

Semiconductors and Conductive Polymers A drop-casting solution of 6,13-Bis(triisopropylsilylethynyl)pentacene (TIPS-pentacene) is prepared by stirring the commercial powder (Merck-Sigma-Aldrich, United States) in a 2:8 (w/w) hexane:toluene mixture for 3 hours at 80°C. Poly(3,4-ethylenedioxythiophene)polystyrene sulfonate (PEDOT:PSS) formulations are prepared by adding Dimethyl Sulfoxide (DMSO, 5% v/v) and (3-Glycidyloxypropyl)trimethoxysilane (GOPS, 0.2% v/v) to a Clevios PH 1000 PEDOT:PSS dispersion (Heraeus, United States). Both DMSO and GOPS are purchased from Merck-Sigma-Aldrich.

2D Material Dispersions and Precursors A commercial graphene oxide (GO) dispersion in water (0.4% w/w, monolayer content > 95%, pH 2.2–2.5; Graphenea Inc., United States) is used for the *in-situ* electrodeposition of reduced-graphene oxide (rGO) after optimization of the dilution factor (Chapter 6).
For MXene synthesis, MAX phase Ti_3AlC_2 (200 mesh) is purchased from Carbon Ukraine Ltd. Hydrofluoric acid (HF, 40% solution) and isopropanol are sourced from Fisher Chemical. Ar 5.0, 5% H_2 in Argon 5.0 and NH_3 5.0 gas cylinders are purchased from Linde and used for the synthesis steps.

Electrolytes Phosphate Buffer Solutions (PBS) are used as the electrolyte matrix. Specifically, 50 mM PBS and 1x PBS (both pH 7.4) are employed for L-Tryptophan (Chapter 4) and Dopamine (Chapter 5) biosensing experiments, respectively. A 1 M PBS solution (pH 7.4, Sigma-Aldrich) is used as the electrolyte for the neuromorphic characterization of rGO-EGTs. Lithium chloride, sodium chloride and potassium chloride are purchased from Sigma Aldrich and prepared at different concentrations.

Surface Functionalization and Biosensor Assembly Chemicals for gate electrode functionalization are sourced as follows: Aqueous glutaraldehyde (GA, 50%), sodium hydroxide, ethanolamine, 6-mercaptohexanol, 11-mercaptoundecanoic acid, N-(3-dimethylaminopropyl)-N-ethylcarbodiimide (EDC), and N-hydroxysuccinimide (NHS) are purchased from Merck-Sigma-Aldrich. 2-

Mercaptoethylamine hydrochloride (Cysteamine, CYS) is obtained from Thermo Scientific. These reagents are combined to form a Self-Assembled Monolayer (SAM) on the gate electrode for grafting a purified monoclonal antibody for L-Tryptophan (Immunoglobulin G; Immusmol). This process completed the fabrication of the EGOT immunosensor for L-Tryptophan enantiodetection.

3.2 EGOT fabrication

3.2.1 EGOT substrates

This study employs distinct substrate configurations for the fabrication of Electrolyte-Gated Organic Transistors (EGOTs), tailored to specific sensing applications and fundamental characterization goals. The substrates described below range from flexible polyimide and glass-based substrates employed for biosensors fabrication (Chapters 4 and 5) to quartz and polyimide-based test patterns, used to investigate the interactions between ions and the organic semiconductor (OSC) at the channel/electrolyte interface (Chapter 6).

Kapton-Based Substrates for L-Tryptophan Immunosensors As discussed in Chapter 4 for the development of the L-Tryptophan immunosensors is proposed a sided-gate architecture. The source-drain interdigitated electrodes (IDEs) are microfabricated on flexible, gold-metallized DuPont Kapton EN foil (Creavac, Dresden, Germany). The polyimide foil thickness ranges from 7.5 to 25 μm. The vacuum-deposited metallization consists of a 3 nm chromium adhesion layer and a 70 nm gold film. Substrate patterning is performed via laser scanning ablation using a custom *in-house* designed and assembled infrared laser scan ablation machine (property of Istituto Italiano di Tecnologia). This system allows for the selection of an optimal ablation power (≈ 2 mW) to avoid melting and deformation of the polymer film. The resulting source-drain IDEs exhibit a channel Width (W) to Length (L) ratio (W/L) equal to 3000. Before semiconductor deposition, the gold-polyimide substrates are cleaned by sonication in ethanol for ten minutes, followed by rinsing with deionized (DI) water and drying with a gentle nitrogen (N_2) flow.

Glass-Based Substrates for Dopamine Sensors The fabrication of MXene-functionalized EGOTs for Dopamine detection (Chapter 5) utilizes commercial test patterns on glass (Model ED-IDE1-Au, Micrux, Spain). These patterns feature 90

pairs of interdigitated gold electrodes with a 10 μm gap width, yielding a W/L ratio of 49000. To ensure the removal of organic contaminants, the IDEs are subjected to a three-step cleaning procedure:

(i) ultrasonication in 2% Hellmanex detergent solution,

(ii) ultrasonication in distilled water,

(iii) ultrasonication in ethanol.

Each step is followed by rinsing with the respective solvent and drying under an N_2 flow.

Substrates for Characterizing Ion-Electronic Interactions The rGO and PEDOT:PSS-based EGOTs, detailed in Chapter 6, are fabricated on test patterns (TPs) supplied by FBK (Fondazione Bruno Kessler, Italy). These 1 cm^2 TPs are fabricated on quartz substrates featuring a surface roughness below 2 nm. The electrodes consist of a 50 nm thick gold layer and a thin chromium adhesion layer. Each TP contains four pairs of IDEs patterned using standard photolithography and lift-off techniques. Two distinct geometries are selected:

- rGO-EGTs: W/L ratio = 500 (L = 15 μm, W = 7.5 mm).
- PEDOT:PSS-EGOTs: W/L ratio = 2000 (L = 15 μm, W = 30 mm).

Prior to semiconductor deposition, the quartz TPs are cleaned by rinsing with acetone to remove photoresist residues, followed by rinsing with DI water and drying with N_2. For PEDOT:PSS-EGOTs specifically, an additional cleaning step is performed: immersion in a hot (80°C) piranha solution (H_2SO_4 : H_2O_2, 1:1), followed by abundant rinsing with DI water and N_2 drying.

To explore the effect of electrolyte pH on the steady-state performance of PEDOT:PSS EGOTs, an alternative substrate is necessary to decouple measurements from secondary gating effects often observed with quartz substrates at varying pH levels.[1] For these experiments, custom test patterns designed and manufactured by Phoenix PCB (Ivrea, Italy) are employed. These feature nine independent pairs of gold source/drain electrodes (W = 400 μm, L = 100 μm, W/L = 4) patterned onto a flexible polyimide substrate. Electrical insulation is ensured by an additional polyimide layer containing nine rectangular openings, which covers the entire layout and exposes only the active channel area and the terminal portions (0.8 mm x 0.9 mm) of the electrode leads.

3.2.2 Organic Semiconductor Thin-Films Deposition

In this work, two p-type semiconductors (TIPS-pentacene and PEDOT:PSS) and one 2D ambipolar semiconductor (rGO) are used as the active channel materials for the EGOTs (Figure 1.6).

TIPS-pentacene A 1% (w/w) TIPS-pentacene (TIPS-P5) solution is prepared by stirring the commercial (Merck-Sigma-Aldrich) dark-blue powder in a 2:8 (v/v) hexane:toluene mixture for 3 hours at 80°C. A 1 µL droplet of the resulting solution is drop-cast onto gold-metallized Kapton IDEs and allowed to evaporate at room temperature. As detailed in Chapter 4, this TIPS-pentacene channel is integrated with a functionalized gate electrode to fabricate the L-Tryptophan immunosensor.

PEDOT:PSS PEDOT:PSS is used as the active channel material for two different applications. First, for the development of MXene-functionalized EGOTs for Dopamine sensing, the commercial PEDOT:PSS formulation (see Chapter 3.1 for details) is diluted 1:1000 in MilliQ water. A 10 µL drop of this solution is cast onto the ED-IDE1-Au IDEs. The final fabrication step involved curing the film in a thermostatic oven at 120°C for 30 minutes. Atomic Force Microscopy (AFM) analysis showed a resulting film thickness of 19 ± 7 nm.[2]
Second, PEDOT:PSS is applied as the active material to study cation-semiconductor interactions in EGOT architectures. For this application, the formulation is diluted 1:250 in MilliQ water. A 4 µL drop of the solution is cast onto the FBK test patterns (W/L = 2000) and subsequently cured at 120°C for 30 minutes. This deposition and curing process is repeated twice.
As described in the previous paragraph, to assess the influence of the electrolyte solution pH, custom test patterns on polyimide substrate are necessary. For these PEDOT:PSS EGOTs, the (semi)conductive channels and the gate electrodes are obtained filling each of the nine pools with 500 nL of the PEDOT:PS formulation, diluted 1:10 with MilliQ water. The last fabrication step is PEDOT:PSS curing in a thermostatic oven (120°C, 30 minutes). Obtained films exhibit an average thickness of 1 µm.[3]

Reduced Graphene Oxide (rGO) For the rGO-EGTs, a novel method for rGO growth via *in-situ* electrochemical reduction of a GO dispersion is proposed. The source and drain electrodes of an FBK test pattern (W/L = 500) are short-circuited

and connected to the "High-Force" terminal of a Keysight B2912A Source Measure Unit (SMU). This setup served as the working electrode (WE) in a two-electrode configuration. A platinum (Pt) wire, connected to the grounded "Low-Force" terminal, serves as the combined counter and reference electrode (CE/RE). As depicted in **Figure 3.1**, the liquid GO dispersion contacts both the WE (the IDEs) and the Pt wire, closing the electrochemical circuit. A reductive Cyclic Voltammetry (CV) scan is applied by sweeping the WE voltage from -1.3 V to a final voltage V_{end} at a scan rate of 90 mV/s. Various GO dispersion concentrations (0.1, 0.2, 0.3, and 0.4 %w/w) and V_{end} values (ranging from -2.8 V to -2.4 V) are tested to achieve optimal steady-state transfer characteristics.

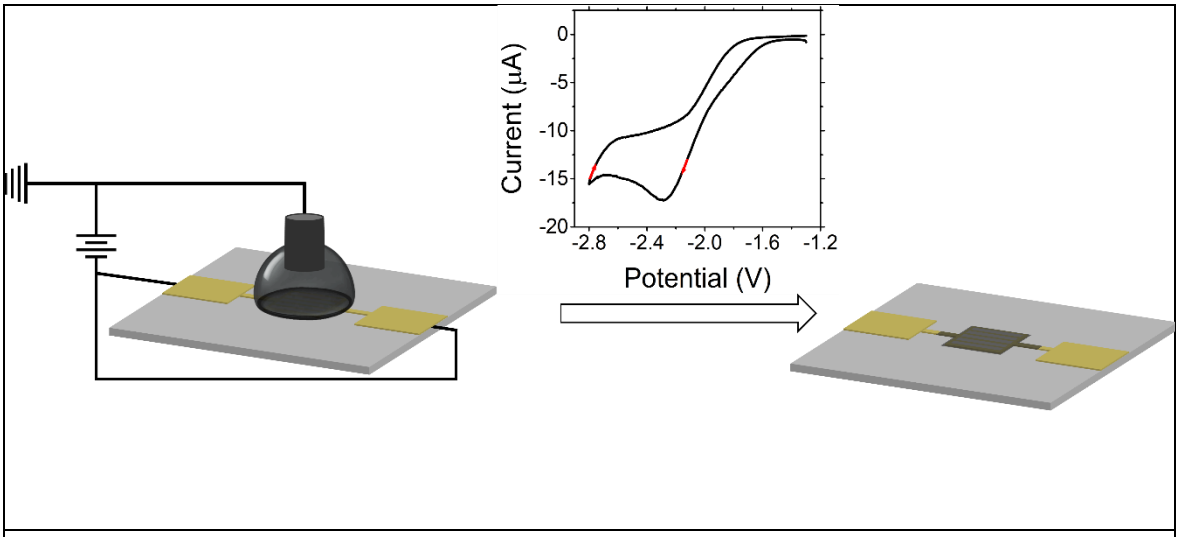

***Figure 3.1**: Schematic representation of electrodeposition setup for in-situ fabrication of rGO-EGTs.*

3.3 Gate Functionalization

The response of the EGOT-based biosensors is enhanced by tailoring the gate electrode surface chemistry. Firstly, for the L-Tryptophan immunosensor (Chapter 4), the gate is functionalized with an anti-L-Tryptophan antibody. Two anchoring strategies based on Self-Assembled Monolayer (SAM)-forming linkers are compared: the Schiff Base Reaction (SBR) and amide bond formation via EDC-NHS activation.

Secondly, to enhance the EGOT's sensitivity towards Dopamine (Chapter 5), the gate electrode is functionalized using chemically-engineered MXenes. The

experimental procedures for these functionalization strategies are detailed in this section.

3.3.1 Self-Assembled Monolayer for Grafting Antibody

Planar gold gate electrodes, fabricated on gold-polyimide substrates, are first subjected to a standardized cleaning procedure. The electrodes are sonicated in ethanol for 10 minutes, rinsed with deionized (DI) water, and dried with a gentle N_2 flow. Subsequently, they are immersed in a hot (80°C) piranha solution (H_2SO_4 : H_2O_2 1:1), rinsed abundantly with DI water, and dried again with N_2.

Schiff Base Reaction (SBR) Strategy The cleaned gold gate electrode is functionalized by immersion in a 30 mM ethanolic solution of cysteamine (CYS), followed by treatment with a 10% aqueous solution of glutaraldehyde (GA). The pH of the GA solution is systematically controlled to optimize the subsequent antibody grafting. The CYS-GA functionalized electrode is then incubated with the anti-L-Trp antibody solution (0.1 mg/mL) at 4°C. Finally, a 30 mM ethanolamine solution is employed as a passivating agent.

EDC-NHS Activation Strategy The cleaned gate electrode is incubated overnight at room temperature in an ethanolic solution containing a 10 mM mixture of SAM-forming molecules (11-mercaptoundecanoic acid and 6-mercaptohexanol at a 1:9 molar ratio). The electrode is then rinsed with ethanol and dried with N_2. The terminal carboxylic groups are activated by incubating the surface with 20 µL of an aqueous solution containing 20 mM N-(3-dimethylaminopropyl)-N-ethylcarbodiimide (EDC) and 50 mM N-hydroxysuccinimide (NHS). After washing with DI water and drying with N_2, the electrode is incubated with the anti-L-Trp antibody solution (0.1 mg/mL) at room temperature and subsequently passivated with ethanolamine.

3.3.2 MXenes

3.3.2.1 MXenes Synthesis

The synthesis of the MXenes is carried out in collaboration with the group of the group of Prof. Ioan-Alexandru Baragau (National Institute of Materials Physics, Romania). Briefly,6 g of commercial Ti_3AlC_2 MAX phase powder is slowly added to a 27.7% HF solution while under magnetic stirring (Teflon-coated stirrer). (This HF

solution is previously prepared by carefully adding 150 mL of 40% HF to 75 mL of DI water). The reaction between HF and the Al atoms in the MAX phase structure results in H_2 gas formation. After the MAX phase addition is completed, the mixture is kept under constant stirring at room temperature for 24 hours.

The resulting mixture is filtered under vacuum and washed multiple times with DI water until the filtrate reached a pH of 6-7. The collected solid (HF-MXene $Ti_3C_2T_x$) is then washed on the filter with 100 mL of isopropanol, collected, and vacuum dried at 100°C for 6 hours.

Next, 1 g of the synthesized HF-MXene is loaded into a quartz boat and transferred into a horizontal MIT OTF-1200X tubular furnace (equipped with an 8-inch heating zone and a 1 m length quartz tube, OD: 25 mm, ID: 23 mm). The system is sealed, and a gas flow (100 mL/min) of either Ar (5.0), 5% H_2 in Ar (5.0), or NH_3 (5.0) is introduced. The furnace is heated to 400°C at a rate of 5°C/min and held at that temperature for 3 hours. The sample is then cooled down at a rate of 5°C/min. During cooling, the reactive gas (H_2 or NH_3) is switched off and replaced with a pure Ar (5.0) flow, which is maintained until the samples reached room temperature (20-25°C). The final MXene samples are stored in glass vials under vacuum for further testing and characterization. The schematic representation of the synthesis procedure is reported in **Figure 3.2**.

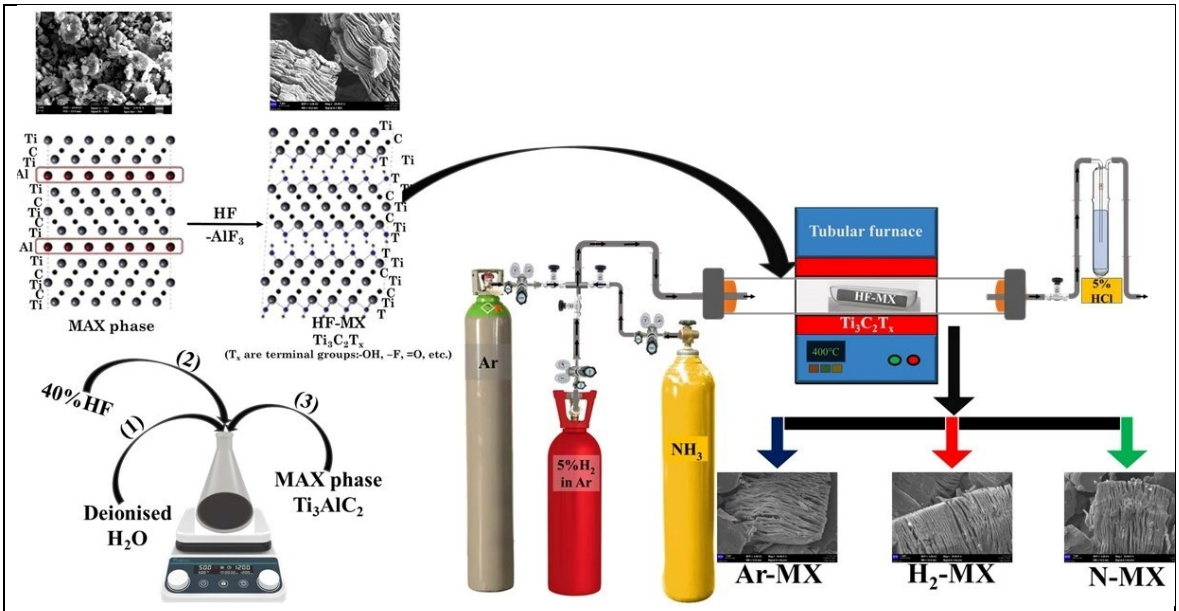

***Figure 3.2**: The schematic representation of the synthesis process of HF-MX, Ar-MX, H_2-MX , N-MX.*

3.3.2.2 Electrode Functionalization with MXenes

Gold (Au) disc electrodes are cleaned by ultrasonication in ethanol for 10 minutes and dried with an N_2 flow. The electrodes are then polished with 0.05 µm alumina powder, rinsed abundantly with DI water, and dried with N_2.
A 5 mg/mL MXene dispersion is prepared in DMSO. The dispersion is sonicated for 10-minute intervals, repeated six times. A further sonication step is performed for 15 minutes while N_2 is bubbled through the dispersion.
The cleaned Au electrodes are functionalized by drop-casting 4 µL of the 5 mg/mL MXene dispersion onto the gold surface. The Au-MXene electrodes are then cured using a two-step process: 50°C for 30 minutes, followed by an additional 30 minutes at 70°C. This deposition and curing process is repeated twice.

3.4 EGOTs Standard Electrical Characterization

The electrical characterization of the EGOTs is conducted using a Keysight B2912A dual-channel Source Measure Unit (SMU), equipped with one or two N1294A Opt001 banana-to-triaxial adapters. All measurements are performed in a standard common-source, common-ground configuration. This layout is achieved by connecting the source electrode to the short-circuited "Low" terminals of both SMU channels. The gate and drain electrodes are connected to the "High" terminals of Channel 1 and Channel 2, respectively. All measurements are carried out in air under ambient laboratory conditions (temperature and humidity). The specific parameters used to collect the Current-Voltage (I-V) transfer characteristics for the different EGOTs developed in this thesis are summarized in **Table 3.1**.

***Table 3.1**: Experimental parameters, including V_{DS} and V_{GS}, the scan rate and the electrolyte composition, used to characterize the EGOT-based devices.*

	TIPS-P5 EGOT	**PEDOT:PSS EGOT**	**rGO-EGT**	**PEDOT:PSS EGOT**
V_{GS} (V)	From -0.7 to 0.1 V	From -0.5 to 0.7 V	From -0.8 to 1.2 V	From -0.5 to 0.7 V
V_{DS} (V)	- 0.2 V	- 0.2 V	0.3 V	- 0.3, - 0.5, - 0.7 V
Scan rate	50 mVs^{-1}	250 mVs^{-1}	90 mVs^{-1}	250 mVs^{-1}
Electrolyte	PBS 10 mM (PBS 1x)	PBS 50mM	PBS 1M	LiCl, NaCl, KCl
Chapter	4	5	6	6

To explore the neuromorphic (synaptic) response of the rGO-EGTs (Chapter 6), the devices are stimulated with single square voltage pulses and square pulse trains applied to the pre-synaptic terminal (*i.e.,* the gate electrode, V_{GS}).

During stimulation, a constant drain-source voltage (V_{DS}) of 0.3 V is maintained, while the post-synaptic drain current (I_{DS}) is recorded. The applied pulses are designed with their baseline voltage set to the charge-neutrality point (V_{CNP}) of the transistor. The pulse amplitude ($V_{GS,pulse}$) is varied within the range of -0.8 V to +0.7 V for both single pulse and pulse train experiments. The pulse time duration (Δt) is fixed at 1 s, utilizing a 50% duty cycle for the pulse trains.

3.5 Electrochemical Study of Surface Functionalization

Electrochemical characterization is employed to monitor and validate the stepwise surface modifications during the gate electrode functionalization processes (see Chapter 4 and Chapter 5 for the results). To obtain a comprehensive assessment of the surface changes, CV and Electrochemical Impedance Spectroscopy (EIS) are performed in a faradaic solution containing 5 mM $K_3[Fe(CN)_6]$, acting as redox probe, dissolved in 1 M KCl, serving as supporting electrolyte.

All measurements are collected using a CH Instruments (Model 760c) potentiostat in a three-electrode cell, with the modified gate electrode served as the working electrode (WE), a platinum (Pt) wire as the counter electrode (CE), and an Ag|AgCl (3 M KCl) as the reference electrode (RE). **Figure 3.3** shows the experimental setup used to characterize the polyimide-based, planar gold electrode, functionalized the detection of L-Tryptophan (Chapter 4 for further details).

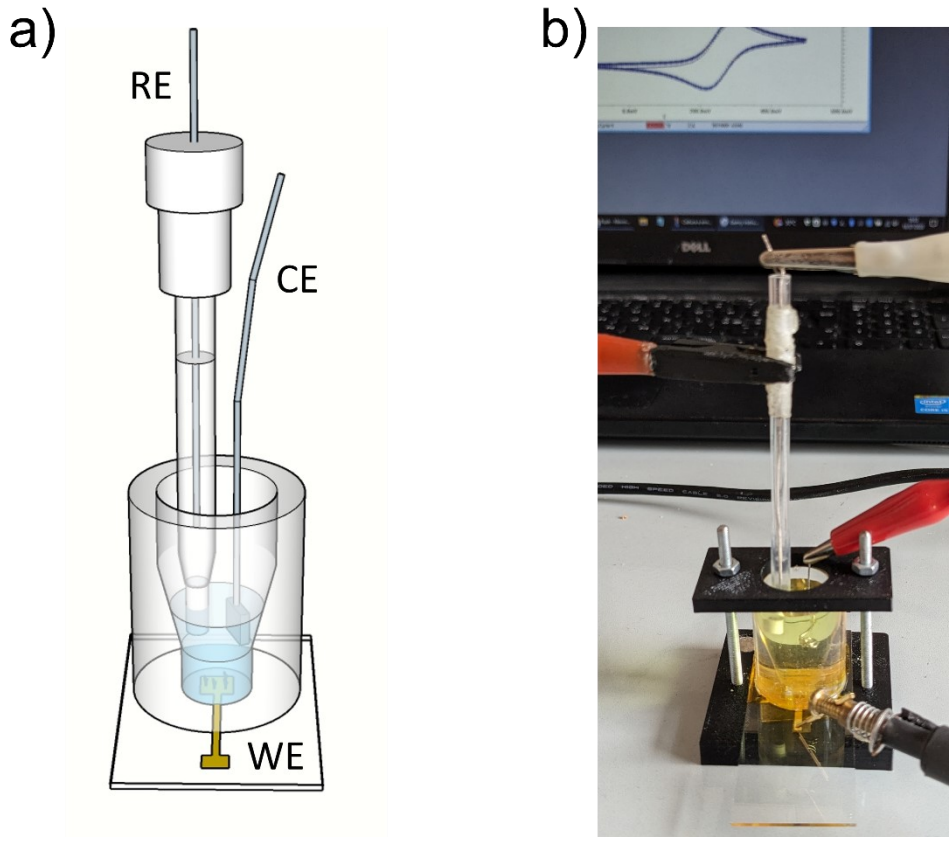

***Figure 3.3**: Electrochemical setup for the characterization of a planar electrode. a) Schematic representation b) Photograph of the experimental setup in presence of $K_3Fe(CN)_6$ to monitor the functionalization of a planar gold electrode.*

EIS measurements are recorded over a frequency range from 10 kHz down to 0.1 Hz. A 10 mV (rms) AC voltage amplitude is applied, superimposed on a DC potential (*vs* Ag|AgCl) of +0.26 V for the redox probe solution. In the non-faradaic buffer, the same AC amplitude is applied but with a DC potential (*vs* Ag|AgCl) of 0 V.
CVs are recorded by applying a 100 mV/s scan rate, from -0.2 to 0.5 V (*vs* Ag|AgCl).

3.6 Morphological Characterization

Topography and morphology characteristics of functionalized gate electrode and of active material in the channel of EGOTs are important parameters to evaluate during the development of an organic bioelectronic device. In this thesis work, mainly two microscopy techniques are used to collect morphological and topographic information of the active surface (*viz.,* both channel and functionalized gate electrode), including Scanning Electron Microscopy (SEM) and Atomic Force Microscopy (AFM)

3.6.1 Scanning Electron Microscopy (SEM)

The Scanning Electron Microscopy (SEM) collected for MXene samples (see Chapter 5 for the results) before the deposition on gold electrodes are recorded using a field emission scanning electron microscope (FESEM) Zeiss Gemini 500 equipped with an energy dispersive X-ray (EDS) detector from Bruker. The EDS measurements are used to reveal the chemical composition of the MXene samples. The MAX phase (Ti_3AlC_2) sample's SEM and EDS images are recorded using an EVO 50 XVP microscope from Zeiss, equipped with an EDS from Quanta Bruker 200. This experimental part is carried out by the group of Prof. Ioan-Alexandru Baragau at the National Institute of Materials Physics, Romania.

3.6.2 Atomic Force Microscopy (AFM)

The AFM is employed to study the surface topography of the electrodeposited rGO (see Chapter 6 for the results). The AFM images are collected using a Park XE7AFM System (Park Systems, Suwon, Korea), operating in tapping mode, in air, at room temperature. The instrumentation features pre-mounted silicon cantilevers (OMCL-AC160TS, Olympus Micro Cantilevers, Tokyo, Japan) with aluminium backside reflective coatings, tip curvature radius of ≈7 nm, elastic constant of ≈26 N/m, and resonance frequency of ≈300Hz. The AFM images are analysed using Park Systems XEI software (Park Systems, Suwon, Korea) and Gwyddion freeware (version 2.62 http://gwyddion.net/) to extract the thickness and the roughness of the rGO film. The thickness reported is calculated as the average of nine different regions across the scratch edge. The roughness value is calculated from 5 μm × 5 μm topographic images of the sur-face acquired for three different samples. Data are presented as mean ± SEM.

3.7 Data Analysis

All the presented data are analysed using Matlab (version R2024a, Mathworks, Natick, MA, USA) and OriginPro 2016. The chemometric data analysis is processed with PLS Toolbox 8.9.1 (2024) (Eigenvector Research, Inc., Manson, WA USA 98831 software).

The faradic EIS spectra of gold electrodes functionalized with MXenes are analysed using an *ad-hoc* Matlab code. This Matlab code allows the user to select the proper

equivalent circuit and fit the trend of -Z'' vs Z' (*viz.,* Nyquist plot) by a non-linear least-squares optimization using two distinct initial parameter guesses to robustly minimize the real and imaginary residuals of the impedance spectra to determine the best-fit circuit parameters.

A crucial part of this thesis work involves the demonstration of chemometric tools to enhance the response of EGOT-based (bio)sensors (results in Chapter 4 and Chapter 5). For the enantiodiscrimination of Tryptophan enantiomers (Chapter 4) the transfer curves are fitted according to the model developed by Zanotti *et al.,*[4] (Equation 4.1). The turn-on voltage shift ΔV_T, rescaled vs σ, the α parameter shift (Δα) and the signals $S_{g_{m,I}}$, and $S_{I_{DS}}$ at V_{GS} = -0.4 V are used as basis set for the principal component analysis (PCA). Prior to the development of PCA decomposition, the input basis set undergoes autoscaling (*viz.,* adjusted to zero mean and unit variance by dividing each column by its standard deviation). Leave-one-out cross-validation method is used to assess the optimal number of principal components.

Partial least square discriminant analysis (PLS-DA) is applied to increase the robustness of the enantiodiscrimination. In PLS-DA input arrays, the parameters ($S_{I_{DS}}$, $S_{g_{m,I}}$, $\frac{e\Delta V_T}{\sigma}$, Δα) extracted from transfer curves of all the L-Trp and D-Trp samples are used as a set of predictors. These samples are used as a training set with a binary-coded column vector that encoded the classification information (0 for L-Trp and 1 for D-Trp). The classification model is assessed with Receiver Operating Characteristics Curve (ROC curve), which report the specificity (number of samples predicted as not in the class divided by actual number not in the class) *versus* the sensitivity (number of samples predicted as in the class divided by number actually in the class). The model is further evaluated with four independent experimental points within a concentration range of 1 pM to 1 nM.

For MXene-bases EGOT sensor for Dopamine detection (developed as detail in Chapter 5), the transfer curves are fitted according to Equation 4.1. To further investigate the interaction between differently functionalized MXenes and Dopamine, the parameters extracted from the sensing platform, including the signals $S_{g_{m,I}}$, and $S_{I_{DS}}$ at V_{GS} = -0.5 V, +0.2V and +0.7 V, the turn-on voltage shift ΔV_T, the parameters shift Δα and Δσ, are used as basis set for the PCA. Autoscale is used as preprocess method and Leave-one-out as cross-validation algorithm to assess the optimal number of principal components.

3.8 Bibliography

[1] M. Di Lauro, S. Casalini, M. Berto, A. Campana, T. Cramer, M. Murgia, M. Geoghegan, C. A. Bortolotti, F. Biscarini, *ACS Appl. Mater. Interfaces* **2016**, *8*, 31783–31790.

[2] I. Sergi, M. Sensi, R. Zanotti, T. Tsironi, E. Flemetakis, D. M. Power, C. A. Bortolotti, F. Biscarini, *Biosens. Bioelectron.* **2025**, *271*, DOI 10.1016/j.bios.2024.117098.

[3] M. Di Lauro, A. De Salvo, G. C. Sebastianella, M. Bianchi, S. Carli, M. Murgia, L. Fadiga, F. Biscarini, *ACS Appl. Electron. Mater.* **2020**, *2*, 1849–1854.

[4] R. Zanotti, M. Sensi, M. Berto, A. Paradisi, M. Bianchi, P. Greco, C. A. Bortolotti, M. Di Lauro, F. Biscarini, *Adv. Mater.* **2024**, *36*, DOI 10.1002/adma.202410940.

Chapter 4: Discrimination of Tryptophan Enantiomers at sub-pM level by Multiparametric Analysis of a Label-free Organic Immunosensor

This chapter details the development of a label-free Electrolyte-Gated Organic Transistor (EGOT) immunosensor for the chiral discrimination of Tryptophan (Trp) enantiomers. Chiral interaction is one of the most exquisite mechanisms of specific recognition adopted in most of the processes in living systems. Here, the discrimination of the Trp enantiomers with the EGOT-based biosensor functionalized with an antibody designed for specific recognition of the L-Trp enantiomer is challenging, since the recognition occurs at large distance from the gate electrode and the target amino acid is small. Indeed, the EGOT biosensor responds to both enantiomers with a slightly larger affinity constant for the L-Trp with respect to D-Trp, which is counterintuitive with respect to the expected "all-or-none" effect. Therefore, we devise a new synergistic experimental/data analysis approach to enhance the differences at the lowest concentrations. Key to the device's performance is an optimized antibody anchoring protocol, achieved by tailoring the gate electrode's surface chemistry. Furthermore, a novel model, that was recently developed in our group to describe EGOT transfer curves, is used to leverage the EGOT's multiparametric response into multivariate data analysis. The outcome is the unambiguous discrimination between L- and D-Tryptophan at unprecedented sub-picoMolar concentrations. These results highlight the impact of applying multivariate data analysis to advanced EGOT-based sensing platforms moving beyond the usual construction of a dose curve.

Chirality is a fundamental molecular property in biorecognition.[1] As the origin of homochirality remains unclear, biological systems exhibit remarkable selectivity for chiral molecules, such as peptides, carbohydrates, and nucleic acids, to regulate cellular metabolic processes.[2] Enantiomers exhibit different pharmacological, pharmacokinetic, and toxicological activities[3], and is important to resolve the chirality of synthetic molecules prior their interaction with a living system. Amino acids, except glycine which is achiral, are among the smallest chiral molecules in Nature.[4] The L-amino acids are the building blocks in proteins synthesis, while D-amino acids can be incorporated into proteins only via modified ribosomes.[5] Among the L-amino acids, L-Tryptophan (L-Trp) plays a crucial role in the L-Kynurenine pathway, and in the Serotonin pathway.[6] Alterations in the physiological concentration of L-Tryptophan (L-Trp) (4 μM in blood, 2 μM in cerebrospinal fluid)[7] are correlated with pathological disorders, including cancer[8], depression[9], Alzheimer's disease[10], and AIDS-related dementia complex.[11]

The other enantiomer, D-Tryptophan (D-Trp), albeit present in microorganisms, does not participate in metabolic pathways in the human body[12]; however, D-Trp plays a significant role as an intermediate in the synthesis of peptide antibiotics and as an immunosuppressant in the pharmaceutical industry.[13] Trp derivatives (*viz.,* serotonin, melatonin, and halogenated Trp) play a crucial role in the food, chemical (polymers, pesticides) and pharmaceutical industries.[14] Since the biosynthesis of these compounds originates from enantiomerically pure Trp, the discrimination between enantiomers is of paramount importance to enhance both the efficacy and safety of the production processes. Currently, a variety of analytical methods, including high-performance liquid chromatography (HPLC)[15–17], colorimetry[18], capillary electrophoresis combined with circular dichroism[19], and electrochemical analysis[20–22] are employed for enantiomeric discrimination. A detailed comparison of the techniques successfully applied for chiral recognition of Trp enantiomers is reported in **Table 5.1**.

***Table 5.1**: Summary of the Tryptophan sensors exploiting different transduction techniques and material for enantiorecognition of Tryptophan.*

Techniques	*Stereo-selective material*	*Transducer material*	*[Trp] range*	*Ref*
Chromatography :				
High-Performance Liquid Chromatography	o-Phthalaldehyde, N-acetyl-L-cysteine	Chemiluminescence	1.2 μM – 59 μM	[15]
	Teicoplanin chiral stationary phase	Diode array detector	24.5 μM – 2.5 mM	[16]
	(−)-(18-crown-6)-2 3, 11, 12-tetracarboxylic acid (Chirosil-SCA)	Photodiode array detector	450 μM – 3.3 mM	[17]
Capillary Electrophoresis:				
Capillary Electrophoresis	n.g.	Circular dichroism	n.g.	[19]
Mechanical:				
Microcantilevers deflection	Monoclonal anti-Trp antibody	Nanostructured microcantilever	2.5 μM	[23]
Temperature	N-Acetyl-L-Cysteine	Mxene-Au NPs	1.0 mM - 6.0 mM	[24]
Optical:				
SERS-spectroscopy	6-mercapto-6-deoxy-β-CD	TiO_2 NPs	100 nM - 1 mM	[25]
UV-spectroscopy	ZnFe2O4-L-Cys	n.g.	0.020 pM - 0.090 μM	[26]
Surface Plasmon Resonance	Polyclonal antibody-anchored to enantiomeric pure ligand	n.g.	3 nM- 500 mM	[27]
Colorimetric sensor	Zif-8 His MOF MIP, L-Tartaric acid-capped Au NPs	Nano-ovals shaped Au NPs, n.g.	250 μM - 1.25 mM	[18,28]
Fluorescence	Self-Assembled fluorescence nanoprobe, CD and Bovine Serum Albumin	n.g.	1 μM - 6 mM	[29,30]Wei 2010
Electrochemical:				
Cyclic voltammetry (CV)	Poly-L-Cys MWCNTs; L-alanine ethyl ester modified carbon MWCNTs	GCE	0.1 mM - 5.0 Mm	[31,32]
Electrochemical impedance spectroscopy (EIS)	Au-Ag nanoparticles	GCE	0.1 mM – 10 mM	[33]
Differential pulse voltammetry (DPV)	L-Lysine based MOF	Ferrocene-modified MWCNTs	2 μM - 100 μM	[34]
	N-acetyl-L-cysteine	MXene-Au NPs	0.2 mM - 1.0 mM	[24]
	MWCNTs self-assembled with Cu^{2+}-β-CD; β-CD modified with PL-Cys	GCE	3 μM - 4 mM	[31,33]
	Sodium alginate - Chitosan	N-doped graphene CNT-GCE	5 mM	[35]
	Sodium carboxymethyl cellulose; Copper-Cys mercaptide nanorods; Glutamic acid functionalized graphene-gold NPs, MIP/CS/MWCNTs/	GCE	1 μM - 7 mM	[20–22,36]
CV-DPV	Biomimetic MOF, Polyaniline twisted nanoribbon	GCE	0.2 mM - 5 mM	[37]
Transistor	MIP-modified gate electrode	PEDOT:PSS-based EGOT	1 nM - 3 μM	[38]
	Nafion GO functionalized with BSA	MOSFET	1 pM - 1μM	[39]

Notably, only a few studies[25–27,38,39] have explored Trp concentrations below physiological levels. Enantiomeric discrimination in the nanomolar range is achieved with high-cost, time-consuming techniques such as UV spectroscopy and surface plasmon resonance (SPR), which require sophisticated laboratory equipment and

highly trained personnel.[25–27] The remaining two studies that explore low-concentration ranges are based on more portable and user-friendly transistor platforms.[38,39] Specifically, Li and co-workers developed a MOSFET capable of partial enantiodiscrimination in the nanomolar range[39], while Zhang *et al.,* implemented a molecularly imprinted polymer (MIP) on the gate electrode of an Electrolyte Gated Organic Transistor (EGOT), achieving chiral discrimination at a concentration of a few μM.[38] To the best of our knowledge, there are no studies of chiral discrimination at concentrations smaller than nM.

This chapter details the technological steps undertaken to develop a highly sensitive organic transistor immunosensor targeting L-Tryptophan (L-Trp). The optimization protocol begins with the design of an extended-gate architecture, whose dimensions are systematically investigated to optimize the immunosensor's response (Section 4.1). Once the optimal design is selected, two antibody anchoring strategies - Schiff Base Reaction (SBR) and EDC-NHS activation - are compared (Section 4.2). It is demonstrated that by tailoring the pH of the crosslinking step in the SBR protocol, the EGOT-immunosensor's sensitivity is enhanced to detect L-Trp in the 1 fM – 10 nM concentration range, well below its physiological concentration.

In contrast, the EDC-NHS approach yields a response solely in terms of current and transconductance variation, whereas the SBR functionalization enables a multiparametric response upon Trp exposure.

The EGOT immunosensor, functionalized with the anti-L-Trp antibody using the optimized SBR strategy, is tested for its chiral selectivity against the two enantiomers, L-Trp and D-Trp. Nevertheless, the standard univariate analysis of the variation of a single parameter extracted from the transfer characteristics does not unambiguously differentiate L from D enantiomers. To overcome this limitation, a novel and straightforward approach to analyse EGOT biosensor data by combining the multiparametric response extracted from the transfer curves with chemometric tools is proposed in Section 4.3. By applying Principal Component Analysis (PCA) and Partial-Least Square Discriminant Analysis (PLS-DA) the discrimination of between L-Trp and D-Trp is achieved at unprecedented sub-pM level.

4.1 Immunosensor Architecture

The EGOT-immunosensor for L-Tryptophan enantiodiscrimination is fabricated using the architecture schematically illustrated in **Figure 4.1a**. The EGOT features an extended-gate configuration, where both the interdigitated source (S) and drain (D) electrodes and the gate (G) electrode are fabricated on separate, metalized polyimide substrates (see Section 3.2.1 for fabrication details).

Two elastomeric molds are placed in contact with the polymeric substrates to provide sealed, confined compartments: one for the electrolyte interfacing the organic semiconductor (OSC) channel (hereafter, the 'OSC chamber', left in **Figure 4.1a**), and a separate chamber for the gate electrode, where biorecognition occurs (the 'sensing chamber', right).

A bridge between the two chambers containing the electrolyte is maintained by means of a silicon tube (500 µm internal diameter). A unidirectional flow is actuated by a syringe pump from the OSC chamber towards the sensing chamber, initially to fill the system with PBS buffer solution before analyte addition. In this configuration, the tubing length is kept shorter than 10 cm, since it has been previously reported that tubing lengths greater than 30 cm can adversely affect the device's transfer characteristics.[40]

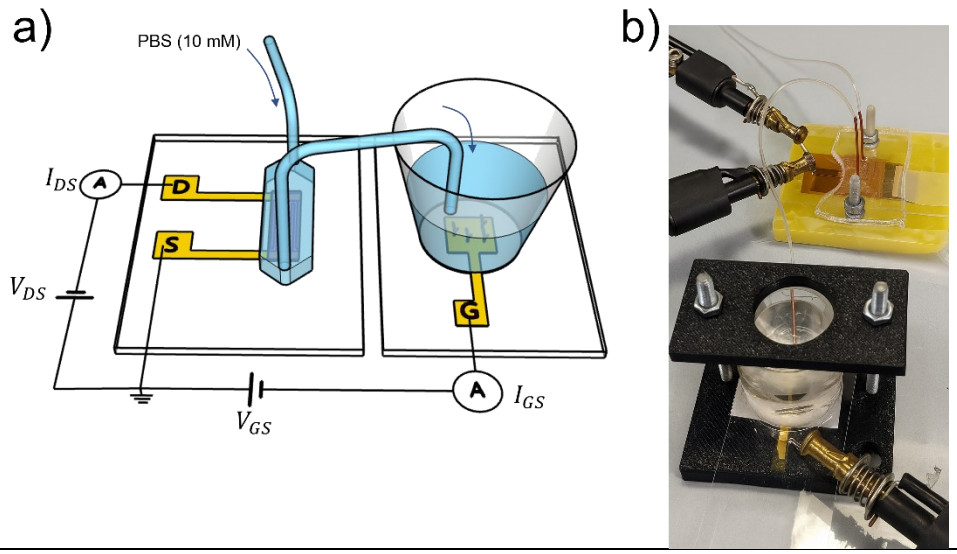

***Figure 4.1**: The extended-gate EGOT architecture. (a) Schematic of the experimental setup. The OSC (on the S-D substrate) and the functionalized gate (G) are physically separated into two distinct chambers. An ionic connection is established via a silicon tube, which also allows for fluidic control (blue arrow) from the OSC chamber to the sensing chamber. (b) Photograph of the physical device holder used for the measurements.*

To optimize the EGOT-immunosensor response, the device architecture is systematically investigated. Firstly, the transfer characteristics of the extended-gate device are measured using gate electrodes with different areas (A_G), while keeping the channel area (A_{ch}) constant. The representative transfer curves (**Figure 4.2a**) show that devices with large gate electrodes (*viz.,* a low A_{ch}/A_G ratio) exhibit a higher drain-source current (I_{DS}) at V_{GS} = -0.7 V, compared to those with smaller gate areas (a high A_{ch}/A_G ratio), as summarized in **Figure 4.2b**. This enhancement is attributed to an increase in the areal charge carrier density in the TIPS-pentacene channel, resulting from the larger gate capacitance afforded by the larger A_G, as previously demonstrated for different semiconductors.[41]

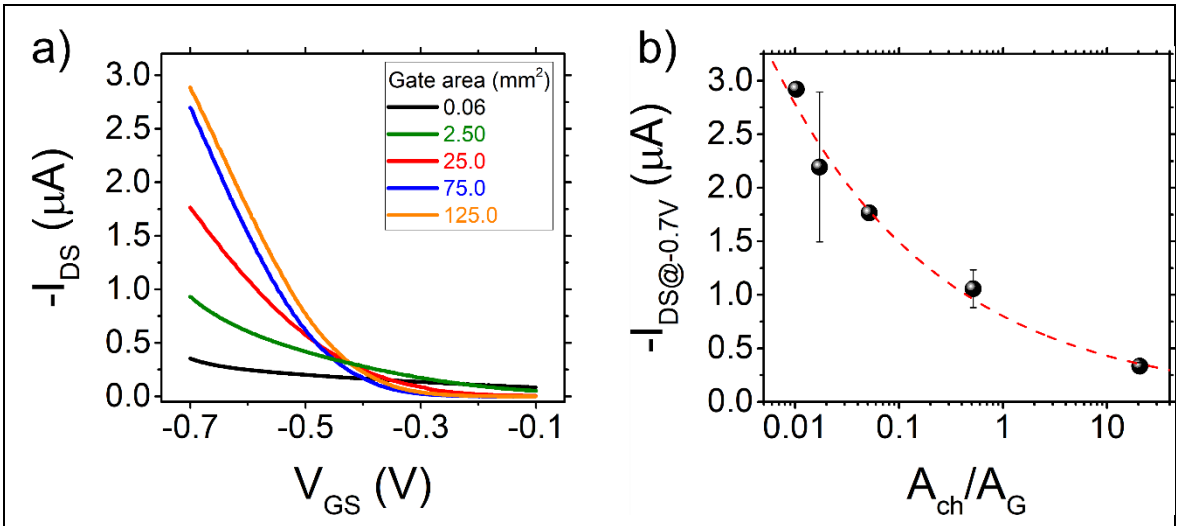

***Figure 4.2**: Optimization of the EGOT gate geometry. (a) Representative TIPS-pentacene transfer characteristics in the extended-gate architecture, using 1x PBS as the electrolyte and a V_{DS} of -0.2 V. (b) Scaling of the drain-source current (I_{DS}) measured at V_{GS} = -0.7 V as a function of the A_{ch}/ A_G ratio. A power law fit (dashed red line) is included as a guide for the eyes. Error bars are the standard deviation of three different gate electrodes.*

Although increasing the gate electrode area generally amplifies the drain-source current (I_{DS}) in EGOTs, a strategic balance is required to maximize device performance while ensuring the uniform and reproducible immobilization of biorecognition elements.

Consequently, a reduced gate area of 4 mm^2 is initially adopted as a preliminary platform. This configuration facilitates the electrochemical characterization and the systematic optimization of the pH for the SBR functionalization route (see Section 3.3.1 for experimental details and Section 4.2 for SBR optimization results).

Following the validation of the functionalization protocol on the 4 mm^2 geometry, device performance is assessed using an expanded gate area (15.85 mm^2) to leverage a more efficient transistor performance. Direct comparison demonstrates that the enlarged gate area consistently yields higher post-functionalization I_{DS}, compared to the smaller gate electrode (**Figure 4.3**). This observation confirms that the 15.85 mm^2 geometry not only aligns with the initial optimization trend (**Figure 4.2b**) but also maintains superior signal output post-functionalization. Therefore, the 15.85 mm^2 gate is selected as the optimal configuration for developing the final, high-sensitivity immunosensor for L-Tryptophan enantiomer discrimination (discussed in Section 4.3).

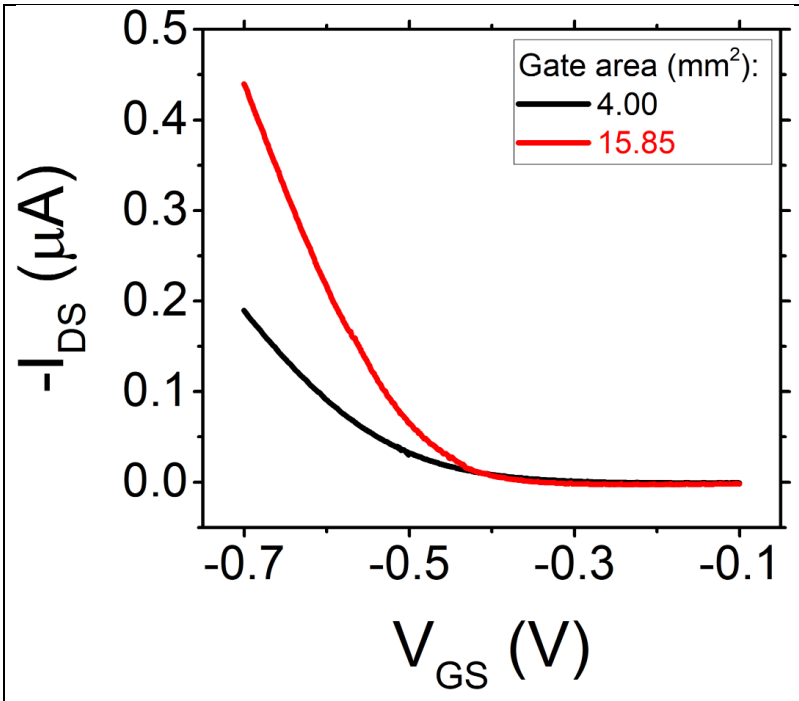

***Figure 4.3**: Comparison of EGOT performance post. SBR functionalization. Representative transfer characteristics of TIPS-pentacene EGOTs featuring SBR-functionalized gate electrodes with areas of 4 mm² (black line) and 15.85 mm² (red line).*

4.2 Optimization of Surface Functionalization for Antibody Grafting

This study employs two strategies to immobilize antibodies onto the gate electrode surface, as depicted in **Figure 4.4**. The first protocol, based on a SBR (**Figure 4.4a**), starts with the formation of a cysteamine (CYS) Self-Assembled Monolayer (SAM). This amine-terminated surface is subsequently activated with glutaraldehyde (GA), a homo-bifunctional crosslinker. The remaining free aldehyde moieties are then reacted with the exposed amino groups of the monoclonal L-Trp antibodies, forming a stable imine (C=N) bond.

The second strategy, the EDC-NHS functionalization procedure (**Figure 4.4b**), involved co-assembling a mixed SAM of 11-mercaptoundeanoic acid (11-MUA) and 6-mercaptohexanol (6-MH). The monoclonal L-Trp antibodies are then covalently bound to the SAM's carboxylate functional groups via N-(3-dimethylaminopropyl)-N-ethylcarbodiimide (EDC) and N-Hydroxysuccinimide (NHS) coupling chemistry. Full experimental details are reported in Section 3.3.1.

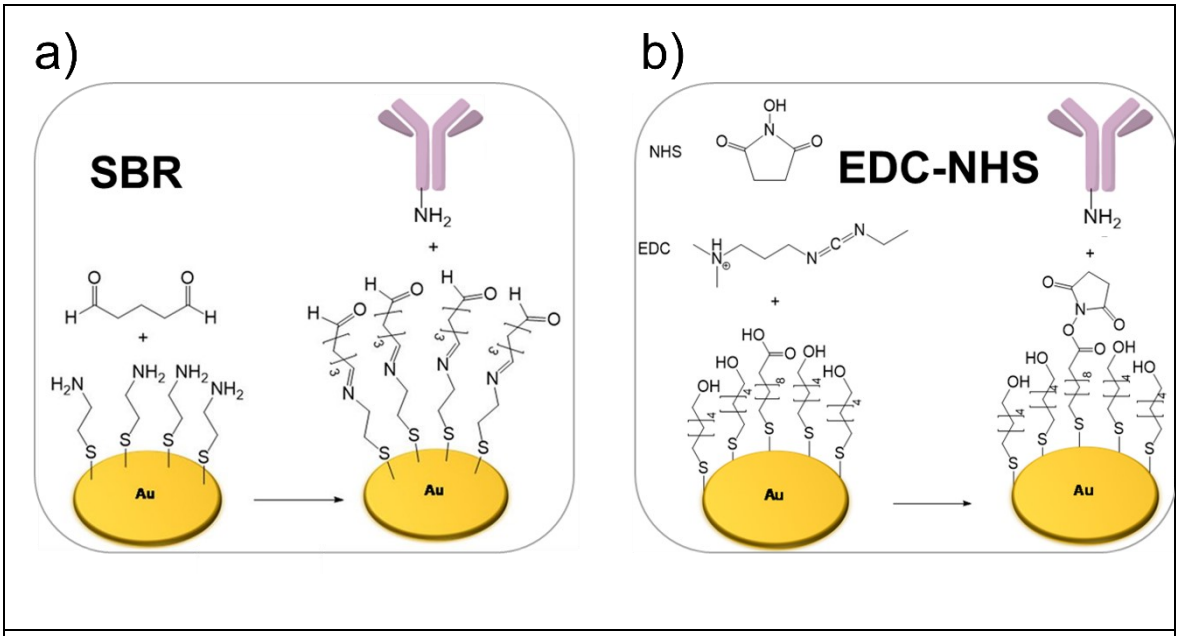

***Figure 4.4**: Schematic of the antibody immobilization strategies on the gold (Au) gate electrode. (a) The Schiff Base Reaction (SBR) protocol: a cysteamine (CYS) SAM is activated by glutaraldehyde (GA), which crosslinks the SAM's primary amines to the antibody's amine groups via imine bond formation. (b) The EDC-NHS protocol: A mixed SAM of 11-mercaptoundeanoic acid (11-MUA) and 6-mercaptohexanol (6-MH) is formed. The carboxyl groups of 11-MUA are activated by EDC and NHS to form a stable N-succinimidyl ester, which subsequently reacts with the antibody's amine groups to form a covalent amide bond.*

4.2.1 Tailoring the pH of the Schiff Base Reaction Functionalization Strategy

Glutaraldehyde (GA) is a bifunctional, highly reactive aldehydic reagent[42] used for the fixation of tissues[43] since the beginning of the 1960s. Although the widespread use of GA for enzyme immobilization[44], the chemistry of the glutaraldehyde in aqueous solution is not completely understood, since the GA molecule can exist in different monomeric, oligomeric, polymeric forms (**Figure 4.5**) according to the experimental conditions (concentrations, pH, temperature).[45]

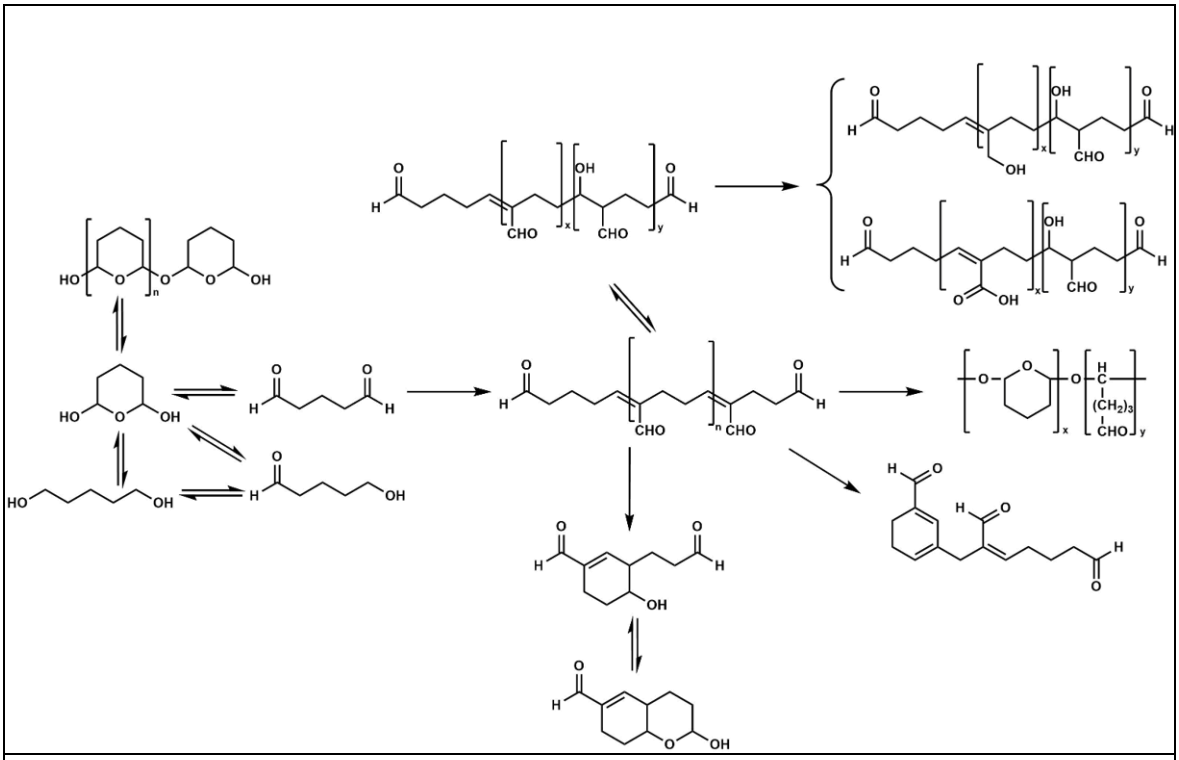

***Figure 4.5**: Summary of possible forms of GA in aqueous solution. Adapted from:*[45].

In biosensors development, GA is used as activating reagent by covalently bind -amino (or -sulphur) terminated molecules adsorbed on gold substrates to link the biorecognition element (*viz.,* antibody) via the SBR between the aldehydic groups of GA and the -NH_2 groups of the protein.[46] A few examples of SBR between the nucleophilic, amino-terminated SAM and the carbonylic groups of GA are reported for (organic) field-effect transistors (FET).[47–49] It has been demonstrated that the activation of SAM amino-terminated with GA using non-optimised functionalisation protocols leads to a decrease in the (randomly oriented) antibody anchored to the gate electrode and therefore to a decrease in the sensitivity of the device, compared to (oriented) antibody anchoring strategies that involve the use of His-tagged recombinant Protein G (PG).[49] One of the possible explanations could be ascribed to the low stability of the imine bond (Schiff base products, C=N) under acidic conditions, where it tends to break down to regenerate the aldehyde and the amine.[44,45] Since GA aqueous solutions show acid pH (pH = 3.68), we hypothesize that a systematic study about the pH of GA solution could increase the quantity of the antibody grafted onto the SAM-functionalized gold gate electrode. Under alkaline conditions, GA exist as α,β-unsaturated oligomeric forms (**Figure 4.5**), that react with primary amine (*e.g.,* cysteamine adsorbed onto gold surface) giving two products robust to acid hydrolysis. **(Figure 4.6**). The Schiff base product (**structure**

1, **Figure 4.6**) is stabilized by the resonance effect of the conjugated C-C double bond.[50] The second mechanism involves a Michael addition to the C-C double bond linkage and results in a less stable product due to loss of resonance effected the conjugated C-C double bonds.[44]

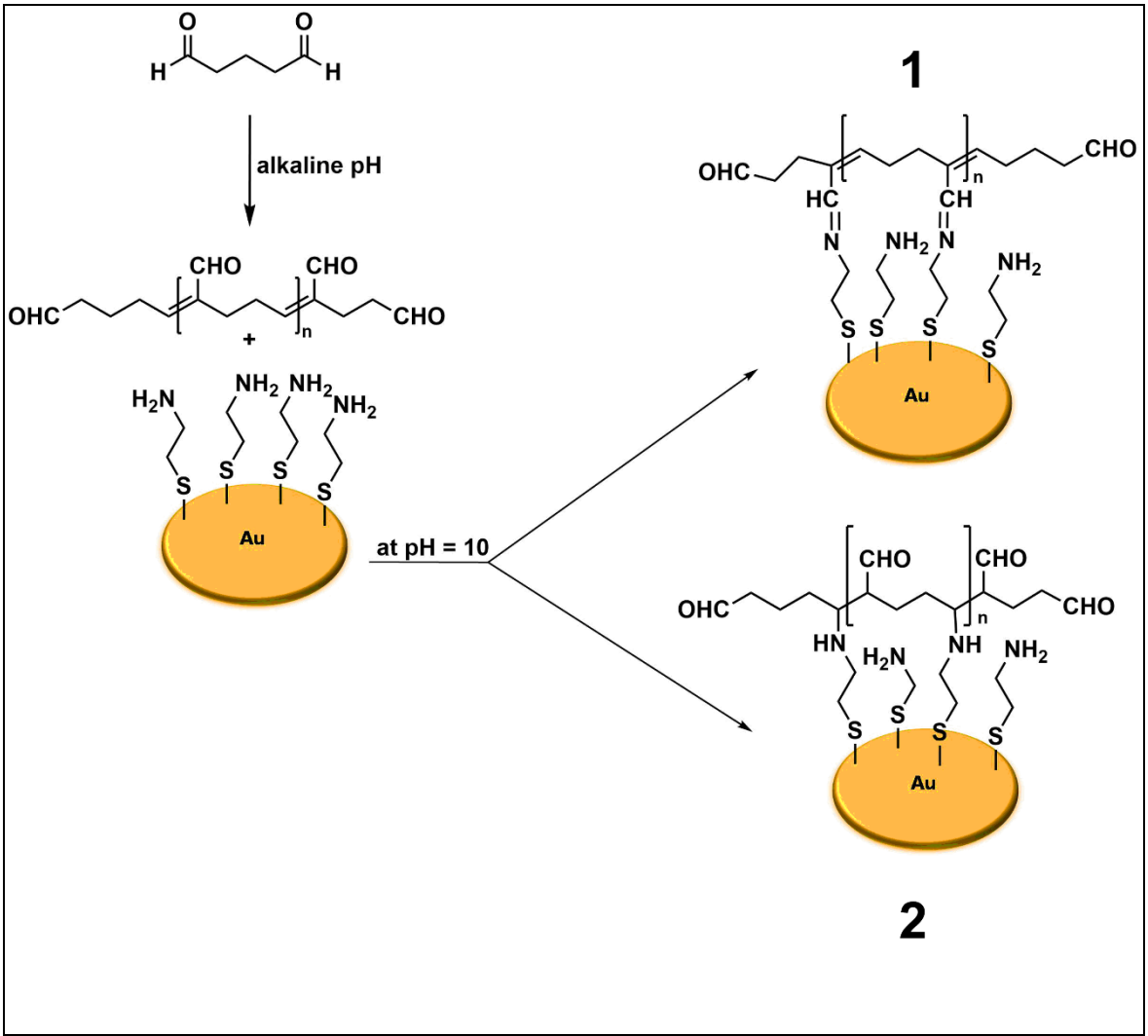

***Figure 4.6**: Proposed reaction mechanism of (polymeric) GA with primary amines (cysteamine linked to gold surface) exposing terminated amino group.*

Recently, Macchia and co-workers recently demonstrated the role of pH-conditioning of the detecting surface area to achieve ultralow detection limits.[51]

In this thesis work, the effects of the pH of the aqueous GA solution in SBR functionalization strategy is systematically investigated to improve the response against the target analyte of the EGOT-immunosensor. **Figure 4.7** reports the Cyclic Voltammetry (CV) recorded for gold electrodes functionalized with cysteamine and GA (CYS-GA) processed at different pH values (4, 6, 8, and 10), using a ferricyanide ($K_3[Fe(CN)_6]$) as redox probe.

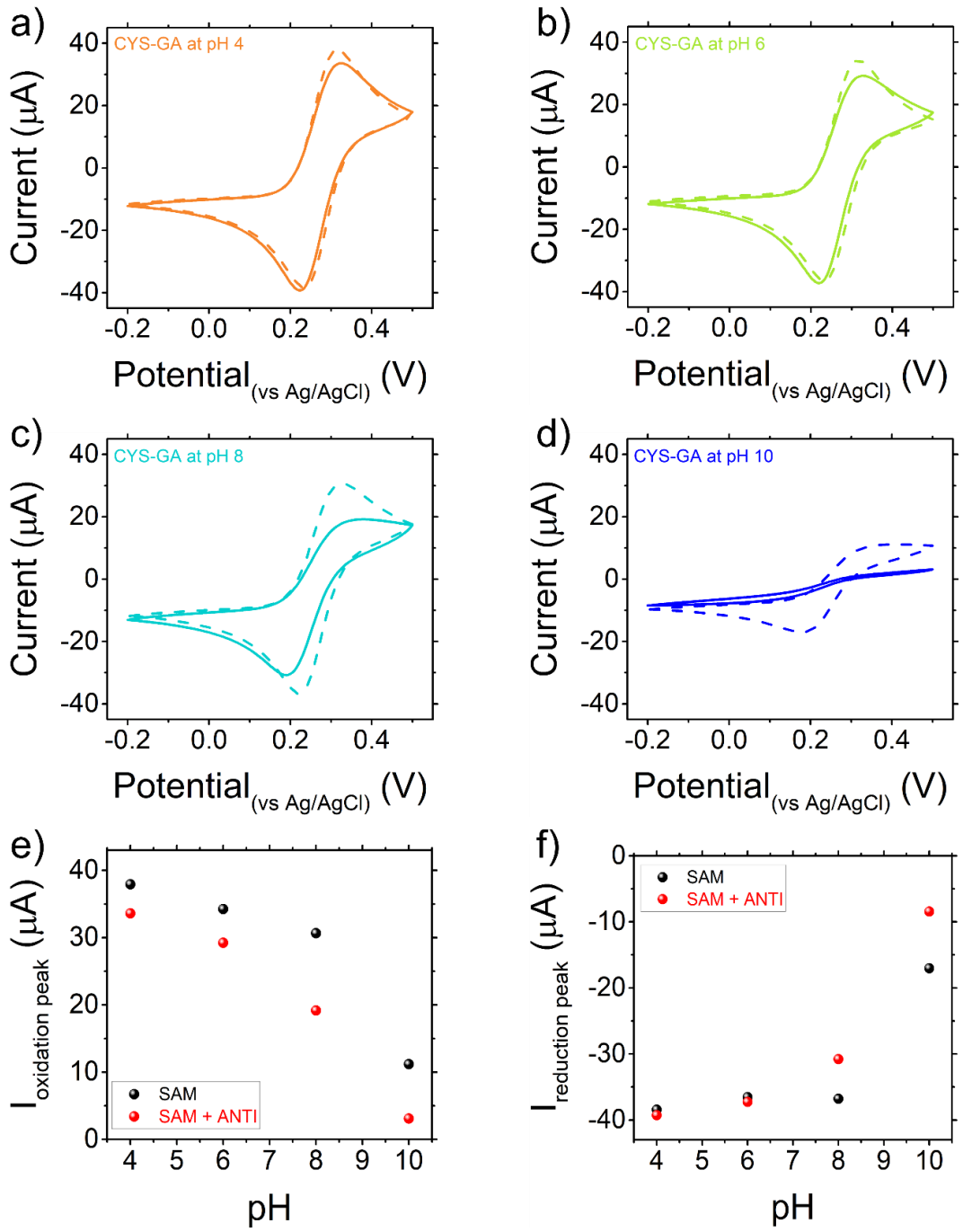

***Figure 4.7**: Electrochemical characterization. The cyclic voltammetry is plot before (dashed lines) and after (continuous line) incubation with Tryptophan antibody. The four panels highlight the effect of pH, in the glutaraldehyde step, on recorded CV current, pH 4 (orange, panel a), pH 6 (green, panel b), pH 8 (cyan, panel c), pH 10 (blue, panel d). e) Oxidation peak current for electrodes covered with CYS and GA (SAM) and after incubation with antibody (SAM+ANTI) vs pH of the GA solution. f) Reduction peak current for the same electrodes as in panel e.*

The CVs recorded after the formation of the Cysteamine-GA (CYS-GA) layer (dashed lines in **Figure 4.7a-d**, black dots in **Figure 4.7e-f**) reveal a strong pH dependence. As the pH of the GA solution increases, the oxidation and reduction peak currents decrease significantly. This is consistent with a more efficient formation of the imine bond between cysteamine and GA at neutral to alkaline pH. However, at a strongly alkaline pH of 10, GA is known to undergo aldolic condensation, forming a polymeric network. This process creates a dense, passivating layer on the electrode, which explains the very low initial faradic current observed in **Figure 4.7d**. This increased surface passivation is also confirmed by the dramatic broadening of the peak-to-peak separation, which increases from 80 mV at pH 4 to 230 mV at pH 10, indicating a significant inhibition of the electron transfer kinetics. While this polymerization at pH 10 passivates the electrode, the crucial step is the subsequent antibody immobilization. The CVs recorded after antibody incubation (solid lines in **Figure 4.7a-d**, red dots in **Figure 4.7e-f**) show a critical difference: at low pH (4 and 6), there is only a modest change in current. In contrast, at pH 8 and particularly at pH 10, there is a substantial further reduction in both oxidation and reduction peaks. This large current drop upon antibody incubation at pH 10, even from a low baseline, demonstrates a highly successful and dense immobilization of the antibody, which creates an even more insulating final layer (SAM+ANTI).

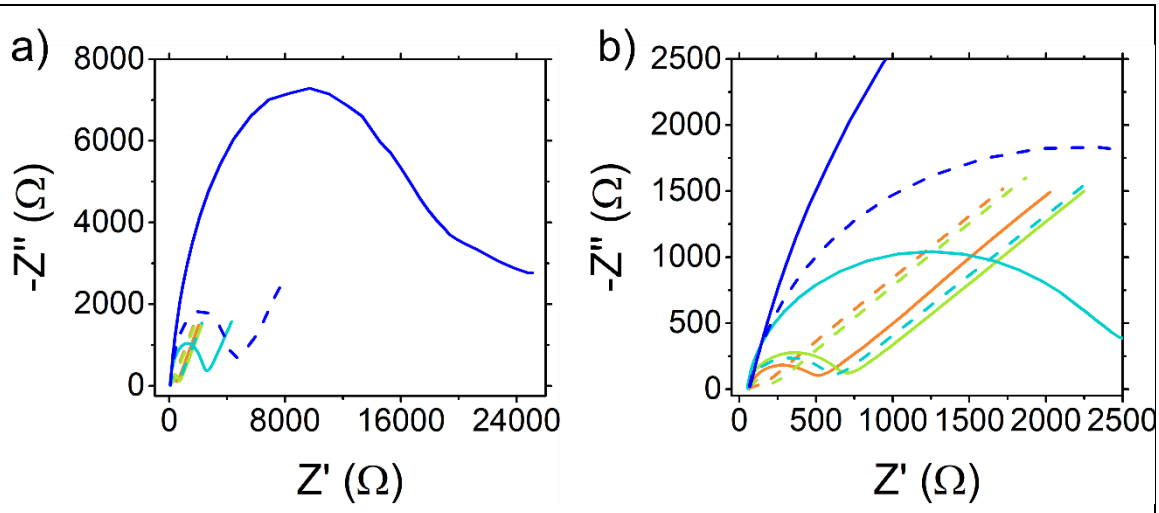

***Figure 4.8**: Electrochemical Impedance Spectroscopy (EIS) on electrodes functionalized with SBR strategy. a) complete Nyquist plot of faradic EIS, reported with the same colour code as in Figure 4.7; b) magnification of the Nyquist plot that shows the limited increase of charge-transfer resistance obtained upon antibody incubation when GA is processed at 4 < pH < 8.*

This efficient anchoring of the antibody at alkaline pH is confirmed with Electrochemical Impedance Spectroscopy (EIS). In **Figure 4.8a** the Nyquist plot of the respective faradic EIS is reported. In **Figure 4.8b** the magnification of the curves displays the increase of the charge-transfer resistance of SAM-functionalized gold electrodes at different pHs (dashed lines) after antibody incubation (solid lines). At pH 8, the real part of impedance is increased by 4 times, and almost 5 times for pH 10, reaching approximately 7.5 kΩ, confirming that the SBR functionalization at alkaline pH yields compact functionalization layers.

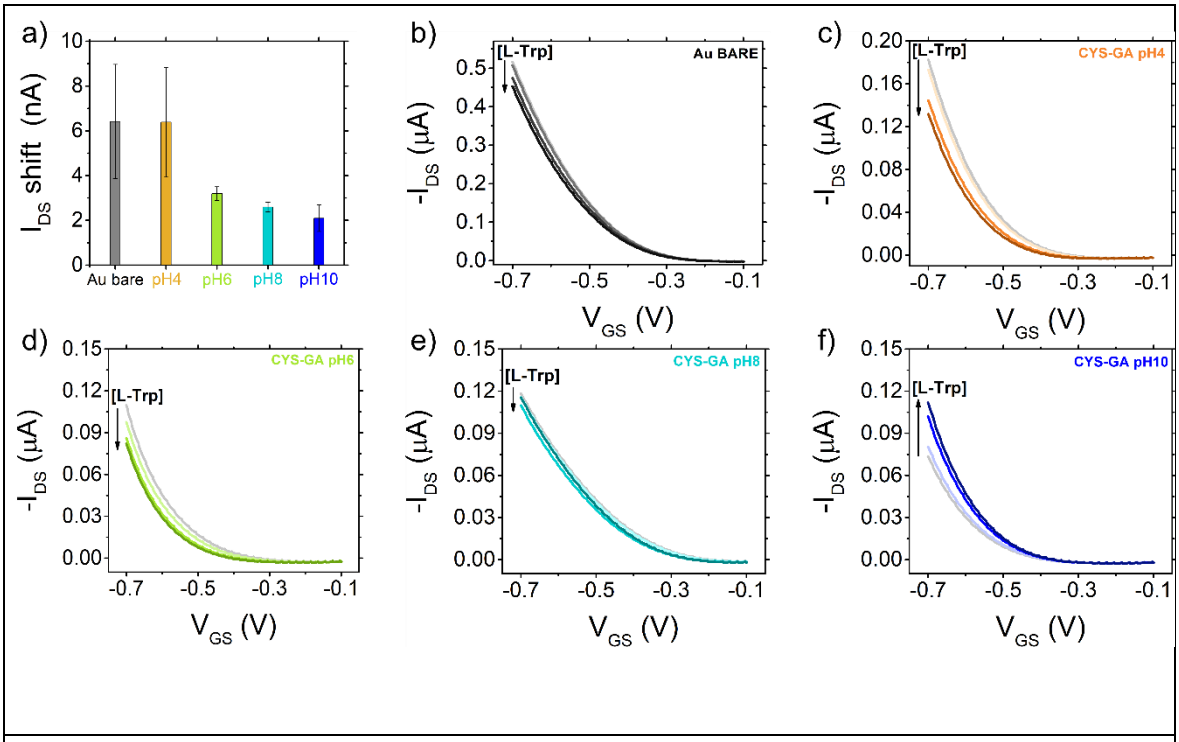

***Figure 4.9**: Integration of functionalized electrodes in EGOT architecture. a) the variability of I_{DS} @V_{GS} = -0.7V (reported as the SD of I_{DS} @V_{GS} = -0.7V) in PBS before the addition of the target analyte. Error bars are the standard deviation of three different devices. b-f) Representative transfer characteristics collected with gate electrodes functionalized at different GA pHs, in PBS (light grey) and at increasing concentration of L-Trp (11 pM, 60 pM, 425 pM).*

Following the electrochemical assessment of the coatings, the gate electrodes are assembled into the EGOT devices as described in Section 4.1.

First, the baseline stability of the devices is evaluated. This is quantified by calculating the standard deviation of the I_{DS} current (extracted at V_{GS} = -0.7 V) across the final 20 transfer characteristics recorded in PBS 1x. As indicated by the **Figure 4.9a**, gate electrodes functionalized with GA at alkaline pHs exhibit significantly higher stability (*viz.,* lower variability) compared to the bare gold and the acidic (pH 4) functionalized electrodes.

Figure 4.9(b-f) qualitatively illustrates the device response to increasing L-Trp concentrations (0 - 425 pM). It is important to note that these measurements are carried out without the ethanolamine passivation step (see Section 3.3.1 for details), performed in the optimized EGOT-immunosensor architecture. Ethanolamine is expected to prevent non-specific reaction, by quenching the SAM-unreacted sites.

Electrodes functionalized at pH < 8 (**Figure 4.9c-e**) show a distinct negative shift in the I-V transfer characteristics upon exposure to L-Trp. This trend, representing a decrease in drain-source current at a fixed gate voltage, mirrors the behaviour observed for the unfunctionalized, bare gold electrode (**Figure 4.9b**).

This evidence, combined with the electrochemical data (discussed previously) indicating low gold surface coverage for functionalizations performed at pH < 8, suggests that the I_{DS} decrease at increasing concentration of L-Trp is dominated by the non-specific adsorption of L-Trp molecules onto the exposed gold surface.

In contrast, functionalization carried out with GA in alkaline medium (pH 10) completely reverses the sensing trend (**Figure 4.9f**), causing the I_{DS} to increase with rising L-Trp concentration. This is a critical finding, as it indicates that the specific antigen-antibody binding event successfully outweighs the non-specific adsorption background signal. This conclusion is further corroborated by data presented in Section 4.2.3, where the "gold-standard" EDC-NHS coupling chemistry is used. That chemistry also yielded a positive current increase, reinforcing that an alkaline environment (pH 10) for GA solution is the optimal condition to promote efficient antibody grafting and enable specific, reliable target detection.

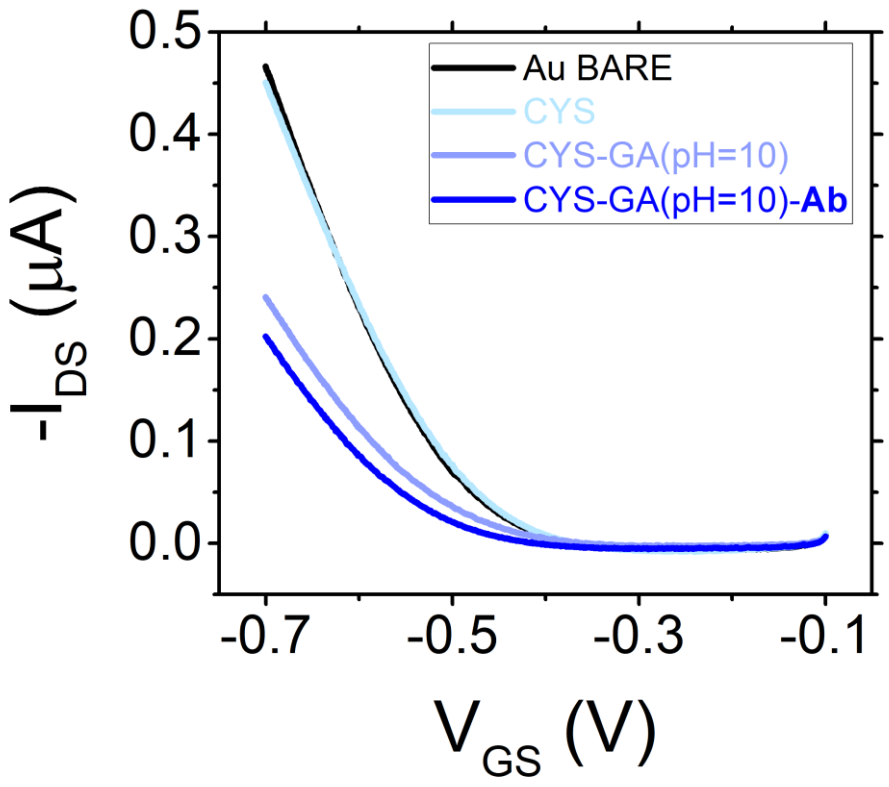

***Figure 4.10**: Representative transfer characteristics of the EGOT device (V_{DS} = -0.2 V) obtained after the consecutive steps of functionalization with SBR protocol at pH=10. It appears evident the increase of resistance after the formation of GA polymeric layer and a further decrease of maximum current is evident when the antibody is anchored and the final passivation is performed with ethanolamine.*

After identifying pH 10 as the optimal condition for the SBR functionalization strategy, our efforts are directed toward enhancing the performance of the EGOT biosensor to achieve discrimination of Tryptophan enantiomers. To mitigate non-specific interactions, gate electrodes are immersed in ethanolamine. Moreover, the gate electrode area is increased to 15.85 mm^2 (see Section 4.1). The impact of each step in the SBR functionalization protocol on EGOT transfer characteristics is shown in **Figure 4.10**. The shape and maximum current remain largely unchanged following CYS adsorption on the electrode surface, as the short chain length of CYS results in a slight increase in interface resistance between the electrode and electrolyte. However, incubation with GA solution at pH 10 leads to a more than 40% decrease in maximum I_{DS} current. Subsequent incubation with the L-Tryptophan

antibody and ethanolamine causes a further 15% reduction in maximum current compared to the GA step. Although this additional decrease may appear modest compared to impedance spectroscopy results, it reflects the intrinsic characteristics of immunoglobulins, which are typically negatively charged. This intrinsic charge partially offsets the higher impedance at the interface by accumulating negative charges near the gate, effectively increasing the gate potential beyond the applied value.

4.2.2 Electrochemical and morphological comparison between SBR and EDC-NHS strategies

Following the optimization of the SBR functionalization strategy, based on a systematic investigation of the GA solution pH, pH 10 is identified as the optimal condition. This optimized SBR protocol is then benchmarked against the EDC-NHS coupling strategy, a method widely used to graft biorecognition elements onto EGOT-based biosensors.[41,52,53]

It is important to note that both SBR and EDC-NHS are non-oriented immobilization strategies. Unlike affinity-based methods (*e.g.,* mediated by Protein G/A) that ensure an oriented conformation, these techniques create robust covalent bonds by reacting with functional groups (like primary amines) randomly distributed on the antibody's surface.[49] This comparison is therefore performed to evaluate two different, yet mechanistically similar, covalent anchoring methods for EGOTs.

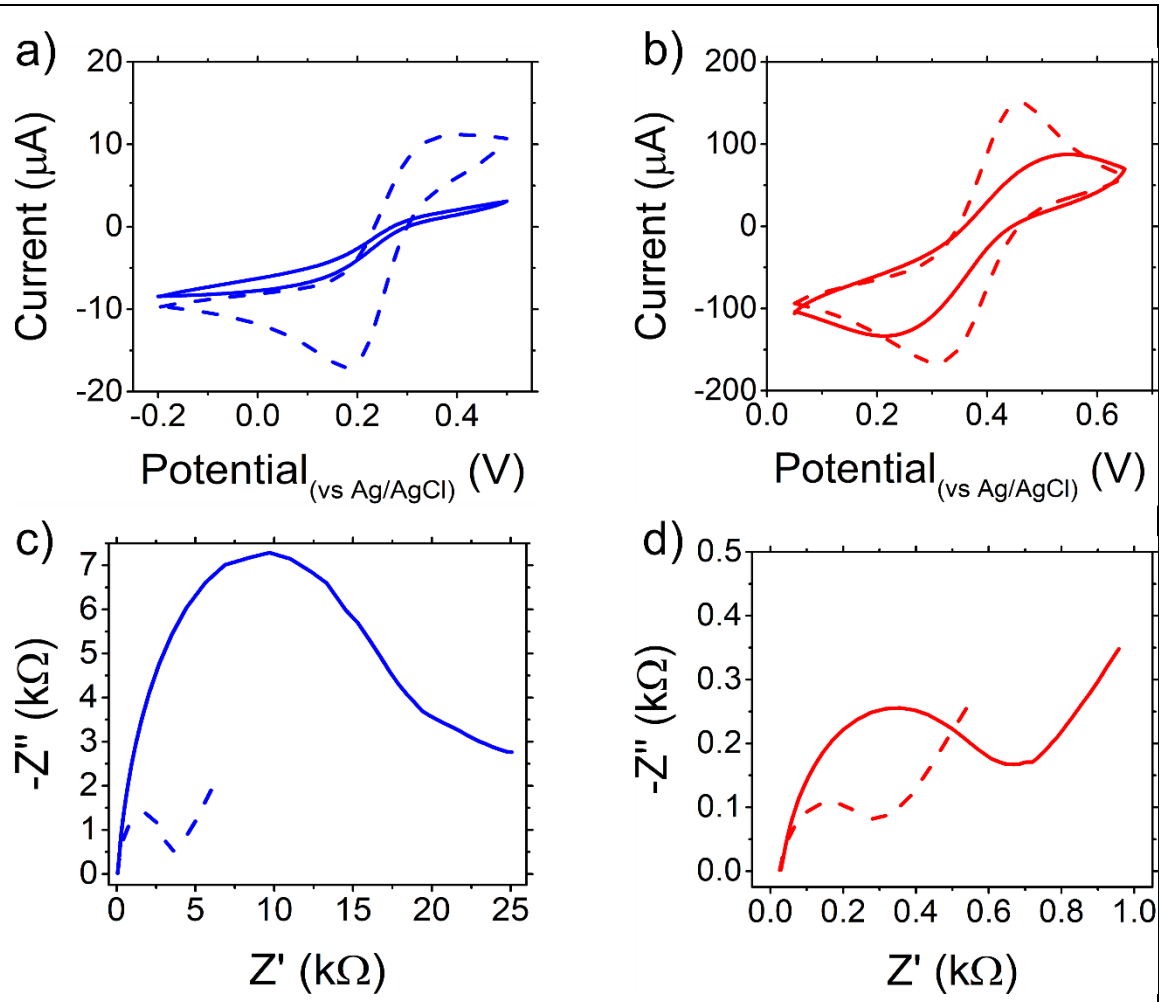

***Figure 4.11**: Electrochemical comparison between SBR (blue) and EDC-NHS (red) functionalization strategies. CV voltammograms before (dashed line) and after (continuous line) incubation with anti-L-Trp antibody for SBR (a) and EDC-NHS (b). EIS Nyquist's plots for SBR (c) and EDC-NHS (d) that evidences the increase of the impedance upon antibody binding.*

Firstly, the immobilization steps of the two functionalization strategies are assessed by CV and EIS measurements, using the $K_3[Fe(CN)_6]$ redox probe (see Section 3.5 for details). The CVs (**Figure 4.11a-b**) reveal significant differences. For the SBR strategy (**Figure 4.11a**), the initial CYS-GA layer (dashed blue line) formed with GA at pH 10 tends to polymerize, creating a passivating layer that significantly hinders electron transfer even before antibody binding. The subsequent antibody incubation (solid blue line) further reduces the peak currents.

In contrast, for the EDC-NHS strategy (**Figure 4.11b**), the initial SAM (dashed red line) shows higher peak currents (*viz.,* lower passivation) than the initial CYS-GA

layer in SBR strategy. Nonetheless, the subsequent incubation with the antibody (solid red line) causes a clear reduction in the oxidation and reduction peak currents. This indicates the successful grafting of an insulating layer of immunoglobulins onto the electrode surface for both functionalization strategies.

The Nyquist plots (**Figure 4.11c-d**) confirm this interpretation. For both strategies, incubation with the antibody (dashed lines) results in a significant increase of the charge-transfer resistance, visible as a larger semicircle diameter. This is consistent with the antibody layer further insulating the electrode, both by increasing the distance for electron transfer and by causing electrostatic repulsion between the typically negatively charged immunoglobulins and the anionic $[Fe(CN)_6)]^{3-}$.[41]

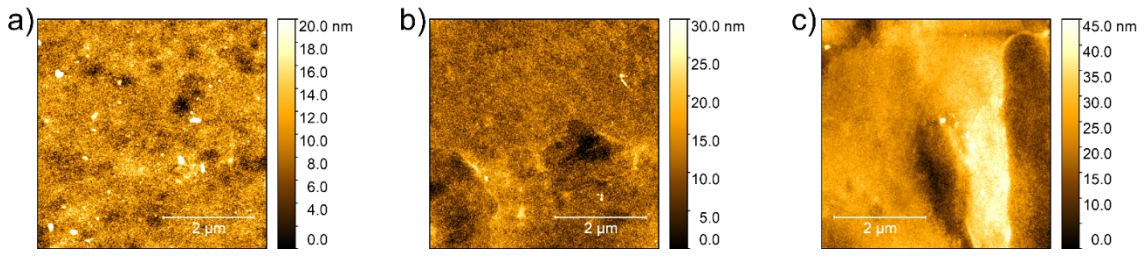

***Figure 4.12**: Topography of (functionalized) gate electrodes. Atomic Force Microscopy (AFM) images of a) bare gold electrode after cleaning procedure; b) morphology of EDC-NHS-functionalized electrode; c) morphology of electrode activated with SBR functionalization showing wavy feature.*

The morphology of the SBR and EDC-NHS functionalization strategies is compared by tapping-mode Atomic Force Microscopy (AFM), with experimental details reported in Section 3.6.

The resulting images (**Figure 4.12**) show clear differences. The chemisorbed SAM activated with EDC-NHS (**Figure 4.12b**) forms a thin film, as expected[54], and induces only a modest increase in surface roughness (3.61 nm) compared to the bare gold electrode (**Figure 4.12a**, 3.21 nm).

In contrast, the SBR activation protocol (**Figure 4.12c**) leads to the formation of a much rougher, non-uniform film (estimated roughness: 7.33 nm). This morphology is consistent with the GA forming an oligomeric, porous layer at alkaline pH. Although a complete characterization of the functionalized substrates would require complementary techniques (*e.g.,* Surface Plasmon Resonance), the AFM data

reveals that the SBR layer possesses a significantly larger topographical surface area. This plausibly provides a higher density of binding sites for antibody grafting, thereby offering a morphological interpretation for the high antibody loading previously observed in the electrochemical characterization.

4.2.3 EGOT-biosensor response with SBR and EDC-NHS functionalization strategies

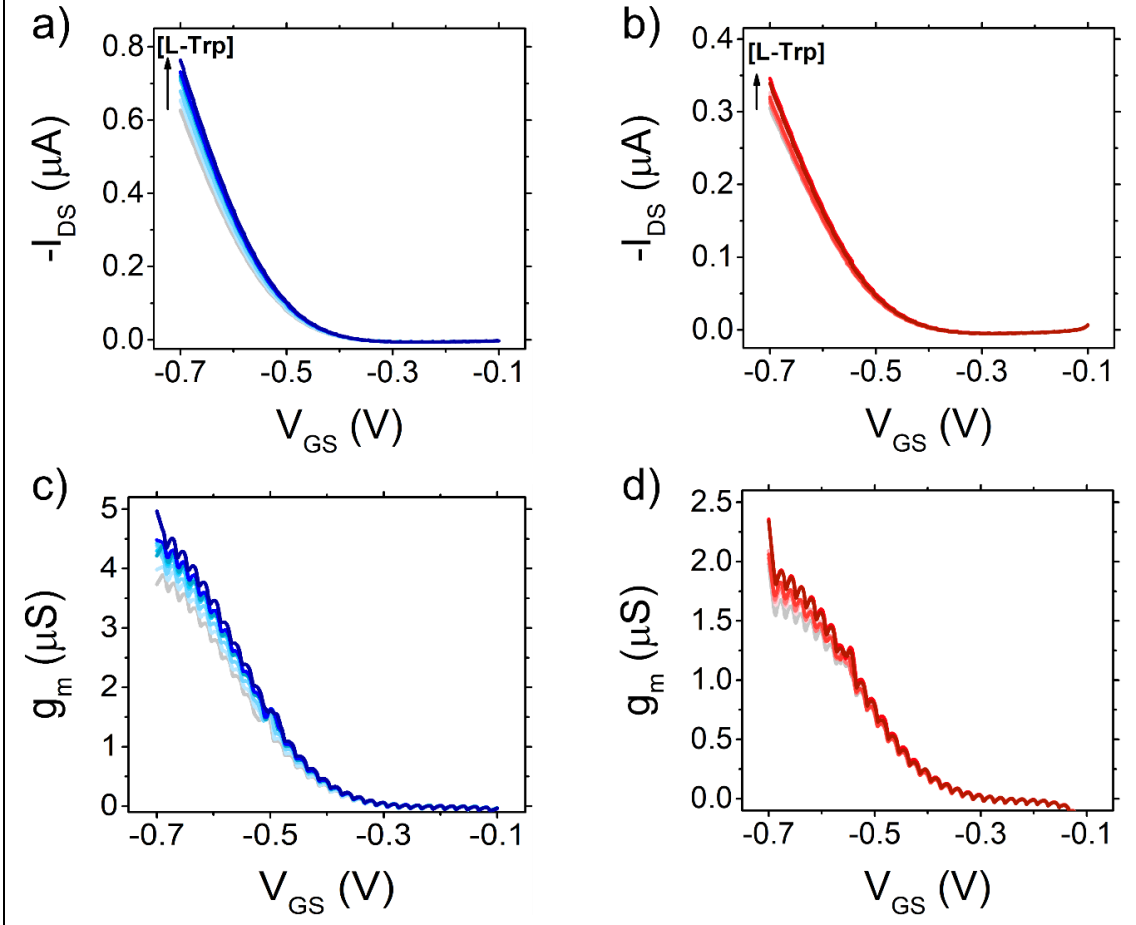

***Figure 4.13**: Electrical characterization in presence of increasing concentration of L-Trp. Representative transfer curves of EGOT device (V_{DS} = -0.2 V) with gate electrode functionalized with SBR (blue, a) and with the EDC-NHS protocol (red, b) upon interaction with L-Trp. Transconductance (viz., first derivative $\frac{dI_{DS}}{dV_{GS}}$) vs V_{GS} for SBR (blue, c) and EDC-NHS (red, d) upon increasing concentration of target analyte.*

Figure 4.13 displays the response of EGOT biosensor for SBR (blue curves, **Figure 4.13a**) and EDC-NHS (red curves, **Figure 4.13b**) strategy to the increasing

concentration [L-Trp]. The current increase for both functionalization strategies could be explained by considering that L-Trp molecules are negatively charged ($pI_{L\text{-}Trp}$ = 5.89)[55] at the experimental pH 7.4. Their binding to the functionalized electrode makes the effective gate voltage more negative and hence increases the carrier density in the p-type channel.[56,57] The magnitude of the I_{DS} shift cannot be attributed solely to the charge of the target analyte as it is clearly dependent on the functionalization strategy adopted. The functionalization procedure affects the density and binding distance of the molecular target to the antibody. For the SBR functionalized electrodes, the transfer curves shift up by approximately 20% for L-Trp concentration increasing from 1 fM up to 10 nM. Comparatively, EDC-NHS functionalized electrode the current increase is 15% lower in the same range. The increasing of the I_{DS} current upon exposure to increasing concentration of the target analyte is corroborated by the increasing of transconductance, taken as the first derivative $g_m = \left(\frac{dI_{DS}}{dV_{GS}}\right)$ of the I_{DS} current, as shown in **Figure 4.13c,d**.

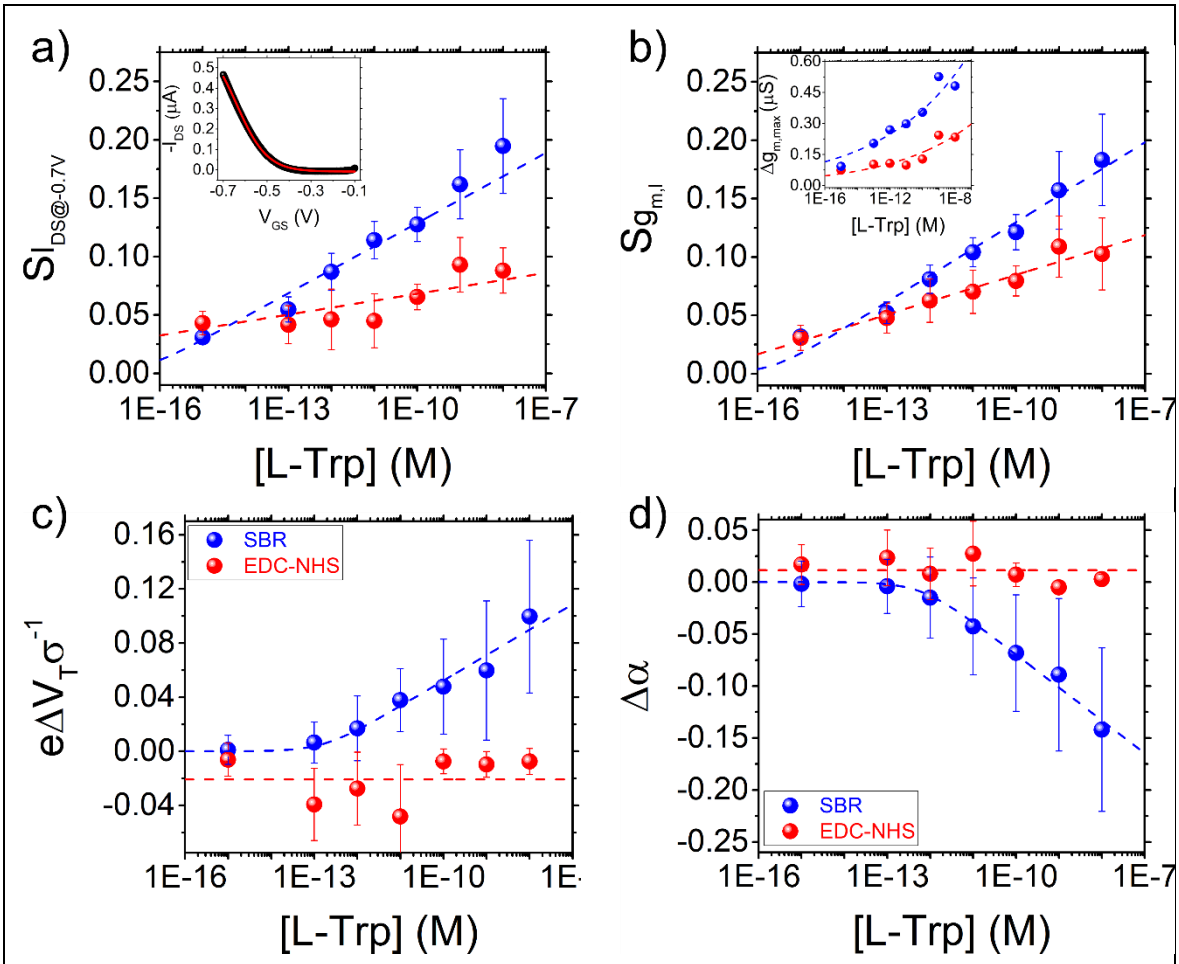

***Figure 4.14**: L-Tryptophan sensing with SBR (blue) and EDC-NHS (red). a) Semilog plot of the current signal $S_{I_{DS}}$ vs [L-Trp]. In the inset of panel a, a representative transfer curve is fitted according to Equation 4.1. b) Semilog plot of the signal $S_{g_{m,I}}$ vs [L-Trp]. In the inset of Figure 4.14b the dashed line is power law used as guide to the eye to describe $\Delta g_{m,max}$ vs [L-Trp]. c) Semilog plot of the turn-on voltage shift ΔV_T vs [L-Trp]. d) Semilog plot of the shift of the parameter α vs [L-Trp]. Dashed lines are guide-to-the-eye obtained by best fit with ULM Equation 4.2.*

To quantify the current variation of the EGOT biosensor when exposed at increasing concentration of the target analyte, a calibration dose curve is built by displaying the current signal recorded against the target concentration. In **Figure 4.14a**, the signal is defined as the normalized current variation with respect to the PBS buffer sample $S_{I_{DS}}([L-Trp]) = \langle \frac{I_{DS}([L-Trp]) - I_{DS}(0M)}{I_{DS}(0M)} \rangle$, where I_{DS}([L-Trp]) is the current recorded at a

fixed gate potential (in this case V_{GS} = -0.7 V) and I_{DS}(0 M]) is the current measured at the same gate potential in the blank sample.

To obtain a deeper understanding of the response of the EGOT immunosensor when exposed to increasing L-Trp concentration, the whole transfer curves are fitted with Equation 4.1, derived from the EGOTs unified analytical model, recently published by Zanotti *et al.*[58]:

$$I_{DS}(V_{GS};\, V_{DS}) \approx I_{DS,off}(V_{DS}) + g_{m,l} \left\{ \frac{\alpha\sigma}{e} \frac{\sinh\left(2e\frac{V_{GS}-V_T}{\sigma}\right) - \sinh\left(e\frac{V_{GS}-V_T}{\sigma}\right)}{\sinh\left(\frac{\Delta E_{gap}}{2\sigma}\right) + \alpha \cosh\left(2e\frac{V_{GS}-V_T}{\sigma}\right)} \right\} \qquad \text{(Eq. 4.1)}$$

where e is the elementary charge, V_T is the switch-on voltage, σ is the energy disorder of the density of states (DOS) of the organic semiconductor channel, its band gap ΔE_{gap} is a material property, and the parameter $\alpha = \frac{2e^2 dn_{max}}{C_{DL}\sigma}$ is the ratio between the maximum of areal charge carrier density $2edn_{max}$ in the DOS tail and the interfacial charge carrier density $C_{DL}\sigma/e$. The energy disorder σ embodies the variations of morphology of the thin films whose thickness is d. The accuracy in fitting the nonlinear variation of I_{DS} as a function of V_{GS} is shown in the inset of **Figure 4.14a**, where a transfer curve is overlaid with the best fit I_{DS} as from Eq.1.

The EGOT response is thus represented by the variation of the free parameters $g_{m,l}$, α, V_T vs [L-Trp].

Figure 4.14b shows the signal $S_{g_{m,l}}([L-Trp]) = \langle \frac{g_{m,l}([L-Trp]) - g_{m,l}(0M)}{g_{m,l}(0M)} \rangle$, defined as the relative variation of the linear transconductance $g_{m,l} = \frac{W}{L}\mu C_{DL} V_{DS}$ extracted as a best fit parameter of Equation 1. The inset of **Figure 4.14b** shows the increasing trend of the maximum transconductance, taken as the first derivative $g_{m,max} = \max\left(\frac{dI_{DS}}{dV_{GS}}\right)$ of the I_{DS} current in the transfer curves reported in **Figure 4.13**. **Figure 4.14c** displays the dimensionless shift of the turn-on voltage $e\Delta V_T([L-Trp])/\sigma = e\langle V_T([L-Trp]) - V_T(0M)\rangle/\sigma$ and in **Figure 4.14d** the dimensionless shift of $\Delta\alpha([L-Trp]) = \langle \alpha([L-Trp]) - \alpha(0M)\rangle$.

The displayed error bars are estimated as standard error of the mean (SEM), calculated according to the definition (Equation 4.2):

$$SEM = \frac{1}{\sqrt{N}} \sqrt{\left(\frac{\sum_{j=1}^{N} (x_j - \bar{X})^2}{N-1} \right)} \qquad \text{(Eq. 4.2)}$$

SEM provides a more precise and robust estimate of the deviation from the mean parameter values. For each concentration step, sample means are obtained from

modelled transfer curves, computed as the average of the last three curves for each of the four datasets analysed.[59] As displayed in **Figure 4.14**, SEM increases with signal amplitude, a characteristic feature of exponentially varying observables, consistent with the functional form of the signal in our framework.

To describe the binding process between the Tryptophan molecule with the anti L-Trp antibody, the monotonic trend of the signal $S_{g_{m,I}}$ vs the logarithm of [L-Trp] is modelled with an isotherm function. Among several isotherms assessed, the Uniform Langmuir Model (ULM, Equation 4.3)[52,56,60] yields the most accurate description of the $S_{g_{m,I}}$ vs [L-Trp] trend (R^2 COD = 0.98 for SBR (pH=10), R^2 COD = 0.97 for EDC-NHS). The ULM model accounts for a distribution of binding sites on the electrode surface, characterized by a binding energy interval $U \in [U_{min}; U_{max}]$. The distribution of binding sites energies may arise from the random orientation of antibodies, present in both SBR and EDC-NHS, or from the local inhomogeneity of the thin film, leading to a heterogeneous energy landscape across the gate electrode surface. The ULM isotherm reads:

$$S_X = \frac{S_{X,max}}{2A} \ln\left\{\frac{1+K_{avg}[L-Trp]\exp(A)}{1+K_{avg}[L-Trp]\exp(-A)}\right\} \quad \text{(Eq. 4.3)}$$

where S_{max} is the plateau reached at [L-Trp] > 10 nM; K_{avg} is the average binding constant; $A = \frac{(U_{max}-U_{min})}{2RT}$ is the rescaled energy variable describing the energy distribution of the adsorption sites; R the universal gas constant and T is the absolute temperature. Assuming that the average affinity between the target analyte and the antibody does not depend on the functionalization strategy, a best fit value K_{avg} = 1.4 (± 1.1)E9 for both functionalization strategies is extracted as a global parameter. S_{max} describes the behaviour of $S_{g_{m,I}}$ at concentrations above 10 nM and is larger for SBR S_{max} = 0.30 (± 0.01), than that of EDC-NHS S_{max} = 0.20 (± 0.01). The differences between the two functionalization strategies are explained by the distribution of the binding energies: for SBR A = 15.0 (± 0.9), while for EDC-NHS A = 19.1(± 1.5).

The data showed in **Figure 4.14c** and **4.14d** are fitted using the same functional in Equation 4.3. In **Figure 4.14c** the trend of the turn-on voltage shift ΔV_T vs [L-Trp] reveals the greater sensitivity of the SBR functionalization with respect to the EDC-NHS functionalization, which remains nearly constant vs [L-Trp] for this parameter. In **Figure 4.14d**, the response Δα vs [L-Trp] evidences the change of capacitance of the gate upon binding of the Trp to the antibody. The EDC-NHS functionalized gate exhibits a weak variation of Δα with increasing L-Trp concentration, whereas

a marked variation is observed with the SBR functionalization. The α parameter being the ratio of two areal density of carriers, is subjected to sizable changes from one gate electrode to another. The change of the gate areal capacitance C_G may ultimately be related to the quantity of antibody grafted to the surface, which is supposed to be higher for the SBR functionalization with respect to EDC-NHS, as corroborated by EIS (**Figure 4.8**).

At this point, it is important to highlight that the response of the EGOT device - in terms of turn-on voltage shift and Δα, upon exposure of the gate electrode to increasing concentrations of L-Trp, depends on the functionalization strategy. In particular, with the SBR functionalization strategy, four distinct dose-response curves can be exploited (as from **Figure 4.14a-d**) for the quantification of L-Trp, whereas for EDC-NHS the only significant variations are observed in the current and transconductance signals (**Figure 4.14a,b**). This differing behaviour can be attributed to variations in the surface morphology of the functionalized gold electrodes prior to antibody anchoring, as discussed in Section 4.2.2.

To verify whether the measured signal in the SBR functionalization strategy is indeed originated from the specific binding of L-Tryptophan to the monoclonal antibody on the gate electrode, two control experiments are conducted: the first in the absence of antibody and the second by keeping the functionalization protocol unaltered but exposing the gate to a different amino acid, (*viz.,* L-arginine). In absence of biorecognition unit, the device shows only a modest, negative response when incubated with L-Trp (grey bars in **Figure 4.15a**), with respect to positive signal reported for the specific anti L-Trp antibody binding (blue bars). When the antibody-functionalized gate electrode is exposed to L-Arginine, the immunosensor provides an almost negligible response ($S < 0.05$) also in presence of [L-Arg] higher than 1 nM (**Figure 4.15b**)

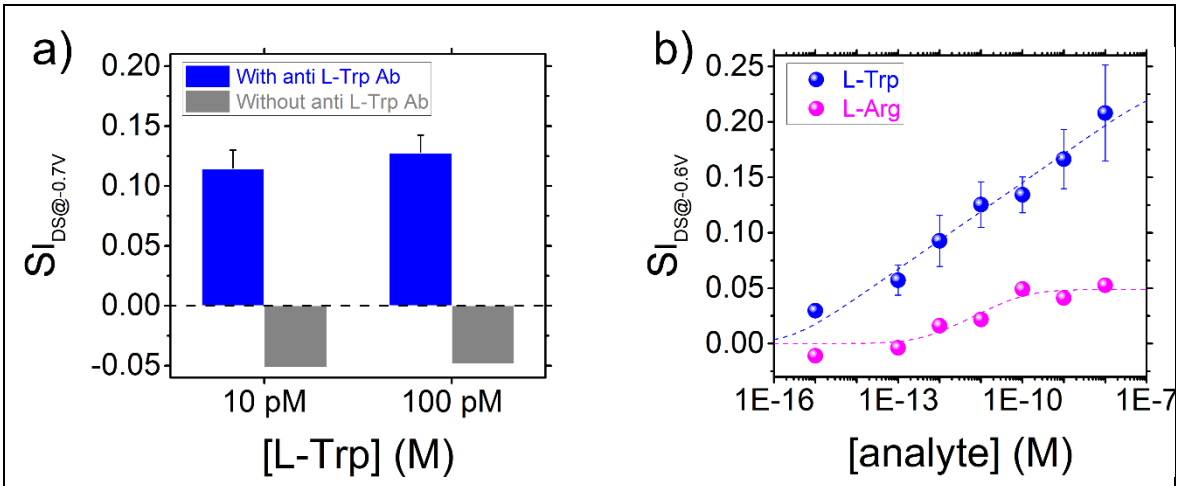

***Figure 4.15**: Control experiments. a) Signal calculated on current in control experiments performed with gate electrodes functionalized with or and without the monoclonal anti-L-Trp antibody. b) Device response when the functionalized gate electrodes functionalized with the complete SBR protocol is exposed to L-Arginine (magenta dots). In the semilog plot of the signal vs [analyte], the experimental data are fitted with ULM Equation 4.3 as guide-to-the-eye.*

Building upon the comparison of the two functionalization strategies, which demonstrated that SBR anchoring protocol fully leverages the multiparametric response of EGOT devices, the following paragraph (Section 4.3) assesses the EGOT-immunosensor's chiral selectivity towards the two Tryptophan enantiomers.

4.3 Enantiodiscrimination using Multivariate analysis

The response of the EGOT immunosensor functionalized with the anti-L-Trp antibody using SBR functionalization strategy is tested to achieve the enantiodscrimination between L-Trp and D-Trp.

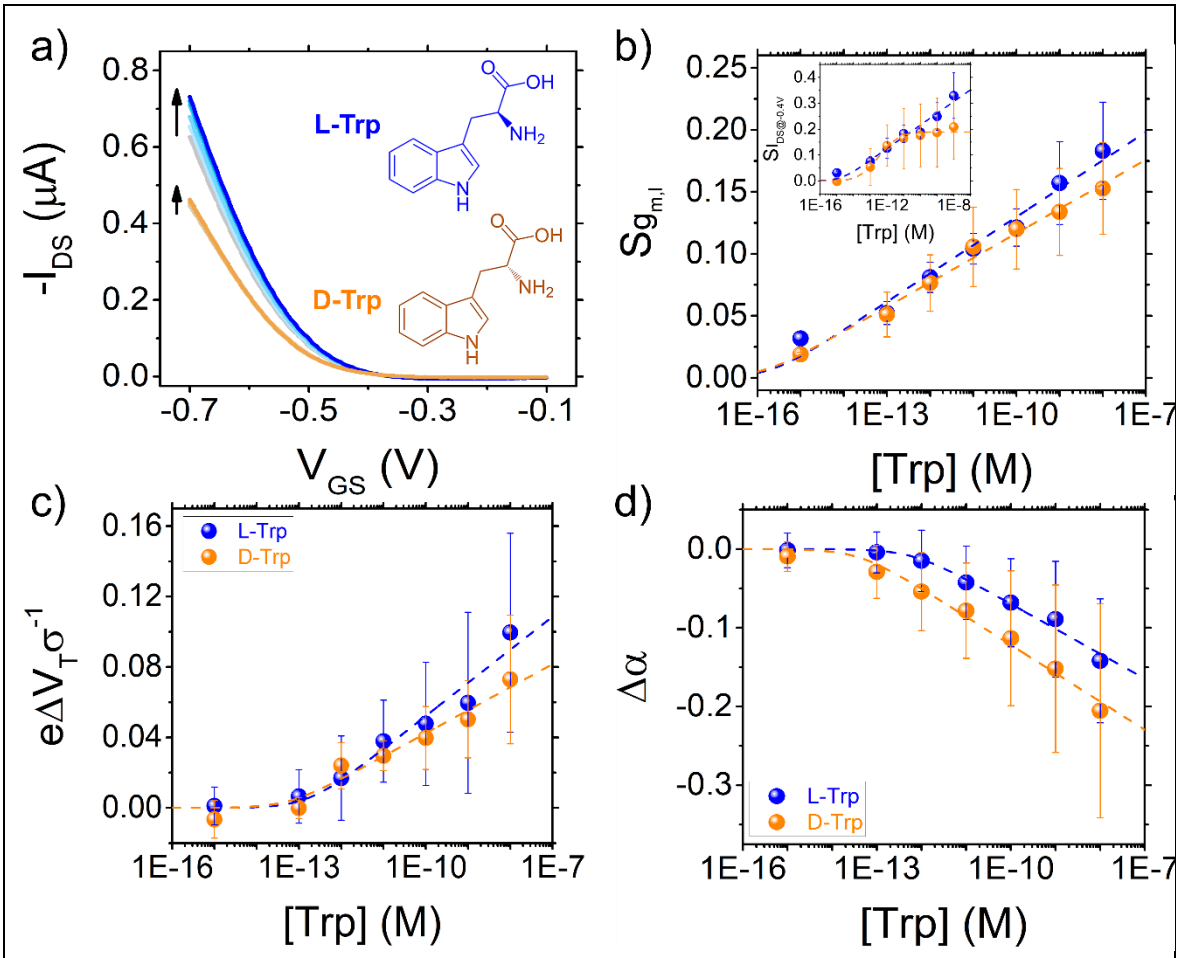

***Figure 4.16**: Analysis of the response of SBR functionalized EGOT upon exposure to L-Trp (blue markers) and D-Trp (orange markers) solutions. a) Representative transfer curves of EGOT device (V_{DS} = -0.2 V) with the gate electrode functionalized with optimum SBR protocol. The inset shows the chemical structure of L and D Tryptophan enantiomers. b) Semilog plot of the signal $Sg_{m,I}$ vs [Trp]. The inset shows the semilog of the current signal at V_{GS} -0.4 V vs [Trp]. c) Semilog plot of the renormalized turn-on voltage shift ΔV_T vs [Trp]. d) Semilog plot of the shift of the parameter Δα vs [Trp]. Dashed lines are guide-to-the-eyes obtained by best fit with ULM Equation 4.3.*

The EGOT response at different concentrations of L-Trp and D-Trp is displayed in **Figure 4.16**. The dashed lines, serving as guide to the eyes, are fitted according to Eq.3. **Figure 4.16a** presents the transfer curves I_{DS} vs V_{GS} at increasing concentrations of the two enantiomeric forms, whose chemical structures are reported in the inset of **Figure 4.16a**. The curves of the D-Trp (orange lines) are always below the ones for L-Trp (blue), however the distance between the two

bundles of curves is device-dependent. **Figure 4.16b** shows $Sg_{m,I}$ (Trp) at increasing concentration of the target analyte. The dose curve of L-Trp is about 10% higher than that of D-Trp at all concentrations, with the same ambiguity generated by the error bars overlapping the two curves. In the inset of **Figure 4.16b** it is reported the current signal $S_{I_{DS}}([Trp]) = \langle \frac{I_{DS}([Trp]) - I_{DS}(0\ M)}{I_{DS}(0\ M)} \rangle$ estimated at V_{GS} = -0.4 V. The trends of the two dose curves are comparable, with SI_{DS} (L-Trp) > SI_{DS} (D-Trp) although the error bars prevent the unambiguous direct assignment of a signal to one of the enantiomers below 100 pM. Dose curves are calculated also for the shifts of turn-on voltage ΔV_T in **Figure 4.16c** and Δα(Trp) in **Figure 4.16d**. Among the parameters, Δα(Trp) appears to be the parameter allowing for better discrimination between the two chiral forms, although the error bars introduce a substantial uncertainty in the discrimination of the two enantiomers. To assess the possibility to perform enantiodiscrimination using a standard univariate analysis, a one-way ANOVA test is carried out on each parameter reported in **Figure 4.16** (*viz.,* SI_{DS}, $Sg_{m,I}$, $\frac{e\Delta V_T}{\sigma}$, Δα) for each concentration tested. This individual analysis yielded *p*-values greater than 0.05 for each parameter at all concentrations, thus supporting the statement that univariate analysis of the parameters does not enable a significant differentiation between the response signals of L-Trp and D-Trp within the concentration range explored (from 1 fM to 10 nM).

This limitation may be attributed to the partial affinity of D-Trp towards the anti-L-Trp antibody. By assuming that the surface binding obeys to thermodynamic equilibrium, parameters extracted from EGOT transfer curves have been demonstrated to provide a good description of antigen-antibody affinity constant.[52,56,61] **Table 4.1** reports the estimated value of the affinity constant (K_{avg}), extracted from the ULM fit for the two enantiomeric forms for each parameter reported in **Figure 4.16**.

***Table 4.1**: parameters extracted by fitting the dose response of different parameters (SI_{DS}, $Sg_{m,I}$, ΔV_T, Δα) with Universal Langmuir Model (ULM).*

	$SI_{DS\ @\ -0.7V}$		$Sg_{m,I}$		$e\Delta V_T\sigma^{-1}$		Δα	
	L-Trp	D-Trp	L-Trp	D-Trp	L-Trp	D-Trp	L-Trp	D-Trp
S_{max}	0.28 ± 0	0.28 ± 0	0.3 ± 0	0.3 ± 0	-0.15 ± 0	-0.15 ± 0	-0.40 ± 0	-0.40 ± 0
A	13.4 ± 0.8	15.9 ± 1.1	15.0 ± 0.6	17.3 ± 1.1	9.0 ± 1.0	13.0 ± 1.8	14.6 ± 1.5	12.8 ± 0.8
K_{avg}	(7.1 ± 2.3)E9	(7.3 ± 3.5)E8	(1.4 ± 1.1)E9	(2.3 ± 1.1)E8	(7.2 ± 3.2)E8	(4.0 ± 3.8)E7	(7.5 ± 6.8)E5	(6.5 ± 2.6)E7
R^2	0.99	0.99	0.98	0.99	0.97	0.97	0.99	0.99

The K_{avg} value extracted from $S_{gm,I}$ for the binding of L-Trp with the antibody is consistent with the affinity binding constant (K_A (L-Trp)= (3.9 ± 0.6)E8) calculated from the ELISA test performed using the same mouse monoclonal anti L-Trp antibody employed in the EGOT immunosensor (**Figure 4.17a**). Conversely, the K_A extracted from the ELISA test for D-Trp (4.1 ± 2.1)E6 is lower than the K_{avg} estimated from $S_{gm,I}$ dose curve for D-Trp (**Table 4.1**). Such a difference may be explained by the derivatization process involving bovine proteins, which is applied to the Trp enantiomers prior to the competitive ELISA assay. Furthermore, the K_A(D-Trp) is lower than K_A(L-Trp) but clearly not zero, indicating a weaker, yet still detectable, affinity of D-Trp for the anti-L-Trp antibody. This partial (non-zero) affinity of D-Trp is also confirmed using an ELISA kit developed to quantify Trp in real matrices and using a polyclonal rabbit anti-L-Trp antibody, as shown in **Figure 4.17b**.

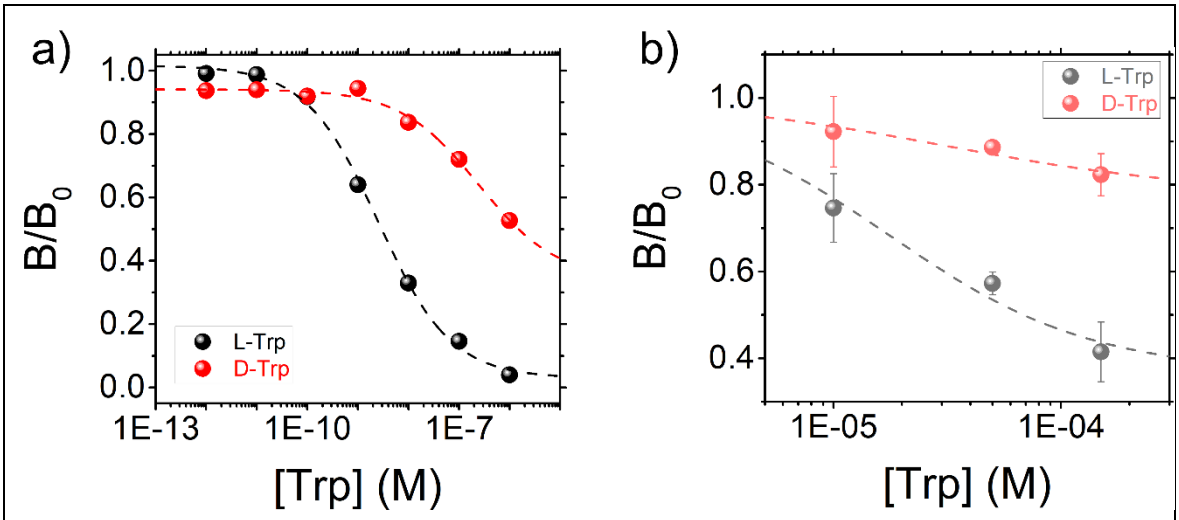

***Figure 4.17**: ELISA assays. a) Normalized results obtained from the ELISA test for L-Trp (black marker) and D-Trp (red marker), performed using the mouse monoclonal anti-L-Trp antibody (the same used in the EGOT immunosensor). The sensitivity range is between 1 pM and 1 μM. Dashed lines represent the best-fit curves obtained using the following expression:* $\frac{B}{B_0} = START + (END - START)\left(1 - \frac{{K_A}^n[Trp]^n}{1+{K_A}^n[Trp]^n}\right)$. *b) Normalized results obtained from the ELISA test using the rabbit polyclonal anti-L-Trp antibody for L-Trp (grey marker) and D-Trp (light red marker), within the sensitivity range declared by the manufacturer (from 10 μM to 1 mM).*

To identify an optimum criterion that would allow us to unambiguously discriminate L-Trp from D-Trp at low concentrations, all the renormalized parameters extracted from transfer curves are combined into Principal Component Analysis (PCA), including the data sets for both L-Trp (blue) and D-Trp (orange) (**Figure 4.18**). PCA, a bilinear decomposition/projection technique able to condense large amounts of data into few parameters, is successfully exploited for multivariate analysis in biosensing.[56,62–66] Further details are reported in Section 3.7.

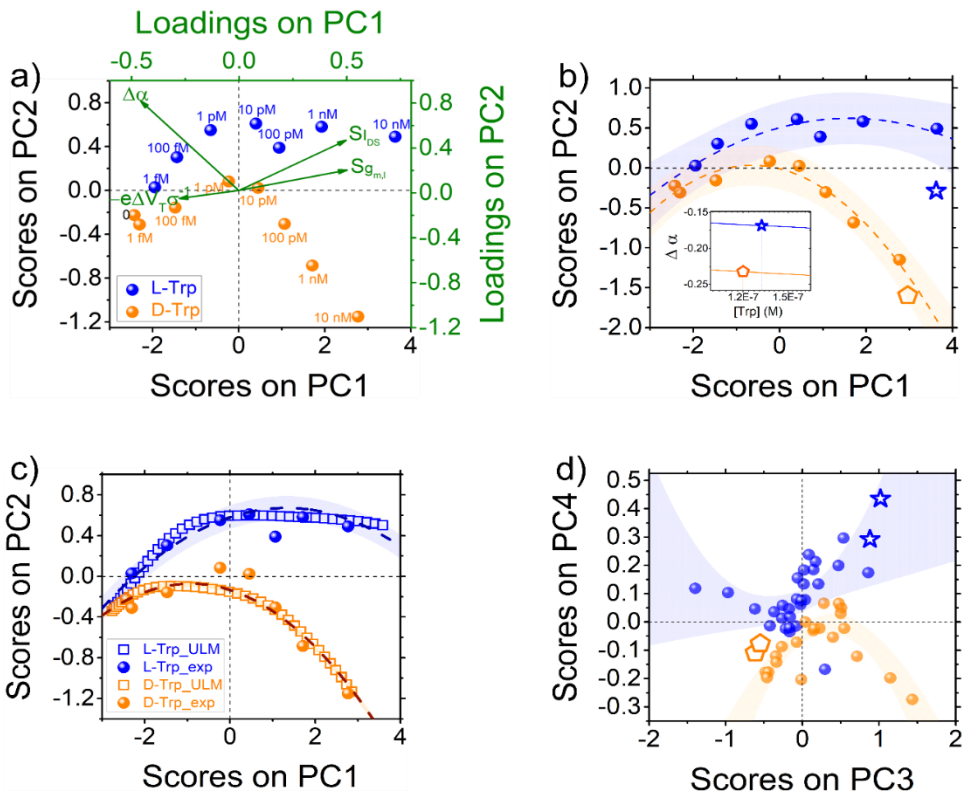

***Figure 4.18**: PCA analysis EGOT immunosensor. (a) Scores (black axes) and loadings (green axes) biplot obtained from the PCA analysis from SBR functionalized EGOTs for L-Trp (orange markers) and D-Trp (blue markers). (b) Same data of Figure 4.18a with their respective parabolic fit (continuous lines) and their prediction ranges at 90% level (shadowed areas). Two unknown concentration samples (star and pentagon) assigned to L or D clusters in the PC biplot and later correlated to the points on the dose curve Δα vs [Trp] (inset) yielding their concentration. (c) PCA score plot computed by combining all points of the best fit curves of the four variables shown in Figure 4.16 (empty markers, ULM for the dose curves) superimposed to the experimental ones (filled markers, exp). Parabolic fit is plotted as guide for the eyes. (d) The score plot of PC3 versus PC4 obtained from PCA analysis carried out on the entire dataset for L-Trp (blue markers) and D-Trp (orange markers). The clusterization of the two enantiomeric forms is highlighted by the parabolic fit (reported with 95% confidence bands, shadowed areas) included as a guide for the eyes. The EGOT-PCA model si validated with four independent experimental points.*

Figure 4.18a displays the biplot (*viz.,* score and loading) of PCA obtained from SBR data set by using as input variables the three renormalized model parameters, displayed in **Figure 4.16b-d**, and the current signal $S_{I_{DS}}$ at V_{GS} = -0.4 V (in the subthreshold regime). The score plot, black axes, of PC1 and PC2 (which accounts for 98.5% of variance) yields a net separation of the experimental points all concentrations, with the L-Trp data but the one at zero concentrations in the positive PC2 quadrants (with the exception of [L-Trp] = 0 M), whereas all the D-Trp data lie in the negative quadrants (apart from the point at [D-Trp] = 1 pM, which nevertheless lies close to the zero line). Hence, a first criterium to account for the chirality sign at glance is to look at the resulting sign of the PC2. The identification of the enantiomeric form is unambiguous at concentrations higher than 10 pM: L-Trp exhibits positive PC1 and PC2 scores, while D-Trp exhibits positive PC1 and negative PC2 scores. The loading plot (green axes) displays the variables contributing to the PCs as vectors (green dashed arrows). The variables $S_{I_{DS}}$ and $S_{g_{m,I}}$ appear strongly correlated, within L-Trp samples at concentration higher than 1 pM. In contrast, Δα is negatively correlated with D-Trp samples, consistently with the observation that D-Trp samples exhibit more negative Δα values. The parameter $-\frac{e\Delta V_T}{\sigma}$ is inversely correlated with [L-Trp] > 1 pM suggesting a positive shift in the turn-on voltage observed for L-Trp binding. This is consistent with the increase in I_{DS} current observed in the transfer characteristics upon exposure to Trp (as evident in **Figures 4.16a**).

To establish what is the minimum significant concentration (alike the LOD of a sensor) where the two enantiomers can be distinguished, the rescaled experimental data are categorised based on either the confidence or the prediction intervals. In **Figure 4.18b**, the experimental score plot points are fitted with a parabola (dashed line), which is superimposed with the 90% prediction interval (shaded band). As a result, the overlap of the prediction interval for L- a D- disappears at concentrations larger than 10 pM. Taking the same 90% level for the confidence interval, in alternative to prediction, the shadowed bands are separated already at 1 pM level. At this point, it is possible to infer that the LOD extracted with our approach for the enantiodiscrimination of L- and D-Trp with EGOT is on the level of a few pM. These unprecedented results should be compared to the values reported earlier, where chiral discrimination levels are on the order of hundreds of μM when a chiral

recognition group is assembled at the organic semiconductor channel[67] and 200 pM when the gate electrode is functionalized with the odorant binding protein.[68]

The outcome is that PCA alone can be effectively used to assign with low level of uncertainty the chirality of the enantiomer solution probed with the EGOT. It is worth nothing that the combination between the PCA jointly with the dose curves of the renormalized parameters can be effectively used to assign both the chirality and the concentration of blind samples. **Figure 4.18b** projects the PC1 and PC2 scores obtained by combining the parameters ($S_{I_{DS}}$ at V_{GS} = -0.4 V, $S_{g_{m,I}}$, ΔV_T, $\Delta\alpha$) extracted from the transfer curves of two blind samples, on the PCA loadings reported in **Figure 4.18a**. The orange pentagon allows us to assign with no ambiguity the chirality to D-Trp, as it falls into the range of prediction above 10 nM concentration. The blue star has an almost zero PC2 value and a strongly positive PC1 value which make the probability of the blind sample to belong to L-Trp more likely. The corresponding concentration can be extracted from the dose curves. The inset of **Figure 4.18b** shows where these points are placed in the dose curve of $\Delta\alpha$ as from **Figure 4.16d**. For the orange pentagon we find a concentration [D-Trp] = 120 nM, and for the blue star a concentration [L-Trp] = 130 nM, to be compared to nominal concentrations of the blind samples of 100 nM each.

To lower the level of discrimination of the two enantiomers, the whole calibration curves on the four characteristic variables in **Figure 4.16**, instead of the experimental data points, are used as input for PCA. In this alternative approach, a much larger dataset obtained by combining 1000 points of each best fit dose curve vs concentration. This represents a predictive estimate of the PCs from the maximum likelihood data derived from the experimental data. The result of this novel PCA approach is shown in **Figure 4.18c**, where the score curves (continuous lines) are displayed: L-Trp points (but the one at zero concentration) are all in positive PC2 quadrants, whereas the ones for D-Trp are all negative. The prediction ranges at 95% confidence (shadowed bands) are extremely narrow, and they do not overlap as concentration reaches values as low as 100 fM. Hence, this “preprocessing” based on non-linear regression of concentration dependent parameters from experimental data pushes further down the level of discrimination to sub-pM level , *viz.,* by one-two orders of magnitude with respect to the standard PCA in **Figure 4.18b**.

The novel EGOT-PCA method optimized for SBR functionalization strategy identifies distinct clusters for each enantiomer. To assess the robustness of the approach,

PCA is applied to the entire dataset comprising both L-Trp and D-Trp samples. In this case the clustering on first two principal components is smeared and of no straightforward assignment. **Figure 4.18d** shows the PC3-PC4 scores effectively separate the two chiral Trp forms. This demonstrates that the integration of multiple parameters can significantly enhance the analytical performance of the EGOT-based biosensor even at the level of single measurements. The proposed EGOT-PCA model is validated using four independent experimental points within a concentration range from 1 pM to 1 nM. As shown in **Figure 4.18d**, the two validation points for L-Trp (blue stars) exhibit positive PC4 values, whereas the D-Trp validation points (orange pentagon) are projected onto negative PC4 values.

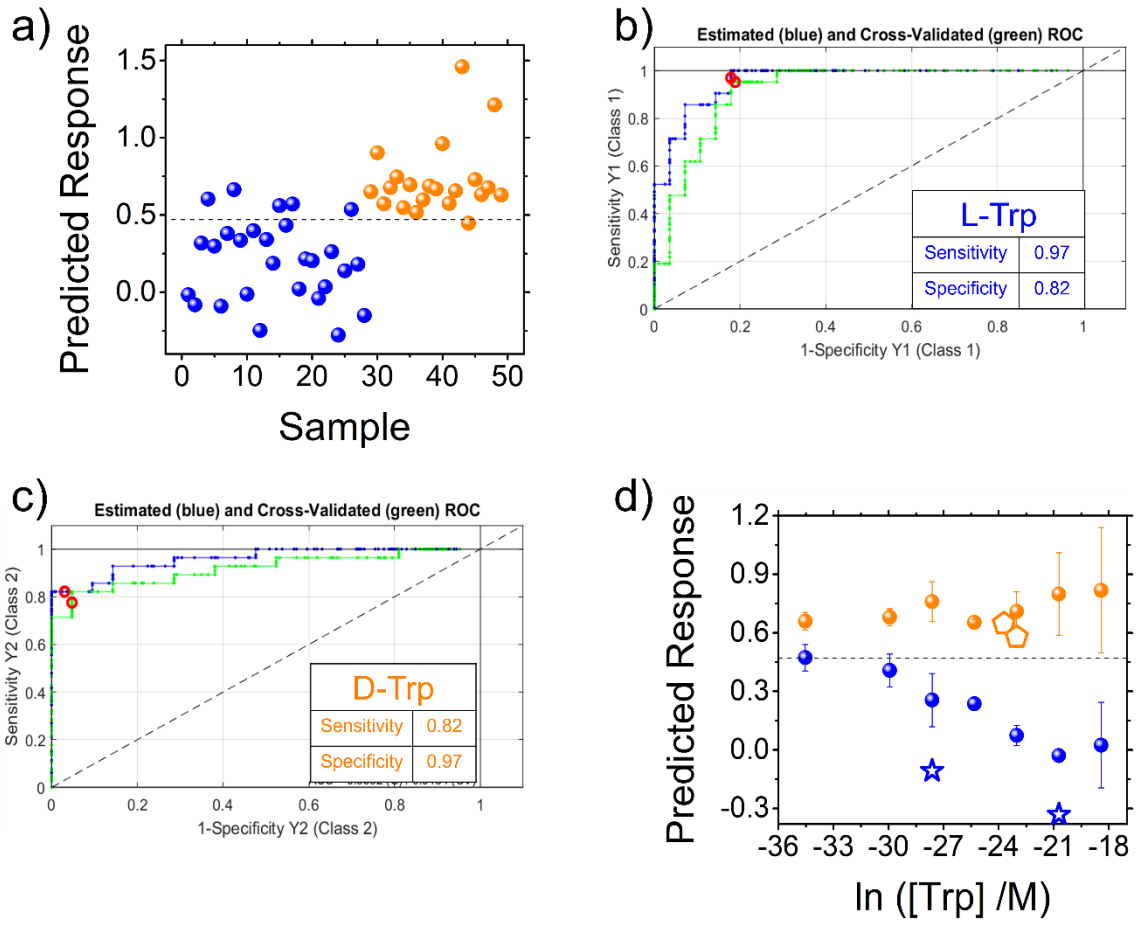

***Figure 4.19**: Validation of EGOT-chemometric model through Partial Least Square-Discriminant Analysis (PLS-DA). a) Illustration of PLS-DA classification model based on predicted response calculated for L-Trp (blue markers) and D-Trp (orange markers) at all concentrations. The black dashed line represents the calculated classification threshold (y=0.47): samples falling above the line are assigned to D-Trp, while samples falling below are assigned to L-Trp. b-c) Receiver Operating Characteristic (ROC) curves for PLS-DA model for L-Trp (b) and D-Trp (c) samples. d) Plot of predicted response against the concentration to highlight the correct association of four independent validation points to the enantiomeric group (blue stars for L-Trp and orange pentagons for D-Trp).*

To increase the robustness of the enantiodiscrimination achieved through the innovative EGOT-chemometric model a classification method - Partial Least Squares Discriminant Analysis (PLS-DA) - is applied to the entire dataset comprising

both L-Trp and D-Trp samples. PLS-DA extends the advantages of Partial Least Squares Regression (PLS-R) to classification problems.[69] Additional methodological details are provided in the Section 3.7. Specifically, a PLS regression model is built by correlating the experimental data extracted from the L-Trp and D-Trp transfer curves with a binary-coded matrix representing class membership. This approach yielded, for each sample, a vector of predicted responses (**Figure 4.19a**). The performance of the classification model is evaluated using Receiver Operating Characteristic (ROC) curves, shown in **Figure 4.19b** and **Figure 4.19c** for L-Trp and D-Trp, respectively. In **Figure 4.19d**, an original visualization of the PLS-DA model is proposed: the predicted response is plotted against the logarithm of the Tryptophan concentration.

The proposed multivariate analysis leveraging the multiparametric response of the EGOT device is demonstrated to identify different clusters for Trp enantiomers down to unprecedented levels. To confirm the robustness, the classification model is validated using four independent experimental points within the concentration range from 1 pM to 1 nM (the same used for validation in the EGOT-PCA classification, **Figure 4.18d**).

This chapter demonstrates that the synergistic interplay between tailored gate electrode functionalization and chemometric analysis of EGOT response enables enantiomeric discrimination at unprecedented concentration levels. We anticipate that this approach will be valuable for both point-of-use and benchtop applications, paving the way for high-sensitivity analysis in drug synthesis and pharmacokinetics, as well as for detecting undesired enantiomers and monitoring metabolic processes leading to chiral inversion.

4.4 Bibliography

1. Niu X *et al.* “Chiral Materials: Progress, Applications, and Prospects.” *Small* 2023; 19(38): 1–50. doi:10.1002/smll.202303059.
2. Zhao X *et al.* “Stereospecific interactions between chiral inorganic nanomaterials and biological systems.” *Chem Soc Rev* 2020; 49(8): 2481–2503. doi:10.1039/d0cs00093k.
3. Brooks WH *et al.* “The Significance of Chirality in Drug Design and Development.” *Curr Top Med Chem* 2011; 11(7).
4. Wu S *et al.* “Enantioselective Recognition of Chiral Tryptophan with Achiral

Glycine through the Strategy of Chirality Transfer." *Anal Chem* 2020; 92(17): 11927–11934. doi:10.1021/acs.analchem.0c02335.

5. Cava F *et al.* "Emerging knowledge of regulatory roles of d-amino acids in bacteria." *Cell Mol Life Sci* 2011; 68(5): 817–831. doi:10.1007/s00018-010-0571-8.
6. Barik S. "The uniqueness of tryptophan in biology: Properties, metabolism, interactions and localization in proteins." *Int J Mol Sci* 2020; 21(22): 1–22. doi:10.3390/ijms21228776.
7. Stavrum AK *et al.* "Model of tryptophan metabolism, readily scalable using tissue-specific gene expression data." *J Biol Chem* 2013; 288(48): 34555–34566. doi:10.1074/jbc.M113.474908.
8. Lanser L *et al.* "Inflammation-Induced Tryptophan Breakdown is Related With Anemia, Fatigue, and Depression in Cancer." *Front Immunol* 2020; 11(February): 1–21. doi:10.3389/fimmu.2020.00249.
9. Hughes MM *et al.* "Tryptophan depletion in depressed patients occurs independent of kynurenine pathway activation." *Brain Behav Immun* 2012; 26(6): 979–987. doi:10.1016/j.bbi.2012.05.010.
10. Comai S *et al. Tryptophan in health and disease*., 1st ed. Elsevier Inc., 2020. doi:10.1016/bs.acc.2019.08.005.
11. Ruddick JP *et al.* "Tryptophan metabolism in the central nervous system: Medical implications." *Expert Rev Mol Med* 2006; 8(20): 1–27. doi:10.1017/S1462399406000068.
12. Keszthelyi D *et al.* "Understanding the role of tryptophan and serotonin metabolism in gastrointestinal function." *Neurogastroenterol Motil* 2009; 21(12): 1239–1249. doi:10.1111/j.1365-2982.2009.01370.x.
13. Kino K *et al.* "Synthesis of DL-tryptophan by modified broad specificity amino acid racemase from Pseudomonas putida IFO 12996." *Appl Microbiol Biotechnol* 2007; 73(6): 1299–1305. doi:10.1007/s00253-006-0600-6.
14. Xiao S *et al.* "Expanding the application of tryptophan: Industrial biomanufacturing of tryptophan derivatives." *Front Microbiol* 2023; 14(March): 1–16. doi:10.3389/fmicb.2023.1099098.
15. Zhou J *et al.* "Indirect chiral separation of tryptophan enantiomers by high performance liquid chromatography with indirect chemiluminiscence detection." *J Chromatogr B Anal Technol Biomed Life Sci* 2015; 1006: 65–70. doi:10.1016/j.jchromb.2015.10.017.

16. Lomenova A, Hroboňová K. “Application of achiral–chiral two-dimensional HPLC for separation of phenylalanine and tryptophan enantiomers in dietary supplement.” *Biomed Chromatogr* 2020; 35(e4972).
17. Lee SY *et al.* “Determination of chromatographic separation parameters of tryptophan enantiomers on a Chirosil-SCA chiral stationary phase by using the inverse method based on the initial guesses estimated from elution by characteristic point method.” *J Chromatogr A* 2011; 1218(8): 1195–1202. doi:10.1016/j.chroma.2010.12.102.
18. Song G *et al.* “A universal strategy for visual chiral recognition of α-amino acids with l-tartaric acid-capped gold nanoparticles as colorimetric probes.” *Analyst* 2016; 141(4): 1257–1265. doi:10.1039/c5an02434j.
19. Liu M *et al.* “Identification and Quantitation of Enantiomers by Capillary Electrophoresis and Circular Dichroism Independent of Single Enantiomer Standard.” *Anal Chem* 2019; 91(21): 13803–13809. doi:10.1021/acs.analchem.9b03276.
20. Han S *et al.* “Chiral electrochemical recognition of tryptophan enantiomers by polysaccharide modified MOFs.” *J Electroanal Chem* 2023; 935(December 2022). doi:10.1016/j.jelechem.2023.117326.
21. Pan Q xiu *et al.* “Development of a chiral electrochemical sensor based on copper–amino acid mercaptide nanorods for enantioselective discrimination of tryptophan enantiomers.” *Anal Chim Acta* 2023; 1272(June): 341480. doi:10.1016/j.aca.2023.341480.
22. Li YJ *et al.* “Constructing electrochemical sensor using molecular-imprinted polysaccharide for rapid identification and determination of L-tryptophan in diet.” *Food Chem* 2023; 425(December 2022). doi:10.1016/j.foodchem.2023.136486.
23. Dutta P *et al.* “Enantioselective sensors based on antibody-mediated nanomechanics.” *Anal Chem* 2003; 75(10): 2342–2348. doi:10.1021/ac034031z.
24. Jing P *et al.* “Highly Reliable Chiral Discrimination of Tryptophan Enantiomers through Two Different Modes: Electrochemistry and Temperature.” *Anal Chem* 2023; 95(22): 8569–8577. doi:10.1021/acs.analchem.3c00669.
25. Wang Y *et al.* “A chiral signal-amplified sensor for enantioselective discrimination of amino acids based on charge transfer-induced SERS.” *Chem Commun* 2019; 55(65): 9697–9700. doi:10.1039/c9cc04665h.

26. Deng K *et al.* “Chiral recognition of tryptophan enantiomers with UV–Vis spectrophotometry approach by using L-cysteine modified ZnFe2O4 nanoparticles in the presence of Cu2+.” *Spectrochim Acta - Part A Mol Biomol Spectrosc* 2022; 270: 120847. doi:10.1016/j.saa.2021.120847.
27. Hofstetter O *et al.* “Chiral discrimination using an immunosensor.” *Nat Biotechnol* 1999; 17(4): 371–374. doi:10.1038/7927.
28. Karimian M *et al.* “Paper-based microfluidic system and chiroptical functionalized gold nano-oval for colorimetric detection of L-Tryptophan.” *Anal Chim Acta* 2024; 1285(August 2023). doi:10.1016/j.aca.2023.342022.
29. Fahimi-Kashani N *et al.* “Visual Recognition of Tryptophan Enantiomers Using Chiral Self Assemblies of Quantum Dots.” *ACS Appl Nano Mater* 2022; 5(1): 1460–1471. doi:10.1021/acsanm.1c02928.
30. Wei Y *et al.* “Chiral discrimination between d- and l-tryptophan based on the alteration of the fluorescence lifetimes by the chiral additives.” *Talanta* 2010; 81(4–5): 1800–1805. doi:10.1016/j.talanta.2010.03.044.
31. Guo D *et al.* “A sensing interface for recognition of tryptophan enantiomers based on porous cluster-like nanocomposite films.” *New J Chem* 2014; 38(12): 5880–5885. doi:10.1039/c4nj01484g.
32. Kang SZ *et al.* “Preparation of L-alanine ethyl ester modified multiwalled carbon nanotubes and their chiral discrimination between D- and L-tryptophan.” *Diam Relat Mater* 2010; 19(10): 1221–1224. doi:10.1016/j.diamond.2010.06.014.
33. Gong T *et al.* “A renewable electrochemical sensor based on a self-assembled framework of chiral molecules for efficient identification of tryptophan isomers.” *Anal Chim Acta* 2022; 1191: 339276. doi:10.1016/j.aca.2021.339276.
34. Chen J *et al.* “L-Lysine-Functionalized Nickel-Zinc Bis(Dithiolene) Metal-Organic Framework for Electrochemical Chiral Recognition of Tryptophan Enantiomers.” *Chem Mater* 2024; 36(7): 3215–3222. doi:10.1021/acs.chemmater.3c02945.
35. Niu X *et al.* “Fabrication of an electrochemical chiral sensor via an integrated polysaccharides/3D nitrogen-doped graphene-CNT frame.” *Bioelectrochemistry* 2020; 131: 107396. doi:10.1016/j.bioelechem.2019.107396.
36. Pei H *et al.* “An electrochemical chiral sensor based on glutamic acid

functionalized graphene-gold nanocomposites for chiral recognition of tryptophan enantiomers." *J Electroanal Chem* 2022; 913(April): 1–12. doi:10.1016/j.jelechem.2022.116283.

37. Niu X *et al.* "Adaptive host-guest chiral recognition in nanoarchitectonics with biomimetic MOF mimicking DNA." *J Mater Chem A* 2023; 11(43): 23376–23386. doi:10.1039/d3ta05570a.
38. Zhang L *et al.* "Chirality detection of amino acid enantiomers by organic electrochemical transistor." *Biosens Bioelectron* 2018; 105(October 2017): 121–128. doi:10.1016/j.bios.2018.01.035.
39. Li L *et al.* "Construction and application of graphene oxide-bovine serum albumin modified extended gate field effect transistor chiral sensor." *Sensors* 2021; 21(11). doi:10.3390/s21113921.
40. Saygin GD *et al.* "Concentration gradients probed in microfluidics by gate-array electrolyte organic transistor." *Sensors Actuators B Chem* 2024; 404(December 2023): 135185. doi:10.1016/j.snb.2023.135185.
41. Sensi M *et al.* "Reduced Graphene Oxide Electrolyte-Gated Transistor Immunosensor with Highly Selective Multiparametric Detection ofAnti-Drug Antibodies." *Adv Mater* 2023; 35(2211352).
42. Walt DR, Agayn VI. "The chemistry of enzyme and protein immobilization with glutaraldehyde." *TrAC - Trends Anal Chem* 1994; 13(10): 425–430. doi:10.1016/0165-9936(94)85023-2.
43. SABATINI DD *et al.* "Cytochemistry and electron microscopy. The preservation of cellular ultrastructure and enzymatic activity by aldehyde fixation." *J Cell Biol* 1963; 17: 19–58. doi:10.1083/jcb.17.1.19.
44. Barbosa O *et al.* "Glutaraldehyde in bio-catalysts design: A useful crosslinker and a versatile tool in enzyme immobilization." *RSC Adv* 2014; 4(4): 1583–1600. doi:10.1039/c3ra45991h.
45. Migneault I *et al.* "Glutaraldehyde: Behavior in aqueous solution, reaction with proteins, and application to enzyme crosslinking." *Biotechniques* 2004; 37(5): 790–802. doi:10.2144/04375rv01.
46. Ionescu RE. "Use of Cysteamine and Glutaraldehyde Chemicals for Robust Functionalization of Substrates with Protein Biomarkers — An Overview on the Construction of Biosensors with Different Transductions." 2022.
47. Casalini S *et al.* "Multiscale sensing of antibody-antigen interactions by organic transistors and single-molecule force spectroscopy." *ACS Nano* 2015;

9(5): 5051–5062. doi:10.1021/acsnano.5b00136.

48. Vieira NCS *et al.* “Label-free electrical recognition of a dengue virus protein using the SEGFET simplified measurement system.” *Anal Methods* 2014; 6(22): 8882–8885. doi:10.1039/c4ay01803f.
49. Ricci S *et al.* “Label-free immunodetection of α-synuclein by using a microfluidics coplanar electrolyte-gated organic field-effect transistor.” *Biosens Bioelectron* 2020; 167(March): 112433. doi:10.1016/j.bios.2020.112433.
50. Richards FM, Knowles JR. “Glutaraldehyde as a protein cross-linking reagent.” *J Mol Biol* 1968; 37(1): 231–233. doi:10.1016/0022-2836(68)90086-7.
51. Macchia E *et al.* “Plasmonic Single-Molecule Affinity Detection at 10−20 Molar.” *Adv Mater* 2025; 37(2418610).
52. Paradisi A *et al.* “Robust Biosensor Based on Carbon Nanotubes/Protein Hybrid Electrolyte Gated Transistors.” *Chem - A Eur J* 2023; 29(55). doi:10.1002/chem.202301704.
53. Macchia E *et al.* “Single-molecule detection with a millimetre-sized transistor.” *Nat Commun* 2018; 9(1). doi:10.1038/s41467-018-05235-z.
54. Holzer B *et al.* “Characterization of Covalently Bound Anti-Human Immunoglobulins on Self-Assembled Monolayer Modified Gold Electrodes Brigitte.” *Adv Biosyst* 2017; 1(1700055).
55. Brandão-Lima LC *et al.* “Clay mineral minerals as a strategy for biomolecule incorporation: Amino acids approach.” *Materials (Basel)* 2022; 15(1): 1–13. doi:10.3390/ma15010064.
56. Sensi M *et al.* “Investigation of transcription factor-DNA binding with electrolyte-gated organic transistors.” *J Mater Chem C* 2024; 12(21): 7596–7604. doi:10.1039/d4tc00260a.
57. Manco Urbina PA *et al.* “Physical insights from the Frumkin isotherm applied to electrolyte gated organic transistors as protein biosensors.” *J Mater Chem C* 2021; 9(33): 10965–10974. doi:10.1039/d1tc02546e.
58. Zanotti R *et al.* “Charge Carrier Density in Organic Semiconductors Modulates the Effective Capacitance: A Unified View of Electrolyte Gated Organic Transistors.” *Adv Mater* 2024; 36(49). doi:10.1002/adma.202410940.
59. Press WH *et al. Numerical Recipes*., 2007.
60. Swenson H, Stadie NP. “Langmuir’s Theory of Adsorption: A Centennial

Review.” *Langmuir* 2019; 35(16): 5409–5426. doi:10.1021/acs.langmuir.9b00154.

61. Zanotti R *et al.* “Fluorophobic Effect Enables Selective Detection of PFAS in Water with Electrolyte-Gated Organic Transistors.” *Adv Funct Mater* 2025; 08425: 1–12. doi:10.1002/adfm.202508425.
62. Genco E *et al.* “A Single-Molecule Bioelectronic Portable Array for Early Diagnosis of Pancreatic Cancer Precursors.” *Adv Mater* 2023; 35(2304102).
63. Scandurra C *et al.* “Analysis of Clinical Samples of Pancreatic Cyst’s Lesions with A Multi-Analyte Bioelectronic Simot Array Benchmarked Against Ultrasensitive Chemiluminescent Immunoassay.” *Adv Sci* 2024; 11: 230814.
64. Caputo M *et al.* “Piercing the Shadows: Exploring the Influence of Signal Preprocessing on Interpreting Ultrasensitive Bioelectronic Sensor Data.” *Chempluschem* 2025; 90(2). doi:10.1002/cplu.202400520.
65. Martynko E, Kirsanov D. “Application of Chemometrics in Biosensing: A Brief Review.” *Biosensors* 2020; 10(8). doi:10.3390/bios10080100.
66. Montes-García V *et al.* “Ultrasensitivie Isomer Discrimination: A Joint Surface-Enhanced Raman Scattering (SERS) Spectroscopy and Machine Learning Strategy.” *Adv Sens Res* 2025; 2400160.
67. Torsi L *et al.* “A sensitivity-enhanced field-effect chiralsensor.” *Nat Mater* 2008; 7(5): 412–417. doi:10.1038/nmat2167.
68. Mulla MY *et al.* “Capacitance-modulated transistor detects odorant binding protein chiral interactions.” *Nat Commun* 2015; 6. doi:10.1038/ncomms7010.
69. Cocchi M *et al. Chemometric Methods for Classification and Feature Selection*., 1st ed. Elsevier B.V., 2018. doi:10.1016/bs.coac.2018.08.006.

Chapter 5: Leveraging MXene Surface Chemistry for Ultrasensitive Dopamine Detection in Organic Transistor Biosensors

This chapter highlights the versatility of Electrolyte-Gated Organic Transistors (EGOTs) as a platform for sensing of small-molecule biomarkers. To push the sensitivity limits of these devices, $Ti_3C_2T_x$ MXenes are synthesized and integrated as the sensing element on the gate electrode of an EGOT-based sensor for Dopamine detection. Specifically, MXenes are produced under different synthesis conditions to tailor the material's surface chemistry and are extensively characterized using X-ray Diffraction (XRD), Raman and Fourier Transform Infrared (FTIR) spectroscopies, High-Resolution X-ray Photoelectron Spectroscopy (HRXPS), and Scanning Electron Microscopy coupled with Energy-Dispersive X-ray Spectroscopy (SEM-EDS).

Furthermore, the MXenes are integrated into Poly(3,4-ethylenedioxythiophene)polystyrene sulfonate (PEDOT:PSS)-based EGOTs. These chemically-engineered materials are successfully demonstrated as sensing probes for the ultrasensitive detection of Dopamine, achieving limits of detection in the femtoMolar (fM) range. Finally, the analysis of the multiparametric transistor response provides crucial insights into the interaction mechanism between Dopamine and the functionalized MXene surface.

The importance of the gate electrode functionalization to enhance the sensitivity of EGOT-based (bio)sensors for the detection of biologically relevant molecules continues in this Chapter 5.

MXenes ($Ti_3C_2T_X$), an emerging class of two-dimensional materials which are promising for bioelectronic sensing for their versatile surface chemistry, are integrated in EGOT-based sensor to lower the Limit of Detection (LOD) for Dopamine (DA) into the femtoMolar range. DA is a critical neurotransmitter regulating reward pathways, memory, learning, attention, and motor control in the mammalian central nervous system.[1] Extracellular DA concentrations in brain tissue are tightly regulated at sub-microMolar levels. Deviations from this narrow physiological window correlate with major pathological conditions, including Parkinson's disease (PD), depression, and schizophrenia[2,3] For instance, a 50% decrease in DA concentration in the *caudate-putamen* region is considered a main pathogenic hallmark of PD.[2] Early interventions necessitate analytical tools capable of detecting picoMolar DA fluctuations before this critical tipping point.

Electrochemical DA sensors primarily rely on the electrochemical oxidation of DA to Dopaminequinone (DQ) at the electrode surface.[4–7] However, this approach suffers from severe selectivity limitations: physiological interferents such as ascorbic acid (AA), uric acid (UA), and DA metabolites undergo oxidation at similar potentials, generating indistinguishable signals.[8,9] While surface modifications using conductive polymers[10] and inorganic nanocomposites[11,12] have improved selectivity against AA and UA, most electrochemical platforms still fail to achieve the required picoMolar sensitivity for early-stage diagnostics.[13] Although the integration of nanostructured MXenes into EGOT architectures[14] has led to the development of high-performance sensing platforms[15–17], detection of DA via MXene-functionalized EGOTs remains largely unexplored. At the best of our knowledge, only a couple of studies are available: Xu and co-workers achieved micromolar DA detection using ultrathin Ti_3C_2 FET devices[18], while Zhou and collaborators reached 50 nM sensitivity through MXene/Pt nanoparticles-functionalized gate in graphene transistors.[19]

Here, three different chemically-engineered MXene are tested as sensing probe in the EGOT platform towards DA. The interactions between the MXenes functionalization layer with DA is transduced by a PEDOT:PSS channel and results in a limit of detection in the femtoMolar range, making this prototype promising for

future applications in DA sensing in patients with reduced neurotransmitter levels (such as those with Parkinson's disease).

Section 5.1 shows the synthesis and the chemical characterization of MXene samples with engineered surface terminations modification, carried out in collaboration with the group of Prof. Ion-Alexandru Baragau of the National Institute of Materials Physics, Romania. Section 5.2 presents the functionalization of the gate with the chemically-modified MXenes and their integration into a Poly(3,4-ethylenedioxythiophene)polystyrene sulfonate (PEDOT:PSS) EGOT-device. The response of MXene-EGOT sensor across the tested concentration range (100 fM to 10 μM) is interpreted by considering two distinct MXene-DA interaction mechanisms, including a high-affinity interaction between DA and the MXene surface at low concentration, dominated by electrostatic attraction and possible coordination effects and a non-specific process associated with DA electro-oxidation at concentrations higher than 1 μM. Finally, in Section 5.3 the interaction mechanisms occurring between the different surface-functionalized MXenes and the DA is hypothesized by leveraging the multiparametric response of EGOT-based devices with Principal Component Analysis (PCA).

5.1 MXenes synthesis and characterization

This chapter reports the synthesis and the characterization of the chemically-modified MXenes powder, carried out in collaboration with the group of Ion-Alexandru Baragau of the National Institute of Materials Physics, Romania.

MXenes are defined by the general formula $M_{n+1}X_nT_x$, composed of n + 1 layers (n = 1 - 4) of early transition metals (M, groups 3 – 6), alternating by n layers of carbon and/or nitrogen atoms ('X'). The term T_x denotes the surface terminations (*e.g.,* -F, -O, -OH) attached to the outer metal layers.[20] In the first reaction step for the MXenes ($Ti_3C_2T_X$) synthesis, a commercial MAX phase (Ti_3AlT_X) is chemically etched through the addition of HF resulting in the formation of the HF-MX. The reaction between HF and the Al atoms in the MAX phase structure results in the exfoliation of the MAX phase by the cleavage of the M-A bonds with the removal of the A layers, while maintaining the $MX_{n+1}X_n$ layers.[21] In the second step of the synthesis, the HF-MX samples is thermal annealed in different gas flows (argon 5%, hydrogen in argon and pure ammonia) to synthesized Ar-MX, H_2-MX and N-MX respectively.

As is normally the case in MXene experimental research, the complete chemical extraction of Al atoms between the Ti_3C_2 layers, resulting in the formation of two-dimensional, multilayered HF-MXene is confirmed through chemical characterization techniques, including X-ray diffraction (XRD), Raman Spectroscopy, Fourier Transform Infrared Spectroscopy (FTIR), X-ray Photoelectron Spectroscopy (XPS), and Scanning Electron Microscopy (SEM) coupled with Energy-Dispersive X-ray Spectroscopy (EDS) (**Figure 5.1**).

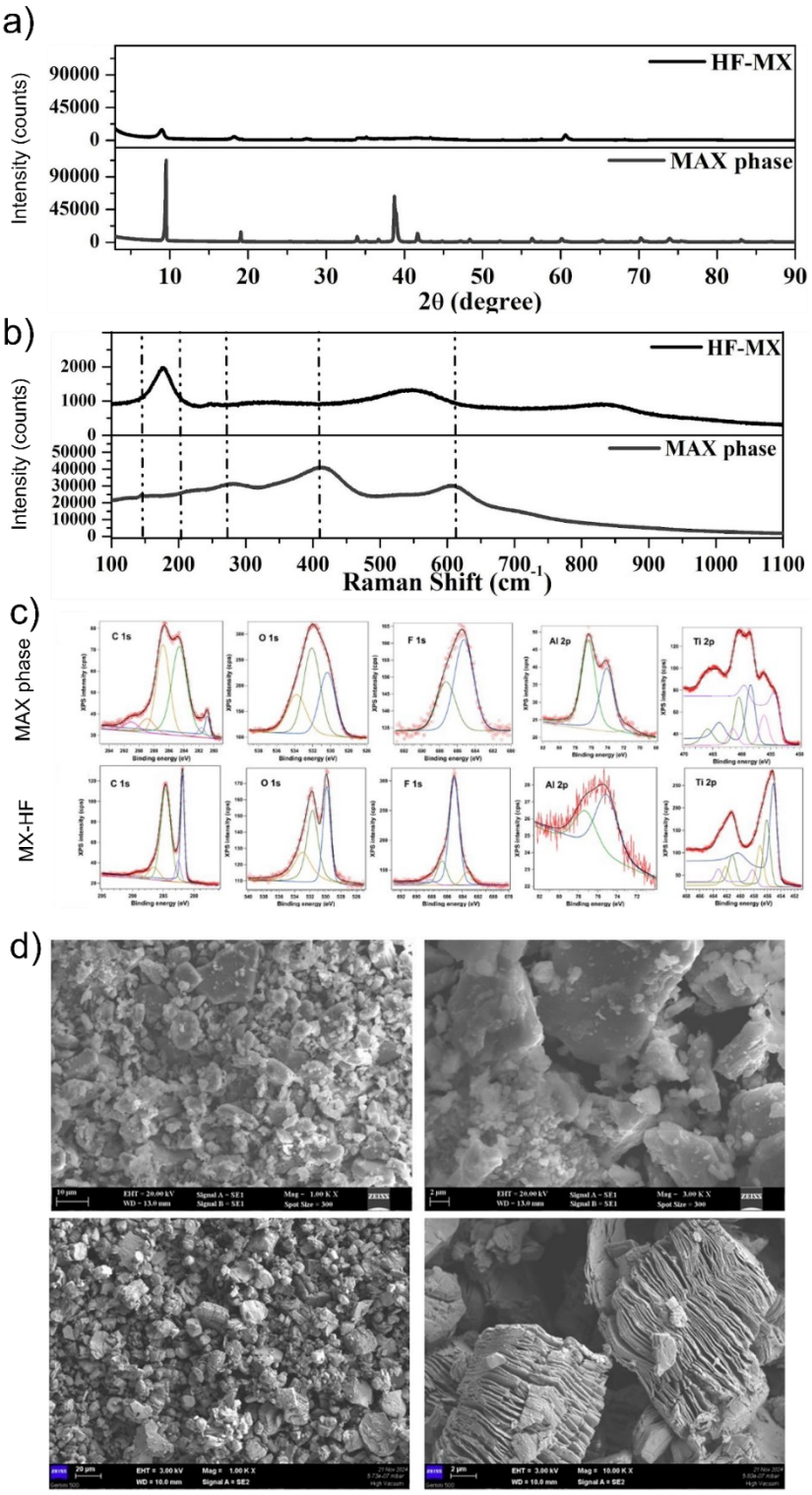

***Figure 5.1**: Comprehensive characterization of the MAX phase. a) X-ray diffraction patterns of MAX phase (black) and HF-MX (grey). b) Raman spectra of MAX phase (black) and HF-MX (grey). c) The high-resolution C1s, O1s, N1s, F1s, Al2p, Ti2p XPS spectra of MAX phase and HF-MX. d) The SEM images at low (left) and high (right) magnification for MAX phase (top) and HF-MX samples (bottom).*

The successful etching of the MAX phase and its conversion into $Ti_3C_2T_x$ MXene (HF-MX) is comprehensively validated by multiple characterization techniques (**Figure 5.1**).

The XRD patterns (**Figure 5.1a**) confirms the structural evolution. The pristine MAX phase exhibits an intense (002) peak at 9.5° 2θ and a second order (006) reflection at 19.07°. In the HF-MX sample these peaks exhibit a significant broadening, a decrease in intensity, and a shift to lower angles (9.02° for (002) and 18.22° for (006)). This shift confirms an increase in the c-lattice parameter (*viz.,* the interlayer distance between Ti_3C_2 layers), which is the primary indicator of A-layer (Al) extraction and replacement by -F and -OH terminal groups.[22] This transformation is further supported by the (004) peak (38.72°), characteristic of the MAX phase, which is nearly suppressed in the HF-MX sample and shifted to 37.75°. Furthermore, the appearance of a (008) diffraction peak at ~27° is characteristic of $Ti_3C_2(OH)_2$ formation.[23]

Raman spectroscopy (**Figure 5.1b**) corroborates this chemical change. The A_{1g} vibrational mode at 227 cm^{-1}, corresponding to the out-of-plane vibration of Ti-Al bonds in the MAX phase, is absent in the HF-MX spectrum. This peak is replaced by the characteristic A_{1g} mode of $Ti_3C_2T_x$ MXene at 204 cm^{-1} (out-of-plane Ti atom vibration) (Hu 2015), confirming the successful cleavage of the Ti-Al bonds. Moreover, the appearance of the D-band, absent in the MAX phase, indicates the formation of structural defects in the carbon lattice, likely due to the etching and concomitant degradation processes.[24]

Finally, the compositional and morphological evolution is assessed by XPS and SEM/EDS (**Figures 5.1c-d**, **Table 5.1**). XPS analysis confirms a significant decrease in Al content following etching. SEM imaging reveals the morphological transition from the dense, bulk MAX phase to the characteristic multilayered, "accordion-like" structure of the HF-MX sample. This is further substantiated by SEM-coupled EDS, which confirms the drastic reduction in Al content and a corresponding increase in C, O, and F, consistent with the formation of $Ti_3C_2T_x$ MXene.

***Table 5.1**: XPS (top) and EDS chemical composition (bottom) for MAX phase and HF-MX.*

Sample	XPS elemental composition (%)					
	C1s	O1s	N1s	F1s	Al2p	Ti2p
MAX phase	33.46	45.43	/	3.70	5.22	12.19
HF-MX	45.93	13.10	/	13.98	0.43	26.56
	EDS elemental composition (%)					
	C	O	N	F	Al	Ti
MAX phase	5.80	17.04	/	2.65	31.69	42.83
HF-MX	17.70	23.23	/	18.15	3.43	38.59

The HF-MX sample is then surface modified into three new MXene samples to enhance its electronic properties and surface stability by removing or replacing labile functionalities. The surface modification is studied with spectroscopy techniques (*viz.,* Raman, FTIR and XPS) and with SEM coupled with EDS. (**Figure 5.2**) During the annealing process at 400°C in gas flow (argon in Ar-MX, argon doped with 5% H_2 in H_2-MX, in pure ammonia for N-MX), all volatile compounds present between the Ti_3C_2 layers are removed, together with thermally unstable surface functional groups.

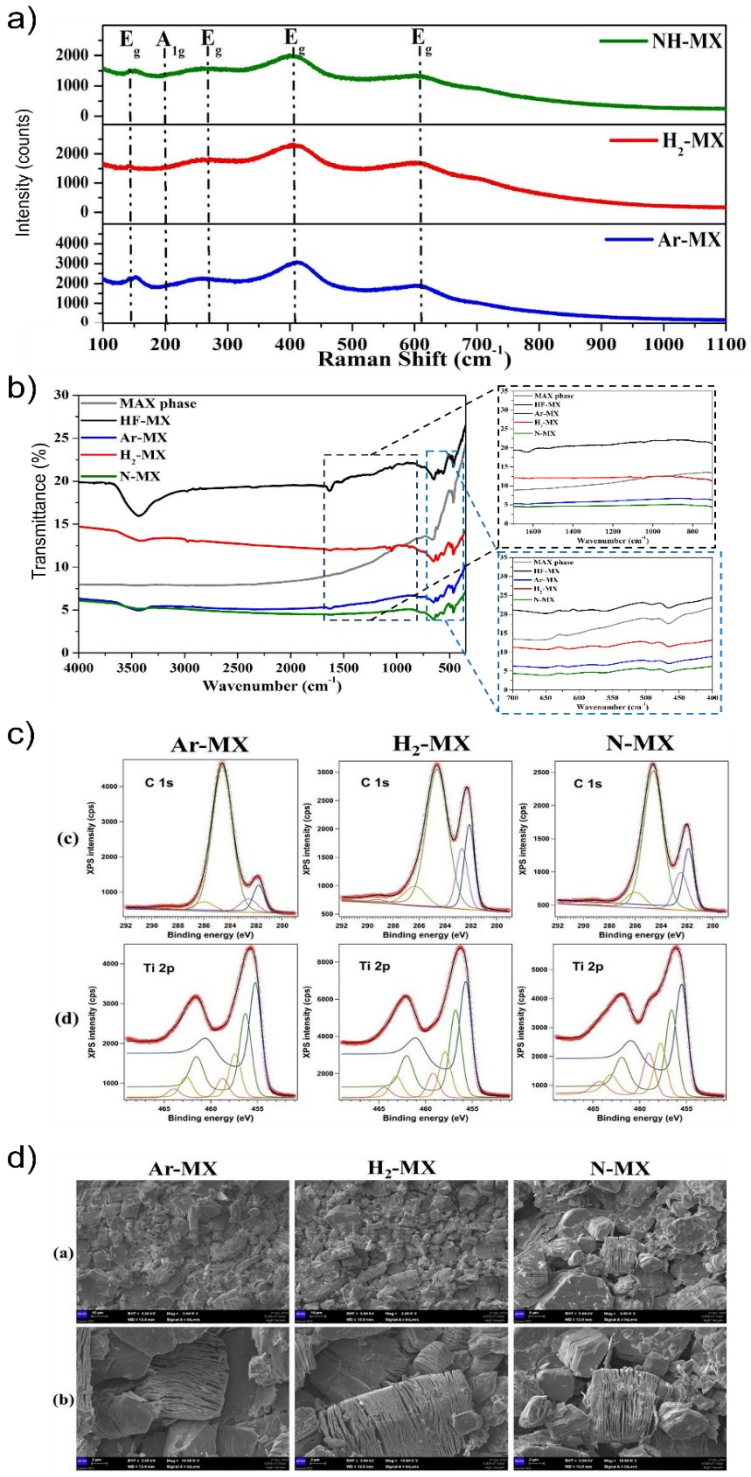

***Figure 5.2**: Comprehensive characterization of the chemically-engineered MXenes. a) Raman spectra of HF-MX (grey), Ar-MX (blue), H_2-MX (red), N-MX (green). b) FITR spectra of HF-MX (grey), Ar-MX (blue), H_2-MX (red), N-MX (green). c) The high-resolution C1s, O1s, N1s, F1s, Al2p, Ti2p XPS spectra of Ar-MX (left), H_2-MX (center), N-MX (right). d) The SEM images at low (left) and high (right) magnification for Ar-MX (left), H_2-MX (center), N-MX (right).*

The chemical modifications induced by the different annealing atmospheres are first assessed by Raman and FTIR spectroscopy (**Figure 5.2a, b**).

The Raman spectra (**Figure 5.2a**) show that the E_g vibration mode at 154.26 cm^{-1} in HF-MX, associated with $Ti_{3-n}C_2$-$Ti_n(O/OH)_x$, undergoes to a major intensity decrease in both H_2-MX and N-MX samples. This peak also exhibits a redshift to 144.5 cm^{-1}, which is often attributed to the characteristic of Ti-O vibrations[24], and this indicates a significant reduction of the -O and -OH functionalities bonded to titanium.

The removal of functional groups, particularly water, is confirmed by FTIR (**Figure 5.2b**). All annealed samples exhibit a marked reduction in the broad band at ~3430 cm^{-1} (O-H stretch) and the associated peak at ~1630 cm^{-1} (H-O-H bend), confirming the desorption of intercalated water. The redshift of the latter peak to ~1620 cm^{-1} in H_2-MX and N-MX suggests that C=O functionalities become prominent once the weakly adsorbed water molecules are efficiently removed from the interlayer space. This shift indicates that any remaining water molecules are likely strongly interacting with the MXene surface via hydrogen bonding.

Furthermore, the reactive atmospheres induce specific changes. The H_2-MX sample show a more intense and well-defined C-H stretching peak at ~2970 cm^{-1}, confirming that hydrogenation of the carbon phase occurred as a side reaction.

XPS is employed to quantify the extensive changes in surface elemental composition and chemistry (**Figure 5.2c**, **Table 5.2**). XPS Survey analysis reveals distinct trends. Annealing in inert argon (Ar-MX) leads to an increase in carbon (from 45.95% to 58.88%) and a decrease in oxygen (13.1% to 12.6%) and fluorine (13.98% to 8.81%), consistent with the desorption of volatile species. Conversely, processing in reactive atmospheres (H_2-MX and N-MX) results in a decrease in C1s concentration (to 36.41% and 34%, respectively) and a slight increase in O1s concentration (to 17.44% and 18.48%, respectively). For N-MX, successful nitrogen-doping is confirmed by a 4.47% N1s signal. The high-resolution XPS (HRXPS) provides an indication of the bonding type for each element. Firstly, the HRXPS data confirm that the thermal treatments successfully reduced Ti-bonded functionalities: the C1s spectra show a decrease in the C-$Ti(OH/F)_x$ component (from 24.67% in HF-MX to 17.35% in H_2-MX and 8.27% in Ar-MX), while the O1s spectra exhibit C-$Ti-O_x$/C-$Ti-OH_x$ component (from 40.8% in HF-MX to 20.06% in H_2-MX).

These observations corroborate the Raman data. Critically, the O1s spectra also reveals a concurrent and significant increase in C-OH hydroxyl groups, which rise

from 29.28% in HF-MX to 45.78% in H_2-MX. This finding directly corroborates the FTIR data, confirming why the H_2-MX sample shows the most intense C-O stretching peak at ~1050 cm^{-1} (**Figure 5.2b, black inset**). This dataset provides a clear mechanism: the thermal treatment removes intercalated water and labile Ti-O/Ti-OH groups, potentially forming C=O functionalities (seen in FTIR). In the H_2 reducing atmosphere, these C=O groups are subsequently reduced to C-OH groups, leading to an overall increase in surface oxygen (O1s) even as the Ti-O bonds are cleaved.

SEM images (**Figure 5.2d**) confirm the morphological integrity of the samples. The materials show no signs of thermal degradation or decomposition at 400°C, suggesting high structural stability. Finally, EDS mapping (**Table 5.2**), which is more bulk-sensitive, show a homogenous distribution of Ti and C, and a relatively constant concentration of bulk oxygen atoms across all samples. This contrasts with the variable surface oxygen (O1s) measured by XPS, further highlighting that the chemical changes observed (Ti-O removal and C-OH formation) are a surface-dominated phenomenon driven by the annealing atmosphere.

***Table 5.2**: XPS and EDS elemental composition of Ar-MX, H_2-MX, and N-MX samples compared with HF-MX.*

Sample	XPS elemental composition (%)					
	C1s	O1s	N1s	F1s	Al2p	Ti2p
HF-MX	45.93	13.10	/	13.98	0.43	26.56
Ar-MX	58.88	12.60	/	8.81	1.86	17.85
H2-MX	36.41	17.44	/	14.31	3.18	28.67
N-MX	34.00	18.48	4.74	11.74	4.10	26.93
	EDS elemental composition (%)					
	C	O	N	F	Al	Ti
HF-MX	17.70	23.23	/	18.15	3.43	38.59
Ar-MX	21.41	21.92	/	16.92	4.62	35.05
H2-MX	17.29	21.68	/	17.20	4.62	39.21
N-MX	16.41	23.75	4.29	13.69	5.70	36.79

***Table 5.3**: HR-XPS components and chemical assignment of C1s, O1s, N1s, F1s, Al2p, Ti2p spectra of HF-MX, Ar-MX, H_2-MX , and N-MX samples.*

Sample name	Element	Assignment						
	C1s	C-Ti-(O/OH)x	C-Ti-(OH/F)x	C-Ti-C	C-C (sp2)	C-O/C-N	C=O	O-C=O
HF-MX		0.00	24.67	6.71	56.89	9.02		
Ar-MX		0.00	8.27	6.34	79.29	5.05	1.05	0.00
H2-MX		0.00	17.35	13.83	58.87	8.29	1.66	0.00
N-MX		0.00	15.50	12.53	64.06	7.23	0.69	0.00
	O1s	Ti-O (TiO2)	C-Ti-Ox/c-Ti-OHx/C=O	C-OH/Al2O3				
HF-MX		29.92	40.08	29.28				
Ar-MX		35.78	29.40	34.88				
H2-MX		34.16	20.06	45.78				
N-MX		35.78	29.34	34.88				
	N1s	Ti-N	C≡N/Pyrrolic-N	Graphitic-N				
HF-MX		0.00	0.00	0.00				
Ar-MX		0.00	0.00	0.00				
H2-MX		0.00	0.00	0.00				
N-MX		64.83	25.04	10.14				
	Al2p	Al-O(Al2O3)	Al-OH (Al(OH)3	Al-F(AlF3)				
HF-MX		100.00	0.00	0.00				
Ar-MX		80.08	0.00	19.92				
H2-MX		0.00	74.69	25.31				
N-MX		80.08	0.00	19.92				
	F1s	C-Ti-F	O-Ti-F/AlFx	C-F/Al(OF)x				
HF-MX		71.55	15.90	3.72				
Ar-MX		66.50	33.47	0.00				
H2-MX		64.40	23.22	12.38				
N-MX		64.94	19.82	15.24				
	Ti2p	C-Ti	Ti2+/Ti-O/Ti-C	Ti3+/Ti-F	C-Ti-O/Fx	TiO(Ti4+)/TiO2		
HF-MX		42.73	30.24	18.89	8.14	0.00		
Ar-MX		40.86	33.23	17.95	0.00	7.96		
H2-MX		39.69	32.85	0.00	17.90	9.56		
N-MX		35.64	29.98	18.82	0.00	15.57		

5.2 MXenes as Functionalization Layer for Dopamine Sensing

As a first step toward developing a DA sensor based on electrolyte-gated organic transistor (EGOT) devices, the gate electrodes are functionalized using the chemically-engineered MXenes. Electrochemical methods are employed to assess the success of the functionalization procedure and to evaluate the impact of the different chemical modifications on the MXene structures.

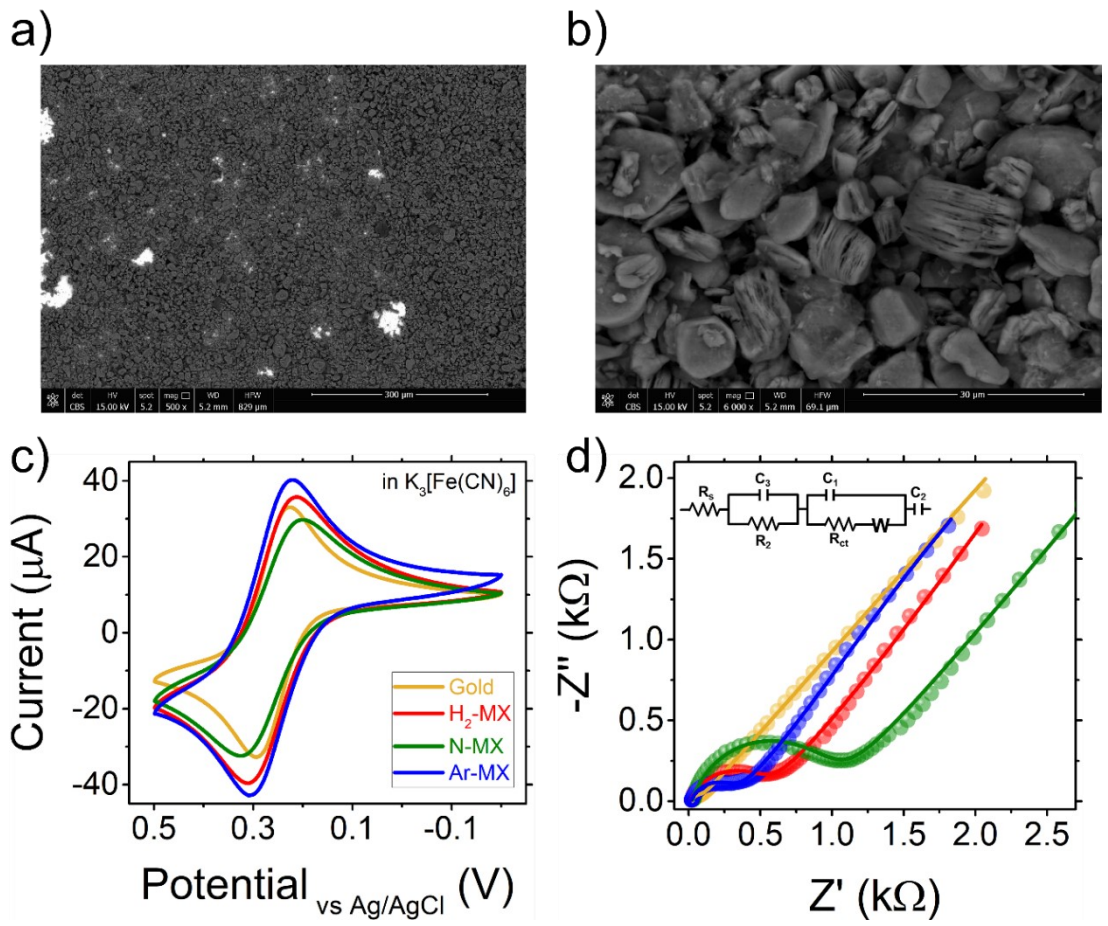

***Figure 5.3**: Functionalization of gold electrodes with chemically-modified MXenes. a) Low and b) high magnification SEM images of gold electrodes covered with surface-engineered MXenes. c) Cyclic Voltammetry (CV) plots of the Au and Au/MXenes electrodes, recorded in the $K_3[Fe(CN)_6]$ redox probe, scan rate 100 mV/s. d) Electrochemical Impedance Spectroscopy (EIS) Nyquist plots of the Au and Au/MXenes electrodes, recorded in the $K_3[Fe(CN)_6]$ redox probe, E = 260 mV vs Ag/AgCl.*

Leveraging the hydrophilic nature and highly negative zeta potential characteristic of MXenes[25], stable MXene dispersions are prepared in Dimethyl Sulfoxide (DMSO) and subsequently deposited onto gold electrodes via drop-casting. SEM analysis of the resulting Au/MXene electrodes reveal a network of interconnected, randomly oriented flakes providing extensive coverage of the gold substrate (**Figure 5.3a**). At higher magnification, individual flakes exhibit the characteristic layered, accordion-like morphology (**Figure 5.3b**), consistent with previous reports.[26]

The electrochemical properties of the Au/MXene electrodes are investigated using Cyclic Voltammetry (CV) and Electrochemical Impedance Spectroscopy (EIS) with $K_3[Fe(CN)_6]$ as redox probe. As shown in **Figure 5.3c**, the Ar-MX and H_2-MX functionalized electrodes exhibit a larger peak current envelope in the CV plots compared to the bare gold electrode, following the trend Ar-MX > H_2-MX. Conversely, the Au/N-MX electrode exhibits a significantly lower peak current, even lower than that of bare gold. This suggests that the NH_3-based treatment (N-MX) impairs the faradaic electrochemical performance, plausibly by reducing the film's electrical conductivity.[27]

This hypothesis is strongly supported by the EIS data. The Nyquist plots (**Figure 5.3 d**) are fitted using a modified equivalent circuit (**inset of Figure 5.3d**) proposed by Anjum *et al.,* for MXene-functionalized electrodes[28] and a standard Randles circuit for bare gold (R^2 > 0.99 for all the electrodes). In the equivalent circuit, C_1 accounts for the double-layer capacitance, while R_{ct} for charge-transfer resistance. C_2 accounts for the porosity of the MXene film and models its intrinsic supercapacitor behaviour. Additionally, a capacitive element (C_3) is placed in parallel with a resistor (R_d) to describe the surface film impedance arising from the formation of an insulating TiO_2 layer, generated by aqueous oxidation at anodic potentials.[28] The resulting parameters, listed in **Table 5.4**, confirm the success of the functionalization process.

Table 5.4**: list of the parameters extracted from fitting faradic EIS with the equivalent circuit reported in the inset of **Figure 5.3d

Parameter	Gold		H_2-MX		N-MX		Ar-MX	
	Value	Error	Value	Error	Value	Error	Value	Error
Equivalent circuit	Randles		inset Fig. 5.3d		inset Fig. 5.3d		inset Fig. 5.3d	
R_s (Ω)	26.49	0.73	31.27	4.85	48.87	7.60	37.76	6.55
R_2 (Ω)	n.d.		251.59	19.66	316.05	35.51	156.50	224.30
C_1 (F)	1.75E-06	4.60E-07	4.30E-06	6.71E-07	5.28E-07	2.51E-08	1.02E-06	9.37E-08
C_2 (F)	n.d.		7.19E-03	8.57E-04	5.90E-02	9.53E-02	6.65E-03	3.56E-03
C_3 (F)	n.d.		6.83E-07	4.74E-08	7.71E-06	1.86E-06	9.59E-03	5.94E-03
R_{ct} (Ω)	54.80	1.22	253.68	16.00	601.66	36.15	253.82	9.79
Wo	4.09E-04	3.07E-06	5.39E-04	5.24E-06	4.56E-04	6.04E-06	5.66E-04	1.62E-05

The charge transfer resistance (R_{ct}) increases significantly from approx. 55 Ω (bare Gold) to 254 Ω (Ar-MX), 254 Ω (H_2-MX), and 602 Ω (N-MX). This increase is consistent with the highly negative surface charge of MXenes[29], which electrostatically repels the anionic $[Fe(CN)_6]^{3-/4-}$ probe. Moreover, the increase of R_{ct} could be ascribed to the formation of the insulating thin layer of TiO_2, discussed above.

Regarding the interfacial properties, the double-layer capacitance (C_1) is highest for H_2-MX (4.30 µF), lower for Ar-MX (1.02 µF), and lowest for N-MX (0.53 µF). The high C_1 of H_2-MX is consistent with its HRXPS data (**Table 5.3**), which shows the highest concentration of polar C-OH groups (45.78%), resulting in a more hydrophilic and electrostatically active surface.

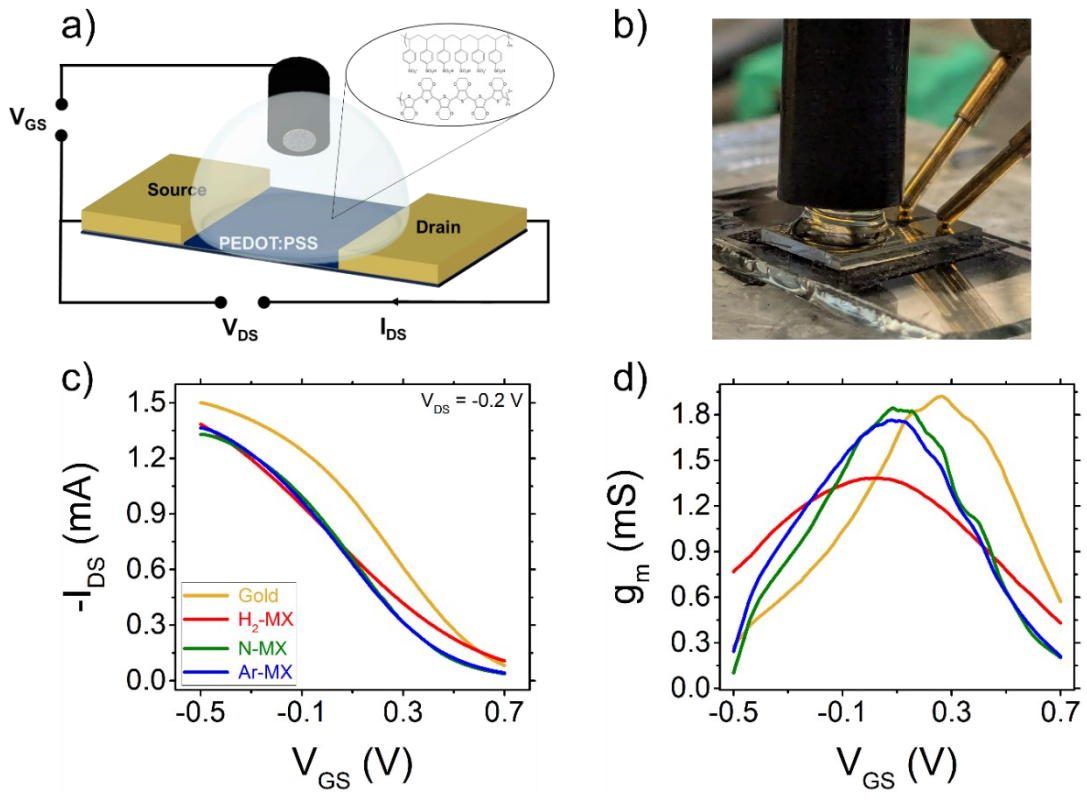

***Figure 5.4**: Architecture and electrical characterisation of the MXene-functionalized EGOT device. a) Scheme of the EGOT device; b) Layout of the DA sensor; c) Representative transfer curves recorded with gold (yellow), H_2-MX (red), N-MX (green), Ar-MX (blue) electrode; d) corresponding transconductance (viz., first derivative of I_{DS}) V_{DS} = -0.2 V, 50 mM PBS as electrolyte.*

The Au/MXene electrodes are integrated on gate electrodes in an Electrolyte-Gated Organic Transistor (EGOT) architecture, acting as sensitive probes for DA detection. **Figure 5.4a** shows the schematic representation of top-gated EGOT configuration, in which the gate electrode is positioned directly above the source and the drain interdigitated electrodes (IDEs), connected by a thin film of PEDOT:PSS channel. Once the gate electrode and IDEs substrate are assembled and bridged by buffer solution, the device layout appears as reported in **Figure 5.4b**. The operation of the

device with gate electrodes functionalized with chemically-engineered MXenes is assessed by measuring transfer curves (**Figure 5.4c**). The voltage between the source and drain electrodes (V_{DS}) is fixed at -0.2 V and the current variation in the channel (I_{DS}) is measured as a function of the voltage applied between the gate and the source (V_{GS}). The transconductance (g_m) is extracted as the first derivative of the transfer curve (**Figure 5.4d**), which describes the ability of the device to amplify a small voltage variation (*e.g.,* interaction of the target molecule with the functionalized gate) in a large current difference. Functionalizing the gate electrode with a MXene film as the sensing probe is a key innovation for EGOT-based sensors. Unlike functionalization with antibodies grafted onto organic Self-Assembled Monolayers (SAMs), which typically causes a two-orders-of-magnitude current reduction as demonstrated in **Figure 4.10** and elsewhere[30], the MXene film induces only a minimal decrease in the I_{DS} current (**Figure 5.4c**). Moreover, the maximum of the transconductance is very similar for gate electrodes functionalized with N-MX and Ar-MX, while it is slightly lower for the H_2-MX functionalized electrodes. All the MXenes functionalized electrodes shift the voltage of the maximum of transconductance closer to 0 V, that is a key point for physiological applications (**Figure 5.4d**).

A critical difference between the different chemically-engineered MXenes emerges in the off state (*viz.,* at V_{GS} = +0.7 V): the H_2-MX device exhibits a significantly higher off-current (poor switching) compared to the Ar-MX and N-MX devices, which both switch off effectively.

This interesting observation could be explained considering the HRXPS spectrum of H_2-MX, which shows the highest concentration for C-OH bond (45.78%) and the lowest concentration for C-Ti-OH bond (20.06%). The oxidation reaction that takes place at the interface between MXenes and aqueous electrolyte at positive potential[28] involves the nucleophilic attack of water molecules on the metal atom of MXene structure.[31] In H_2-MX the relative low concentration of C-Ti-OH bond on the MXene surface should inhibit the oxidation reaction at the H_2-MX surface. This results in a decrease of the passivating TiO_2 layer and therefore in an increasing interfacial capacitance (C_1) for H_2-MX, as discussed for EIS data. These assumptions are corroborated by evaluating the peculiar capacitive behaviour endowed by MXens layers.[32] $Ti_3C_2T_x$ electrodes exhibit a large chemical capacitance and at high rates perform a spontaneous, fast intercalation of cations, which make MXenes ideal candidate as supercapacitor.[33] Furthermore, in acidic

electrolyte MXenes show a pseudocapacitive behaviour due to the surface redox chemistry.[23,34–36] According to the faradic EIS (**Figure 5.3**), the pseudocapacitance accounts in C_2 and C_3 results higher for Ar-MX and N-MX because the presence of redox reactive groups, such as carbonyl[37] and amino group[38], respectively. The effective device modulation (low off-current) observed for the N-MX and Ar-MX gates is driven by their high pseudocapacitance, which favours the de-doping of the PEDOT:PSS channel. Conversely, the H_2-MX gate exhibits poor switching (*viz.,* a high off-current) precisely because its reducing treatment eliminated these redox-active functional groups, resulting in a lower pseudocapacitive contribution.

At this point, it is worth highlighting that the presented analysis strongly corroborates the findings from XPS, electrochemical measurements, and the functionalized gate's performance in the PEDOT:PSS EGOT device. Nevertheless, it must be emphasized that a systematic study of the capacitive behaviour of MXene films under various surface terminations is beyond the scope of this article and would necessitate a dedicated, *ad-hoc* investigation.

The sensing capability of the device towards DA is evaluated by recording its transfer curves in the presence of increasing DA concentrations to generate a dose-response profile.

For the three chemically-engineered MXenes, it is observed a monotonic decrease of I_{DS} at $V_{GS} < 0.3$ V, as well as a reduction in the maximum of transconductance g_m of the device (*viz.,* the first derivative of I_{DS} vs V_{GS}) as the DA concentration increased. (**Figure 5.5)**. The current decrease could be explained by considering that DA molecules are positively charged ($pKa_{DA} = 8.9$) at the experimental pH 7.4. When DA molecules approach the Au/MXene gate electrode, the effective gate voltage becomes more positive (less negative), pushing more cations (less anions) towards the channel.[39,40] This results in a decrease of the hole carrier density in the PEDOT:PSS channel, with I_{DS} current that decreases upon increasing the concentration of DA. Conversely, at $V_{GS} > 0.3$ V, the trend inverts, and I_{DS} increases with higher DA concentrations. At these positive gate potentials, the protonated DA is likely driven towards the PEDOT:PSS channel. Its interaction with the semiconductor may reduce the negative charge density on the PSS^- sites, thereby increasing hole concentration in the $PEDOT^+$ chains and enhancing the current.[41]

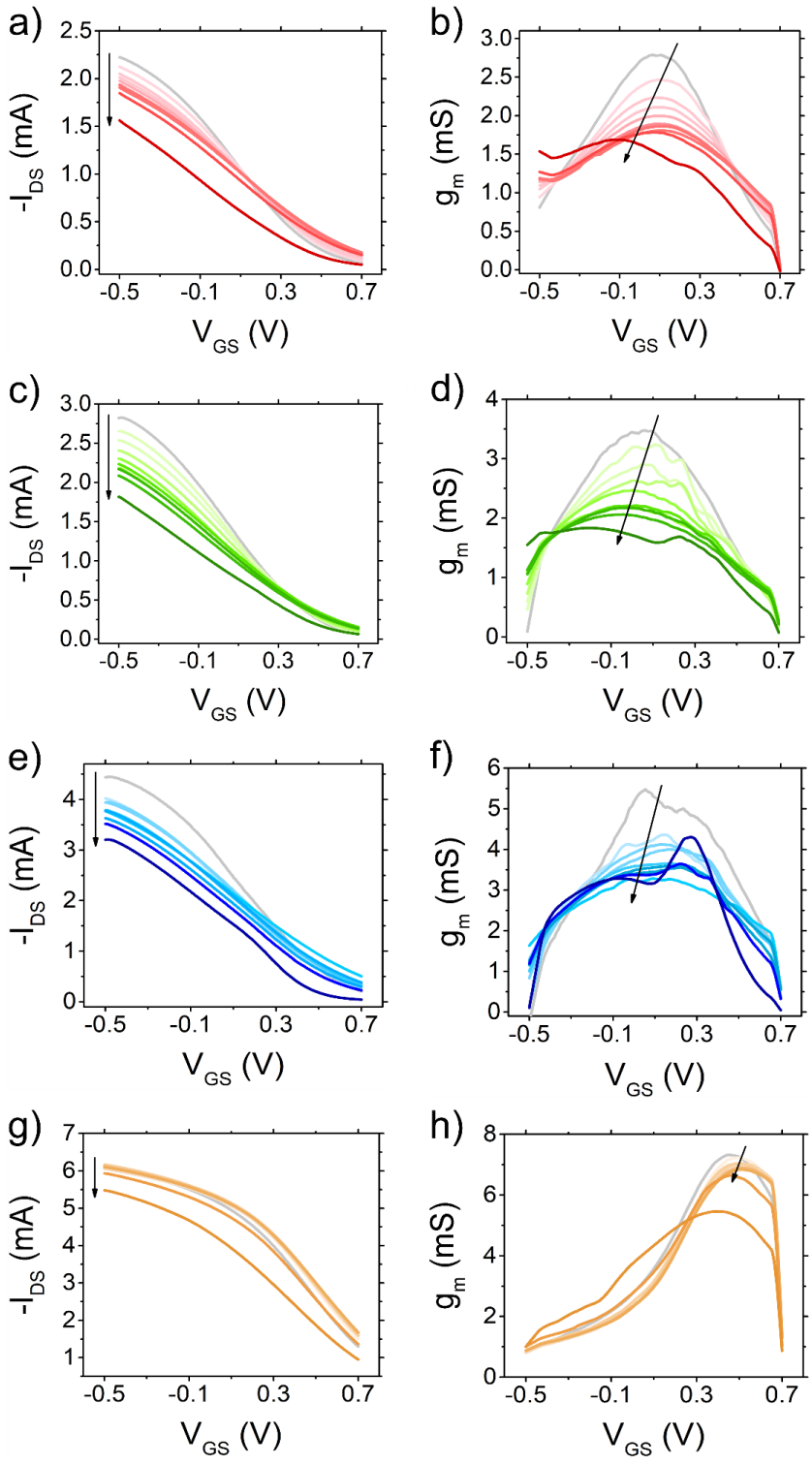

***Figure 5.5**: Electrical characterization in presence of Dopamine. Representative transfer curves and the corresponding transconductance (g_m) profile for H_2-MX electrode (red curves, a-b), N-MX electrode (green curves, c-d), Ar-MX electrode (blue curves, e-f) and bare gold (g-h).*

The I_{GS} currents (**Figure 5.6**) exhibit no faradic peaks for the MXenes functionalized gate electrode at [DA] below the micromolar range, suggesting that the sensing mechanism is related to the specific interaction between the functionalization layer and the target analyte. When DA concentration exceeds 1 µM, the positive gate potential applied to the PEDOT:PSS EGOTs could lead to the (partial) electro-oxidation of DA to DQ and subsequent electrodeposition of polydopamine, as demonstrated by the voltammetric peak observed around 0.7 V, particularly pronounced for Ar-MX.

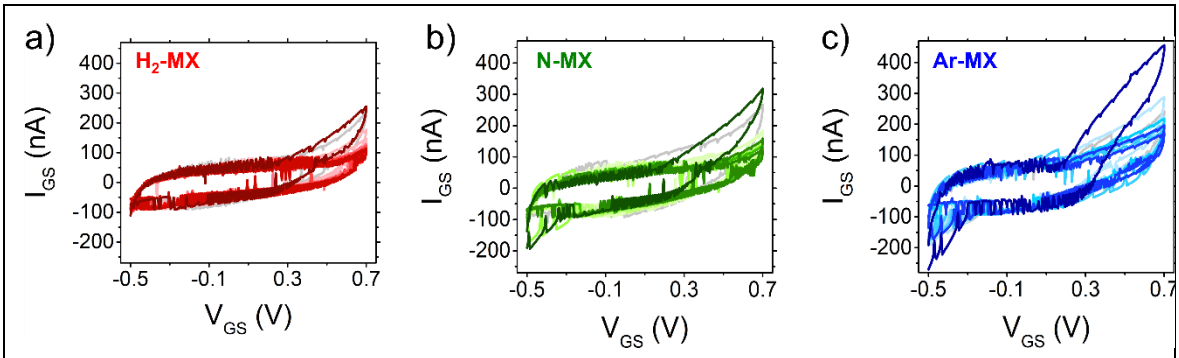

***Figure 5.6**: Gate electrode current during Dopamine sensing. I_{GS} measured during the sensing experiments reported in **Figure 5.5** for H_2-MX electrode (red curves, a), N-MX electrode (green curves, b), Ar-MX electrode (blue curves, c).*

To quantify the sensor's performance, dose-response calibration curves are constructed by plotting the signal response against the DA concentration. The signal (S_{IDS}) is defined as the normalized current modulation relative to the blank sample (*i.e.,* buffer solution without DA) (Equation 5.1):

$$S_{IDS} = \frac{I_{DS}([DA]) - I_{DS}(0)}{I_{DS}(0)} \qquad \text{(Eq. 5.1)}$$

where $I_{DS,[DA]}$ is the current at a specific V_{GS} and $I_{DS,0}$ is the baseline current measured at the same V_{GS} in the blank sample.

For all the chemically-engineered MXenes, the I_{DS} at V_{GS} = -0.5 V decreases upon exposure to increasing [DA] concentrations. Consequently, $-S_{IDS}$ is plotted (**Figure 5.7**), revealing a monotonic increase across the investigated concentration range. The S_{IDS} dose-response curves for the three chemical-engineered MXenes exhibit a clear bi-phasic (sigmoidal) trend: i) a rapid signal increase at low concentration (10 pM for H_2-MX and N-MX, 1 pM for Ar-MX); ii) a plateau or a region of slower

increase (up to 100 nM); iii) a second, sharp signal rise at concentrations above 1µM. This complex trend (**Figure 5.7**) strongly suggests the presence of two distinct interaction mechanisms at the MXene-electrolyte interface, in the concentration range investigated.

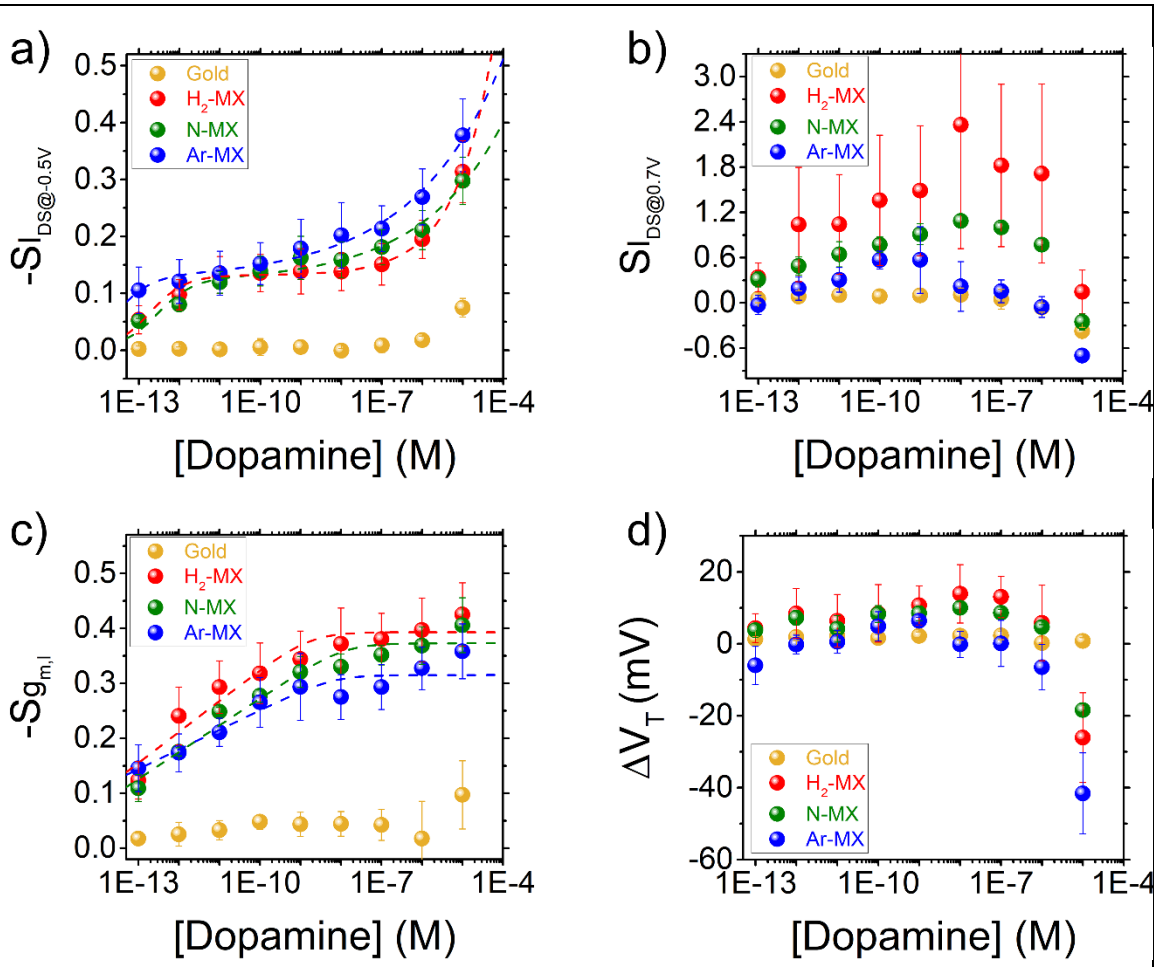

***Figure 5.7**: Dopamine sensing. a,b) Semilog plot of the current signal SI_{DS} calculated at -0.5 V and +0.7 V, respectively vs [Dopamine]; c) Semilog plot of the transconductance signal Sgm,I vs [Dopamine]; d) Semilog plot of the ΔVT vs [Dopamine]. Orange markers for not-functionalized, bare gold electrodes, red markers for H_2-MX, green markers for N-MX and blue markers for Ar-MX functionalized electrodes.*

To model this behaviour, the experimental data ($-SI_{DS}$ at V_{GS} -0.5 V vs [Dopamine]) are fitted using an *ad-hoc*, two term, phenomenological model (Equation 5.2):

$$SI_{DS} = S_{max}\frac{[DA]}{(K_D+[DA])} + \left(\frac{[DA]}{C_0}\right)^n \quad \text{(Eq. 5.2)}$$

The first term, a Langmuir-like isotherm, describes the high-affinity, specific binding of DA to the functionalized MXene surface. This process dominates at low concentrations, saturates at a maximum signal S_{max}, and is characterized by an apparent dissociation constant K_D.

The second term models the interaction mechanism that becomes dominant at concentrations higher than 1 μM. In this term, C_0 represents an upper limit of detection[41,42], and n is its characteristic growth exponent. We hypothesize that this second signal rise (at concentration higher than 1 μM) could be explained as a non-specific adsorption related to the electro-oxidation of DA to DQ and subsequent partial electrodeposition of polydopamine.

This two-mechanism hypothesis is strongly corroborated by our control experiment. The non-functionalized, bare gold electrode (orange data in **Figure 5.7**) shows a negligible response at low concentrations, confirming that the high-affinity binding is specific to MXenes functionalization. However, the signal extracted from bare gold electrodes exhibit a signal increase (in absolute value) at 10 μM, supporting the idea that the high-concentration mechanism is non-specific and related to DA electro-oxidation.

In **Figure 5.7b**, the signal calculated with the current at the off state (I_{DS} at V_{GS} = +0.7 V) is plotted against target concentration and provides compelling evidence for two distinct mechanisms. For all the MXenes, the signal shows an increase towards positive values for increasing [DA] concentrations up to values equal to 1 nM for Ar-MX and 10 nM for H_2-MX and N-MX. At higher concentrations, the trend of the signal clearly reverses, approaching zero or negative values at the same high concentration (> 1 μM) where the DA oxidation process is hypothesized to begin.

To obtain a deeper understanding of the response of the MXene-functionalized EGOT when exposed to increasing DA concentration, the transfer curves are fitted with the unified analytical model for EGOTs, recently published by Zanotti *et al.,*[43].Fitting the transfer curves with Equation 4.1, the following parameters are extracted and monitored as a function of the analyte concentration for the three MXene samples: V_T (switch-on voltage), σ (energy disorder of the density of states (DOS) of the organic semiconductor), $g_{m,l}$ (linear transconductance) and the parameter α ($\alpha = 2e^2dn_{max}/C_{DL}\sigma$, which describes the ratio of the areal charge densities.

The outcome of the analysis confirms the presence of two binding modes between MXenes and DA. The signal of the linear transconductance $S_{g_{m,l}} = (g_{m,l}[DA]$ -

$gm_{,I0})/g_{m,I0}$ shows a decreasing monotonic trend, reaching a reduction of 35-40% at the highest DA concentration for all three chemically-engineered MXenes (**Figure 5.8c**). The variation of linear transconductance ($S_{g_{m,I}}$) upon exposure to increasing concentration of DA can be ascribed primarily to the change in interfacial capacitance.[40,44] The monotonic behaviour of $S_{g_{m,I}}$ dose-calibration curve could be well described by the Universal Langmuir Model (UML) (Equation 4.3). The ULM, characterized by a population of binding sites with binding energy within a range of [U_{min}; U_{max}], could encompass the different surface terminations (or local inhomogeneity) of the MXene functionalization layer, leading to a heterogeneous energy landscape across the gate electrode surface. Since ULM is successfully demonstrated to describe the selective binding events between analyte and recognition probe[30,45,46], the $S_{g_{m,I}}$ trend can be confidently attributed to the specific binding between the MXene layer and DA. This interaction results in a variation of the interfacial capacitance and, consequently, of the linear transconductance. This specific binding mechanism exhibits a steep response in the low concentration range (from 10^{-13} to 10^{-7} M), consistent with high affinity interaction, before saturating at concentrations above 100 nM.

Figure 5.7d shows the trend of the switch-on shift $\Delta V_T = V_T[DA] - V_{T,0}$ for the three MXenes, where $V_{T,0}$ is the V_T measured without the target analyte. ΔV_T increases towards positive values for increasing [DA] concentrations, achieving its maximum positive value at 1 nM for Ar-MX and 10 nM for H_2-MX and N-MX. The trend of the ΔV_T then clearly reverses, dropping to negative values (- 27 mV for H_2-MX, - 19 mV for N-MX and -42 mV for Ar-MX) at the 10 μM DA concentration. The switch-on voltage V_T represents the gate voltage at which the semiconductor is in the flatband (or charge neutrality condition). V_T influences the initial doping level of the EGOTs by modulating the effective gate voltage $v = e(V_{GS}-V_T)/\sigma$ and therefore depends on the work function variations of the gate electrode and/or of the semiconductive channel. The “parabolic” trend observed in **Figure 5.7d** provides further evidence for two distinct interaction mechanisms between MXene and DA. As discussed earlier, for low [DA], the interaction between DA and MXene leads to a variation of the interfacial capacitance and therefore of the $S_{g_{m,I}}$. This results in a modest, V_T shift towards positive values, as reported elsewhere for specific DA binding.[39] For [DA] > 1 μM a marked ΔV_T shift at negative values is observed for all the chemically-functionalized MXenes. This behaviour could be ascribed to the electro-oxidation of DA to DQ that takes places at the gate electrode (**Figure 5.6**) and results in a

negative drift of ΔV_T, as previously demonstrated by Mariani and co-workers.[47] The outcome of the presented multiparametric analysis highlights intriguing aspects of the interactions between DA and chemically-engineered MXenes; these aspects can be fully interpreted by processing the EGOT multiparametric response via multivariate analysis techniques, as detailed in the following chapter.

5.3 Probing the MXene-Dopamine Interaction with Multivariate Data Analysis

The primary figures of merit extracted from the transfer curves (**Figure 5.7**) appear largely comparable for all the tested chemically-functionalized MXenes. The inherent structural complexity of MXenes, coupled with their varied surface terminations, prevents the establishment of a direct relationship between the sensor response and specific chemical characteristics of the active materials. Furthermore, the biosensor response itself is demonstrably non-univariate. To further delucidate the interaction mechanisms between the MXene surface structure and the DA, the complex, multiparametric response of EGOT device is leveraged with principal component analysis (PCA). As reported in Chapter 4, PCA enriches the framework for explaining the subtle variations. As a first step, Principal Component Analysis (PCA) is performed on the renormalized parameters extracted from the transfer curves. In addition to the parameters derived in **Figure 5.7**, the dataset for the multivariate analysis is competed with the $\Delta\alpha$, $\Delta\sigma$ parameters, and the current signal calculated at +0.2 V ($S_{I_{DS}}$ at V_{GS} = +0.2 V), to provide a more complete description of the transfer curves, as shown in the dose-response curves of **Figure 5.8**.

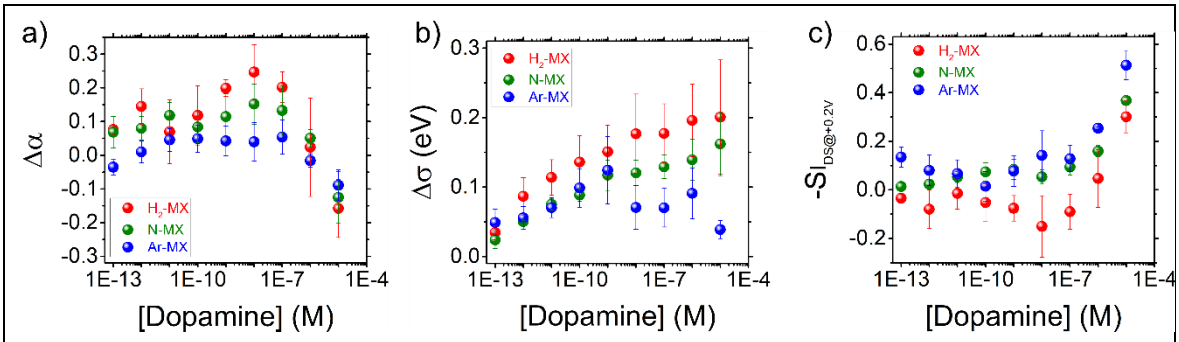

***Figure 5.8**: Dopamine sensing a,b) Semilog plot of the Δα and Δα, respectively vs [Dopamine]; c) Semilog plot of the transconductance signal current signal calculated at + 0.2V vs [Dopamine].*

PCA is an unsupervised technique used as an explorative tool to reduce a large amount of data into a few principal components. The space constructed by these components facilitates the detection of sample groupings and trends more easily than when using the original variables.[48] **Figure 5.9a** displays the PCA scores plot, which clearly clusters the average response of the three chemically-engineered MXenes. The majority of H_2-MX samples (red) are grouped at positive scores on PC1, while Ar-MX samples (blue) are grouped at negative scores on both PC1 and PC5. N-MX samples (green), in contrast, exhibit scores on PC1 close to zero and are distributed around the PC5 centreline, showing positive and slightly negative scores. Despite the high degree of similarity in the single-parameter response exhibited by all three MXene-based sensors, the PCA approach successfully reveals more subtle variations among the chemically-functionalized MXenes.

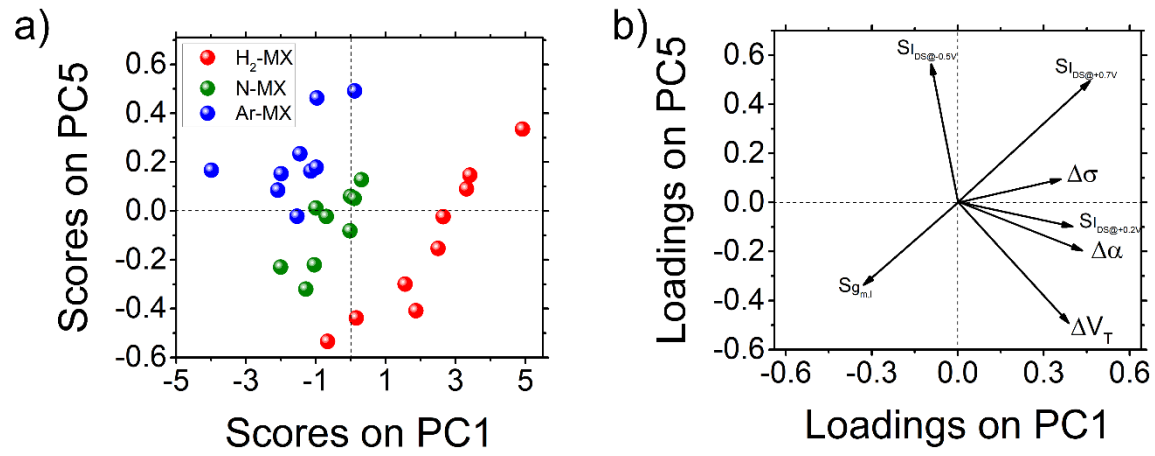

***Figure 5.9**: PCA clusterized the average response of the chemically-engineered MXenes. a) The scores plot obtained by applying the PCA on the renormalized set of the parameters extracted from the MXene-based EGOT devices. b) The corresponding loadings plot.*

In **Figure 5.9b**, the loadings plot (*viz.,* the weight of each variable in determining the direction of the PCs) offers crucial insights into the interaction mechanisms established between the MXene layer and DA during the sensing process. The discussion starts with the H_2-MX samples, which cluster strongly on the positive side of PC1, a region that is anti-correlated with the transconductance-related variable, $Sg_{m,I}$ (located on the negative side of PC1). This strong anti-correlation confirms that H_2-MX exhibits the highest absolute value for $Sg_{m,I}$. Since the variation in transconductance in an EGOT-based biosensor is primarily ascribed to the change in interfacial capacitance[40,44], this finding is consistent with a predominantly electrostatic MXene-DA interaction. The electrochemical character likely becomes active only at very high DA concentrations. The strong electrostatic interaction attributed to H_2-MX is consistent with the high concentration of C-OH bonds and surface Ti atoms, as depicted in the HRXPS analysis.

On the other hand, the Ar-MX samples are strongly anti-correlated with ΔV_T along PC1. This anti-correlation implies that Ar-MX shows a highly negative ΔV_T, which can be explained by the electrochemical oxidation of DA. The higher electrochemical character of the MXene-DA interaction for Ar-MX is consistent with the high concentration of carbonyl groups provided by the Ar-MX surface modification, which typically increases the pseudocapacitance of the MXene layer.

N-MX, however, exhibits a hybrid behaviour with respect to Ar-MX and H_2-MX. This intermediate behaviour, reflected by its central position in the scores plot, can be ascribed to a balanced combination of factors: the high content of Ti and N atoms on the N-MX surface enhances the electrostatic/specific interaction, while the presence of amino groups acts as a pseudocapacitive site, increasing the electrochemical interactions.

Figure 5.10 shows the results of the PCA applied to the entire dataset of the renormalized sensing parameters. While the clustering of samples is less distinct than the analysis performed only on the average values (**Figure 5.8**) due to the inherent variability of the sensor response, clear trends are still observable in the PC1 and PC3 plane.

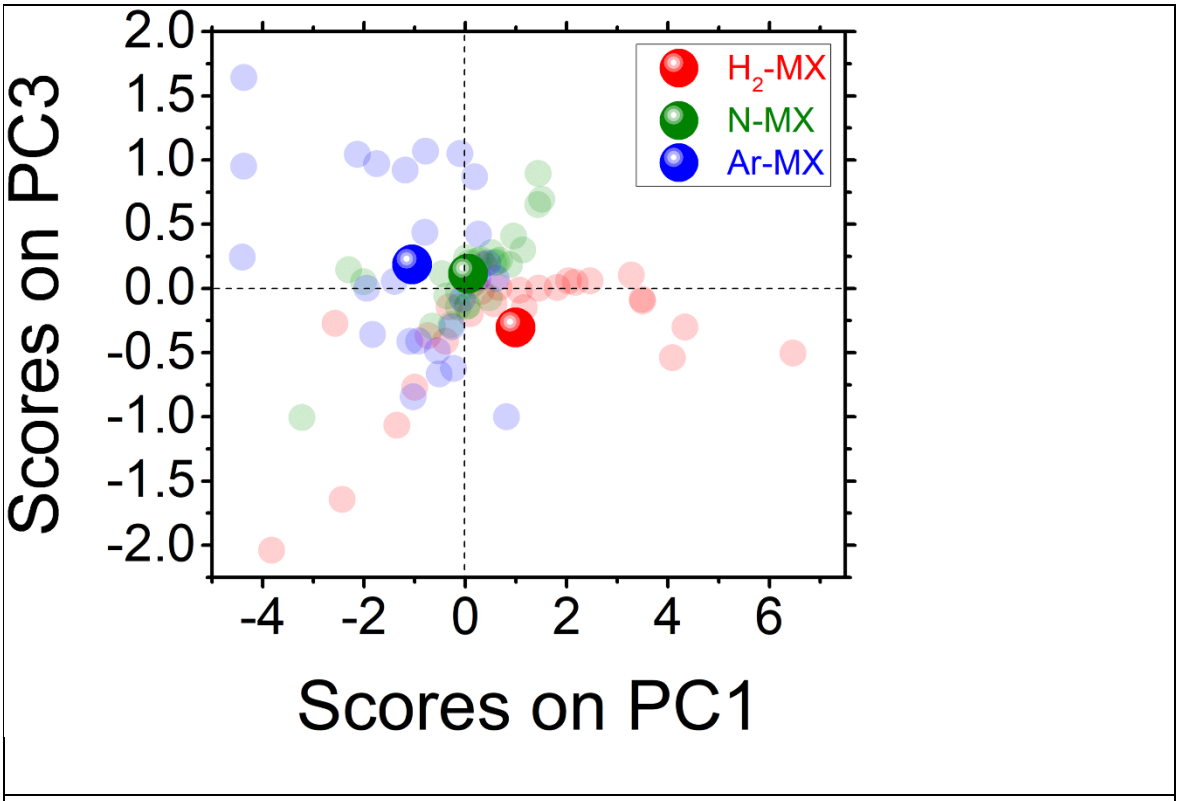

***Figure 5.10**: PCA score plot on the entire data set of the renormalized parameters. Transparent circles represent all the experimental points at different concentrations, whereas spheres are the mean values of the scores on PC1 and PC3.*

The resulting distribution is notably consistent with the separation previously observed when using the average parameters. Specifically, the H_2-MX samples are primarily located in the region exhibiting positive values on PC1 and negative values on PC3. The N-MX samples maintain an intermediate behaviour between H_2-MX

and Ar-MX, with their scores clustering closely around the origin on both the PC1 and PC3 axes. In contrast, Ar-MX provides the largest vertical dispersion of the experimental data points across PC3 yet remains distinctly separated from the other two MXene samples along the PC1 axis. Crucially, this analysis on the full dataset confirms that, despite the experimental variability, the PCA is highly effective in highlighting subtle differences in the behaviour of the various MXenes that single-parameter analysis would not be able to resolve. The resulting clustering strengthens the hypothesis that the distinct surface terminations of the MXenes modulate the relative weight of each proposed sensing mechanism (electrostatic vs. electrochemical) in the DA-MXene interaction.

Although these findings are noteworthy, the mechanistic insight could be further elucidated by employing supervised chemometric algorithms, such as Partial Least Squares (PLS) Regression, to correlate the device response matrix with MXene molecular descriptors. Adopting such strategies opens new avenues in organic bioelectronics, offering a unique opportunity to uncover complex correlations that would otherwise remain elusive to univariate data analysis techniques.

5.4 Bibliography

[1] N. F. Atta, A. Galal, F. M. Abu-Attia, S. M. Azab, *J. Electrochem. Soc.* 2010, *157*, F116.

[2] W. Oertel, J. B. Schulz, *J. Neurochem.* 2016, *139*, 325–337.

[3] L. Speranza, U. Di Porzio, D. Viggiano, A. De Donato, F. Volpicelli, *Cells* 2021, *10*.

[4] S. Lakard, I. A. Pavel, B. Lakard, *Biosensors* 2021, *11*, DOI 10.3390/bios11060179.

[5] G. Burns, M. Y. Ali, M. M. R. Howlader, *TrAC - Trends Anal. Chem.* 2023, *169*, 117367.

[6] Z. F. Lin, H. Li, Z. C. Chen, G. C. Han, X. Z. Feng, H. B. Kraatz, *Microchem. J.* 2025, *212*, DOI 10.1016/j.microc.2025.113535.

[7] H. Zhu, G. Xu, *Clin. Chim. Acta* 2025, *566*, DOI 10.1016/j.cca.2024.120039.

[8] X. Liu, J. Liu, *View* 2021, *2*, 1–16.

[9] F. Rondelli, M. Di Lauro, G. Calandra Sebastianaella, A. De Salvo, M. Genitoni, M. Murgia, P. Greco, C. G. Ferroni, R. Viaro, L. Fadiga, F. Biscarini, *Adv. Electron. Mater.* 2024, *10*, 1–9.

[10] J. A. Johnson, R. Mark Wightman, *Electrochem. Soc. Interface* 2017, *26*, 53–57.

[11] X. B. Joseph, N. M. Umesh, S. F. Wang, J. A. Jesila, *New J. Chem.* 2021, *45*, 18131–18138.

[12] T. Kokulnathan, T. J. Wang, E. A. Kumar, N. Duraisamy, An-Ting Lee, *Sensors Actuators B Chem.* 2021, *349*, 130787.

[13] I. Gualandi, D. Tonelli, F. Mariani, E. Scavetta, M. Marzocchi, B. Fraboni, *Sci. Rep.* 2016, *6*, 1–10.

[14] J. Shakya, M. A. Kang, J. Li, A. VahidMohammadi, W. Tian, E. Zeglio, M. M. Hamedi, *Nanoscale* 2024, *16*, 2883–2893.

[15] Y. Li, Z. Peng, N. J. Holl, M. R. Hassan, J. M. Pappas, C. Wei, O. H. Izadi, Y. Wang, X. Dong, C. Wang, Y. W. Huang, D. Kim, C. Wu, *ACS Omega* 2021, *6*, 6643–6653.

[16] Z. Cai, B. Tu, R. Zhou, D. Xia, H. He, N. Gao, G. Chang, Y. He, *J. Electroanal. Chem.* 2023, *928*, DOI 10.1016/j.jelechem.2022.117012.

[17] H. Wang, J. Guo, Y. Chen, N. Xu, T. Xu, Z. Xu, *Microchem. J.* 2025, *212*, DOI 10.1016/j.microc.2025.113362.

[18] B. Xu, M. Zhu, W. Zhang, X. Zhen, Z. Pei, Q. Xue, C. Zhi, P. Shi, *Adv. Mater.* 2016, *28*, 3333–3339.

[19] R. Zhou, B. Tu, D. Xia, H. He, Z. Cai, N. Gao, G. Chang, Y. He, *Anal. Chim. Acta* 2022, *1201*, DOI 10.1016/j.aca.2022.339653.

[20] Y. Wei, P. Zhang, R. A. Soomro, Q. Zhu, B. Xu, *Adv. Mater.* 2021, *33*, 1–30.

[21] K. R. G. Lim, M. Shekhirev, B. C. Wyatt, B. Anasori, Y. Gogotsi, Z. W. Seh, *Nat. Synth.* 2022, *1*, 601–614.

[22] K. Allen-Perry, W. Straka, D. Keith, S. Han, L. Reynolds, B. Gautam, D. E. Autrey, *Materials (Basel).* 2021, *14*, 1–9.

[23] H. Wang, Y. Wu, J. Zhang, G. Li, H. Huang, X. Zhang, Q. Jiang, *Mater. Lett.* 2015, *160*, 537–540.

[24] S. Adomaviciute-Grabusove, A. Popov, S. Ramanavicius, V. Sablinskas, K. Shevchuk, O. Gogotsi, I. Baginskiy, Y. Gogotsi, A. Ramanavicius, *ACS Nano* 2024, *18*, 13184–13195.

[25] K. Maleski, V. N. Mochalin, Y. Gogotsi, *Chem. Mater.* 2017, *29*, 1632–1640.

[26] M. Mohammadniaei, A. Koyappayil, Y. Sun, J. Min, M. H. Lee, *Biosens. Bioelectron.* 2020, *159*, DOI 10.1016/j.bios.2020.112208.

[27] T. Guo, W. Wei, J. Chai, Y. Ren, Murat Yilmaz, A. Uddin, A. Cabot, D. Zhou,

Small 2025, *e08556*, 1–12.

[28] N. Anjum, A. Al Noman, M. M. Rahman, D. Sen, R. A. Lazenby, O. I. Okoli, *J. Compos. Sci.* 2025, *9*, 1–21.

[29] A. Rozmysłowska-Wojciechowska, J. Mitrzak, A. Szuplewska, M. Chudy, J. Woźniak, M. Petrus, T. Wojciechowski, A. S. Vasilchenko, A. M. Jastrzebska, *Materials (Basel).* 2020, *13*, DOI 10.3390/ma13102347.

[30] R. Zanotti, M. Berto, M. Sensi, A. Paradisi, E. Veronese, L. Pasquato, C. A. Bortolotti, P. Metrangolo, F. Biscarini, *Adv. Funct. Mater.* 2025, *08425*, 1–12.

[31] Y. Tian, P. Hou, H. Zhang, Y. Xie, G. Chen, Q. Li, F. Du, A. Vojvodic, J. Wu, X. Meng, *Nat. Commun.* 2024, *15*, 1–10.

[32] M. D. Levi, M. R. Lukatskaya, S. Sigalo, M. Beidaghi, N. Shpigel, L. Daikhin, D. Aurbach, M. W. Barsoum, Y. Gogotsi, *Adv. Energy Mater.* 2015, *5*.

[33] M. R. Lukatskaya, O. Mashtalir, C. E. Ren, Y. Dall'Agnese, P. Rozier, P. L. Taberna, M. Naguib, P. Simon, M. W. Barsoum, Y. Gogotsia, *MXenes From Discov. to Appl. Two-Dimensional Met. Carbides Nitrides* 2013, *2*, 665–675.

[34] M. R. Lukatskaya, S. M. Bak, X. Yu, X. Q. Yang, M. W. Barsoum, Y. Gogotsi, *Adv. Energy Mater.* 2015, *5*, 2–5.

[35] M. R. Lukatskaya, S. Kota, Z. Lin, M. Q. Zhao, N. Shpigel, M. D. Levi, J. Halim, P. L. Taberna, M. W. Barsoum, P. Simon, Y. Gogotsi, *Nat. Energy* 2017, *6*, 1–6.

[36] C. Zhan, M. Naguib, M. Lukatskaya, P. R. C. Kent, Y. Gogotsi, D. E. Jiang, *J. Phys. Chem. Lett.* 2018, *9*, 1223–1228.

[37] L. X. Li, F. Li, *Xinxing Tan Cailiao/New Carbon Mater.* 2011, *26*, 224–228.

[38] J. Wan, R. Wu, Y. Chen, H. Zhang, H. Li, B. Wang, T. Liskiewicz, S. Shi, *Appl. Surf. Sci.* 2024, *678*, 161154.

[39] S. Casalini, F. Leonardi, T. Cramer, F. Biscarini, *Org. Electron.* 2013, *14*, 156–163.

[40] I. Sergi, M. Sensi, R. Zanotti, T. Tsironi, E. Flemetakis, D. M. Power, C. A. Bortolotti, F. Biscarini, *Biosens. Bioelectron.* 2025, *271*, DOI 10.1016/j.bios.2024.117098.

[41] M. Giordani, M. Sensi, M. Berto, M. Di Lauro, C. A. Bortolotti, H. L. Gomes, M. Zoli, F. Zerbetto, L. Fadiga, F. Biscarini, *Adv. Funct. Mater.* 2020, *30*, 1–13.

[42] M. Giordani, M. Berto, M. Di Lauro, C. A. Bortolotti, M. Zoli, F. Biscarini, *ACS Sensors* 2017, *2*, 1756–1760.

[43] R. Zanotti, M. Sensi, M. Berto, A. Paradisi, M. Bianchi, P. Greco, C. A. Bortolotti, M. Di Lauro, F. Biscarini, *Adv. Mater.* 2024, *36*, DOI 10.1002/adma.202410940.

[44] V. Parkula, M. Berto, C. Diacci, B. Patrahau, M. Di Lauro, A. Kovtun, A. Liscio, M. Sensi, P. Samorì, P. Greco, C. A. Bortolotti, F. Biscarini, *Anal. Chem.* 2020, *92*, 9330–9337.

[45] A. Paradisi, M. Berto, M. Di Giosia, S. Mazzali, M. Borsari, T. D. Marforio, F. Zerbetto, M. Calvaresi, A. Orieshyna, N. Amdursky, C. A. Bortolotti, F. Biscarini, *Chem. - A Eur. J.* 2023, *29*, DOI 10.1002/chem.202301704.

[46] M. Sensi, A. Ricci, G. Rigillo, A. Paradisi, M. Berto, N. Gnesutta, C. Imbriano, F. Biscarini, C. A. Bortolotti, *J. Mater. Chem. C* 2024, *12*, 7596–7604.

[47] F. Mariani, T. Quast, C. Andronescu, I. Gualandi, B. Fraboni, D. Tonelli, E. Scavetta, W. Schuhmann, *Microchim. Acta* 2020, *187*, 1–11.

[48] M. Li Vigni, C. Durante, M. Cocchi, *Exploratory Data Analysis*, Copyright © 2013 Elsevier B.V. All Rights Reserved., 2013.

Chapter 6: Ion Dynamics at the Electrolyte-Semiconductor Interface Tunes the Transient and the Steady-state Response of EGOTs.

This chapter investigates the fundamental device physics of Electrolyte-Gated Organic Transistors (EGOTs), focusing on the cation interactions at the channel/electrolyte interface, to support the translational potential of Organic-Mixed Ionic Electronic Conductors (OMIECs).

The study is twofold. First, we explore the interaction of ions with reduced Graphene Oxide (rGO)-EGTs, fabricated via a novel and tailorable protocol based on in-situ electrodeposition from a GO dispersion. Following the optimization of a specific electrical conditioning procedure, these devices demonstrate tunable cation intercalation that translates into robust multilevel memory characteristics, paving the way for the development of neuromorphic platforms.

Second, the investigation into ion dynamics is extended to PEDOT:PSS-based EGOTs operating in electrolytes of varying composition (specifically, pH and the nature of the ionic species). Here, the device's multiparametric response is leveraged to explore correlations between steady-state electrical behaviour and the physicochemical properties of the electrolyte. Although the results are preliminary, this analysis offers initial insights into the potential impact of ionic species on modulating the charge transport mechanism within PEDOT:PSS.

In this thesis, the fundamental strategies to tailor the response of EGOT devices are presented in previous chapters, including the gate electrode functionalization and post-process, multivariate data analysis. This sixth chapter explores the interface between the Organic Semiconductor (OSC) and the electrolyte.

Since biological systems rely on the modulation of electronic conductivity and ionic transport, for translational applications aiming to mimic brain behaviour (*viz.,* neuromorphic devices), major attention is focused on organic semiconductors that exhibit higher permeability to external ions (*viz.,* the so-called Organic Mixed Ionic-Electronic Conductors, OMIECs).

As discussed in Section 1.4, the most widely employed material among OMIECs in organic bioelectronic devices is Poly(3,4-ethylenedioxythiophene)polystyrene sulfonate (PEDOT:PSS), a p-type unipolar conductor. Several examples regarding the application of PEDOT:PSS in organic neuromorphic platforms have already been published.[1–10] The neuromorphic response of PEDOT:PSS-based platforms is ascribed to the unbalanced kinetics of ion interaction inside and outside the film when the device is operated by frequency-controlled pulses, which is accompanied by a change of the output current.

Ambipolar conduction (*viz.,* the conduction of both holes and electrons in p-type and n-type regimes, respectively) can reduce the complexity of circuit fabrication and allows for the detection of both cations and anions in a single device.[11]

Among ambipolar materials, reduced Graphene Oxide (rGO) has attracted great interest due to its excellent processability from aqueous Graphene Oxide (GO) dispersions, the tunability of its electronic properties as well as the versatility of the surface chemistry. Furthermore, the intercalation of ionic species within rGO thin films is a well-known phenomenon[12], widely exploited in different applications, including water filtration[13], energy storage[14], and catalysis.[15]

This chapter thoroughly explores the interactions between ionic species and organic semiconductors exhibiting high permeability towards ions, specifically PEDOT:PSS and rGO integrated into the EGOT architecture. As reported by Zanotti *et al.,*[16] both rGO and PEDOT:PSS exhibit a high energy disorder parameter (σ), resulting in the effective capacitance being dominated by the chemical (or quantum for 2D materials) capacitance, which scales linearly with the film thickness. In this context, the description of the phenomenological volumetric capacitance, introduced by Bernards *et al.,* to describe the penetration of ions from the electrolyte into the PEDOT:PSS channel to tune its electronic conductivity[17–20], appears to be less

appropriate, since the charge carrier density in OSCs like PEDOT:PSS can be described by the chemical capacitance, which depends on the material's electronic structure.

Concerning the rGO-EGT platform, a novel fabrication method relying on the *in-situ* electrodeposition of rGO from GO dispersion is discussed in this thesis. To study the dynamic interplay between the active layer and the ionic species, the rGO -EGT is driven with pulsed voltage stimuli and exhibits a tailorable Long-Term Plasticity (LTP). By tuning the transient input signal protocol (*viz.,* applying different numbers of voltage pulses and acting on their amplitudes), it is possible to program multilevel memory with retention timescales over tens of minutes, confirming that *in-situ* electrodeposited rGO-EGTs have promising applications as building blocks for neuromorphic units. On the other hand, the transient response of PEDOT:PSS-based EGOTs is widely studied, both when integrated into neuromorphic platforms[2,5] and in PEDOT:PSS-based EGOTs (*viz.,* organic electrochemical transistors, OECTs) driven by pulsed gate voltage.[21–24] In this thesis, the investigation of the dynamic interaction between ionic species and PEDOT:PSS thin films is further enriched by evaluating the behaviour of PEDOT:PSS-based EGOTs under stability conditions in the presence of different ionic species, a topic which, to the best of our knowledge, has only been explored in a few published studies.[20,25,26] The ion-sensitive properties of PEDOT:PSS-based EGOTs are systematically studied by Lin and collaborators, who tested different cations, including H^+, K^+, Na^+, Ca^{2+}, Al^{3+}.[25] A further contribution on the steady-state response of PEDOT:PSS-based EGOTs in the presence of different cations is provided by Colucci and co-workers, who demonstrated a correlation between the volumetric capacitance and the salting-in ability of the cations.[26]

6.1 Electrodeposited Reduced Graphene Oxide Tunes the Frequency Response in Ambipolar Electrolyte-Gated Transistors

Ambipolar transistors conduct both electrons and holes depending on the gating conditions.[27] Providing n- and p-channel performances, ambipolar devices enable circuit design simplification, low power dissipation, higher robustness by reducing the number of components. Moreover, they work for both positive and negative V_{in} and V_{out} depending on the supply voltage V_{supply}.[28]

Various semiconductors are explored for ambipolar devices: conjugated polymers[29], organic molecules[30], inorganic-organic hybrid materials[31] and 2D materials.[32] One of the most attractive 2D materials for the fabrication of ambipolar Electrolyte-Gated Transistors (EGTs) is reduced Graphene Oxide (rGO). rGO exhibits excellent processability from aqueous graphene oxide (GO) dispersion allowing the coverage of large areas at low costs and easy integrations into various substrates.[33] Moreover, the electronic properties (*viz.,* the conductivity) and surface characteristics (*viz.,* density and variety of oxygen-containing groups) can be tuned according to the fabrication, making rGO a promising material for fabrication of (bio)sensors.[34–38] Additionally, the 2D nature of rGO makes it an excellent host for intercalation of ions and can be exploited to mimic bidirectional signal transmission as well as neurotransmitters intakes/release in biological synapsis.[12,39,40]

The typical route for production of rGO thin films from GO involves two critical aspects: i) GO casting technology; ii) its reduction.[34,35] This complicates the fabrication process and often yields incompletely reduced channels with current in tens of μA range and high off-current. Section 6.1.1 presents a novel, straightforward method for rGO thin film growth *via in-situ* electrochemical reduction of a graphene oxide (GO) dispersion (Experimental details in Section 3.2.2). This fabrication method results in the spontaneous formation of a rGO thin film bridging the source and the drain contacts. Moreover, the presented technology enables thickness control and tailoring of the charge neutrality point. The proposed rGO-EGTs exhibit a stable ambipolar response with I_{DS} current in hundreds of μA range with transconductances higher than 300 μS for both the conductance branches. The peculiar morphological and electrical features exhibiting by the rGO thin film is translated into a strong response of the proposed rGO-EGTs to ion currents. Section

6.1.2 presents the results collected by operating rGO-EGTS in a neuromorphic architecture: the proposed rGO fabrication technology shows LTP, with time-constants and magnitudes that depends on the doping level and hence can be tailored by acting on gate DC bias.

6.1.1 Morphological and Electrical Characterization of rGO-EGTs

In-situ electrodeposition of rGO channels on the interdigitated gold electrodes is performed using a single-run Cyclic Voltammetry (CV), starting from GO dispersion (0.2% in water). The electrodeposition setup features short-circuited source and drain electrodes, acting as working electrode (WE) and a Pt-wire as a self-referenced counter electrode (CE/RE). Details and schematic representation of the setup are reported in Section 3.2.2.

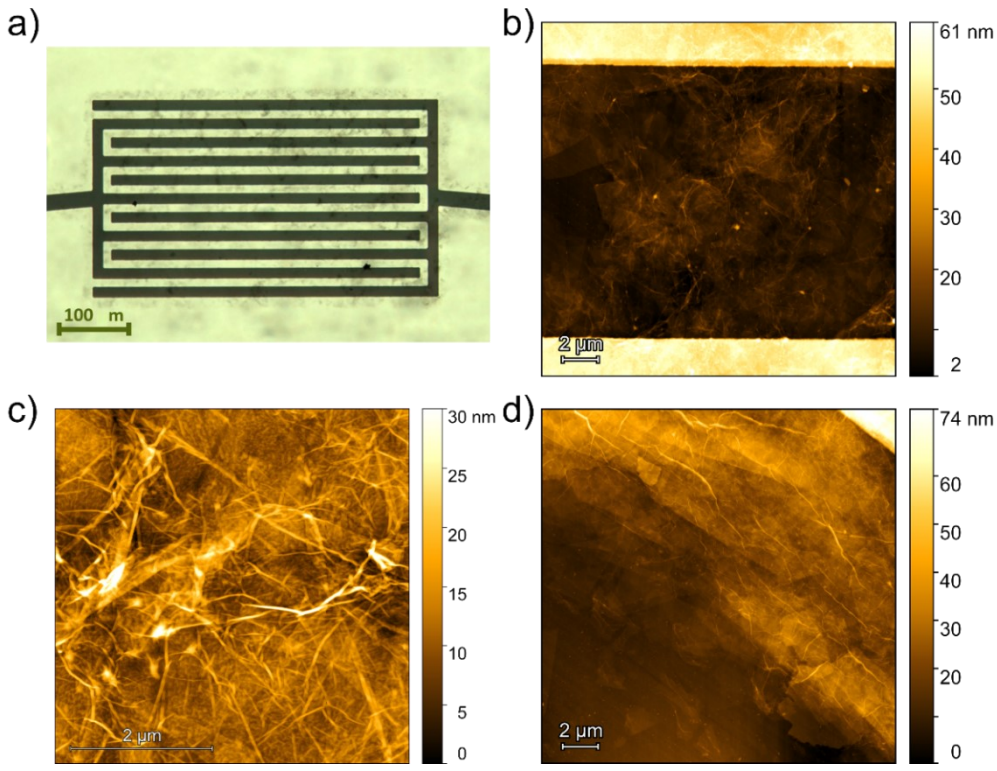

***Figure 6.1**: Morphological characterization of rGO thin films. a) optical image of the interdigitated electrodes (IDEs) after rGO channel deposition. b-c) AFM topography of an rGO single channel at two different magnifications. d) Detail of the edge between rGO and substrate, revealing the stacked, multilayer morphology of the rGO film.*

Figure 6.1 details the morphological characterization of the electrochemically deposited reduced graphene oxide (rGO) film. **Figure 6.1a** provides an optical microscopy image of the gold Interdigitated Electrode (IDE) structure used as the device platform. The electrochemical reduction of the GO solution yields a conductive rGO channel with a spatial resolution of ≈ 25 μm around the IDEs, keeping the residual area of the substrate not conductive. The spatial resolution of such *in-situ*, electrochemical rGO deposition can be tuned with the potential of sweeping rate.[34]

The resulting film morphology is analysed using Atomic Force Microscopy (AFM). **Figure 6.1b** shows the AFM topography of a single channel, capturing two adjacent IDE fingers (the bright, raised areas) and the rGO film connecting them (the darker, central region). **Figure 6.1c** displays a higher-magnification topography scan of the rGO film within the channel. The image reveals a continuous and relatively uniform film formed by overlapping rGO flakes, exhibiting a root-mean-square (rms) roughness of 3.1 ± 0.2 nm ($n_{samples}$ = 3). Further magnification in **Figure 6.1d** of the edge between the gold electrode upon rGO electrodeposition and the substrate confirms the multilayer nature of the deposited film. The network of bright lines clearly shows the wrinkles, folded regions, and boundaries typical of stacked, solution-processed rGO flakes.

The proposed fabrication enables quantitative control over thickness of electrodeposited rGO and over the electrical performance of the rGO-EGT by optimization of the operational parameters, such as the number of electrodeposition cycles, GO concentration and electrochemical potential. Here, it is used a single-run CV, investigating the dependency of rGO thickness and rGO-EGT electrical property on GO concentration and electrodeposition voltage range. To estimate the thickness, rGO films are mechanically scratched and AFM is performed cross the scratch edge (**Figure 6.2**).

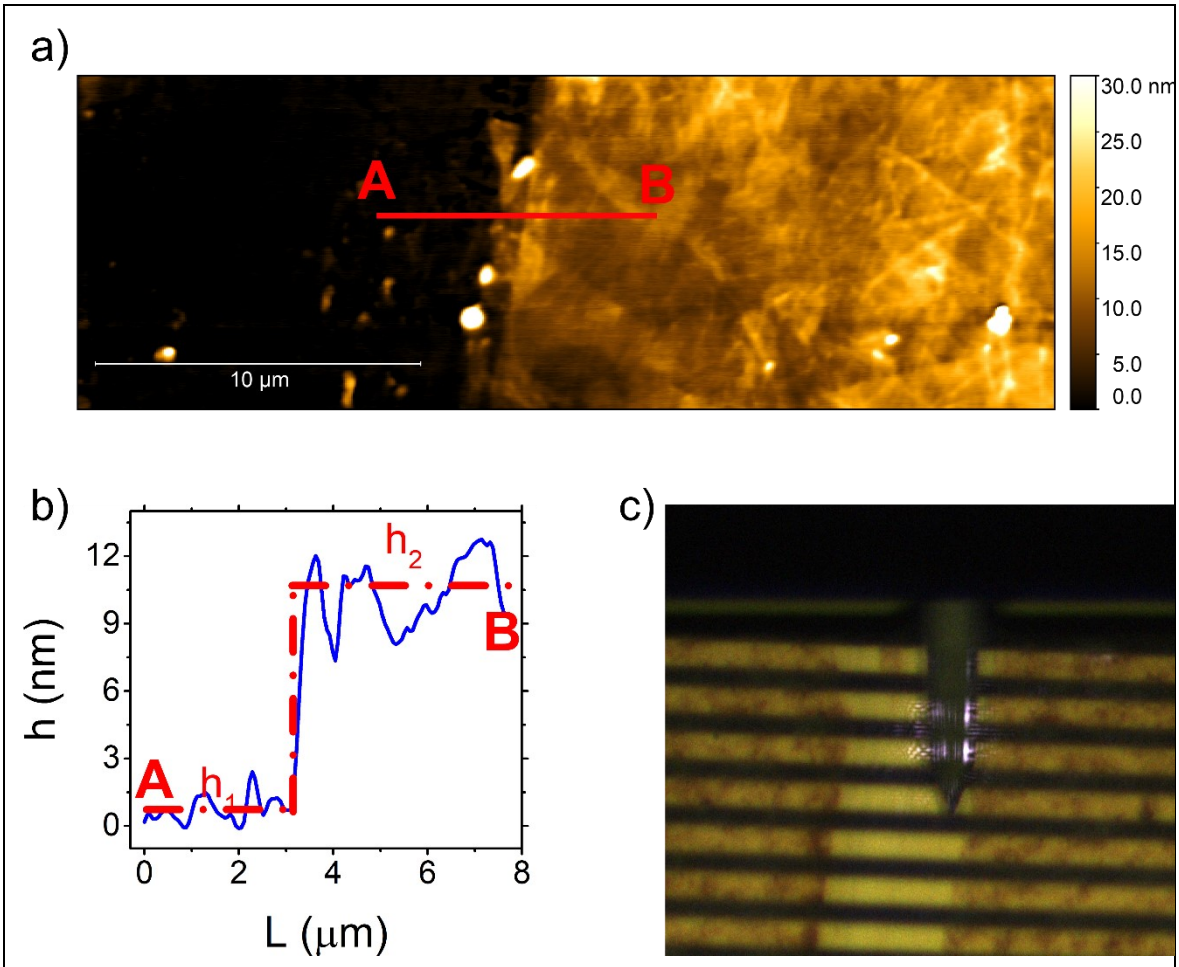

***Figure 6.2**: Thickness assessment: a) AFM image of the edge of the electrodeposited rGO-thin film. b) Corresponding height (h) profile across the scratched edge. Dashed line is step fitting of the height profile. c) The scratched zone on the rGO-EGT channel used for thickness measurement.*

Firstly, the optimization of GO dispersion concentration is assessed. The thickness of the films scales linearly with the GO dispersion concentration (**Figure 6.3a**), in the investigated range (0.1 wt%, 0.4 wt%). The performance of rGO-EGTs fabricated with different GO dispersion concentration reveals that 0.2 wt% of GO dispersion yields the optimal steady-state transfer characteristics in terms of ambipolarity (*viz.,* symmetry), on/off ratio, and V_{CNP} (**Figure 6.3b,d**). At lower concentrations (*viz.,* 0.1 wt%) the thickness of rGO film is very small and does not enable the contact between the IDEs, with I_{DS} current approaching to zero (**Figure 6.3b,c**). Increasing the concentration of GO dispersion up to 0.3 wt% and 0.4 wt% the thickness increases and V_{CNP} is shifted towards more positive values. Moreover, at higher

concentration the on/off ratio of both n- and p- branches decrease, revealing 0.2wt% as optimal concentration of GO dispersion (**Figure 6.3e,f**).

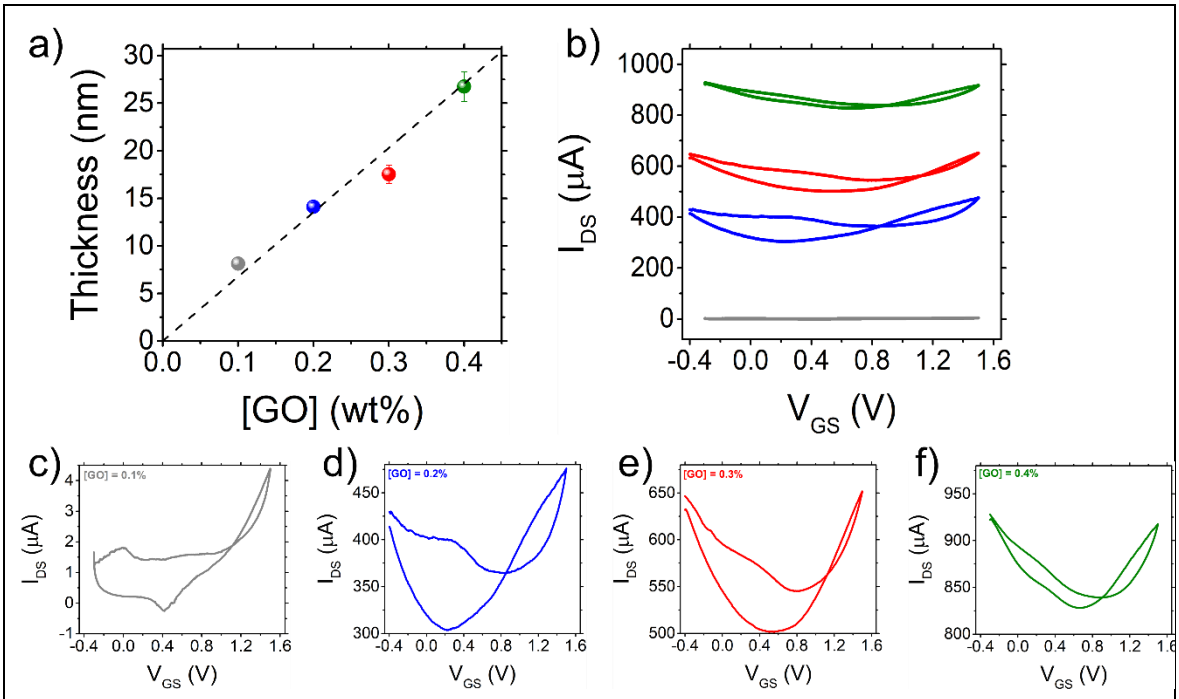

***Figure 6.3**: Evaluation of the GO dispersion concentration over the electrical behaviour of rGO-EGTs. a) Dependency of the thickness of the electrodeposited rGO channels on the concentration of GO dispersions ($n_{samples}$=3, SD as error bars). Dashed lines are linear fitting used as guide for the eyes. b) Representative transfer characteristics (I_{DS} vs V_{GS} plot) after cycling conditioning (viz., the 30th transfer curves, see discussion below for further details) for rGO-EGTs fabricated from GO dispersion at different concentrations. c-f) Details of transfer characteristics with 0.1 wt% (c), 0.2 wt% (d), 0.3 wt% (e), 0.4 wt% (f).*

Furthermore, the effect of CV range during the rGO electrodeposition is investigated by keeping the positive boundary of the scan fixed at -1.3 V and varied the negative boundary (V_{end}) between -2.0 V and -2.8 V. **Figure 6.4** shows the linear variation of rGO films thickness as a function of V_{end}. No electrodeposition is observed for $|V_{end}|$ < -2.4 V (*i.e.*, thickness = 0 nm for -2.3 V < V_{end} < 2.0 V).

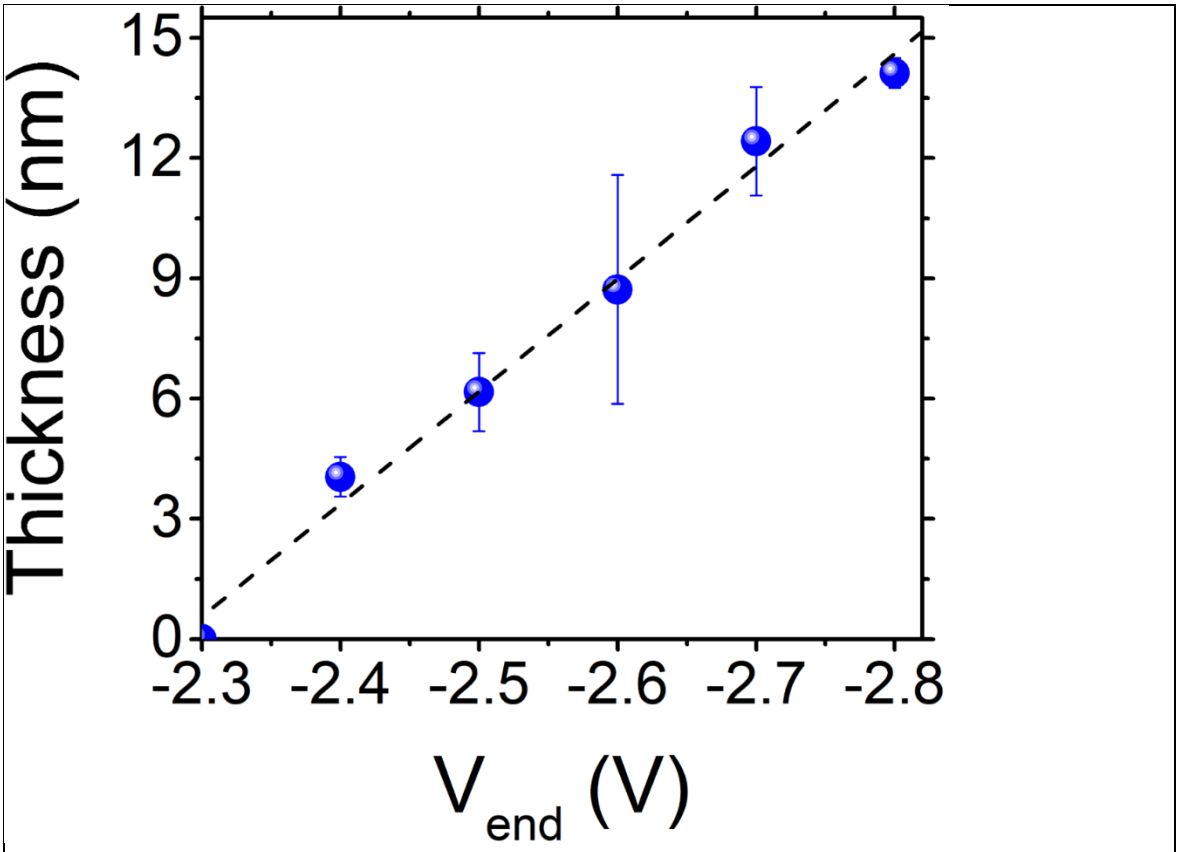

***Figure 6.4**: Dependency of thickness of electrodeposited rGO channels on V_{end} ($n_{samples}$=3, SD as error bars). Dashed lines are linear fitting used as guide for the eyes.*

The combination between the optimal ambipolar response at the steady state, achieved with GO concentration of 0.2 wt%, and the highest possible thickness at the selected GO concentration, achieved for V_{end} = -2.8V, guarantees an optimal number of ion intercalation/adsorption sites. The rGO-EGTs are tested to examine their steady-stated behaviour (*viz.,* the transfer characteristics) and their dynamic response under different bias stimuli by varying the voltage pulses.

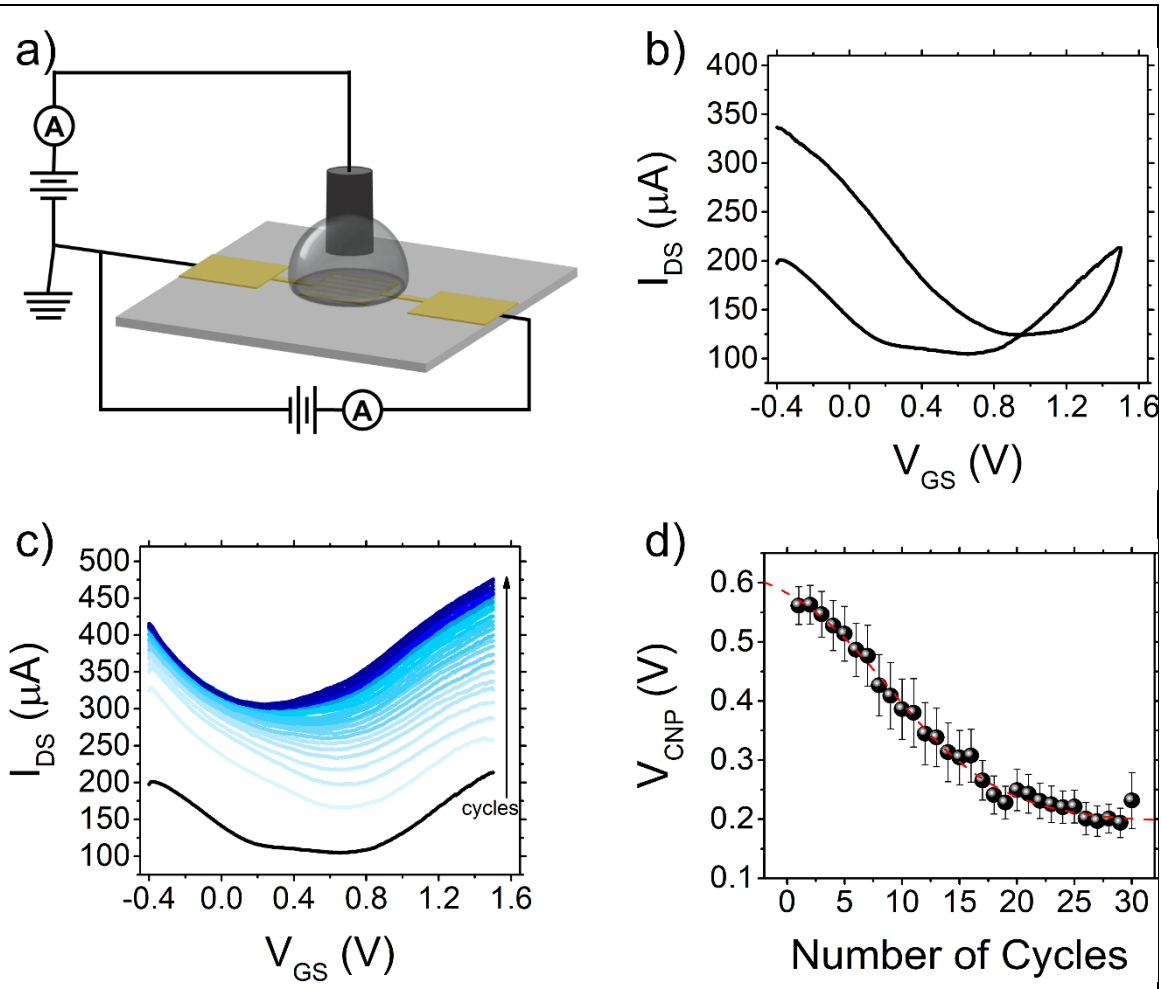

***Figure 6.5**: Electrical characterization of rGO-EGTs. a) rGO-EGT schematics for steady state characterization. b) Transfer characteristic after rGO growth on IDE channels. c) Evaluation of the transfer curves upon iterative VGS cycling (starting from black line to blue line). d) Dependency of VCNP vs the number of the gate sweep cycles ($n_{samples}$ = 9, SEM as error bars).*

rGO-EGTs are characterized in a common-source/common ground configuration (**Figure 6.5a**), using a Pt-wire as gate electrode bathing in a 1M PBS gating electrolyte. **Figure 6.5b** is the representative transfer characteristic of a freshly deposited rGO-EGT. It is possible to observe the hallmarks of ion-gated ambipolar charge transport in the channel: positive gate voltages cause the accumulation/intercalation of cations close to/inside the rGO film, resulting in increased electron transport, *i.e.* n-type branch; the opposite occurs for negative voltages, which cause cation depletion/anion accumulation, resulting in increased hole transport, *i.e.* p-type branch. This behaviour occurs already upon the first gate-

biasing cycle, albeit with a large region (at positive V_{GS}) in which I_{DS} vs V_{GS} is substantially flat. V_{CNP}, which here can be extracted as the V_{GS} value at minimum I_{DS}, lies ≈ 0.7 V, hinting at a strong parasitic p-doping of the channel.[41,42] The pronounced broad minimum of the curve indicates the defect-rich nature of rGO flakes.[43]

The hysteresis behaviour is peculiar, shifting between clockwise hysteresis (*viz.,* easier de-doping than doping) at strongly positive V_{GS} and counter clockwise hysteresis (*viz.,* easier doping than de-doping), typical of organic semi-conductors in electrolytes, which suggests the existence of a critical positive V_{GS} (≈ 0.95 V, **Figure 6.5b**), marking the onset of a region dominated by electrostatic repulsion between incoming and already intercalated cations. Upon repetitive cycling, intercalation/accumulation of cations in the rGO film increases electronic current, corresponding to an increased number of mobile negative charges (*viz.,* additional n-doping, testified by a V_{CNP} negative shift), and to the reduction of junction resistances between adjacent rGO sheets. Typical evolution of the device response upon this iterative conditioning is shown in **Figure 6.5c**. **Figure 6.5d** displays the corresponding V_{CNP} vs cycle trend, demonstrating the attainment of stable device response after ≈ 20 cycles, with a V_{CNP} negative shift greater than 300 mV. To surely achieve stability, all the devices presented herein undergo to 30 conditioning cycles. The sigmoidal trend (**Figure 6.5d**) hints at a two-state transition between states at different free energies. Such bistable behaviour may be due to the metastability of the initial state. The cycle-wise increase of the electron current, which is not quantitatively paralleled by the hole current, results in an increase of I_{DS} at V_{CNP} - termed off current - causing the on/off ratio to decrease.

This shortcoming is addressed by designing a reconditioning procedure, involving the application of a constant negative DC bias at the gate (V_{GS} = -0.5 V, 5 min). The reconditioning procedure removes intercalated cations, yielding a significant off-current lowering (*viz.,* on/off increase) (**Figure 6.6a**). Noteworthy, reconditioning does not restore the parasitic p-doping, instead it brings V_{CNP} closer to 0 V, at the centre of the ideal range for physiological applications. **Figure 6.6a** highlights the effects of reconditioning, showing a before-and-after transfer overlay. The corresponding transconductance vs V_{GS} profiles are shown in **Figure 6.6b**.

The final rGO-EGTs show symmetrical ambipolar behaviour over a wide range of V_{GS} and V_{DS} values (**Figure 6.6c**). Dependency on V_{DS} shows a linear trend with no saturation regime and no substantial contact resistance. A significant symmetry can

be observed when reversing the sign of V_{DS}, as expected for graphene-based transistors.

The necessity of cycling and reconditioning arises from deposition procedure employed for rGO-EGTs fabrication, which favours kinetically controlled local energy minima when it comes to film structure.[44] In particular, partially reduced GO domains embodied in the rGO film would act as p-type dopants (*i.e.,* trap-states for n-type carriers), shifting V_{CNP} to strongly positive values as elsewhere reported.[45] Upon quasi-static cycling followed by DC reconditioning, the system is given the time and the energy to explore a broader free-energy landscape, eventually filling trap-states and ending up in its absolute minimum.

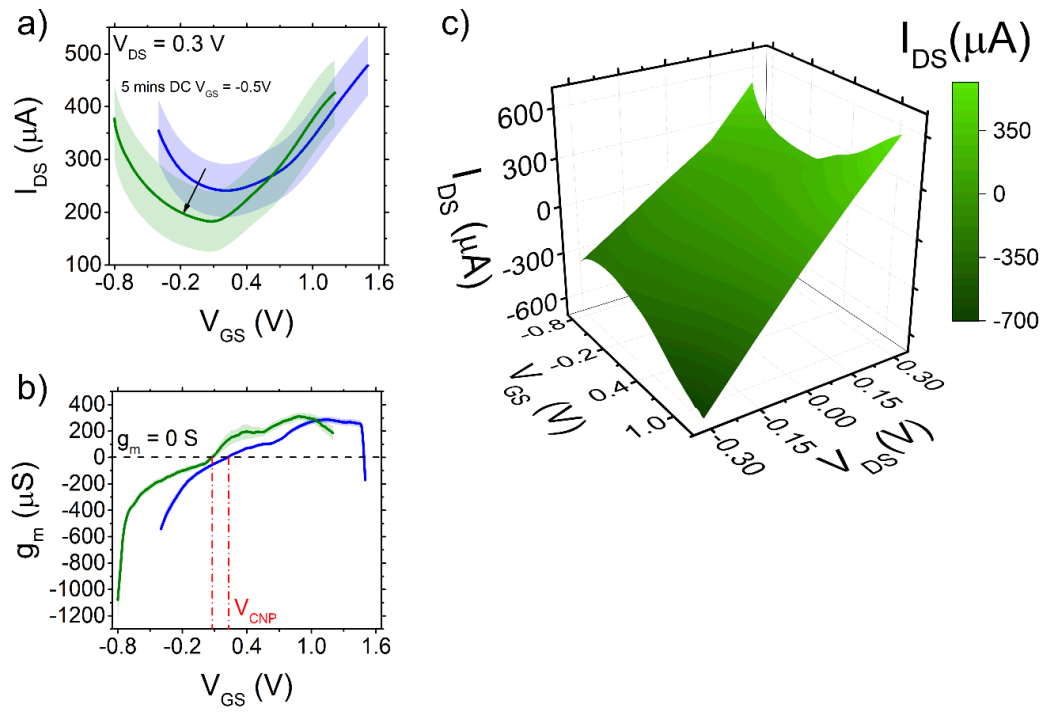

***Figure 6.6**: Effect of the conditioning process on the electrical performance of rGO-EGTs. a) Transfer characteristics of rGO-EGTs before (solid blue line) and after DC gate voltage reconditioning step (green solid line) (n_{sample} = 8 SEM as error bars). b) Improved transconductance (g_m) in rGO-EGTs after reconditioning step (green, solid line) compared to the g_m profile of rGO-EGTs after the 30th V_{GS} sweep (blue solid line) (n_{sample} = 8 SEM as error bars). Negative shift of V_{CNP} after reconditioning is shown as the point at null g_m (red dot-dashed lines). c) 3D representative of I-V characteristics of a representative rGO-EGT.*

6.1.2 rGO-EGTs neuromorphic behaviour

The dynamic response of the rGO-EGTs under different bias stimuli is investigated to elucidate keys aspects of the novel device as ion-to electron transducers. The dynamic response of rGO-EGTs architecture (**Figure 6.7a**) is tested by keeping constant V_{DS} at 0.3 V with V_{GS} that drives square pulses, while recording I_{DS}. In analogy with biological neurons and synapses, V_{GS} represents a presynaptic signal while I_{DS} represents the post synaptic signal. The retention timescale of I_{DS} variations after stimulus removal enables classification of neuromorphic responses between Short-Term Plasticity (STP) and LTP, the former being up to tens of seconds, the latter of tens of minutes at least. A systematic evaluation of the dependency of post-synaptic current upon different amplitudes of single pre-synaptic voltage pulses of amplitude $V_{GS,p}$ is performed by keeping baseline voltage equal to V_{CNP}. Different pulse duration, $\Delta t = t_2 - t_1$, are tested (1, 2, 5, 10 s).The capacitive current spike upon positive pulse application (red solid line in **Figure 6.7b**, bottom panel) relaxes to a plateau during Δt with a trend close to a perfect exponential decay (time-constant τ = 0.10s, stretching exponent β = 0.83) (**inset of Figure 6.7b**). **Figure 6.7c** reports the difference between I_{DS} recorded immediately prior to pulse removal, $I_{DS}(t_2)$, and the baseline current, $I_{DS}(0)$, as a function of $V_{GS,p}$ for Δt = 1 s. Due to rGO ambipolarity, $I_{DS}(t_2) - I_{DS}(0)$, is always positive and its trend mirrors the transfer characteristics of rGO-EGTs (**Figure 6.6a**) since it arises from devices' potentiometric sensitivity.

To quantitatively describe I_{DS} plasticity, Duty-Cycle Plasticity index, DCP_i, is calculated according to Equation 6.1:

$$DCP_i = I_{DS}(t_2 + \Delta t) - I_{DS}(0) \quad \text{(Eq. 6.1)}$$

At positive V_{DS}, I_{DS} is always positive, and $DCP_i < 0$ corresponds to synaptic depression, while $DCP_i > 0$ identifies synaptic potentiation.

The DCP_i dependency on $V_{GS,p}$ for single pulse with a pulse duration Δt = 1 s (**Figure 6.7d**) exhibits a I_{DS} potentiation (*viz.,* positive DCP_i). Such an effect is consistent with the cation intercalation/n-doping into the multi flake rGO matrix[46] and the adsorption of cations onto the rGO surface during Electric Double Layer (EDL) formation.[12] The I_{DS} potentiation under positive V_{GS} suggests the electrostatic interaction of cations with the negatively charged rGO surface.

Conversely, strongly negative $V_{GS,p}$ values ($-0.8\ V < V_{GS,p} < -0.65\ V$) give rise to negative DCP_i (*viz.,* de-doping/depression), with an overall decrease of channel

conductance upon complete cation unloading, despite the potentiating effect which should be observed for anion loading. Interestingly, for single pulses, it is possible to achieve potentiation not only for $V_{GS,p}$ > 0.15 V, but also for negative $V_{GS,p}$ in the range of -0.65 - -0.15 V, hinting that in this region the p-type doping of anion is dominant with respect to the n-de-doping. For -0.15 V < $V_{GS,p}$ < + 0.15 V, DCP_i is close to zero, identifying a region in which only STP might appear, by driving the system with stimuli at high frequency (*i.e.,* $\Delta t < \tau$).

Analysing the influence of pulse duration (Δt) on plasticity reveals a strong asymmetry between the potentiation and depression mechanisms, as shown in **Figure 6.7e**. The depression mechanism, triggered by negative $V_{GS,p}$ pulses, is highly time-dependent. The absolute DCP_i values progressively increase (*viz.,* become more negative) as the pulse duration extends from 1 s to 10 s. This behaviour suggests that depression is a cumulative, diffusion-limited process. This aligns with a mechanism driven by the slow de-intercalation of cations from the rGO channel and the corresponding accumulation of anions at the channel/electrolyte interface, both of which reduce the p-type channel's conductivity.

Conversely, the potentiation mechanism, triggered by positive $V_{GS,p}$ pulses, is largely independent of the pulse width. The DCP_i response saturates quickly, even at the shortest duration of 1 s. This indicates that the cation intercalation into the rGO channel, which dopes the material and increases I_{DS}, is a much faster, non-cumulative process.

These findings highlight a significant advantage of the proposed rGO device. The rapid potentiation achieved with the proposed *in-situ* rGO electrodeposition occurs at substantially shorter pulse durations than those reported for thermally-reduced rGO by Selmi *et al.,*[12] which required pulse widths exceeding 10 s. Furthermore, the maximum I_{DS} potentiation magnitude (**Figure 6.7e**) is considerably higher than that reported by Selmi and co-workers. Taken together, these results demonstrate that the proposed fabrication technique yields rGO thin films with superior modulation efficiency and a more robust charge retention capability. Nonetheless, it is worth noting that differences in experimental parameters, particularly the ionic strength of the electrolyte, prevent drawing definitive conclusions from this comparison. Future work should therefore focus on a systematic study to evaluate the intercalation/de-intercalation capabilities of this *in-situ* approach under identical conditions to those of standard two-step protocols involving GO deposition and post-fabrication reduction.

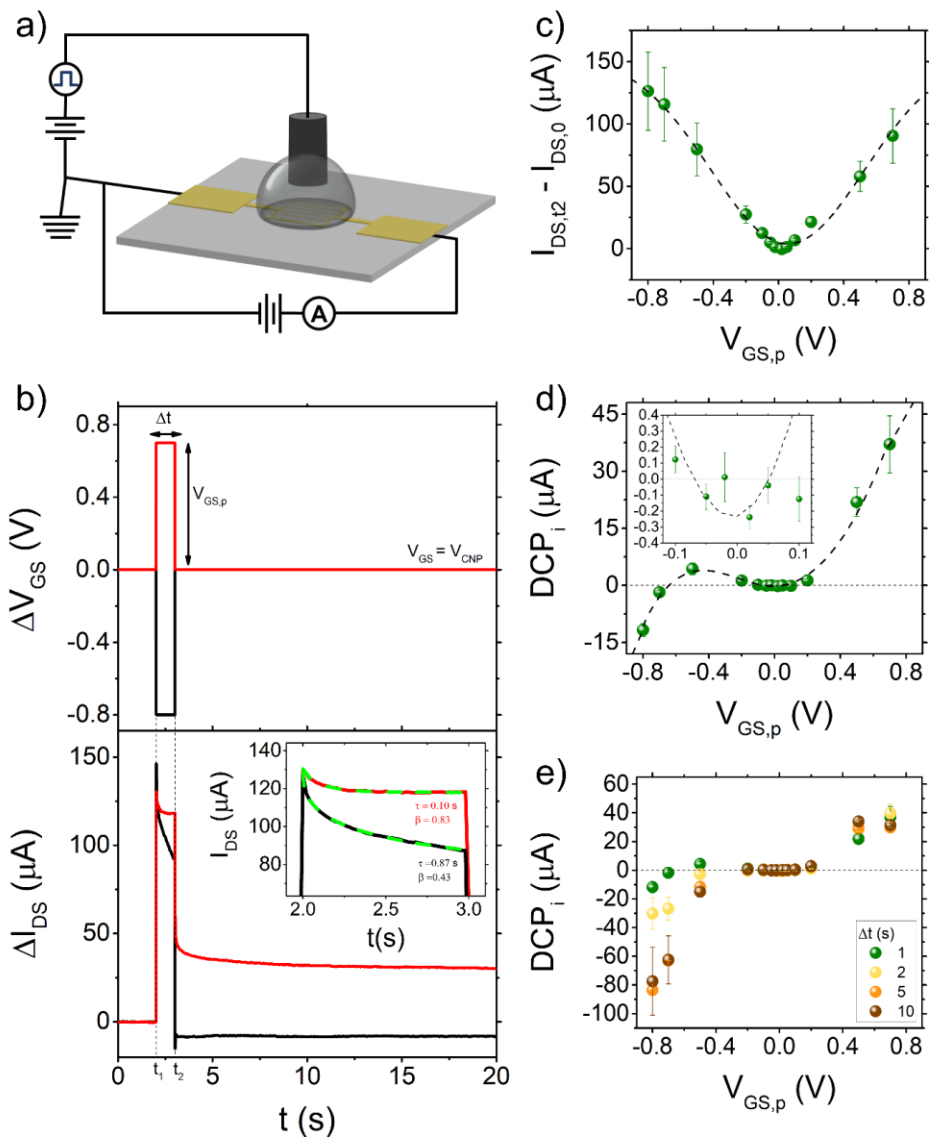

***Figure 6.7**: Single pulse response of rGO-EGTs. a) rGO-EGT schematics for neuromorphic device characterization. b) Representative chronovoltammogram (top) and chronoamperogram (bottom) for positive (red solid line) and negative (black solid line) single voltage pulse administration with a pulse with of 1s. c) Dependency of the pulse current amplitude $I_{DS,t2} - I_{DS,0}$ on $V_{GS,p}$ (n_{sample} = 4, standard error of the mean as error bars). d) DCP_i vs $V_{GS,p}$ trend for Δt = 1 s, highlighting operational windows to achieve tailorable plasticity. It is possible to distinguish four regions: i) $V_{GS,p}$ > 0.15 V elicits potentiation; ii) small values of $V_{GS,p}$ (either positive or negative) do not elicit plasticity, with DCPi values oscillating ≈ 0 μA (zoom in the inset); iii) - 0.65V < $V_{GS,p}$ < −0.15 V elicits potentiation; iv) $V_{GS,p}$ < −0.65V elicits depression (n_{sample} = 4, standard error of the mean as error bars). e) DCP_i vs $V_{GS,p}$ trend for different pulse duration: Δt = 1 s (green), Δt = 2 s (yellow), Δt = 5 s (orange), Δt = 10 s (brown).*

The response of rGO-EGT is also investigated with trains of 320 pulses, keeping the baseline voltage equal to V_{CNP} (**Figure 6.8a,b**).The contour map in **Figure 6.8c** represents the effect of $V_{GS,p}$ and of the number of pulses, n, on the potentiating/depressive plasticity effect, expressed as $\Delta I_{DS,n}$. $\Delta I_{DS,n}$ is defined as the difference between the I_{DS} value prior to administration of the $(n + 1)^{th}$ spike and the I_{DS} value before train administration. According to this contour map, both higher n values and higher $|V_{GS,p}|$ result in a more intense plasticity, either depressive or potentiating. It is worth noticing that, at a fixed $V_{GS,p}$, it is possible to observe a transition between potentiation to depression upon increasing pulse number. This is due to the loss, upon repetitive pulsing, of the dominance of p-type doping with respect to n-type de-doping, already discussed as the origin of the potentiation at negative $V_{GS,p}$ in **Figure 6.7d**.

To achieve full characterization of the performance of rGO-EGTs as multistate memory, the number of distinguishable/accessible conductance states is investigated. An accessible conductance state is defined as the conductance value established after a programming pulse, if it is detectably different from the conductance value prior to the pulse, at a certain pulse frequency. To define the detectability threshold, the number of accessible conductance states is expressed in relation to the noise of the system. Such noise is determined by averaging the rms fluctuations of 52 different 150s-long baseline traces, yielding an average noise value of 0.85 ± 0.15 μA. The noise-limited current resolution, here defined as twice this value, is hence 1.69± 0.29 μA, yielding a nominal conductance resolution of 5.64 ± 0.96 μS. Conservatively, the detectability threshold is set to be slightly higher than the noise-limited current resolution (*viz.,* 2μA, instead of the nominal 1.98 μA).The number of accessible conductance states for programming trains at 0.5 Hz is reported as a function of $V_{GS,p}$ in **Figure 6.8d**, revealing a parabolic-like trend that strongly resembles rGO-EGTs' transfer characteristic, with an asymmetrical behaviour between the potentiation (for $V_{GS,p} > 0$) and the depression ($V_{GS,p} < 0$). In detail, the number of depressive accessible states is larger than the number of potentiating ones. Such asymmetry is rooted in the difference between ion dynamics and relaxation time scales. The depression process is slower, and the saturation of negative train pulses occurs later (*viz.,* at higher n) than for positive train pulses. Subsequently, for negative pulses, the difference between baselines remains for a longer time (*viz.,* for higher n values) above our resolution with respect to what happens for positive ones. As expected from a comparison between DCP_i vs $V_{GS,p}$

(**Figures 6.7d**) and accessible states vs $V_{GS,p}$ (**Figure 6.8d**), small $V_{GS,p}$ values around V_{CNP} identify a region where no plasticity is observed and, hence, a single conductance state is accessible.

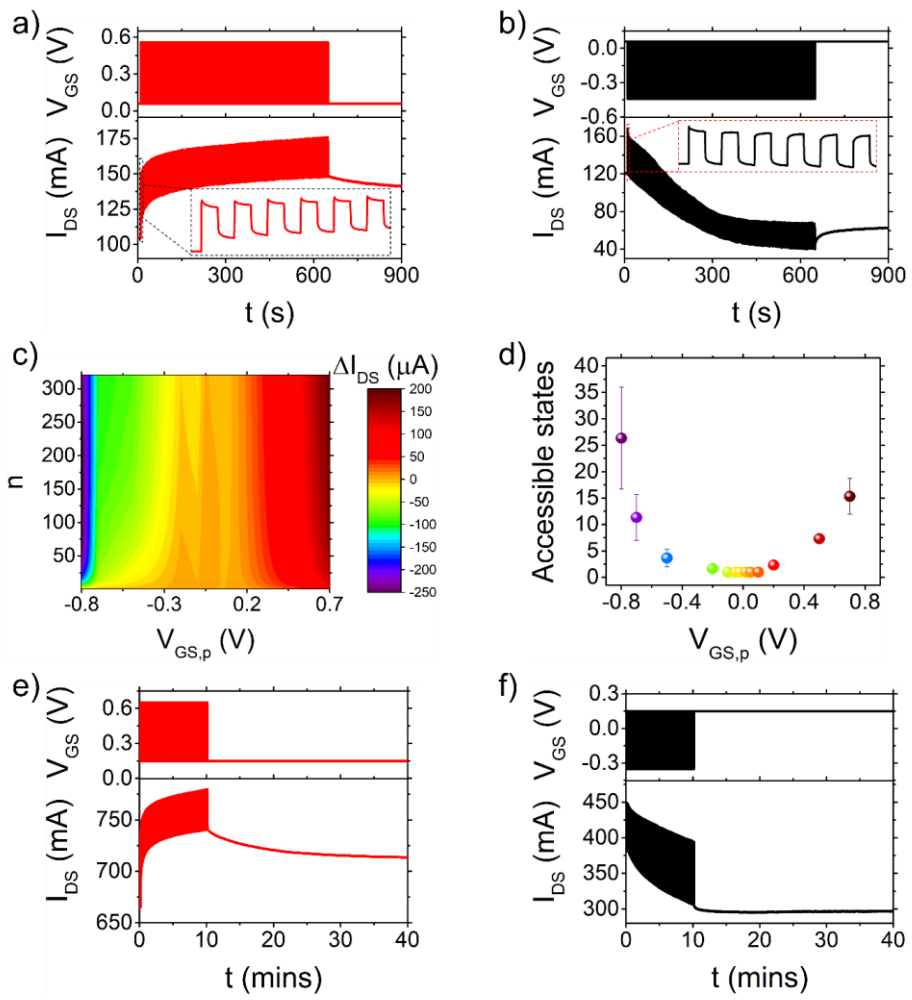

***Figure 6.8**: Response of rGO-EGTs upon pulse train administration. a) Typical input positive square voltage train (top panel, red, $V_{GS,p}$ = +0.5 V, V_{DS} = +0.3 V) and recorded neuromorphic I_{DS} response (bottom panel, red). b) Typical input negative square voltage train (top panel, black, $V_{GS,p}$ = -0.5 V, V_{DS} = +0.3 V) and recorded neuromorphic I_{DS} response (bottom panel, black). Dependency of the baseline current modulation $\Delta I_{DS,n}$ upon the number of administered pulses (n) and upon pulse amplitude ($V_{GS,p}$) (n_{sample} = 3). d) Number of accessible memory states as a function of $V_{GS,p}$ (n_{sample} = 3, SEM as error bars. e) Typical input positive pulse train administration (top panel, red, $V_{GS,p}$ = +0.5 V) and the recorded neuromorphic I_{DS} response (bottom panel, red). f) Typical input negative pulse train administration (top panel, black, $V_{GS,p}$ = -0.5 V) and the recorded neuromorphic I_{DS} response (bottom panel, black).*

Moreover, the long-term retention of plasticity phenomena is assessed by applying pulse trains and recording I_{DS} for 30 min after train removal. This measurement is performed for $V_{GS,p}$ =+ 0.5 V (**Figure 6.8e**) and $V_{GS,p}$ = −0.5 V (**Figure 6.8f**), keeping the voltage fixed at V_{CNP} after pulse train removal. The resulting currents (**Figure 6.8e** and **Figure 6.8f**), show long-term retention of I_{DS} baseline modulation upon programming. This is the hallmark of long-term potentiation (positive $V_{GS,p}$, **Figure 6.8e**) and of long-term depression (negative $V_{GS,p}$, **Figure 6.8f**). LTP amplitudes, estimated as the relative percentage variations between the I_{DS} value at 40 mins and I_{DS} before train administration, amount to roughly 30% for potentiation and 25% for depression.

The demonstrated long-term retention of channel conductance modulated by transient events as square pulse trains are outstanding performances of the rGO-EGT fabrication technology proposed. The device operates as a multilevel, non-volatile memory unit, relying only on rGO-ion interplay, without applying V_{GS} higher than 10 V[47], neither creating rGO-junction exploiting Schottky-barrier height modulation[48] or by developing *ad hoc* composites favouring ion intercalation.[49]

6.2 Influence of Electrolyte Solution Composition on Charge Transport Properties of PEDOT:PSS in Electrolyte-Gated Transistor Architectures (Preliminary Results)

As detailed in the introduction to Chapter 6, this section presents the experimental results concerning the influence of electrolyte solution composition on the performance of EGOTs using PEDOT:PSS as the channel material. Charge transport in a PEDOT:PSS film encompasses the conduction of both electrons and ionic carriers. For this reason, PEDOT:PSS is an archetypical OMIEC.[17–19]

While numerous studies have correlated the transient response of PEDOT:PSS-based EGOTs with the electrolyte composition within the device architecture[21–24], far fewer examples investigate the transistor's response after is stability is reached - specifically, when the steady-state is reached.[20,26,50] Moreover, the existing literature primarily focuses on the nature of the ionic species and generally neglects the influence of the electrolyte's pH on the transistor's electrical performance.

A large body of work has thoroughly investigated how the pH of the PEDOT:PSS solution during the film-casting procedure impacts the thermoelectric, electrical, and morphological properties of the resulting film.[51–54] These studies consistently demonstrated that decreasing the pH of the casting solution (*i.e.,* increasing its acidity) or treating the cast film with an acidic solution significantly enhances the film's conductivity - often by up to five times compared to the pristine film.[51] This enhancement is attributed to structural changes, including the protonation of PSS chains into PSS-H[55], enhanced π-π stacking between PEDOT chains[56], and morphological evolution.[52] Furthermore, PEDOT:PSS is successfully implemented in organic bioelectronic devices for pH sensing, even in complex biological media.[57–59] Herein, we present the preliminary findings aimed at systematically assessing the impact of electrolyte composition on the charge transport dynamics of PEDOT:PSS. Both the effect of the solution pH and of chemical identity of the cations are evaluated. In particular, the homologous series of chlorides of alkali metals (*viz.,* LiCl, NaCl, KCl) is used as benchmark. Although not completed, this study aims to further contribute to the description of PEDOT:PSS charge transport properties in steady-state conditions.

The first part of this section details the effect of electrolyte pH to the performance of the PEDOT:PSS-based EGOT devices.

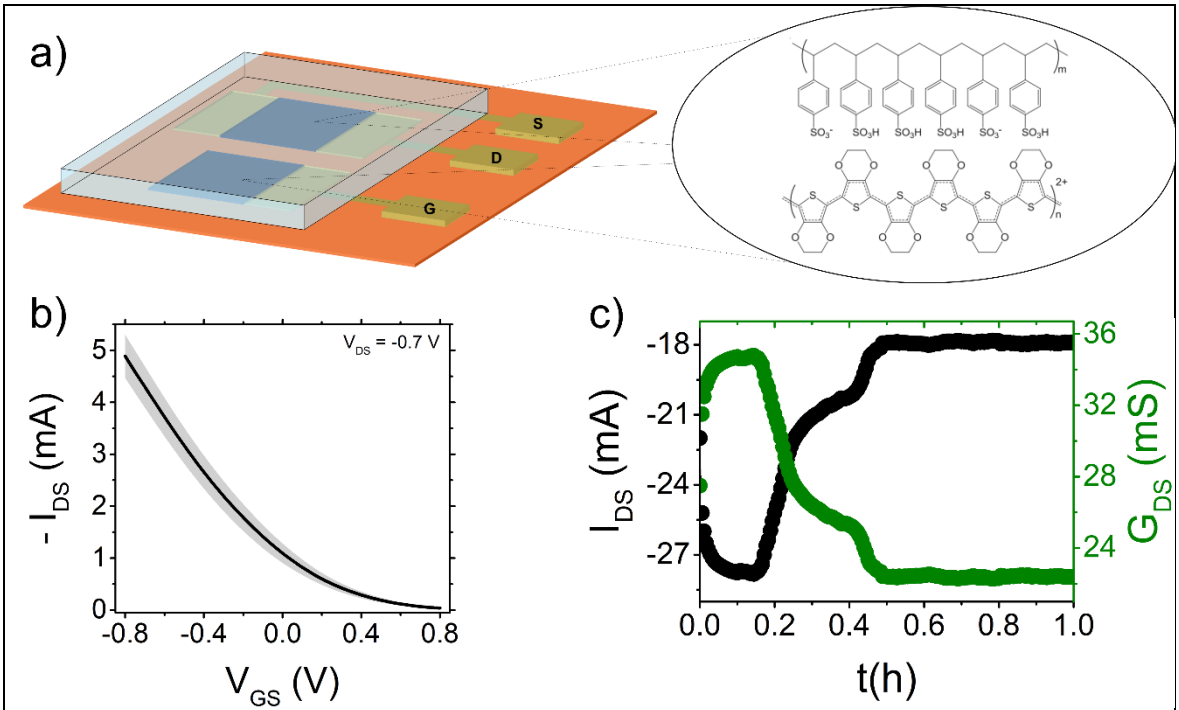

***Figure 6.9**: Architecture and experimental design for assessment of the influence of the electrolyte solution pH on PEDOT:PSS-based EGOT. a) Schematic representation of the EGOT architecture. b-c) Electrical characterization of the steady state conditions, including (b) the typical transfer characteristics (I_{DS} vs V_{GS}) and the current (c) collected at a constant V_{DS} and V_{GS} values (both V_{GS} and V_{DS} equal to -0.8 V) with a measurement time of one hour to reach stability.*

The EGOT architecture (illustrated in **Figure 6.9a**), consisting of a gate and a channel both made of PEDOT:PSS, is built on a polyimide-based substrate. This substrate choice is critical to decouple the measurements from the secondary gating effects previously reported when using a quartz substrate[60], thus ensuring that the observed changes are solely due to the electrolyte/channel interaction.

Two distinct experimental strategies are implemented. In the first, the typical I-V transfer characteristics are collected, sweeping the gate-source voltage V_{GS} between -0.8 and +-0.8 V, while fixing the drain-source voltage (V_{DS}) at -0.7 V (**Figure 6.9b**). In the second experiment, the EGOT current is measured at fixed V_{DS} (*i.e.,* -0.8, -0.7, -0.5, -0.3, -0.1 V) and fixed V_{GS} (*i.e.,* -0.8, -0.6, -0.4, -0.2, 0.2, 0.4, 0.6, 0.8 V) over a one-hour measurement time to ensure the channel reached the stability (**Figure 6.9c**).

The contribution of pH is first evaluated by collecting the transfer characteristics using 0.9% NaCl as the supporting electrolyte, with the pH varied by adding 1M HCl or 1M NaOH. 0.9% NaCl at pH 7 served as the reference electrolyte (the device baseline) to account for experimental variability affecting the array fabrication process. The influence of pH is quantified using a normalized signal $S_{I_{DS}}$ calculated as the relative difference between the current at different pH and the baseline current (Equation 6.2).

$$S_{IDS} = \frac{I_{DS}(pH) - I_{DS}(NaCl\ 0.9\%)}{I_{DS}(NaCl\ 0.9\%)} \qquad \text{(Eq. 6.2)}$$

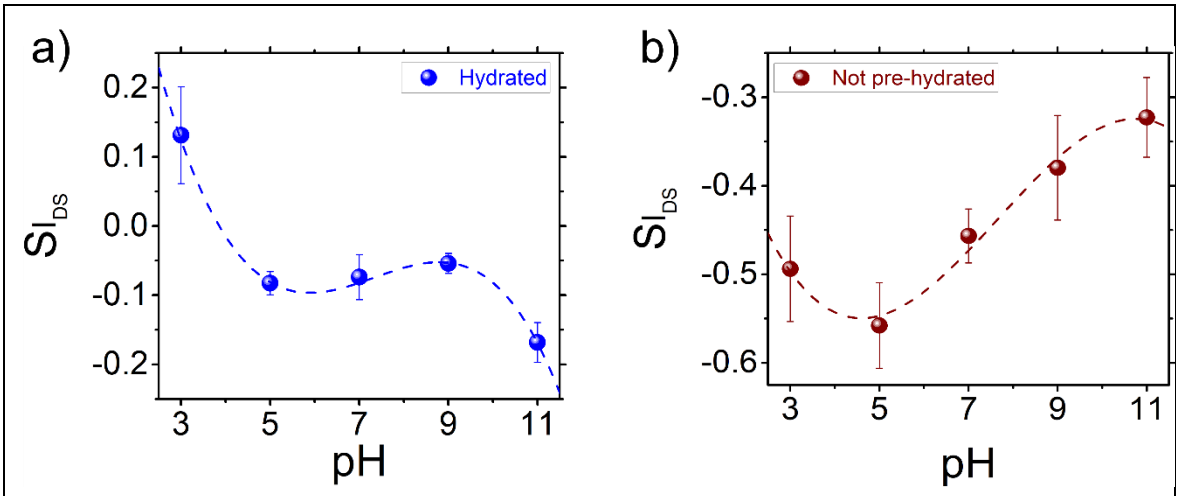

***Figure 6.10**: Influence of pH on PEDOT:PSS-based EGOTs. SI_{DS} trend vs pH for devices after a pre-hydration process in water overnight (blue markers, a) and without the pre-hydration step (brown markers, b). Error bars are the standard error of the mean for 8 devices for each pH value. Cubic fits are used as guide for the eye.*

Figure 6.10a displays the $S_{I_{DS}}$ results obtained from devices pre-hydrated via overnight immersion in a Milli-Q water bath. During this hydration process, the PEDOT:PSS film undergoes gradual swelling, leading to a structural rearrangement of its morphological features.[52,61–63] The $S_{I_{DS}}$ trend versus pH shows at acidic pH a positive $S_{I_{DS}}$ value, indicating an increase of the transistor on-current, compared to the reference electrolyte (0.9% NaCl, pH 7). The higher I_{DS} registered at pH 3 confirms that the protonation of the PSS^- chains results in an increase of film conductivity. Around the neutrality point (5 < pH < 9), substantially no differences are registered by varying the pH of the electrolyte solution (0.9% NaCl). This indicates that the influence of the electrolyte over the PEDOT:PSS film is dominated by the high concentration of the sodium chloride supporting electrolyte, rather than

by the small pH variation. Conversely, at alkaline pH, a negative S_{IDS} value is obtained. This is attributed to the stabilization of the insulating, deprotonated PSS^- chains, leading to a mild reduction in the channel current.

The investigation of the effect of the electrolyte solution pH on PEDOT:PSS films integrated in EGOTs architecture is extended to non-pre-hydrated devices. Surprisingly, the signal exhibited negative values across the entire pH range, indicating a decrease in device current at every tested pH compared to the 0.9% NaCl baseline. This behaviour can be primarily attributed to the early stages of the swelling process occurring within the PEDOT:PSS film during the measurement of non-pre-hydrated films. Modarresi and collaborators[63] demonstrated that PEDOT:PSS swelling is triggered by the deprotonation of sulfonate groups on the PSS^- chains. This deprotonation leads to the expansion of the PSS-rich regions, which function as nanometre-scale insulating layers. This expansion hinders the electronic connections between the conducting PEDOT-rich regions, consequently limiting the overall electronic conductivity of the film.[64]

Since deprotonation is modulated by the pH of the electrolyte solution, the observed S_{IDS} trend versus pH suggests a complex interplay between the electrostatic contribution and the mechanical effects of the PSS^- chains. At alkaline pHs, the degree of deprotonation increases; this should promote swelling, leading to the partial desorption of the strongly negatively charged PSS^- chains from the PEDOT matrix.[64] The removal of excess PSS^- should induce the formation of a highly ordered and densely packed $PEDOT^+$ network, thereby facilitating charge transfer between the polymer chains.[65] This results in less negative S_{IDS} (*viz.,* less pronounced current decrease) at high pH. Conversely, at acidic pH, the deprotonation level is lower (pKa of PSS = 2.9[52]) and therefore the swelling process does not lead to the removal of the insulating PSS^- chains, thus reducing the electronic conductivity (*viz.,* the current) of the PEDOT:PSS film in the EGOT architecture.

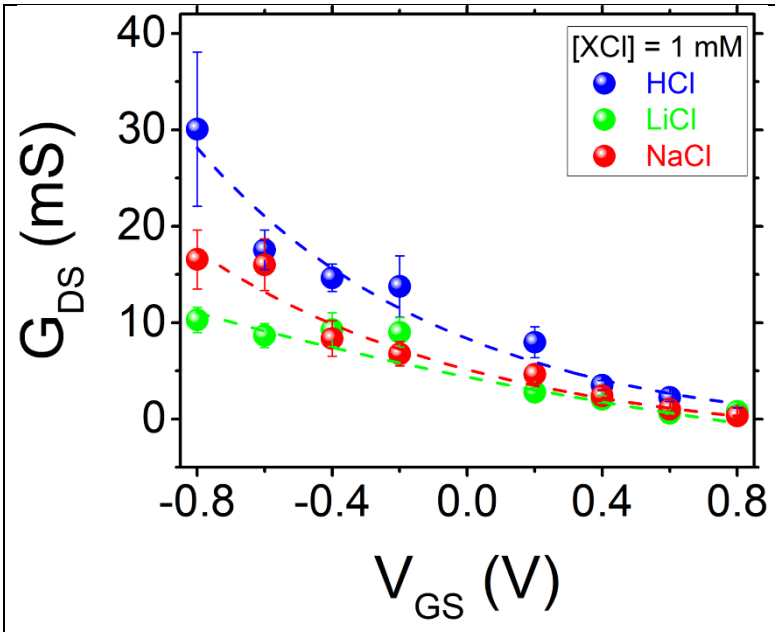

***Figure 6.11**: Average channel conductance (G_{DS}) at different V_{GS} for 1 mM electrolyte solution of HCl (blue), NaCl (red) and LiCl (green).*

To validate the hypothesis that acidic conditions promote enhanced conductivity in the stable, pre-hydrated PEDOT:PSS film, the EGOT architecture is investigated using three different electrolyte solutions at a fixed concentration equal to 1 mM: HCl, LiCl and NaCl. This methodology enables the isolation of the influence of acidity, by comparing an acidic solution (HCl) with non-acidic alkali metals chloride solutions (NaCl, LiCl) with the same molarity. Measurements are performed by applying fixed drain-source potentials V_{DS} (*i.e.,* -0.8, -0.7, -0.5, -0.3, -0.1 V) and fixed V_{GS} (*i.e.,* -0.8, -0.6, -0.4, -0.2, 0.2, 0.4, 0.6, 0.8 V). Each condition is held for one hour to ensure the channel reached the necessary stability condition (**Figure 6.9c**). The channel conductance (G_{DS}) is evaluated as the ratio between the source-drain current (I_{DS} at t = 60 min) and the applied voltage (V_{DS}). **Figure 6.11** displays the average conductance values, (mean of all the V_{DS} conditions) as a function of V_{GS}. The results conclusively confirm the critical role of the acidity in increasing the PEDOT:PSS conductance in stable films, as already reported in literature.[55,65] This effect is, quite obviously, maximized at negative V_{GS} (*i.e.,* when the EGOTs are in the on-state) while it is not visible in the off-state, where cation de-doping dominates over all the other effects. Interestingly, solutions containing Na^+ cations yield higher channel conductance compared to Li^+ solutions, suggesting that the steady-state performance of PEDOT:PSS EGOTs might be tuned by the specific cationic species present in the electrolyte.

To delve deeper into the mechanism governing the influence of cations, both the cation identity and concentration are systematically scanned in a more controlled experimental setup. It features a top-gate architecture with a non-polarizable Ag/AgCl gate electrode and a PEDOT:PSS channel on a quartz substrate, as schematically shown in **Figure 6.12a**.

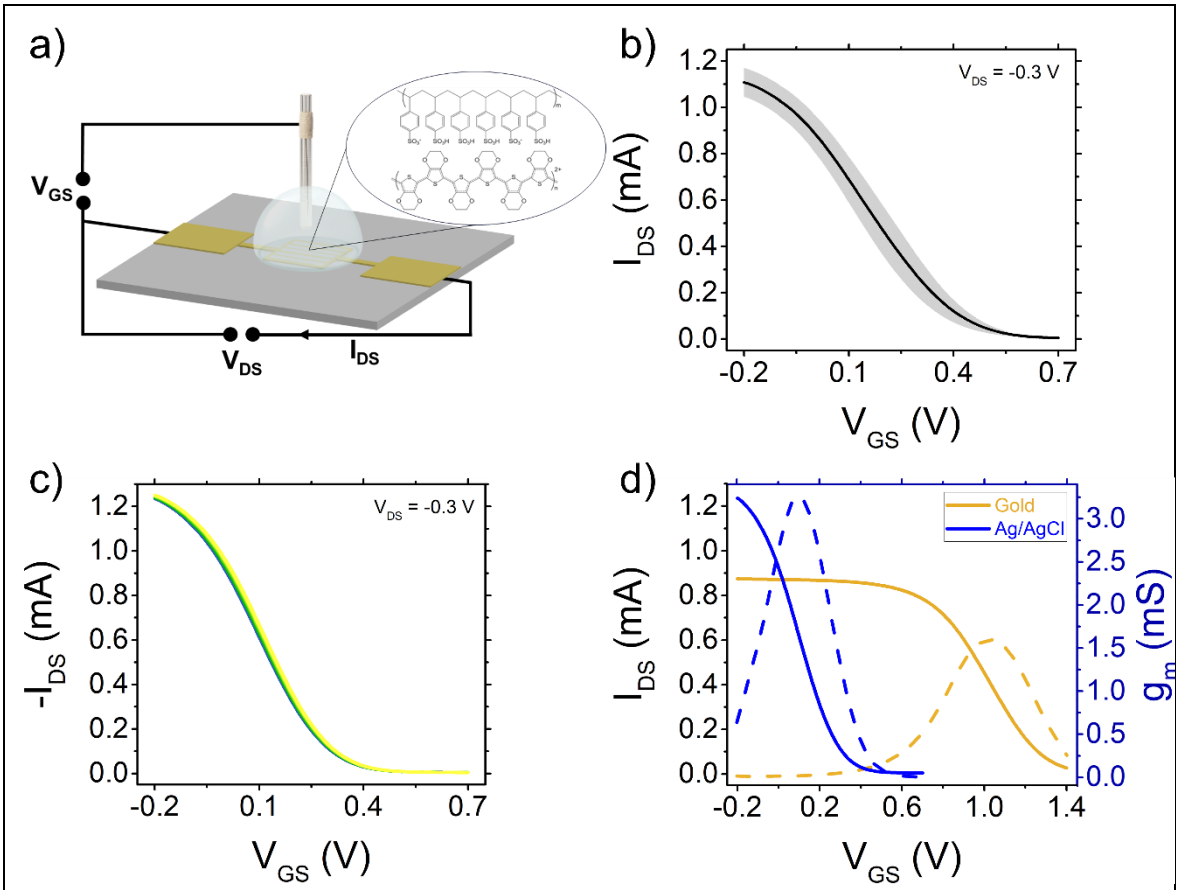

***Figure 6.12**: Setup used to characterize the influence of different cations on PEDOT:PSS channel in the EGOT architecture. a) Design of the experimental setup consisting in an Ag/AgCl top-gate architecture. b) Average transfer characteristics (number of independent channels = 11) of the PEDOT:PSS-EGOT device with VDS = -0.3 V c) Stability of the device during 50 consecutive transfer curve cylces at VDS = -0.3 V. d) Influence of the gate electrode material (Ag/AgCl vs gold) on the PEDOT:PSS-based EGOT.*

This design ensures high stability in the presence of increasing cation concentrations and decouples the interaction between the cations and the gate electrode, which inevitably occurs when using PEDOT:PSS gates (**Figure 6.9a**). Further details regarding the device fabrication process are reported in Chapter 3. **Figure 6.12b** shows the average I-V transfer characteristics, demonstrating the high

reproducibility of the fabrication and characterization procedures, which additionally enable an excellent stability over time (**Figure 6.12c**). Moreover, the use of Ag/AgCl as gate electrode offers the important advantage of shifting the maximum EGOT transconductance towards gate potentials closer to 0 V, if compared with gold electrode (**Figure 6.12d**). This represents a crucial feature when aiming at translation organic electronic devices.[66–68] **Figure 6.13** displays the preliminary results obtained with this experimental setup in presence of increasing concentration of LiCl, NaCl and KCl.

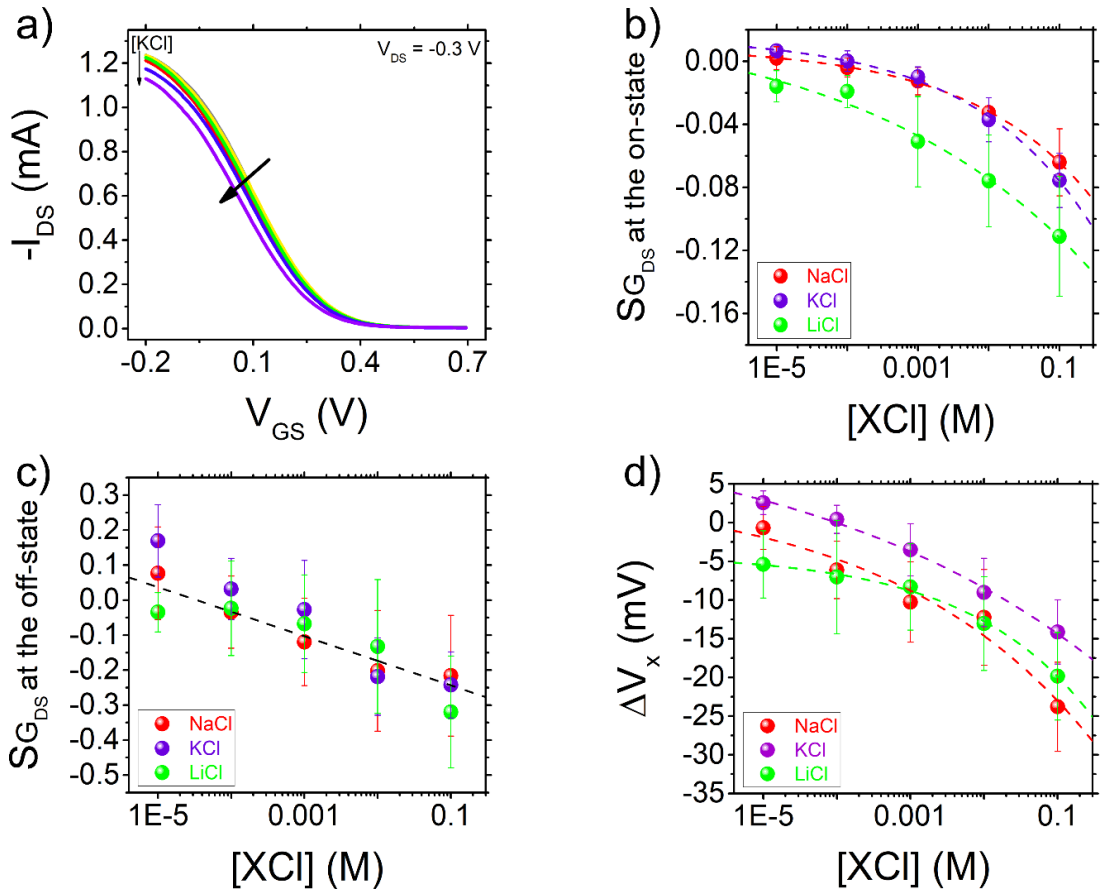

***Figure 6.13**: Influence of increasing concentration of alkali metal chloride solutions on PEDOT:PSS-based EGOT performance. a) Representative transfer characteristics collected at increasing concentration of KCl at V_{DS} = -0.3 V. The same trend is observed for also for LiCl and NaCl. b) Semilogplot of the relative variation of the channel conductance in the on state (viz., V_{GS} = -0.2 V) vs XCl concentration. Equation 6.4 is used as guide for the eyes. c) Semilogplot of the relative variation of the channel conductance in the off state (viz., V_{GS} = 0.6 V) vs XCl concentration. d) Semilog plot of ΔVx vs [XCl], fitted according to Equation 6.4. LiCl are green markers, NaCl red markers, KCl purple markers. Error bars represent the standard error of the mean (SEM) for nine independent devices collected at V_{DS} = -0.3 V, -0.5 V,-0.7 V.*

Figure 6.13a shows representative transfer characteristics recorded while increasing the concentration of alkali metal chloride solutions. As the concentration increases, the transfer curves display a decrease of the on-state current together with a systematic shift of the turn-on voltage (V_T) towards more negative V_{GS} values. To exclude possible artefacts arising from the applied drain-source bias, transfer

curves are acquired at three different V_{DS} values (-0.3 V, -0.5 V, and -0.7 V). The overall influence of the electrolyte composition on device performance is therefore evaluated through the average conductance across all V_{DS} values.

The relative variation of the channel conductance in the on-state (**Figure 6.13b**) - defined as the ratio between the conductance measured at a given salt concentration and that measured in pure water - decreases as the electrolyte concentration increases. This behaviour reflects the fact that PEDOT:PSS is fully doped in pure water and therefore exhibits its highest conductivity. Notably, NaCl and KCl induce comparable responses, whereas LiCl produces a more pronounced decrease, plausibly because the high charge density of Li^+ ions promote stronger interactions with the PSS^- chains, which limits the de-intercalation of cations during the application of a negative V_{GS}.

On the other hand, the conductance in the off-state (V_{GS} = 0.6 V), shown in **Figure 6.13c**, decreases linearly upon increasing salt concentration, with no significant differences among the cation species. In this regime, cations are driven towards the polymer-electrolyte interface by the positive gate bias, and the PEDOT:PSS is fully de-doped. This impairs the distinction between cations, and the sole observable effect is the scaling of conductance with concentration, independently from the chemical identity of the cations.

Equation 6.3 defines a novel observable, V_x, as the variation between the turn-on voltage V_T, extracted by fitting the transfer curves using the Equation 4.1 derived from the model of Zanotti *et al.,*[16], and the drain-source voltage applied to collect the transfer characteristics.

$$V_x = V_T - V_{DS} \quad \text{(Eq. 6.3)}$$

This parameter, with some approximation, represents the effective gate-drain potential at turn on (*i.e.,* when $V_{GS} = V_T$). The use of V_x enables condensation of the information gathered at all V_{DS} values, as previously discussed for conductance. ΔV_x is defined as the difference between V_x measured in the salt solution and V_x measured in water. **Figure 6.13d** shows the dependency of ΔV_x with salt concentration. More negative ΔV_x values indicate that a less positive V_{GD} is required to deactivate the channel. Among the three salts, LiCl exhibits the smallest ΔV_x variation with concentration, consistent with the strong interaction of Li^+ with the PEDOT:PSS matrix, which reduces the extent to which V_T can be modulated.

Interestingly, ΔV_x also provides partial discrimination between Na^+ and K^+, as K^+ yields systematically more positive ΔV_x values. The dependence of ΔV_x on salt concentration can be phenomenologically described by Equation 6.4:

$$\Delta V_x = a + b \cdot [XCl]^c \quad \text{(Eq. 6.4)}$$

The extracted parameters are reported in **Table 6.1**:

***Table 6.1**: Best fit parameters extracted from Equation 6.3 for LiCl, NaCl and KCl.*

	LiCl	NaCl	KCl
a	-4.02 ± 0.94 mV	0.45 ± 10.66 mV	13.95 ± 6.25 mV
b	-0.030 ± 0.002	-0.040 ± 0.006	-0.036 ± 0.0049
c	0.26 ± 0.04	0.16 ± 0.12	0.10 ± 0.04

The parameters *a* and *c* discriminate between Li^+, Na^+, K^+ with a trend that mirrors the trend alongside the first group of the periodic table.

Taken together, these results suggest that the chemical nature of the alkali metals in solution modulates the performances of PEDOT:PSS-based EGOTs, confirming a more complex doping/de-doping mechanism in organic semi-conductors with respect to the “compensation de-doping” model, typically used for PEDOT:PSS.[17] These seminal results, however, do not conclude the complex underlying scientific question, which regards individuation of the specific physicochemical properties of the cations which modulate charge transport within PEDOT:PSS films. To complete this investigation, the effect on PEDOT:PSS-EGOT devices of the full homologous series of alkali-metal chloride solutions will be essential, and it will be the subject of upcoming reports. It is important to emphasize that these preliminary findings demonstrate the relevance and potential of advanced data-analysis strategies when applied to organic bioelectronic devices. Once the complete series of alkali-metal salts is available, the multivariate approaches discussed in this thesis may uncover novel and potentially informative interaction mechanisms between the PEDOT:PSS film and solvated cations, driven by the underlying physicochemical nature of the electrolyte solutions.

6.3 Bibliography

[1] P. Gkoupidenis, N. Schaefer, X. Strakosas, J. A. Fairfield, G. G. Malliaras, *Appl. Phys. Lett.* **2015**, *107*, DOI 10.1063/1.4938553.

[2] P. Gkoupidenis, N. Schaefer, B. Garlan, G. G. Malliaras, *Adv. Mater.* **2015**,

27, 7176–7180.

[3] M. Giordani, M. Berto, M. Di Lauro, C. A. Bortolotti, M. Zoli, F. Biscarini, *ACS Sensors* **2017**, *2*, 1756–1760.

[4] M. Giordani, M. Sensi, M. Berto, M. Di Lauro, C. A. Bortolotti, H. L. Gomes, M. Zoli, F. Zerbetto, L. Fadiga, F. Biscarini, *Adv. Funct. Mater.* **2020**, *30*, 1–13.

[5] M. Di Lauro, A. De Salvo, G. C. Sebastianella, M. Bianchi, S. Carli, M. Murgia, L. Fadiga, F. Biscarini, *ACS Appl. Electron. Mater.* **2020**, *2*, 1849–1854.

[6] H. F. P. Barbosa, G. D. G. Higuita, F. Gunther, G. C. Faria, *Adv. Electron. Mater.* **2022**, *8*.

[7] F. Rondelli, A. De Salvo, G. C. Sebastianella, M. Murgia, L. Fadiga, F. Biscarini, M. Di Lauro, *Neuromorphic Comput. Eng.* **2023**, *3*, 0–8.

[8] K. Janzakova, I. Balafrej, A. Kumar, N. Garg, C. Scholaert, J. Rouat, D. Drouin, Y. Coffinier, S. Pecqueur, F. Alibart, *Nat. Commun.* **2023**, *14*, 1–10.

[9] F. Rondelli, M. Di Lauro, G. Calandra Sebastianaella, A. De Salvo, M. Genitoni, M. Murgia, P. Greco, C. G. Ferroni, R. Viaro, L. Fadiga, F. Biscarini, *Adv. Electron. Mater.* **2024**, *10*, 1–9.

[10] N. L. Nozella, G. S. Selmi, N. B. Guerra, M. R. Piton, C. F. O. Graeff, R. F. de Oliveira, *Neuromorphic Comput. Eng.* **2025**, *5*.

[11] E. Stein, O. Nahor, M. Stolov, V. Freger, I. M. Petruta, I. McCulloch, G. L. Frey, *Nat. Commun.* **2022**, *13*, DOI 10.1038/s41467-022-33264-2.

[12] G. S. Selmi, E. R. Lourenço Neto, G. C. Lelis, A. K. Okazaki, A. Riul, M. L. Braunger, R. F. de Oliveira, *Adv. Electron. Mater.* **2025**, *11*, DOI 10.1002/aelm.202400791.

[13] S. Yuan, Y. Li, Y. Xia, C. Selomulya, X. Zhang, *J. Memb. Sci.* **2021**, *621*, 118995.

[14] P. R. Ferrer, A. Mace, S. N. Thomas, J. W. Jeon, *Nano Converg.* **2017**, *4*, DOI 10.1186/s40580-017-0123-0.

[15] K. Ge, H. Shao, E. Raymundo-Piñero, P. L. Taberna, P. Simon, *Nat. Commun.* **2024**, *15*, DOI 10.1038/s41467-024-46280-1.

[16] R. Zanotti, M. Sensi, M. Berto, A. Paradisi, M. Bianchi, P. Greco, C. A. Bortolotti, M. Di Lauro, F. Biscarini, *Adv. Mater.* **2024**, *36*, DOI 10.1002/adma.202410940.

[17] D. A. Bernards, G. Malliaras, *Adv. Funct. Mater.* **2007**, *17*, 3538–3544.

[18] J. Rivnay, S. Inal, A. Salleo, R. M. Owens, M. Berggren, G. G. Malliaras, *Nat.*

Rev. Mater. **2018**, *3*, DOI 10.1038/natrevmats.2017.86.

[19] J. T. Friedlein, R. R. McLeod, J. Rivnay, *Org. Electron.* **2018**, *63*, 398–414.

[20] E. Stavrinidou, P. Leleux, H. Rajaona, D. Khodagholy, J. Rivnay, M. Lindau, S. Sanaur, G. G. Malliaras, *Adv. Mater.* **2013**, *25*, 4488–4493.

[21] N. Coppedè, M. Villani, F. Gentile, *Sci. Rep.* **2014**, *4*, 1–7.

[22] S. Pecqueur, I. Lončarić, V. Zlatić, D. Vuillaume, Ž. Crljen, *Org. Electron.* **2019**, *71*, 14–23.

[23] S. Pecqueur, D. Vuillaume, Ž. Crljen, I. Lončarić, V. Zlatić, *Electron. Mater.* **2023**, *4*, 80–94.

[24] S. Pecqueur, D. Guérin, D. Vuillaume, F. Alibart, *Org. Electron.* **2018**, *57*, 232–238.

[25] H. Tang, P. Lin, H. L. W. Chan, F. Yan, *Biosens. Bioelectron.* **2011**, *26*, 4559–4563.

[26] R. Colucci, B. de A. Feitosa, G. C. Faria, *Adv. Electron. Mater.* **2024**, *10*.

[27] H. Yoo, M. Ghittorelli, D. K. Lee, E. C. P. Smits, G. H. Gelinck, H. Ahn, H. K. Lee, F. Torricelli, J. J. Kim, *Sci. Rep.* **2017**, *7*, 1–13.

[28] J. Zaumseil, H. Sirringhaus, *Chem. Rev.* **2007**, *107*, 1296–1323.

[29] K. Shi, W. Zhang, D. Gao, S. Zhang, Z. Lin, Y. Zou, L. Wang, G. Yu, *Adv. Mater.* **2018**, *30*, 1–8.

[30] K. Zhou, H. Dong, H. li Zhang, W. Hu, *Phys. Chem. Chem. Phys.* **2014**, *16*, 22448–22457.

[31] F. Li, C. Ma, H. Wang, W. Hu, W. Yu, A. D. Sheikh, T. Wu, *Nat. Commun.* **2015**, *6*, 1–8.

[32] W. Hu, Z. Sheng, X. Hou, H. Chen, Z. Zhang, D. W. Zhang, P. Zhou, *Small Methods* **2021**, *5*, 1–29.

[33] S. Pei, H. M. Cheng, *Carbon N. Y.* **2012**, *50*, 3210–3228.

[34] R. Furlan de Oliveira, P. A. Livio, V. Montes-García, S. Ippolito, M. Eredia, P. Fanjul-Bolado, M. B. González García, S. Casalini, P. Samorì, *Adv. Funct. Mater.* **2019**, *29*, DOI 10.1002/adfm.201905375.

[35] M. Sensi, R. F. de Oliveira, M. Berto, M. Palmieri, E. Ruini, P. A. Livio, A. Conti, M. Pinti, C. Salvarani, A. Cossarizza, J. M. Cabot, J. Ricart, S. Casalini, M. B. Gonzalez-Garcia, P. F. Bolado, C. A. Bortolotti, F. Biscarini, *Adv. Mater.* **2023**, *35*.

[36] M. Sensi, R. F. de Oliveira, M. Berto, A. Paradisi, P. Greco, C. A. Bortolotti, P. Samorì, F. Biscarini, *Adv. Funct. Mater.* **2024**, *34*, 1–14.

[37] P. Guermonprez, L. T. Anh, L. Renaud, P. Nioche, E. Krejci, A. Alleaume-Butaux, N. Battaglini, V. T. Thu, S. Sanaur, B. Piro, *Biosens. Bioelectron. X* **2025**, *23*, 0–6.

[38] L. Kergoat, L. Herlogsson, B. Piro, M. C. Pham, G. Horowitz, X. Crispin, M. Berggren, *Proc. Natl. Acad. Sci. U. S. A.* **2012**, *109*, 8394–8399.

[39] M. T. Sharbati, Y. Du, J. Torres, N. D. Ardolino, M. Yun, F. Xiong, *Adv. Mater.* **2018**, *30*.

[40] T. F. Schranghamer, A. Oberoi, S. Das, *Nat. Commun.* **2020**, *11*, 1–11.

[41] V. López, R. S. Sundaram, C. Gómez-Navarro, D. Olea, M. Burghard, J. Gómez-Herrero, F. Zamora, K. Kern, *Adv. Mater.* **2009**, *21*, 4683–4686.

[42] V. C. Tung, M. J. Allen, Y. Yang, R. B. Kaner, *Nat. Nanotechnol.* **2009**, *4*, 25–29.

[43] W. Gao, L. B. Alemany, L. Ci, P. M. Ajayan, *Nat. Chem.* **2009**, *1*, 403–408.

[44] A. J. Bard, L. R. Fraulkner, *Electrochemical Methods: Fundamentals and Applications*, **2012**.

[45] M. Son, H. Kim, J. Jang, S. Y. Kim, H. C. Ki, B. H. Lee, I. S. Kim, M. H. Ham, *ACS Appl. Mater. Interfaces* **2019**, *11*, 47247–47252.

[46] P. Hu, B. Huang, Q. Miao, H. Wang, L. Liu, W. Tai, T. Liu, Z. Li, S. Chen, L. Qian, *Crystals* **2019**, *9*, DOI 10.3390/cryst9040214.

[47] M. J. Park, Y. Park, J. S. Lee, *ACS Appl. Electron. Mater.* **2020**, *2*, 339–345.

[48] Y. Park, M.-K. Kim, J. S. Lee, *Carbon N. Y.* **2020**, 455–460.

[49] E. K. Jang, Y. Park, J. S. Lee, *Nanoscale* **2019**, *11*, 15382–15388.

[50] P. Lin, F. Yan, H. L. W. Chan, *ACS Appl. Mater. Interfaces* **2010**, *2*, 1637–1641.

[51] F. Kong, C. Liu, H. Song, J. Xu, Y. Huang, H. Zhu, J. Wang, *Synth. Met.* **2013**, *185–186*, 31–37.

[52] M. Modarresi, J. F. Franco-Gonzalez, I. Zozoulenko, *Phys. Chem. Chem. Phys.* **2019**, *21*, 6699–6711.

[53] P. Rathore, J. D. Schiffman, *ACS Eng. Au* **2023**, *3*, 527–536.

[54] T. C. Tsai, H. C. Chang, C. H. Chen, Y. C. Huang, W. T. Whang, *Org. Electron.* **2014**, *15*, 641–645.

[55] Y. Xia, J. Ouyang, *ACS Appl. Mater. Interfaces* **2010**, *2*, 474–483.

[56] J. Kim, J. G. Jang, J. I. Hong, S. H. Kim, J. Kwak, *J. Mater. Sci. Mater. Electron.* **2016**, *27*, 6122–6127.

[57] F. Mariani, I. Gualandi, M. Tessarolo, B. Fraboni, E. Scavetta, *ACS Appl.*

Mater. Interfaces **2018**, *10*, 22474–22484.

[58] F. Mariani, M. Serafini, I. Gualandi, D. Arcangeli, F. Decataldo, L. Possanzini, M. Tessarolo, D. Tonelli, B. Fraboni, E. Scavetta, *ACS Sensors* **2021**, *6*, 2366–2377.

[59] L. Possanzini, F. Decataldo, F. Mariani, I. Gualandi, M. Tessarolo, E. Scavetta, B. Fraboni, *Sci. Rep.* **2020**, *10*, 1–14.

[60] M. Di Lauro, S. Casalini, M. Berto, A. Campana, T. Cramer, M. Murgia, M. Geoghegan, C. A. Bortolotti, F. Biscarini, *ACS Appl. Mater. Interfaces* **2016**, *8*, 31783–31790.

[61] L. Bießmann, L. P. Kreuzer, T. Widmann, N. Hohn, J. F. Moulin, P. Müller-Buschbaum, *ACS Appl. Mater. Interfaces* **2018**, *10*, 9865–9872.

[62] B. Sarkar, M. Jaiswal, D. K. Satapathy, *J. Phys. Condens. Matter* **2018**, *30*, DOI 10.1088/1361-648X/aabe51.

[63] M. Modarresi, A. Mehandzhiyski, M. Fahlman, K. Tybrandt, I. Zozoulenko, *Macromolecules* **2020**, *53*, 6267–6278.

[64] M. Modarresi, I. Zozoulenko, *Phys. Chem. Chem. Phys.* **2022**, *24*, 22073–22082.

[65] C. Yeon, S. J. Yun, J. Kim, J. W. Lim, *Adv. Electron. Mater.* **2015**, *1*, 1–8.

[66] P. R. Paudel, V. Kaphle, D. Dahal, R. K. Radha Krishnan, B. Lüssem, *Adv. Funct. Mater.* **2021**, *31*, 1–12.

[67] D. Khodagholy, J. Rivnay, M. Sessolo, M. Gurfinkel, P. Leleux, L. H. Jimison, E. Stavrinidou, T. Herve, S. Sanaur, R. M. Owens, G. G. Malliaras, *Nat. Commun.* **2013**, *4*, 1–6.

[68] M. Di Lauro, E. Zucchini, A. De Salvo, E. Delfino, M. Bianchi, M. Murgia, S. Carli, F. Biscarini, L. Fadiga, *Adv. Mater. Interfaces* **2022**, *9*.

Chapter 7: Conclusions and Future Perspectives

This chapter concludes the PhD dissertation by summarizing the strategies presented and validated to enhance the performance of EGOT platforms. It highlights how the synergistic integration of interface engineering and data analysis paves the way for future advancements in organic bioelectronics.

This PhD thesis discussed a library of strategies to improve the performance of organic electronic devices, with a primary focus on the Electrolyte-Gated Organic Transistor (EGOT) platform. This work has demonstrated that by tailoring the surface chemistry of the addressable interfaces within the EGOT architecture (namely, the gate/electrolyte and channel/electrolyte interfaces), it is possible to finely tune device performance. Furthermore, this dissertation envisions the application of chemometric tools for advanced data analysis on post-process signals. The impact of such a synergistic hardware/software approach is validated through two (bio)sensing platforms and one neuromorphic system as case studies.

This work demonstrates an EGOT immunosensor for L-Tryptophan detection ranging from 1 fM to 10 nM. We first establish that device sensitivity can be tailored by optimizing the gate surface chemistry. Specifically, controlling the pH of the cysteamine-glutaraldehyde (CYS-GA) self-assembled monolayer (SAM) proves to be a pivotal factor in maximizing anti-L-Tryptophan antibody grafting efficiency. This optimized functionalization strategy (Schiff Base Reaction, SBR) affords higher sensitivity and a robust multiparametric response when benchmarked against the gold-standard EDC-NHS activation. However, since traditional univariate analysis of the dose curve fails to distinguish between Tryptophan enantiomers, we develop a synergistic EGOT/chemometric approach capable of unambiguous enantiomer clustering down to 1-10 pM. These levels are four and six orders of magnitude lower than current label-free methods and circular/magnetic dichroism, respectively. Taken together, these results highlight the impact of applying multivariate data analysis to advanced EGOT sensing platforms, transcending the limitations of traditional dose-response curves.

The tunability of the gate/electrolyte interface is further exploited via MXene surface chemistry to demonstrate ultrasensitive Dopamine detection. In collaboration with Prof. Ioan-Alexandru Baragau, three distinct chemically-functionalized MXenes are synthesized and integrated as sensing layers within the EGOT architecture, resulting in an innovative, high-performance platform capable of lowering Dopamine detection limits to the femtoMolar level. To interpret the complex interplay arising from the heterogeneous MXene surface landscape, the device's multiparametric response is processed using multivariate models. Extending the chemometric framework successfully applied to the L-Tryptophan immunosensor, this analysis

provided crucial insights into the interaction mechanisms between the specific surface terminations of different MXenes and the target molecule.
The results obtained from both sensing platforms confirm that the application of advanced data analysis tools is essential to unlock the full potential of the multiparametric response of EGOT devices. This approach enables enhanced selectivity, as demonstrated by the L-Tryptophan immunosensor, and provides refined monitoring of the biorecognition process, as evidenced by the MXene-EGOT device. Ultimately, this work contributes to overcoming significant bottlenecks in the field of EGOT biosensors, paving the way for future real-world applications.

Following the optimization of the gate/electrolyte interface, the focus of this thesis extends to the investigation of the channel/electrolyte interface. Ion dynamics at this interface are investigated by focusing on rGO and PEDOT:PSS as archetypical materials for Organic Mixed Ionic-Electronic Conductors (OMIECs).
This thesis presents a novel, tunable fabrication method based on the in-situ electrodeposition of rGO from a GO dispersion. The resulting ambipolar rGO-EGTs exhibit high modulation efficiency and robust charge retention capabilities. By tailoring the transient input signal protocol, we have successfully programmed multilevel memory states with retention timescales exceeding tens of minutes. These results validate *in-situ* electrodeposition as a scalable and versatile approach that enhances device memory characteristics, positioning these architectures as promising building blocks for neuromorphic units.
Subsequently, the study of ion dynamics is extended to PEDOT:PSS. While these devices are well-documented as neuromorphic units, our investigation specifically addressed how the solution composition - namely, the pH and the nature of the ionic species - modulates their performance under steady-state conditions. Interestingly, we demonstrate that the hydration history of the device (pre-hydrated vs. non-pre-hydrated) significantly dictates its behaviour when exposed to electrolyte solutions at varying pH values.
When tested in the presence of a homologous series of alkali-metal chlorides, the multiparametric response extracted from PEDOT:PSS transfer curves suggests a plausible influence of the chemical nature of the cations on device performance. These preliminary but significant findings support the hypothesis that the physicochemical properties of the cations modulate charge transport within PEDOT:PSS films. Finally, it is worth emphasizing that the advanced data analysis

tools introduced in this work hold the potential to unveil novel and insightful interactions between the multiparametric response of organic electronic devices and the various descriptors characterizing the ionic species involved.

Looking forward, the synergistic framework validated herein - combining tailored surface chemistry with chemometrics - holds potential for broader applications beyond biosensing, including neuromorphic computing, smart drug delivery systems, and in-vivo recording and stimulation. The advancement of next-generation EGOT-based platforms will rely on the integration of optimized hardware interfaces with predictive machine learning models, creating a powerful tool to elucidate the interplay between device performance and the structural descriptors of pharmacological agents or metabolic species at the biological interface.

List of Publications and Conferences

Publications

Matteo Genitoni, *Pierpaolo Greco*, Alessandro Paradisi, Matteo Sensi, Marcello Berto, Mauro Murgia, Michele Di Lauro, Carlo Augusto Bortolotti, Luciano Fadiga, Fabio Biscarini*.* "**Discrimination of Tryptophan Enantiomers at Sub-pM Level by Multiparametric Analysis of a Label-Free Organic Immunosensor"**. Small Methods, 2025, 2500545. **DOI**: 10.1002/smtd.202500545

Matteo Genitoni, *Ioan-Alexandru Baragau,*, Matteo Sensi, Dana Georgeta Popescu, George Stan, Petru Palade, Outman El Khouja, Sabina Alexandra Nicolae, Cristian Mihail Teodorescu, Fabio Biscarini & Michele Bianchi*.* **"Leveraging MXene Surface Chemistry for Ultrasensitive Dopamine Detection in Organic Transistor Biosensors"**. Manuscript in preparation.

Maryam Abouali, Federico Rondelli, ***Matteo Genitoni****, Mauro Murgia, Michele Di Lauro,* Luciano Fadiga, and Fabio Biscarini.* **"Electrodeposited Reduced Graphene Oxide EnablesLong-Term Memory in Neuromorphic AmbipolarElectrolyte-Gated Transistors"**. Small, 2025, 21, 2502768. DOI: **10.1002/smll.202502768**

Michele Di Lauro, Federico Rondelli, Anna De Salvo, Alessandro Corsini, ***Matteo Genitoni****, Pierpaolo Greco, Mauro Murgia, Luciano Fadiga and Fabio Biscarini.* "**An organic artificial soma for spatio-temporal pattern recognition via dendritic integration**". Neuromorphic Computing and Engineering, 2024, 4, 2. (**DOI**: 10.1088/2634-4386/ad3a96)

Federico Rondelli, Michele Di Lauro, Gioacchino Calandra Sebastianella, Anna De Salvo,* ***Matteo Genitoni****, Mauro Murgia, Pierpaolo Greco, Carolina Giulia Ferroni, Riccardo Viaro, Luciano Fadiga, Fabio Biscarini.* "A Single Electrode Organic Neuromorphic Device for Dopamine Sensing in Vivo". Advanced Electronic Material, 10, 2400467. (**DOI**: 10.1002/aelm.202400467)

Alice Lunghi, Federica Velluto, Luana Di Lisa,* ***Matteo Genitoni****, Fabio Biscarini, Maria Letizia Focarete, Chiara Gualandi and Michele Bianchi*.* "**Fabrication and characterization of bioresorbable, electroactive and highly regular nanomodulated cell interfaces**". Nanotechnology, 36, 015301. (**DOI**: 10.1088/1361-6528/ad8096)

Federico Rondelli, Maryam Abouali, Anna De Salvo, ***Matteo Genitoni****, Michele Di Lauro*, Luciano Fadiga, Fabio Biscarini.* "**Analog Signal Rectification and Filtering by a Single Electrolyte-Gated Transistor Based on Reduced Graphene Oxide**". Advanced Electronic Material, 2025, e00445. (**DOI**: 10.1002/aelm.202500445)

Conferences

Contributed Talk: Increasing the Sensitivity of EGOFET Biosensor for L-Tryptophan Detection: Effect of pH on Glutaraldehyde-Antibody Biorecognition Layer. **International Winter School for Bioelectronics (BIOel)**, Kirchberg in Tirol, Austria 2024.

Contributed Talk: Influence of Electrolyte Solution Composition on Charge Transport Properties of PEDOT:PSS Thin Film in Electrolyte-Gated Transistor Architectures. **18th International Symposium on Flexible Organic Electronics, (ISFOE25)**, Thessaloniki, Greece, 2025.

Poster presentation: Influence of solution composition on PEDOT:PSS-based Electrolyte-Gated Organic Transistors. **XXIII Giornata della Chimica dell'Emilia Romagna**, Modena, Italy, 2024.

Poster presentation: Influence of Electrolyte Solution Composition on Charge Transport Properties of PEDOT:PSS Transistor Architecture. **Orbitaly 2025**, Brescia, Italy, 2025.